

Micro Ion Mobility Spectrometry for Gas-phase Detection



Raquel Cumeras Olmeda

[This page intentionally left blank]



CONSEJO SUPERIOR
DE INVESTIGACIONES
CIENTÍFICAS

Micro Ion Mobility Spectrometry for Gas-phase Detection

Memòria presentada per

Raquel Cumeras i Olmeda

per optar al títol de Doctora en Física per la
Universitat Autònoma de Barcelona
dins del programa de Doctorat de Física,
del Departament de Física de la Facultat de Ciències.

Els Doctors Isabel Gràcia i Tortadès i Eduard Figueras i Costa, Científics Titulars del Centre Nacional de Microelectrónica, i el Doctor Francesc Pi i Vila, Professor Titular d'Universitat del Departament de Física de la UAB,

Certifiquen:

Que la memòria “*Micro Ion Mobility Spectrometry for Gas-phase Detection*” que presenta la Sra. Raquel Cumeras i Olmeda dins del programa de Doctorat en Física de la Universitat Autònoma de Barcelona s’ha dut sota la seva direcció i tutela.

Bellaterra, Juliol 2013

Els directors:

El tutor:

Isabel Gràcia i Tortadès

Eduard Figueras i Costa

Francesc Pi i Vila

[This page intentionally left blank]

Acknowledgments

*Als meus
en especial a la Caterina per canviar-me la visió del món*

I would like to acknowledge the many people who have contributed, in one way or another, to the completion of this thesis.

First of all, I gratefully acknowledge my supervisors Dr. Isabel Gràcia and Dr. Eduard Figueras for their unconditional support, the possibility of being myself and for the opportunity to work in the development of an Ion Mobility Spectrometer. Also I want to thank my Tutor Dr. Francesc Pi for being there anytime I have need him, since the first time we have work together.

I also want to thank all the staff of the *Institut de Microelectrònica de Barcelona* or IMB-CNM (CSIC) for their logistic and professional support. A warm thank to our librarian Elisenda. In special to all the present and past people from the MESSI/gas group, just thank you to the pleasant meetings and the corridor discussions. Also, thanks to Dr. Carles Cané, as he introduced me in the IMB and for having his 'door' open whatever was the needed.

The work developed in this thesis has been certainly multidisciplinary and would not have been achieved without the collaboration of several external groups:

- To the component groups of the ISIS (MICINN-TEC2007-67962-C04) and NAMIRIS (MICINN-TEC2010-21357-C05) projects for the nice projects meetings and for the opportunity to introduce myself in the amazing world of applying projects.
- I would like to acknowledge Prof. Dr. Jörg Ingo Baumbach for welcome me in my stay at the Clinical Diagnostics Group from the Korea Institute of Science and Technology in Europe, KIST-Europe. I had the opportunity to work and learn the insights of the Ion Mobility Spectrometry field. Also I want to thank

Dr. Sasi dhar Maddula for the warm welcome and for his unconditional help and support during and after being at KIST-Europe.

- I would like to acknowledge the Medical Doctors Heiko Buchinger, Sasha Kreuer and Thomas Volk from the Department of Anesthesiology, Intensive Care and Pain Therapy from the Saarland University Medical Center and Saarland University Faculty of Medicine from Homburg in Germany, for welcoming me in their group and in the hospital, and specially for Heiko's support in whatever I needed in the long hours of experiments while surgery and after being at Homburg Hospital.

Acknowledge to the Fellowship *Formación de Personal Investigador* (FPI) with reference: BES-2008-005267 for the economic support during this thesis, and also to the fellowship stage of the FPI (EEBB-2011-43966) for the economic support to carry out a stage on a Research Center related with the work of the PhD. Also support from the *Comissionat* for University and Research of the DIUE of the *Generalitat de Catalunya* (through project n°2009SGR228). A warm acknowledge to the IBERNAM people (*red nacional en nanotecnologías y microsistemas*) for the workshops and meetings.

Do not forget all the PhD travelers... all the PreDoc, friends and colleagues from the IMB-CNM (CSIC), from KIST-Europe and from several other institutes, that made this travel an enjoyment. Specially Diana, Nuria, Isa, Sara, Bergoi, Petra, Kathrin, Patrick, Till, Roser, Rosa, Stella, you ALL know what means doing a PhD!

And the warmest acknowledge thank to my family and my family-in-law, because without them this PhD journey could not have been possible. A warm thank to my aunt Sarah for her support, as you know what means doing a PhD. Especially my parents, without whom it would not be here and for which I am here. And thanks to my little sister for being herself, and for trying to make me a better person every day.

The last but not for this the less important, lots of thanks to Jaume my life traveler, and to our little Caterina for joining us. And for the ones that will come someday. Because they are the ones that have made this work a reality.

Thanks to everyone,

A handwritten signature in black ink, appearing to be 'Roser', written in a cursive style.

Summary

In an ideal world, we might be able to rapidly detect and classify any type of chemical and biological that is found in low concentrations, using instruments of small size and easy implementation. Is in that scenario where the Ion mobility spectrometry (IMS) appeared. It is a technique of measurement and analysis, where ionized analytes are separated by mobility differences under electric field in a flow of neutral gas or air at ambient pressure and temperature. The advantages of IMS include compactness and portability of instrumentation, short separation time (milliseconds scale), and low detection limits, and allow a wide range of applications. In this sense, an intense research effort has been focused towards miniaturization from the available IMS's devices to the micro high-Field Asymmetric waveform Ion Mobility Spectrometers (FAIMS).

This thesis presents the first developments and technological contributions to the FAIMS at IMB-CNM (CSIC). Particularly, this work is dedicated to the simulation, design, and fabrication of a micro planar FAIMS (p-FAIMS) for security applications. The work is organized in five chapters divided in two sections.

The first section consists of three chapters. Chapter one is introductory, and on Chapter two introduces the lector to the actual state-of-the-art of the Ion Mobility Spectrometry in general and in particular for the micro high-Field Asymmetric waveform Ion Mobility Spectrometry. Chapter three described the modeling of a planar type of FAIMS for different electric fields and flow conditions.

The second section consists of two chapters. Chapter four provides a summary of the different designs and materials considered for the p-FAIMS implementation: Glass-Si-Glass and PCB-PMMA-PCB structures; the technological tasks done for each one and the solving strategies that have led to it. UV photoionization has been the chosen as ionization method for safety reasons in all cases. It also presents the characterization with toluene of the new *low-cost* p-FAIMS prototype fabricated in the IMB-CNM. Chapter five provides a summary of the feasibility study of an online-monitoring of an analgesic drug (remifentanyl) in patients breath under anesthesia. A commercial Ion Mobility Spectrometer is used for this medical application in collaboration with the KIST-Europe and the *Chirurgische Universitätsklinik* from Homburg (Germany).

Resum (català)

En un món ideal, podríem ser capaços de detectar ràpidament i classificar qualsevol tipus de substància química i biològica que es trobés en baixes concentracions, utilitzant instruments petits i de fàcil ús. És en aquest escenari on va aparèixer l'espectrometria de mobilitat iònica (IMS). Es tracta d'una tècnica de mesura i anàlisi, on els analits ionitzats es separen per diferències de mobilitat sota la influència d'un camp elèctric en un flux de gas neutre o d'aire a pressió i temperatura ambient. Els avantatges de l'IMS inclouen instrumentació compacte i portàtil, un temps de separació curt (escala de mil·lisegons), i uns límits de detecció baixos, i permeten una àmplia gamma d'aplicacions. En aquest sentit, un esforç intens de recerca s'ha enfocat cap a la miniaturització dels dispositius d'IMS disponibles vers als micro- espectròmetres de mobilitat iònica de forma d'ona asimètrica i d'alt camp (FAIMS).

iv

En aquesta tesi es presenten els primers desenvolupaments i contribucions tecnològiques als FAIMS en el IMB-CNM (CSIC). En particular, aquest treball està dedicat a la simulació, disseny, i fabricació d'un micro FAIMS planar (p-FAIMS) per a aplicacions de seguretat. El treball s'organitza en cinc capítols dividits en dues seccions.

La primera secció consta de tres capítols. El primer capítol és introductori i en el segon capítol s'introdueix al lector en l'actual estat de la tècnica de l'espectrometria de mobilitat iònica en general i en particular per als micro- espectròmetres de mobilitat iònica de forma d'ona asimètrica i d'alt camp. El tercer capítol descriu el modelatge d'un tipus de FAIMS planar per a diferents camps elèctrics i condicions de flux.

La segona part consta de dos capítols. El quart capítol presenta un resum dels diferents dissenys i materials considerats per a la implementació del p-FAIMS: estructures Vidre-Si-Vidre i PCB-PMMA-PCB, les tasques tecnològiques fetes per cada un i les estratègies de solució que hi han conduït. La fotoionització UV ha estat l'escollida com a mètode de ionització en tots els casos per raons de seguretat. També es presenta la caracterització amb toluè del nou prototip de p-FAIMS de *baix cost* fabricat a l'IMB-CNM. El cinquè capítol es presenta un resum de l'estudi de la viabilitat del monitoratge d'un fàrmac analgèsic (remifentanil) en l'alè de pacients sota anestèsia. Un espectròmetre de mobilitat iònica comercial s'utilitza per a aquesta aplicació mèdica en col·laboració amb el KIST-Europe i la *Chirurgische Universitätsklinik* d'Homburg (Alemanya).

Table of Contents

Acknowledgments i

Summary iii

Resum (català) iv

Section 1:

micro p-FAIMS Development 1

v

Chapter 1: Introduction 3

- 1.1 Introduction 5
- 1.2 Aims of the study 7
- 1.3 Scientific Contribution 8
- 1.4 Projects in which is framed 8
- 1.5 Outline of the Thesis 9
- References 9

Chapter 2: Ion Mobility Spectrometry: State-of-the-art 15

- 2.1 Origin and applications 17
- 2.2 Principle of Ion Mobility Spectrometry 18
 - 2.2.a Sample Introduction Systems 24
 - 2.2.b Ionization region 27

2.2.c Drift region	36
2.2.d Detector region	39
2.2.e Hyphenated Methods with Ion Mobility Spectrometers	41
2.2.f Data collection and treatment	50
2.2 high Field Asymmetric waveform Ion Mobility Spectrometers	57
2.3.a Filtering Region electrodes design	58
2.3.b FAIMS Ion Dynamics	66
2.3.c Detection	74
References	88

Chapter 3: Micro p-FAIMS Modeling 105

3.1 Finite element methods (FEM)	107
3.2 Model Definition	109
3.3 Fluid Dynamics	111
3.4 Electric Fields	114
3.5 Ion Concentration	119
3.6 Ion Detection	121
3.7 Modeled compounds	122
3.8 Simulation Results	124
3.8.a Carrier gas flow rate effects	124
3.8.b Electric Field study	128
3.8.c Ions differentiation	131
3.8.d Filtering Electrodes Length Dependence	144
3.9 Validation	146
Discussion and Summary	149
References	150

Section 2:

Ion Mobility Spectrometry Applications 153

Chapter 4: p-FAIMS Security Applications 155

- 4.1 Device design and assembly 157
 - 4.1.a Ionization method 157
 - 4.1.b Glass-Silicon-Glass Design 163
 - 4.1.c PCB-PMMA-PCB Design 172
- 4.2 Measurements set-up 176
 - 4.2.a The gas supply system 176
 - 4.2.b Experimental set-up 177
- 4.3 p-FAIMS Characterization 181
 - 4.3.a Electrodes biasing 181
 - 4.3.b Detection without High Field 188
 - 4.3.c Detection of Toluene Ions with RF field 198
- Discussion and Summary 202
- References 204

Chapter 5: Medical Applications: Online Monitoring of an Exhaled analgesic in Patients under Anesthesia 207

- 5.1 MCC-IMS for Medical Applications 209
- 5.2 MCC-IMS description 210
 - 5.2.a Room Air variations 212
 - 5.2.b Devices data alignment 214
- 5.3 Control Group 216
- 5.4 *in vitro* Blood test with Remifentanyl 218
 - 5.4.a Blood measurements procedure 220
 - 5.4.b Remifentanyl calibration 220
 - 5.4.c Blood measurements with remifentanyl 222
- 5.5 Medical Considerations 225
 - 5.5.a Pre-operative evaluation 225
 - 5.5.b Anesthesia administration 227

5.5.c Experimental Set-up while surgical anesthesia	234
5.6 Operational Background - Plastic Emissions	237
5.6.a Intubation methods	237
5.6.b Measurements methods	238
5.6.c Laboratory Measurements — MCC-IMS and GC/-MSD	241
5.6.d Plastic emissions in Patients Measurements — MCC-IMS	245
5.7 Exhaled Remifentanil in Patients under Anesthesia	249
Discussion and Summary	253
References	255

Conclusions 259

List of Publications 263

List of Abbreviations, Contractions, Symbols and Acronyms 267

viii

Annexes 271

Annex 4-1: LabView program to control the ACI UV-lamp	273
Annex 4-2: LabView program to acquire data of picoAmmeter for UV lamp test	274
Annex 4-3: Errors: Propagation of Uncertainty	275
Annex 4-4: LabView program to acquire data of picoAmmeter continuously	276
Annex 4-5: LabView program to acquire data of picoAmmeter for a fixed Compensation Voltage Scan	277
Annex 5-1: Box-and-whisker plot	278
Annex 5-2: Control Group definition	279
Annex 5-3: Ethics committee approbation	282
Annex 5-4: Propofol peaks in the MCC-IMS Chromatograms	283
Annex 5-5: Respirator systems	285
Annex 5-6: Patient's data	286
References	289

Section 1:

Micro p-FAIMS

Development

[This page intentionally left blank]

Chapter

I

Introduction

*“The reader should come away convinced from this thesis
that you actually did learn something”*

Richard Brooks

Chapter 1: Introduction	3
1.1 Introduction	5
1.2 Aims of the study.....	7
1.3 Scientific Contribution	8
1.4 Projects in which is framed	8
1.5 Outline of the Thesis.....	9
References	9

1.1 Introduction

Ion mobility spectrometry (IMS) is a technique of measurement and analysis, where ionized analytes are separated by mobility differences under electric field in a flow of neutral gas or air at ambient pressure and room temperature [1-5]. The advantages of IMS, including compactness and portability of instrumentation, short separation time (milliseconds scale), and low detection limits (ppt – ppb range [6]), allow a wide range of applications [7, 8].

Although the IMS principle and technique is relatively old, IMS devices have been extensively developed over the last 20 to 30 years [9-12]. Traditionally, IMS instruments use a drift tube to carry out the separation of ions [1, 9] we will refer to them as conventional IMS. However, a number of other instruments, much more in the micro scale, such as high-Field Asymmetric waveform Ion Mobility Spectrometers (FAIMS), also called Differential Mobility Spectrometers (DMS) [9, 13] have been successfully developed.

Conventional IMS and FAIMS techniques have two main differences [14-17]: (1) the size of the drift channels, and (2) the intensity of the applied electric fields. Conventional IMS have big cylindrical drift channels with multiple electrodes, where a low electric field, generally $100\text{--}350\text{ V}\cdot\text{cm}^{-1}$, is applied parallel to the direction of the main flow as can be seen in Figure 1-1A. The FAIMS devices can have different configurations of the drift channels (cylindrical or planar) with two or more electrodes, where a high asymmetric electric field with low E_L and high E_H levels, generally with an amplitude greater than $10,000\text{ V}\cdot\text{cm}^{-1}$, is applied perpendicular to the direction of the flow gas, as can be seen in Figure 1-1B and in Figure 1-1C.

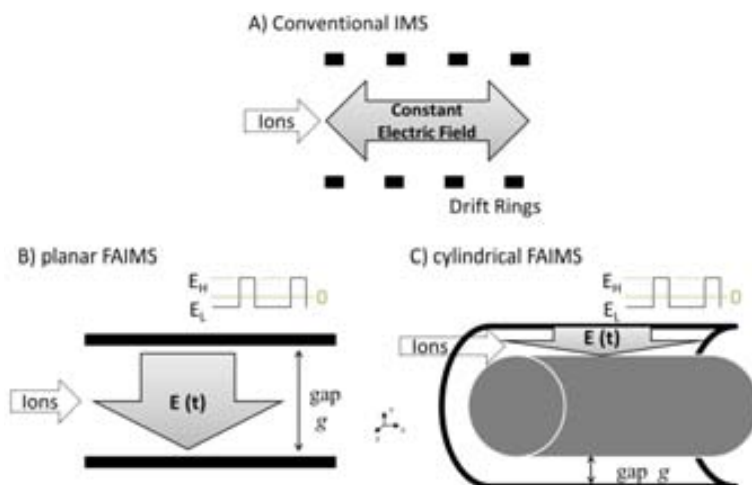


Figure 1-1: Diagrams of ion directions and electric field E application in A) Conventional IMS B) planar FAIMS C) cylindrical FAIMS. Diagrams are not in real scale: A) is more than 10 times larger than B) and C), and also B) and C) have the same order of magnitude for the gap g .

An additional advantage of FAIMS is the possibility to detect positive and negative ions simultaneously [5, 18], although, at the cost of increasing electronics [19]. Also FAIMS instrumentation is emerging in response to the need of discriminate specific gases in both well understood environments (e.g. process control) and complex environments (e.g. volatile organic compound –VOC- measurement, or security). The cylindrical FAIMS technology (c-FAIMS) is moving towards full integration into mass spectrometry for pharmaceutical [20] and protein conformer analysis [21-23] in a tandem FAIMS-MS. Instead, the planar FAIMS technology (p-FAIMS) has been concentrated on healthy risky volatiles [24-26], explosives [27, 28] and chemical warfare agents [29, 30] analysis.

There are numerous analytical detection methods available for medical human breath investigations. The major spectrometric methods used are proton transfer reaction mass spectrometry (PTR-MS) [31-35], solid phase micro extraction-gas chromatography coupled to mass spectrometry (SPME-GC-MS) [36-39], selected ion flow tube mass spectrometry (SIFT-MS) [40-45] and multi-capillary column coupled to ion mobility spectrometry (MCC-IMS) [46-51]. In all mentioned cases, non-invasive and easy methods for early diagnosis or therapy monitoring are developed by identifying disease-specific biomarkers in the breath of patients.

6
Separation by IMS instruments occurs typically at ambient pressure conditions, which makes IMS compatible with many atmospheric pressure ionization techniques, such as atmospheric pressure photo ionization (APPI) [5, 52], electrospray ionization (ESI) [5, 53-58], corona discharge atmospheric pressure chemical ionization (CD-APCI) [5, 59, 60], and radioactive atmospheric pressure chemical ionization (R-APCI) [5, 61]. Various laser based ionization methods have also been used, for example laser desorption/ionization [62-71], laser desorption followed by an another ionization method [72-74], matrix-assisted laser desorption/ionization (MALDI) [69, 75-88], MALDI combined with imaging [89-91], and surface-assisted laser desorption/ionization SALDI [92-95]. R-APCI is the most common ionization method, because it does not require external power for operation and therefore is very suitable for instruments built for field use. The use of radioactive material causes some troublesome safety issues however, thus alternative ionization methods are actively built and studied.

The research in this study is focused on the development of a micro planar high-field asymmetric ion mobility spectrometer (p-FAIMS) for security applications. The p-FAIMS prototype was simulated, designed and built, and was equipped with a commercial photo-ionization source. Also, a medical application is explored for exhaled drugs in breath while patients are anesthetized using a commercial conventional IMS MCC-IMS device.

1.2 Aims of the study

The general aim of this study is the development of a planar micro high-Field Asymmetric waveform Ion Mobility Spectrometry (p-FAIMS) instrument, including the ionization technique for security applications, by means of microelectronic fabrication techniques that allow integration and miniaturization of components, given the need to detect low concentrations \sim ppm (parts per million) of a particular gaseous species, that are not achievable with other type of sensors (e.g. metal oxide semiconductors). But furthermore, a medical application with a conventional IMS (MCC-IMS) is done for a breath drugs studio while patients are anesthetized.

The aims of the studies are:

- **Security Application:**
 - *Simulation of the p-FAIMS with Finite Elements Multiphysics (FEM) Treatment using COMSOL Multiphysics software.* COMSOL allows the interactions of electric fields, fluid flows and transport of chemical species (including diffusion). Special attention is paid to compounds differentiation through a board range of conditions. Also model is validated.
 - *Design, Fabrication and Characterization of a micro UV-p-FAIMS for Toluene Detection.* Full new set-up is implemented and controlled by LabView programming. Different designs of p-FAIMS have been studied. Initial designs with pyrex substrates were analyzed, but due to technical problems other designs were explored. Final designs consist of a PCB sandwich-like configuration with a fully drilled pieces of Poly(methyl methacrylate) to form the channel where the gas es passes through. Final p-FAIMS prototype is characterized for toluene for different experimental conditions.

- **Medical Application:**
 - *Online Monitoring of the analgesic Remifentanil in Exhaled Breath in Patients undergoing Total Intravenous Anesthesia using a commercial MCC-IMS device.* Three commercial multi-capillary ion mobility spectrometers are used. Basic investigations of background emissions and about the alignment of the three different devices are done. Online-monitoring of one analgesic has been done during patient's anesthesia. Also volatiles from plastics involved in anesthesia are studied with Gas Chromatograph - Mass Spectrometry (GC-MS).

Work involving Security Application was carried out at the *Institut de Microelectrònica de Barcelona (IMB-CNM, CSIC)*, Bellaterra (Spain). While the Medical Application work was carried out at the Korean Institute of Science and

Technology in Europe (KIST-Europe), Saarbrücken (Germany) and in the *Chirurgische Universitätsklinik* from Homburg (Germany).

1.3 Scientific Contribution

This dissertation presents a summary of the work in the last four years in developing a micro planar high field asymmetric ion mobility spectrometer (p-FAIMS). The work carried out for this dissertation was experimental in nature and it was complemented by means of an extensive simulation of the device.

The p-FAIMS simulation novelty is that it includes multiphysics of electric fields, fluid dynamics and their effect in the simulation ions including also the diffusion.

The novelty of the micro p-FAIMS device consists in the creation of a compact low cost micro IMS with full flow integration. This fact makes the new IMS portable, reusable, and with less total volume $\sim 28.8 \text{ cm}^3$, having a drift tube volume of 0.16 cm^3 .

Another novelty has been the first study of an online monitoring of the analgesic drug remifentanyl, using a MCC-IMS device, finding one possible specific peak for remifentanyl. Nowadays, new measurements are done to confirm the peak determination.

8

1.4 Projects in which is framed

This thesis has been supported by two national projects (Spain):

- TEC2007-67962, *Integración de Sistemas Inteligentes para Seguridad* (ISIS), funded by MICINN for 2008-2011
- TEC2010-21357-C05, *Modular system based on advanced micro-and nanotechnology for security and environmental quality applications* (NAMIRIS), funded by MICINN for 2010-2013.

The overall objectives of ISIS project are the fabrication of devices and micro-sensor systems to detect harmful vapors and liquids in the security field using different micro-and nano-technologies. And for NAMIRIS project the overall objectives are mostly the same but for safety, security and air quality applications.

1.5 Outline of the Thesis

The thesis has 2 main sections, and 5 chapters:

- **Section I: micro p-FAIMS Development**

This section has 3 chapters. In chapter 1 the ion mobility spectrometers (IMS) and the main objectives of the thesis are introduced. Then in Chapter 2, the state-of-the-art of the Ion Mobility Spectrometry is explored. Finally in Chapter 3 the Micro p-FAIMS Modeling is shown.

- **Section II: Ion Mobility Spectrometry Applications**

This section has 2 chapters where different applications are analyzed. Security Applications are studied in Chapter 4 for the new p-FAIMS device fabricated in the IMB-CNM, focused on the quantification of healthy risky volatiles with the p-FAIMS prototype. Also device design, assembly and measurements set-up are shown. Medical Applications are studied in Chapter 5 for a commercial IMS, specifically in the detection of exhaled drugs during surgical operations.

- **Conclusions:**

Finally the general conclusions and the future perspectives are presented.

At the end of the thesis there is the List of Publications, the various Annexes that supplement the thesis, and the List of Abbreviations, Contractions, Symbols and Acronyms.

References

1. Hill, H.H., et al., *Ion Mobility Spectrometry*. Analytical Chemistry, 1990. **62**(23): p. 1201A-1209A.
2. Baumbach, J.I. and G.A. Eiceman, *Ion Mobility Spectrometry: Arriving On Site and Moving Beyond a Low Profile*. Applied Spectroscopy, 1999. **53**(9): p. 338A-355A.
3. Collins, D.C. and M.L. Lee, *Developments in ion mobility spectrometry-mass spectrometry*. Analytical and Bioanalytical Chemistry, 2002. **372**(1): p. 66-73.
4. Eiceman, G.A., *Ion-mobility spectrometry as a fast monitor of chemical composition*. TrAC Trends in Analytical Chemistry, 2002. **21**(4): p. 259-275.
5. Eiceman, G.A. and Z. Karpas, *Ion Mobility Spectrometry*. 2nd ed. 2005, Boca Raton: CRC Press.
6. Cottingham, K., *Ion mobility spectrometry rediscovered*. Analytical Chemistry, 2003: p. 435A.
7. Armenta, S., M. Alcalá, and M. Blanco, *A review of recent, unconventional applications of ion mobility spectrometry (IMS)*. Analytica Chimica Acta, 2011. **703**(2): p. 114-123.
8. Mäkinen, M., M. Nousiainen, and M. Sillanpää, *Ion spectrometric detection technologies for ultra-traces of explosives: A review*. Mass Spectrometry Reviews, 2011. **30**(5): p. 940-973.

9. Borsdorf, H. and G.A. Eiceman, *Ion mobility spectrometry: Principles and applications*. Applied Spectroscopy Reviews, 2006. **41**(4): p. 323-375.
10. Kanu, A.B., et al., *Ion mobility-mass spectrometry*. Journal of Mass Spectrometry, 2008. **43**(1): p. 1-22.
11. Fernández-Maestre, R. and H. Hill, *Ion mobility spectrometry for the rapid analysis of over-the-counter drugs and beverages*. International Journal for Ion Mobility Spectrometry, 2009. **12**(3): p. 91-102.
12. Pollard, M., et al., *Ion mobility spectrometer—field asymmetric ion mobility spectrometer-mass spectrometry*. International Journal for Ion Mobility Spectrometry, 2011. **14**(1): p. 15-22.
13. Buryakov, I.A., et al., *A New Method of Separation of Multi-Atomic Ions by Mobility at Atmospheric-Pressure Using a High-Frequency Amplitude-Asymmetric Strong Electric-Field*. International Journal of Mass Spectrometry and Ion Processes, 1993. **128**(3): p. 143-148.
14. Miller, R.A., et al., *A novel micromachined high-field asymmetric waveform-ion mobility spectrometer*. Sensors and Actuators B: Chemical, 2000. **67**(3): p. 300-306.
15. Guevremont, R. and R.W. Purves, *Atmospheric pressure ion focusing in a high-field asymmetric waveform ion mobility spectrometer*. Review of Scientific Instruments, 1999. **70**(2): p. 1370-1383.
16. Teepe, M., et al., *Miniaturized ⁶³Ni ion mobility spectrometer*. International Journal for Ion Mobility Spectrometry, 2001. **4**(2): p. 173-176.
17. Shvartsburg, A.A., et al., *Ultrafast Differential Ion Mobility Spectrometry at Extreme Electric Fields in Multichannel Microchips*. Analytical Chemistry, 2009. **81**(15): p. 6489-6495.
18. Shvartsburg, A.A., *Differential Ion Mobility Spectrometry: Nonlinear Ion Transport and Fundamentals of FAIMS*. first ed. 2009, Boca Raton, FL: CRC Press.
19. Kolakowski, B.M. and Z. Mester, *Review of applications of high-field asymmetric waveform ion mobility spectrometry (FAIMS) and differential mobility spectrometry (DMS)*. Analyst, 2007. **132**(9): p. 842-864.
20. Miller, R.A., et al., *A MEMS radio-frequency ion mobility spectrometer for chemical vapor detection*. Sensors and Actuators A: Physical, 2001. **91**: p. 301-312.
21. McCooeye, M.A., et al., *Quantitation of Amphetamine, Methamphetamine, and Their Methylenedioxy Derivatives in Urine by Solid-Phase Microextraction Coupled with Electrospray Ionization-High-Field Asymmetric Waveform Ion Mobility Spectrometry-Mass Spectrometry*. Analytical Chemistry, 2002. **74**(13): p. 3071-3075.
22. Cui, M., L. Ding, and Z. Mester, *Separation of Cisplatin and Its Hydrolysis Products Using Electrospray Ionization High-Field Asymmetric Waveform Ion Mobility Spectrometry Coupled with Ion Trap Mass Spectrometry*. Analytical Chemistry, 2003. **75**(21): p. 5847-5853.
23. Guevremont, R. and B. Kolakowski, *Using FAIMS to increase selectivity for LC-MS analyses*. American Laboratory, 2005. **37**(13): p. 11-14.
24. Purves, R.W., D.A. Barnett, and R. Guevremont, *Separation of protein conformers using electrospray-high field asymmetric waveform ion mobility spectrometry-mass spectrometry*. International Journal of Mass Spectrometry, 2000. **197**: p. 163-177.
25. Purves, R.W., et al., *Elongated conformers of charge states +11 to +15 of bovine ubiquitin studied using ESI-FAIMS-MS*. Journal of the American Society for Mass Spectrometry, 2001. **12**(8): p. 894-901.
26. Venne, K., et al., *Improvement in Peptide Detection for Proteomics Analyses Using NanoLC-MS and High-Field Asymmetry Waveform Ion Mobility Mass Spectrometry*. Analytical Chemistry, 2005. **77**(7): p. 2176-2186.
27. Eiceman, G.A., et al., *Differential mobility spectrometry of chlorocarbons with a micro-fabricated drift tube*. Analyst, 2004. **129**(4): p. 297-304.
28. Veasy, C.A. and C.L.P. Thomas, *Fast quantitative characterisation of differential mobility responses*. Analyst, 2004. **129**: p. 198-204.

29. Buryakov, I.A., *Qualitative analysis of trace constituents by ion mobility increment spectrometer*. Talanta, 2003. **61**: p. 369-375.
30. Eiceman, G.A., et al., *Separation of ions from explosives in differential mobility spectrometry by vapor-modified drift gas*. Analytical Chemistry, 2004. **76**(17): p. 4937-4944.
31. Schwarz, K., W. Filipiak, and A. Amann, *Determining concentration patterns of volatile compounds in exhaled breath by PTR-MS*. Journal of Breath Research, 2009. **3**: p. 1-15.
32. Wisthaler, A., *PTR-MS: a new tool for the rapid detection and quantification of VOCs in air at ultra-trace levels*, 2004, Institut für Ionenphysik, Leopold-Franzens-Universität Innsbruck: Innsbruck.
33. Lindinger, W., A. Hansel, and A. Jordan, *On-Line Monitoring of Volatile Organic Compounds at pptv Levels by Means of Proton-Transfer-Reaction Mass Spectrometry (PTR-MS)*. Medical Applications, Food Control and Environmental Research. International Journal of Mass Spectrometry and Ion Processes, 1998. **173**: p. 191-241.
34. Lindinger, W., A. Hansel, and A. Jordan, *Proton-transfer-reaction mass spectrometry (PTR-MS): on-line monitoring of volatile organic compounds at pptv levels*. Chemical Society Reviews, 1998. **27**: p. 347-354.
35. Thekedar, B., et al., *Investigations on the variability of breath gas sampling using PTR-MS*. Journal of Breath Research, 2009. **3**: p. 1-11.
36. Ligor, M., et al., *Determination of volatile organic compounds in exhaled breath of patients with lung cancer using solid phase microextraction and gas chromatography mass spectrometry*. Clinical Chemistry and Laboratory Medicine, 2009. **47**(5): p. 550-560.
37. Buszewski, B., et al., *Analysis of exhaled breath from smokers, passive smokers and non-smokers by solid-phase microextraction gas chromatography/mass spectrometry*. Biomedical Chromatography, 2009. **23**(5): p. 551-556.
38. Ligor, T., et al., *The analysis of healthy volunteers' exhaled breath by the use of solid-phase microextraction and GC-MS*. Journal of Breath Research, 2008. **2**: p. 1-8.
39. Schubert, J.K., et al., *Determination of antibiotic drug concentrations in circulating human blood by means of solid phase micro-extraction*. Clinica Chimica Acta, 2007. **386**(1-2): p. 57-62.
40. Smith, D., et al., *Isoprene levels in the exhaled breath of 200 healthy pupils within the age range 7-18 years studied using SIFT-MS*. Journal of Breath Research, 2010. **4**: p. 1-7.
41. Enderby, B., et al., *Concentrations of some metabolites in the breath of healthy children aged 7-18 years measured using selected ion flow tube mass spectrometry (SIFT-MS)*. Journal of Breath Research, 2009. **3**: p. 1-11.
42. Spänel, P. and D. Smith, *Quantification of trace levels of the potential cancer biomarkers formaldehyde, acetaldehyde and propanol in breath by SIFT-MS*. Journal of Breath Research, 2008. **2**: p. 1-10.
43. Spänel, P., K. Dryahina, and D. Smith, *The concentration distributions of some metabolites in the exhaled breath of young adults*. Journal of Breath Research, 2007. **1**: p. 1-8.
44. Dryahina, K., M. Polasek, and P. Spänel, *A selected ion flow tube, SIFT, study of the ion chemistry of H₃O⁺, NO⁺ and O₂⁺ ions with several nitroalkanes in the presence of water vapour*. International Journal of Mass Spectrometry, 2004. **239**: p. 57-65.
45. Baumbach, J.I., *Process analysis using ion mobility spectrometry*. Analytical and Bioanalytical Chemistry, 2006. **384**(5): p. 1059-1070.
46. Jünger, M., B. Bödeker, and J.I. Baumbach, *Peak assignment in multi-capillary column - ion mobility spectrometry using comparative studies with gas chromatography - mass spectrometry for exhaled breath analysis*. Analytical and Bioanalytical Chemistry, 2010. **396**(1): p. 471-482.
47. Maddula, S., et al., *Detection of volatile metabolites of Escherichia coli by multi capillary column coupled ion mobility spectrometry*. Analytical and Bioanalytical Chemistry, 2009. **394**(3): p. 791-800.

48. Baumbach, J.I., *Ion Mobility Spectrometry coupled with Multi-Capillary Columns for Metabolic Profiling of Human Breath*. Journal of Breath Research, 2009. **3**: p. 1-16.
49. Bödeker, B., W. Vautz, and J.I. Baumbach, *Peak Comparison in MCC/IMS – Data – Searching for potential biomarkers in human breath data*. International Journal for Ion Mobility Spectrometry, 2008. **11**(1): p. 89-93.
50. Baumbach, J.I. and M. Westhoff, *Ion mobility spectrometry to detect lung cancer and airway infections*. Spectroscopy Europe, 2006. **18**(6): p. 22-27.
51. Moseley, J.T., et al., *Measurement of Transport Properties of Ions in Gases; Results for K⁺ Ions in N₂* Physical Review, 1969. **178**(1): p. 234-239.
52. Laakia, J., et al., *Separation of Different Ion Structures in Atmospheric Pressure Photoionization-Ion Mobility Spectrometry-Mass Spectrometry (APPI-IMS-MS)*. Journal of the American Society for Mass Spectrometry, 2010. **21**(9): p. 1565-1572.
53. Beegle, L.W. and I. Kanik, *Electrospray Ionization High-Resolution Ion Mobility Spectrometry for the Detection of Organic Compounds, 1. Amino Acids*. Analytical Chemistry, 2001. **73**(13): p. 3028-3034.
54. Ells, B., et al., *Detection of Nine Chlorinated and Brominated Haloacetic Acids at Part-per-Trillion Levels Using ESI-FAIMS-MS*. Analytical Chemistry, 2000. **72**(19): p. 4555-4559.
55. Matz, L.M. and H.H. Hill, *Evaluation of Opiate Separation by High-Resolution Electrospray Ionization-Ion Mobility Spectrometry/Mass Spectrometry*. Analytical Chemistry, 2001. **73**(8): p. 1664-1669.
56. Matz, L.M. and H.H. Hill, *Evaluating the Separation of Amphetamines by Electrospray Ionization Ion Mobility Spectrometry/MS and Chrage Competition within the ESI Process*. Analytical Chemistry, 2002. **74**(2): p. 420-427.
57. Srebalus Barnes, C.A., et al., *Resolving Isomeric Peptide Mixtures: A Combined HPLC/Ion Mobility-TOFMS Analysis of a 4000-Component Combinatorial Library*. Analytical Chemistry, 2001. **74**(1): p. 26-36.
58. Dion, H.M., L.K. Ackerman, and H.H. Hill, *Detection of inorganic ions from water by electrospray ionization-ion mobility spectrometry*. Talanta, 2002. **57**(6): p. 1161-1171.
59. Borsdorf, H., E.G. Nazarov, and G.A. Eiceman, *Atmospheric pressure chemical ionization studies of non-polar isomeric hydrocarbons using ion mobility spectrometry and mass spectrometry with different ionization techniques*. Journal of the American Society for Mass Spectrometry, 2002. **13**(9): p. 1078-1087.
60. Hill, C.A. and C.L.P. Thomas, *A pulsed corona discharge switchable high resolution ion mobility spectrometer-mass spectrometer*. Analyst, 2003. **128**(1): p. 55-60.
61. Yamaguchi, S., et al., *Detection performance of a portable ion mobility spectrometer with ⁶³Ni radioactive ionization for chemical warfare agents*. Forensic Toxicology, 2010. **28**(2): p. 84-95.
62. Eiceman, G.A., et al., *Laser desorption and ionization of solid polycyclic aromatic hydrocarbons in air with analysis by ion mobility spectrometry*. Analytical Letters, 1988. **21**(4): p. 539-552.
63. Phillips, J. and J. Gormally, *The laser desorption of organic molecules in ion mobility spectrometry*. International Journal of Mass Spectrometry and Ion Processes, 1992. **112**(2-3): p. 205-214.
64. Bowers, M.T., et al., *Gas-Phase Ion Chromatography: Transition Metal State Selection and Carbon Cluster Formation*. Science, 1993. **260**(5113): p. 1446-1451.
65. Jarrold, M.F. and J.E. Bower, *Mobilities of metal cluster ions: Aluminum and the electronic shell model* Journal of Chemical Physics, 1993. **98**(3): p. 2399-2407.
66. Roch, T. and J.I. Baumbach, *Laser-based ion mobility spectrometry as an analytical tool for soil analysis*. International Journal for Ion Mobility Spectrometry, 1998. **1**(1): p. 43-47.

67. Illenseer, C. and H.-G. Löhmannsröben, *Investigation of ion-molecule collisions with laser-based ion mobility spectrometry*. *Physical Chemistry Chemical Physics*, 2001. **3**(12): p. 2388-2393.
68. Young, D., et al., *Laser desorption-ionization of polycyclic aromatic hydrocarbons from glass surfaces with ion mobility spectrometry analysis*. *Analytica Chimica Acta*, 2002. **453**(2): p. 231-243.
69. Weis, P., et al., *A time-of-flight, drift cell, quadrupole apparatus for ion mobility measurements*. *International Journal of Mass Spectrometry*, 2002. **216**: p. 59-73.
70. Beitz, T., et al., *Ion Mobility Spectrometric Investigation of Aromatic Cations in the Gas Phase*. *Journal of Physical Chemistry A*, 2006. **110**(10): p. 3514-3520.
71. Eiceman, G.A., et al., *Ion mobility spectrometry of gas-phase ions from laser ablation of solids in air at ambient pressure*. *Applied Spectroscopy*, 2007. **61**(10): p. 1076-1083.
72. Huang, S.D., L. Kolaitis, and D.M. Lubman, *Detection of explosives using laser desorption in ion mobility spectrometry/mass spectrometry*. *Applied Spectroscopy*, 1987. **41**(8): p. 1371-1376.
73. Simpson, M., et al., *Polymer characterization using laser desorption - ion mobility spectrometry*. *Analyst*, 1993. **118**: p. 449-451.
74. Borsdorf, H., et al., *Rapid screening of pesticides from fruit surfaces: preliminary examinations using a laser desorption—differential mobility spectrometry coupling*. *International Journal for Ion Mobility Spectrometry*, 2009. **12**(1): p. 15-22.
75. von Helden, G., T. Wyttenbach, and M.T. Bowers, *Inclusion of a MALDI ion source in the ion chromatography technique: conformational information on polymer and biomolecular ions*. *International Journal of Mass Spectrometry and Ion Processes*, 1995. **146–147**(0): p. 349-364.
76. Lee, S., T. Wyttenbach, and M.T. Bowers, *Gas phase structures of sodiated oligosaccharides by ion mobility/ion chromatography methods*. *International Journal of Mass Spectrometry and Ion Processes*, 1997. **167–168**(0): p. 605-614.
77. Gidden, J., et al., *Poly (ethylene terephthalate) oligomers cationized by alkali ions: Structures, energetics, and their effect on mass spectra and the matrix-assisted laser desorption/ionization process*. *Journal of the American Society for Mass Spectrometry*, 1999. **10**(9): p. 883-895.
78. Gillig, K.J., et al., *Coupling High-Pressure MALDI with Ion Mobility/Orthogonal Time-of-Flight Mass Spectrometry*. *Analytical Chemistry*, 2000. **72**(17): p. 3965-3971.
79. Bramwell, C.J., et al., *Atmospheric Pressure Matrix-Assisted Laser Desorption/Ionization Combined with Ion Mobility Spectrometry*. *International Journal for Ion Mobility Spectrometry*, 2002. **5**(3): p. 87-90.
80. Tong, H., et al., *Solid phase microextraction with matrix assisted laser desorption/ionization introduction to mass spectrometry and ion mobility spectrometry*. *Analyst*, 2002. **127**(9): p. 1207-1210.
81. Ruotolo, B.T., et al., *Analysis of protein mixtures by matrix-assisted laser desorption ionization-ion mobility-orthogonal-time-of-flight mass spectrometry*. *International Journal of Mass Spectrometry*, 2002. **219**(1): p. 253-267.
82. Steiner, W.E., et al., *Atmospheric pressure matrix-assisted laser desorption/ionization with analysis by ion mobility time-of-flight mass spectrometry*. *Rapid Communications in Mass Spectrometry*, 2004. **18**(8): p. 882-888.
83. Eiceman, G.A., D. Young, and G.B. Smith, *Mobility spectrometry of amino acids and peptides with matrix assisted laser desorption and ionization in air at ambient pressure*. *Microchemical Journal*, 2005. **81**(1): p. 108-116.
84. McLean, J.A., et al., *Ion mobility-mass spectrometry: a new paradigm for proteomics*. *International Journal of Mass Spectrometry*, 2005. **240**(3): p. 301-315.
85. Dwivedi, P., A.J. Schultz, and H.H.H. Jr, *Metabolic profiling of human blood by high-resolution ion mobility mass spectrometry (IM-MS)*. *International Journal of Mass Spectrometry*, 2010. **298**(1–3): p. 78-90.

86. Harkness, K.M., et al., *Surface Fragmentation of Complexes from Thiolate Protected Gold Nanoparticles by Ion Mobility-Mass Spectrometry*. Analytical Chemistry, 2010. **82**(7): p. 3061-3066.
87. Jackson, S.N., et al., *Gangliosides' analysis by MALDI-ion mobility MS*. Analyst, 2011. **136**(3): p. 463-466.
88. Chen, L., et al., *Molecular dynamics and ion mobility spectrometry study of model β -hairpin peptide, trpzip1*. Journal of Physical Chemistry A, 2011. **115**(17): p. 4427-35.
89. Wang, H.-Y.J., S.N.J.J. Post, and A.S. Woods, *A minimalist approach to MALDI imaging of glycerophospholipids and sphingolipids in rat brain sections*. International Journal of Mass Spectrometry, 2008. **278**(2-3): p. 143-149.
90. Trimpin, S., et al., *Automated Solvent-Free Matrix Deposition for Tissue Imaging by Mass Spectrometry*. Analytical Chemistry, 2009. **82**(1): p. 359-367.
91. Stauber, J., et al., *On-tissue protein identification and imaging by MALDI-Ion mobility mass spectrometry*. Journal of the American Society for Mass Spectrometry, 2010. **21**(3): p. 338-347.
92. Tempez, A., et al., *Matrix Implanted Laser Desorption Ionization (MILDI) Combined with Ion Mobility-Mass Spectrometry for Bio-Surface Analysis*. Journal of Proteome Research, 2005. **4**(2): p. 540-545.
93. Ugarov, M.V., et al., *MALDI Matrices for Biomolecular Analysis Based on Functionalized Carbon Nanomaterials*. Analytical Chemistry, 2004. **76**(22): p. 6734-6742.
94. Wang, Y., et al., *Solid-phase microextraction combined with surface-enhanced laser desorption/ionization introduction for ion mobility spectrometry and mass spectrometry using polypyrrole coatings*. Rapid Communications in Mass Spectrometry, 2004. **18**(2): p. 157-162.
95. Martynov, I.L., et al., *Ion mobility spectrometer with ion source based on laser-irradiated porous silicon*. Technical Physics Letters, 2011. **37**(1): p. 15-18.

Chapter

2

**Ion Mobility
Spectrometry**

State-of-the-art

Chapter 2: Ion Mobility Spectrometry: State-of-the-art.....	15
2.1 Origin and applications.....	17
2.2 Principle of Ion Mobility Spectrometry.....	18
2.2.a Sample Introduction Systems.....	24
2.2.b Ionization region.....	27
2.2.c Drift region.....	36
2.2.d Detector region.....	39
2.2.e Hyphenated Methods with Ion Mobility Spectrometers.....	41
2.2.f Data collection and treatment.....	50
2.3 high Field Asymmetric waveform Ion Mobility Spectrometers.....	57
2.3.a Filtering Region electrodes design.....	58
2.3.b FAIMS Ion Dynamics.....	66
2.3.c Detection.....	74
References.....	88

This chapter provides an explanation of the underlying principles involved in ion motion in an IMS, and the various components involved in this device, along with the theory of ion formation in gases.

The science of ion formation in ambient air has been known since the end of the nineteenth century [1]. In the early twentieth century, the famous physicist Paul Langevin studied the motion of ions in an electric field [2, 3]. These results later proved to be the basis for the governing principles of Ion Mobility Spectrometry (IMS). The instrumentation, however, took almost 70 years to be first developed under the name of Plasma Chromatography [4], a gas phase electrophoretic analytic technique [5-7] in which the ionization source is similar to that employed in an electron capture detector and the sample chamber is designed for the continuous introduction of organic compounds of high purity.

2.1 Origin and applications

Ion Mobility Spectrometry (IMS) is an analytical technique based on ion separation in gaseous phase based on the different mobility under an electric field. The early IMS instrumentation in the 1970s was developed for laboratory use only. At that time, there was no guarantee that the IMS technique would appear as a portable device for in-field use [8]. Technology has been improved since that time however, and modern IMS devices have become portable [9-12]. This improved portability has dramatically extended the application ranges of the IMS instruments, which have become widely used analytical techniques not only in the laboratory, but in the field as well.

Over the past few decades, Ion Mobility Spectrometry has evolved into an inexpensive and powerful analytical technique for the detection of gas phase samples in the lower $\text{ng}\cdot\text{L}^{-1}$ (ppb_v) levels at ambient pressures and temperatures. This instrument was initially used by the military establishments of the U.S.A and the United Kingdom to detect human activities in the jungles of Vietnam [13, 14]. In the late 1970s and early 1980s, several research and development programs were started at universities, government organizations and small companies with the IMS to develop the instrumentation of this analytical device which proved attractive with its advantages such as lower detection limits, ruggedness, reasonable selectivity and the potential for miniaturization [15].

The IMS instrumentation has wide range of application, such as: chemical weapons monitoring [16, 17]; detection of explosives [18-22]; environmental analysis [23-31]; medical diagnostics [32-38]; bio and proteomics analysis [39-41]; biological and clinical analysis [42-45]; food quality analysis [46-53]; process control [54-58]; illegal drugs detection [21, 59-64]; air quality analysis [65, 66]; airport security [19, 67];, locations security [28, 54, 68-71]; forensic examination [61, 72]; customs

control [73]; and fermentation control applications [74]. The list of applications continues expanding. Moreover, future new IMS applications cannot be predicted.

In recent years, the instrument is increasingly in demand for new applications specifically on biological samples (cells, fungi, bacteria) [32, 33, 41, 75-81], in medicine (diagnosis, therapy and medication control e.g. from breath analysis) [36, 82-90]. For the analysis of these complex mixtures, the ion mobility alone will not be sufficient for the identification of analytes in the mixture. Several analytes have similar or even the same mobility. Therefore, additional rapid pre-separation techniques like Gas Chromatography (GC) or Multi-Capillary Column (MCC) are applied to conventional Ion Mobility Spectrometer devices. Ergo, for every analyte, there is a specific ion mobility value (or diffusion time) and the time it takes to elute out from the pre-separation column, known as the retention time, which are the characteristics of the particular analyte at a specific temperature, pressure, column length, polarity and flow rate. Providing this database of relevant analytes for every analysis enables the identification of compounds in a sample.

2.2 Principle of Ion Mobility Spectrometry

It's important to appreciate that different types of IMS exist. Drift tube IMS is the traditional equipment/configuration in which ions move through a homogeneous, continuous electric field in a drift tube in the presence of neutral gas molecules, we would refer to it as **Conventional IMS**. The time ions take to travel down the drift tube is directly proportional to their mobility. A conventional Ion Mobility Spectrometer, as shown in Figure 2-1, has three main parts [8, 91]: (1) Ionization Region, where samples are ionized; (2) Drift Region, where ions are separated due to their mobility; and (3) Detection Region, where ions are collected.

The second type of IMS is the **Traveling-wave IMS** (TWIMS) [92-95], based on "traveling waves" where a series of low-voltage waves push the ions down the drift tube after they emerge from an electrospray ion source. As the ions are pushed by the low-voltage waves, they are separated by sizes, small ions collide less frequently with gas molecules and make it first to the mass spectrometer, and large ions collide more and get delayed in their journey, see Figure 2-2.

The third type is the **Aspiration-type IMS** (AIMS) [17, 22, 96-99], that was developed in 1975 based on an ion-counting technology for mobility measurements and had a cylindrical design [100], which had three cylindrical electrodes: one central and two external. However, most modern aspiration-type spectrometers have been built in planar form [96-99]. The device was used for measurements of mobilities of atmospheric ions. The concept of the ion-focusing aspiration condenser is shown in Figure 2-3. It is based on two different gas flows that form parallel gas streams under

laminar flow conditions. The ions travel within the upper ion carrier gas stream, which is focused by means of geometric constrains. The parallel drift gas stream fills most of the separation region so that a thin layer of ion carrier gas is formed at the detector electrode. While traveling through the transverse electric field ions are forced out of the ion carrier gas through the drift gas towards the bottom electrode setup. Ion species with different ion mobilities are eventually separated into individual ion beams. Space charge effects and diffusion cause poor spatial ion separation. Both effects can be reduced by increasing the flow rates in order to minimize ion concentration and drift time.

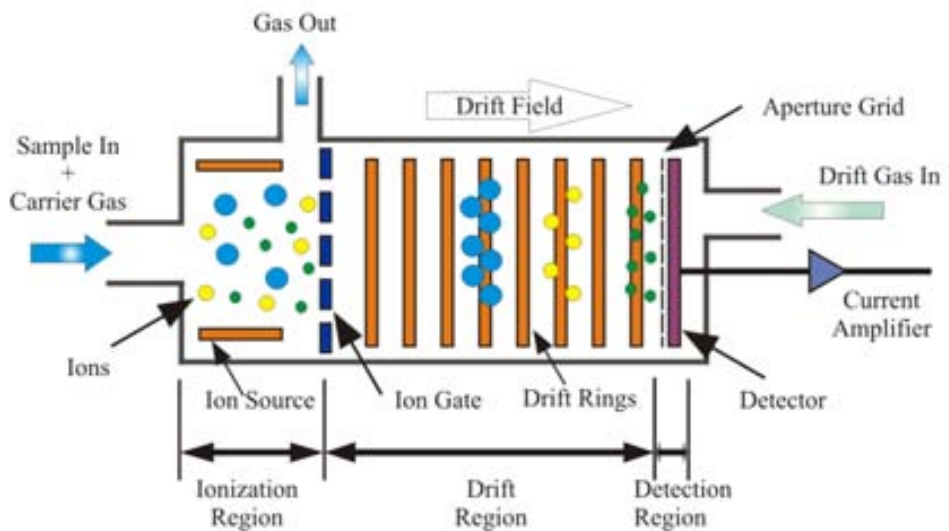


Figure 2-1: Schematic of a conventional IMS system showing three ions of different size in the reaction region and then migrating at different velocities in the drift region.

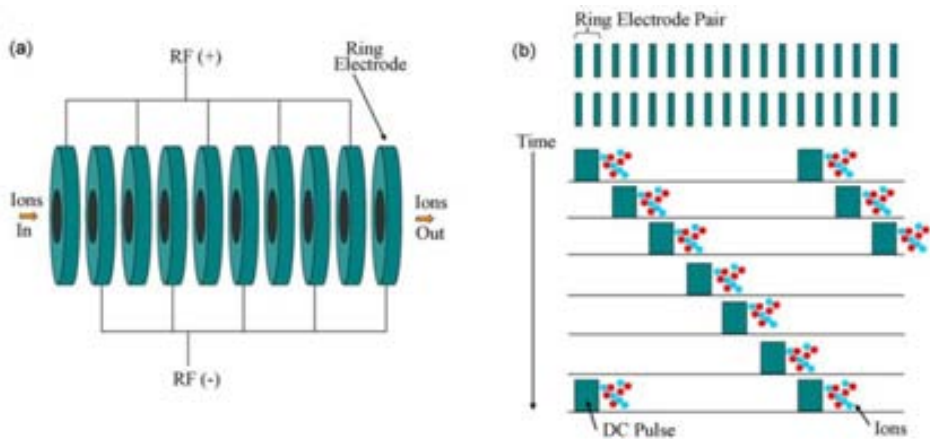


Figure 2-2: (a) Schematic diagram of the filtering region of a traveling wave Ion Mobility Spectrometer (TWIMS); (b) an illustration of the motion of the travelling wave through the filtering region. Adapted from [94].

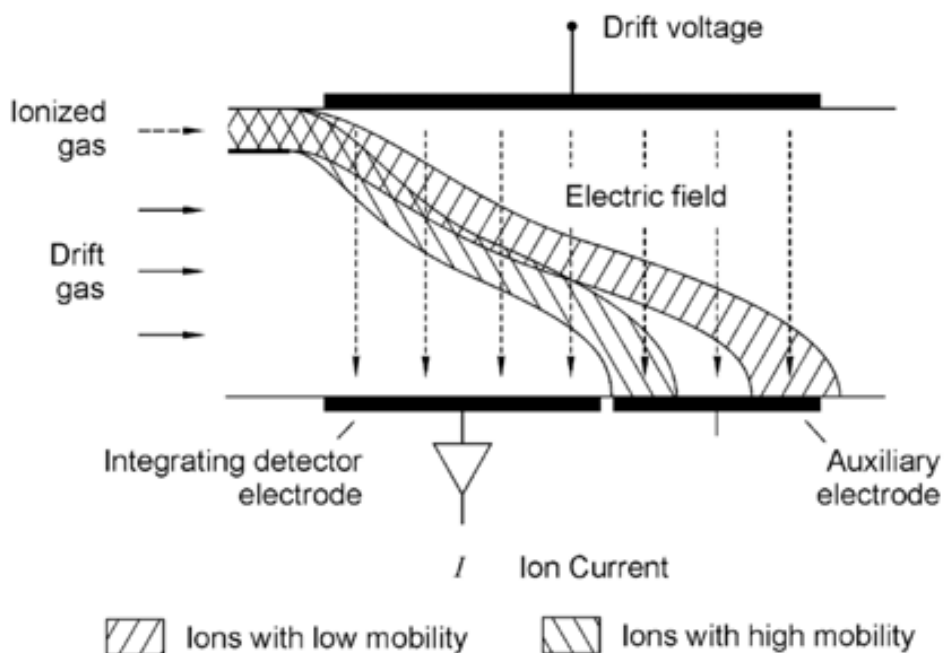


Figure 2-3: Schematic diagram of the first order differential ion-focusing aspiration condenser with two ion species [97]. The ions travel within the upper focused ion carrier gas stream. The parallel drift gas stream fills most of the separation region so that a thin layer of ion carrier gas is formed at the counter electrode. While traveling through the transverse electric field ions are forced out of the ion carrier gas flow through the drift gas flow towards the bottom electrode set-up.

The fourth IMS type is the **Differential Mobility Analyzers (DMA)** [101], in which the ions migrate between two electrodes held at different potentials while being transported by a stream of gas (initially clean) flowing parallel to the electrodes. Cylindrical DMAs are widely used for the analysis of submicrometer aerosols. Planar DMAs [102] permit coupling with virtually any atmospheric pressure ionization – mass spectrometer (API-MS) [102] and provide an improved transmission of ions. In addition, because planar DMAs operate at ambient pressure, mobility is measured at moderated ionic temperatures with little fragmentation, which makes structural interpretation of the data easier [103-105].

High Flow DMA is a particular type of Ion Mobility Spectrometer in which ions are actively separated by a high speed and laminar flow of gas [106]. An electric field is superimposed in the perpendicular direction so that ions are driven by the combination of the electrical force and fluid drift. More mobile (smaller) ions are less deflected by the sheath gas than less mobile (larger) ions. Every field-flow combination results in the classification of a current of ions, all having the same mobility, that flow through a sampling slit and are detected by an electrometer.

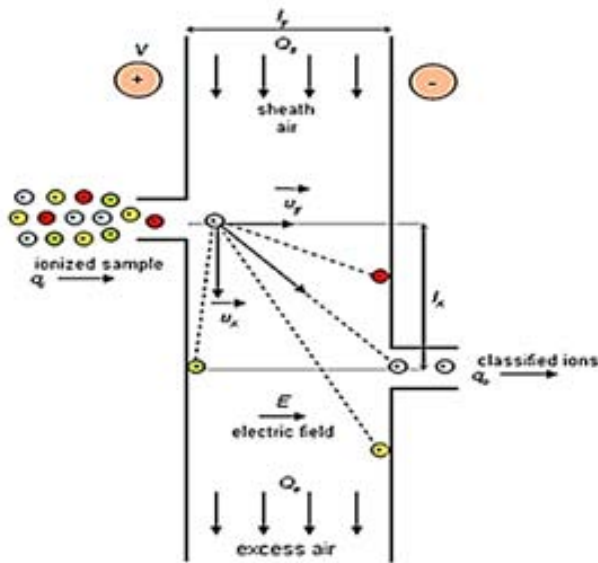


Figure 2-4: Layout of parallel plate electrodes Differential Mobility Analyzer (DMA). From Ramem S.A [107], available at [108].

The fifth IMS type is the **Transversal Modulation IMS (TMIMS)** which separates ions according to their mobility using only electric fields. The selected ions coalesce at the analyzer outlet, while other ions are deflected away and not transferred, a schema is shown in Figure 2-5a. Ions are separated in space and thus a continuous flow of filtered ions with a narrow range of selected mobility ions is produced, as in Differential Mobility Analyzers (DMAs); yet no high fluid velocity field is required, thus avoiding the limitations in DMAs associated with low unsteadiness, compressibility, and turbulent transition.

In TM-IMS technology ions are pushed by an axial electric field at a velocity proportional to their mobility and travel through the TM-IMS during a time inversely proportional to their mobility. When this time resonates with the period of the transversal (termed deflector) electric field, the trajectories of the selected ions are brought away from the central axis during half the cycle of the deflector electric field, and then they are brought back to the central axis during the remainder of the cycle, and they coalesce at the analyzer outlet, while other ions having different mobilities do not. Figure 2-5b illustrates schematically the different trajectories of ions in a TM-IMS including two parallel electrodes (responsible for the axial steady electric field) with aligned inlets and outlets, and two deflector electrodes (responsible for the deflector electric field). There are three types of behavior: (i) the selected ions, whose trajectories coalesce at the outlet; (ii) overspeeding ions with higher mobility than the selected ones; and (iii) lagging ions with lower mobility than the selected ones.

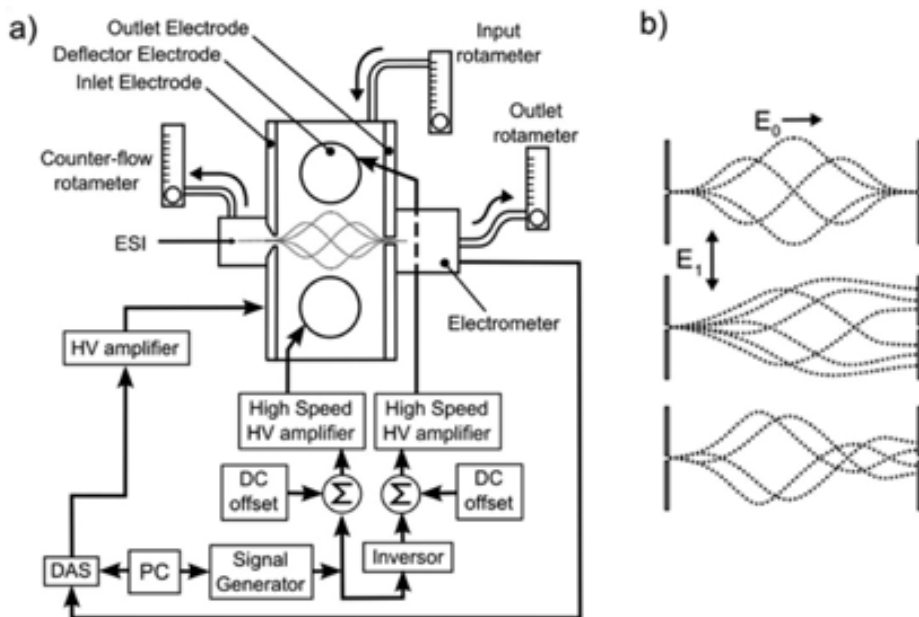


Figure 2-5: a) Schematic illustration of the TM-IMS including an ESI source, an inlet electrode with an inlet slit, the deflector electrodes, the outlet electrode with the outlet slit, and the architecture of the electronics used to control the voltages of the TM-IMS and measure the output of ions. b) Different types of trajectories of ions through the TM-IMS: ions with the selected mobility (top), overspeeding ions (middle), and lagging ions (bottom). Adapted from [109].

Regardless of the different available types of IMS, a miniaturization trend has increased the number of instruments in the micro scale, such as **high-Field Asymmetric waveform Ion Mobility Spectrometers** (FAIMS) [8, 110]. The fundamental distinction between them is in the physical principle underlying the separation (the separation parameter).

While in a conventional IMS a pulse of the sample is introduced in the drift tube and the different elements are detected along his drift time, in the case of FAIMS the gas sample is introduced continuously and the different elements are detected along the tension applied.

1. Conventional IMS includes methods based on the different mobility values of ions and under the influence of a weak electric field ($<1,000 \text{ V cm}^{-1}$ [111]) at ambient conditions, and uses electric fields (E) on the same direction that ions displacement (shown in Figure 2-6a), so that ions entering at the same time are separated according to their mobility, reaching the detector at different times [15]. The drift tube IMS device typically has a linear drift tube with potential gradient and countercurrent flow of neutral gas, called the drift gas [8, 15, 91, 112-114].

- high field asymmetric waveform IMS or FAIMS uses an E field perpendicular to ions displacement to separate and select them (shown in Figure 2-6b-c). This is allowed taking advantage of the slight dependence of the ion mobility with strong fields. Using an adequate AC E field the ions are displaced of their main path depending of their mobility dependence to the E field, and only one type can reach the detector [115-117]. Due to the novelty of this technique, it has received multiplicity of names like Differential Mobility Spectrometry (DMS) [39], as is common for emerging technologies, but the prevailing one today is (high) Field Asymmetric waveform IMS (FAIMS), indicating the implementation of a strong time-dependent electric field as a periodic asymmetric waveform.

Conventional ion mobility spectrometry (IMS) measures the absolute mobility, and miniaturized Field Asymmetric waveform IMS (FAIMS) exploits the difference between mobilities at high and low electric fields. An additional advantage of FAIMS is the possibility to detect positive and negative ions simultaneously [15, 118], although, at the cost of increasing electronics [119].

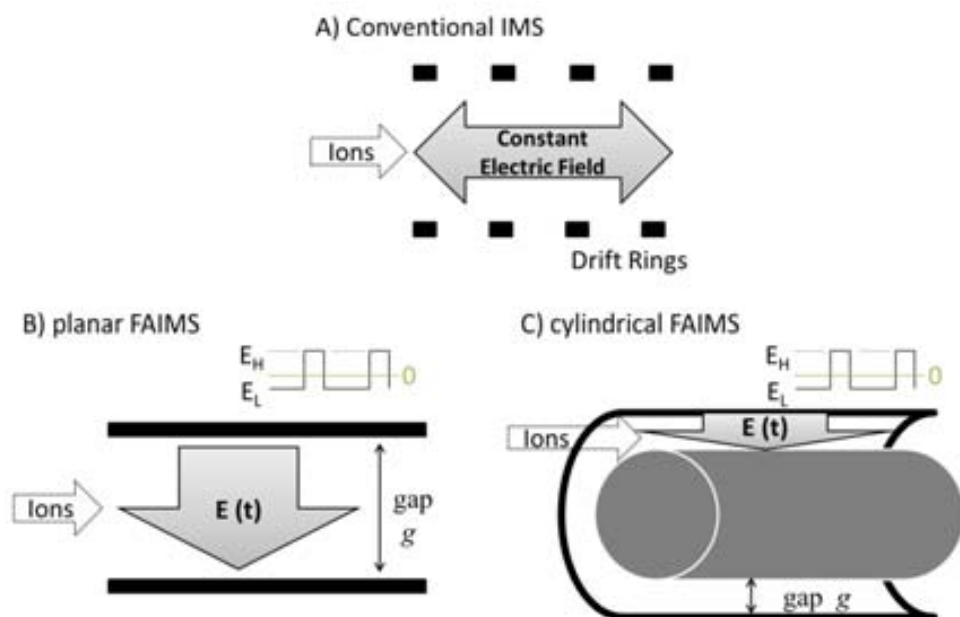


Figure 2-6: Diagrams of ion directions and electric field E application in A) Conventional IMS where a low electric field E is applied parallel to the ions direction, and B) planar FAIMS and C) cylindrical FAIMS where an oscillating electric field $E(t)$ from the high level E_H to the low level E_L is applied perpendicular to the ions direction. Note that diagrams are not in real scale: A) is more than 10 times bigger than B) and C), and also B) and C) have the same order of magnitude for the gap g .

2.2.a Sample Introduction Systems

The process by which a small but representative fraction is acquired is termed sampling. The composition this small fraction must reflect as closely as possible to the average composition of the bulk of the material or population. Calibration determines the relationship between the analytical response and the analyte concentration, usually accomplished by the use of very well-known samples. These samples are prepared using chemical standards and are used to calibrate instruments and procedures avoiding interference effects from other components as are in real samples. A series of such external standards containing the wanted analyte in known concentrations is prepared. Calibration is accomplished by obtaining the response signal (intensity, peak height, peak area) as a function of the known analyte concentration. A calibration curve is prepared by plotting the data or by fitting them to a suitable mathematical equation.

A wide variety of devices are currently in use to introduce gas, liquid and solid calibration samples into IMS instruments. Permeation tubes, purge vessels and dilution glass flasks, headspace samplers and evaporation units are common and will probably continue to be among the most widely used Sample Introduction Systems or SISs for converting liquid or solid substances into volatile analytes prior to their IMS determination by virtue of their low cost and easy operation [120].

Permeation tubes

Permeation tubes are small containers filled with a pure chemical in a two-phase equilibrium between gas and liquid phases, for real and calibration samples. Tubes can be custom-made or purchased from a number of international manufacturers. The containers are made of a suitable inert polymeric material and used at a constant temperature. The potential of permeation tubes for coupling to IMS was illustrated by Borsdorf *et al.* [121]. In Figure 2-7 is shown a permeation tube of ~ 8mL from Owlstone Nanotech Inc. [122]. The permeation tube is a polymer tube (in this case PTFE) sealed and crimped at both ends. The chemical permeates through the walls of the tube at a constant rate for a given temperature; it then mixes with, and is carried away by a diluent, or make-up flow. Permeation devices are usually calibrated gravimetrically for a given temperature.

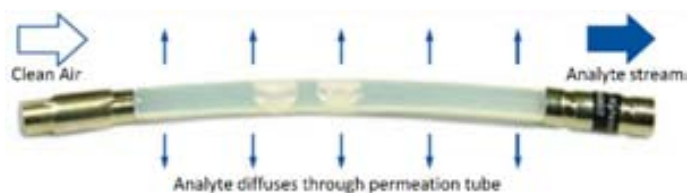


Figure 2-7: Permeation tube [122].

Permeation tubes are inexpensive, easy to use so that they can be constructed in different sizes and from various materials, which affords universal use. Also, empty tubes can be easily disposed of once all compounds have permeated through them. Their main disadvantage is that they must be handled manually, so they cannot be deemed robust components.

Evaporation units

Evaporation units can be custom-built in the laboratory or purchased from various manufacturers. In general, they consist of a robust conductive ceramic material and an additional ceramic inset. The evaporator can be assembled on a water-cooled base plate simultaneously acting as an electrical ground contact. The opposite pole is insulated electrically, but not thermally. The earliest ceramic evaporation unit used in conjunction with an IMS was employed in the detection of various pesticides in liquid matrices in 2000 by Touvinen [30]. The LODs for the pesticides were in the ng or pg range. A solution volume of 10 μL was injected and vaporized in an evaporator at 300°C for insertion into an IMS by means of an air pump.

Purge vessels and Dilution glass flasks

Dilution methods may be used to avoid saturation of the sample in the ionization region of an IMS analyzer. These devices are easy to handle, inexpensive and suitable for on-site analyses. Their main weakness is that they do not afford automation of the process. Another drawback is related to rubber septum; thus, vessels closed with a rubber septum allow the vapor phase to come into contact with a relatively large area of the rubber surface; this may result in significant adsorption of some components and have an adverse effect on the results [120]. The amount of sample introduced into the IMS depends on the type of vessel or glass flask used, and also on the length of the tube connecting the two systems.

Figure 2-8 shows a purge system developed by Borsdorf *et al.* in 2001 [123]. Samples were continuously diluted with pure water and then propelled to the purge vessel by a peristaltic pump. Volatile organic compounds in the sample were purged with purified air. The resulting sample gas stream was rarefied with purified, dried ambient air and fed to the IMS by an internal sample gas pump. This analytical procedure allows the determination of chlorobenzene over the concentration range 3–30 mg/L in water samples.

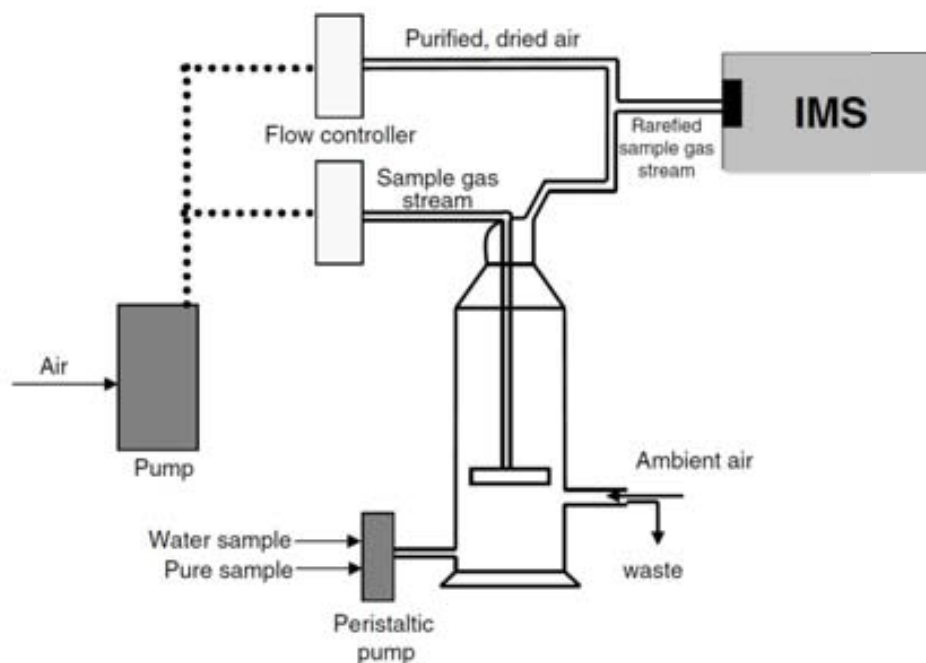


Figure 2-8: Glass flask for extracting volatile organic compounds from water samples. Adapted from [120], originally from [123].

Headspace samplers

Headspace samplers consist of a vaporization container, a heating device intended to keep the headspace container at a constant temperature, and an injection device for transfer the vapor phase from the headspace container into the IMS equipment [120]. Early headspace systems consisted of a glass vial sealed with a rubber septum where vapors were transferred by using a gas-tight syringe [124]. These systems have remained in use for some time. In 1989, Karpas *et al.* [125] used one to obtain the positive ion mobility spectra for various aliphatic and aromatic amines.

Some headspace samplers required opening the sample bottles and drawing in the headspace to the IMS system via an integral pump. This procedure was time-consuming, and prone to inaccuracies and cross-contamination, so it was eventually replaced with an automated alternative. Conventional auto-sampling methods allow the detection of headspace gases in a membrane-sealed vial by using a hypodermic needle. However, the large flow rate to be used with the IMS system (120 mL/min) and the need to sample each vial at hourly intervals led Strachan *et al.* in 1995 [126] to develop a mechanical system consisting of a carousel capable of accommodating multiple 20-mL disposable plastic syringes for the rapid detection of bacteria. Each syringe was controlled to discharge 10 mL of headspace gas into the IMS via a solenoid-activated manifold. Headspace devices are among the simplest SISs used to introduce gases into IMS equipment.

In Figure 2-9, different systems tested by Criado-García *et al.* [127] to perform head-space method are shown, namely: placing a 1.5 mL vial inside a 10 mL vial (A); a 250 μ L Eppendorf tube inside a 10 mL vial (B) and a 1.5 mL vial inside a 20 mL vial (C). In all systems, 100 μ L of acetone was placed inside an opened vial which was in turn placed in a tightly closed vial. These vials were heated at 50 $^{\circ}$ C during times from 1 to 30 min. During these times, a loss weight of the liquid standard was observed due to the fact that liquid molecules of acetone passed to the gas phase in the head-space inside the bigger vials. As can be seen in Figure 2-9, an almost identical amount of gaseous acetone was produced in all systems used during the different heating times tested. For this reason, any of these devices could be used to measure VOCs present in liquid samples.

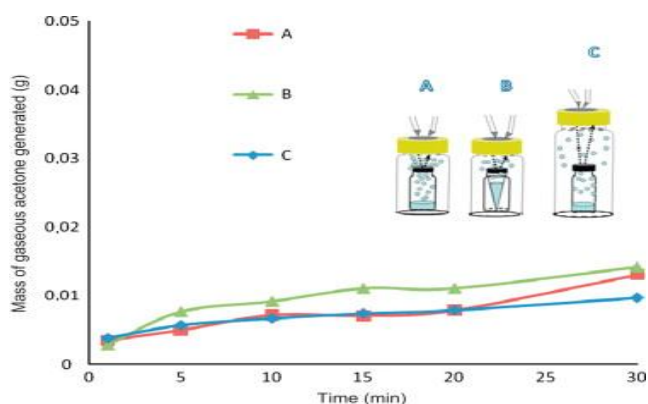


Figure 2-9: Different head-space methods [127].

2.2.b Ionization region

Once the sample arrives to the ion mobility spectrometer, the initial step of every mobility separation is ionization of sample molecules. The kind of ions will differ depending on the ionization method [8, 112].

Ion process formation

The ionization energy or ionization potential for a molecule is the energy necessary to remove an electron from the neutral molecule. So the basic mechanism of ionization is the formation of **positive ions**, and the release of an electron with a maximum energy $E_{e^-} = IP - E_{\gamma}$ [128]:



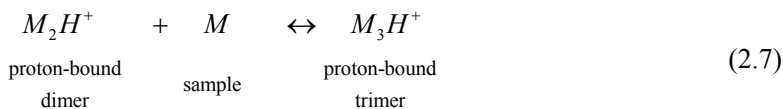
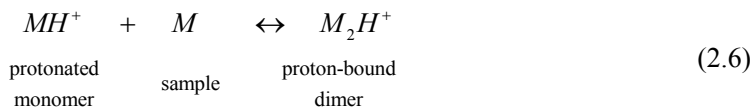
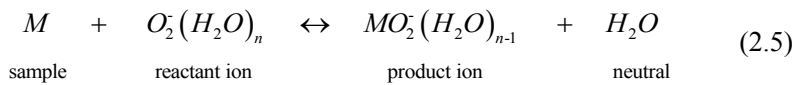
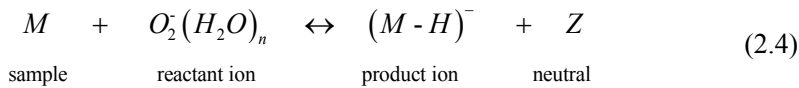
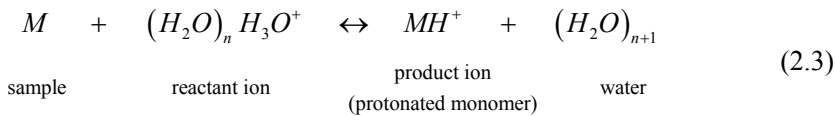
In many cases, M^{+*} will be thermalized through collisions with non-reactive molecules in the air, such as nitrogen (N_2) and oxygen (O_2). The thermalized molecules M^+ may participate in reactions ion-neutral molecule (M) at a rate determined by the reaction constants and the concentration of neutral molecules.

Negative ions are not formed directly due to the ionization process, but are formed by the electron excess chemical reactions of positive ions. The electron can directly bind to a molecule [15]:

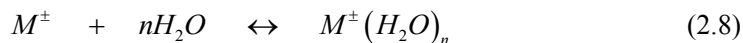


However, the most frequently observed ions in Atmospheric Pressure PhotoIonization are the monomers MH^+ . For example, the product ions of ketones include more protonated monomers MH^+ than monomers like M^+ . This suggests that intermediate species are generated in ionization at ambient pressure, although the reactions are not fully described. Therefore, the exact mechanism of formation of ions in air at ambient pressure should be considered incomplete for high proton affinity compounds or for compounds that can release protons.

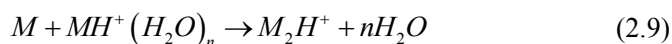
The positive and negative ions produced from the sample can participate in other reactions, from which the most important are the association reactions with neutral molecules, as are the formation of **monomers** MH^+ , $(M-H)^-$ or MO_2^- , of **dimers** M_2H^+ or **trimers** M_3H^+ [15, 129, 130]:



In a series of reactions positive/negative ion with water vapor molecules, results the formation of ions $(H_2O)_n(H_3O)^+$ and $O_2^-(H_2O)_n$, called **reactant ions** [15]. In addition, for both positive and negative ions, and for monomers, dimers and trimers, the hydration reaction (formation of Ion Clusters) is done as follows:



This reaction will be favorable if the gas-phase proton affinity of the sample molecule is larger than that of the water ($691 \text{ kJ}\cdot\text{mol}^{-1}$). Whereas for low concentrations only equation (2.8) apply, in case of higher concentration of analyte in the ionization region, the formation of dimer products according to equation (2.9) are observed [15, 112, 131].



The dimer cluster M_2H^+ is a proton-bound dimer and can be also attached to several molecules of water ($M_2(H_2O)_nH^+$), or for even higher concentrations undergo further reactions to form proton-bound trimers or tetramers.

Figure 2-10 shows a schema of the main pathways that can suffer a sample (M) in a Photo Ionization process in air. Ions shown correspond to: positive ions M^+ [Equation (2.1)]; negative ions [Equation (2.2)]; positive and negative Monomer ions [Equations (2.3), (2.5)]; positive and negative Ion Clusters [Equation (2.8)]; and positive dimer ions [Equation (2.6)].

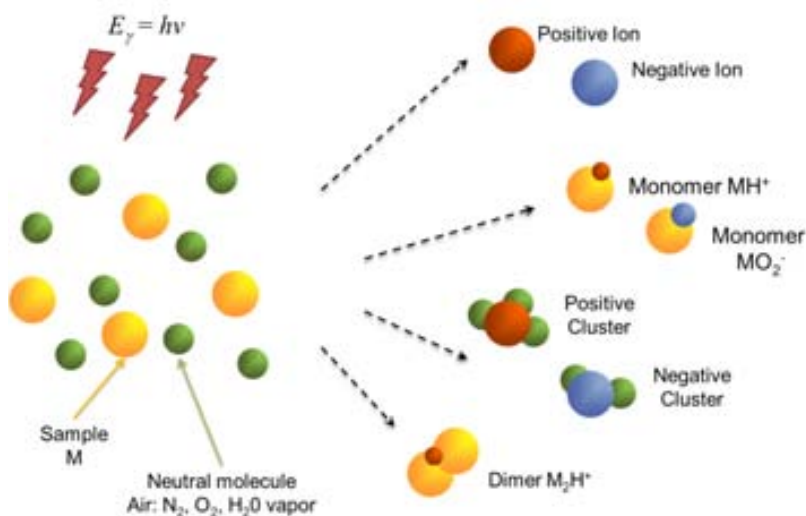
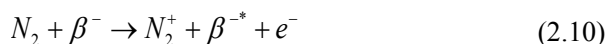


Figure 2-10: Schema of the main ionic pathways in a Photo Ionization process in air.

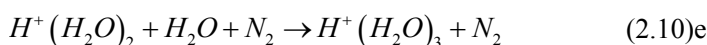
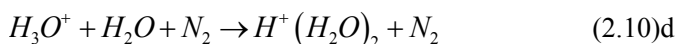
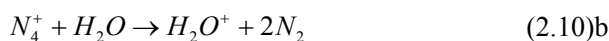
Radioactive Atmospheric Pressure Chemical Ionization

The most used and historical ionization method in IMS is Radioactive Atmospheric Pressure Chemical Ionization or R-APCI [8, 15]. For IMS devices, the most used ionization method is a radioactive atmospheric pressure chemical ionization (R-APCI) by a β -source from a small foil of radioactive nickel-63 or ^{63}Ni of 550MBq^1 [110, 132]. The radioactive half-life of ^{63}Ni is approximately 100 years and the beta particles have a distribution of energies with a average value of 17 keV and with a maximum of 67 keV. Electrons emitted from the foil collide with the molecules of the supporting atmosphere and in the instance of air or nitrogen, produce N_2^+ as shown in Equation(2.10). Nitrogen is ionized as long as the energy of the radiation is higher than its ionization potential of 15.58 eV.



Here, β is the beta particle emitted from the ^{63}Ni source and β^* is the beta particle after some of its energy has been used in ionization of nitrogen molecules. The loss of energy for the electron (β) in this ionization step is ~ 35 eV, so highly energetic electrons diminished slightly from 67 keV will undergo further collisions and ionizations repeatedly so that one electron can produce $\sim 2,200$ ion pairs. The electrons produced in equation (2.10) and also primary electrons (β), after collisions and ionization reactions, will eventually reach thermal energies and become attached to oxygen forming negative ions.

These primary positive ions (known as reaction ions) will undergo different chemical reactions with the analyte ions to form product ions by: proton transfer [133-136], nucleophilic attachment [137, 138], and/or hydride abstraction and other pathways [8, 112]. N_2^+ ions, although short-lived and therefore do not appear in the mobility spectrum, will induce new collisions which can lead to a sequence of reactions and productions of **positive ions** [8]:

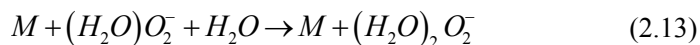
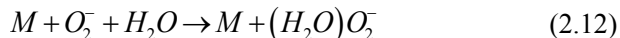


¹ A Becquerel is one disintegration (dimensionless) in a second, namely: $1\text{Bq} = 1/\text{s}$. Previously was used the Curie unit (Ci) named in honor to Marie and Pierre Curie, being: $1\text{Ci} = 3,7 \times 10^{10}\text{Bq}$.

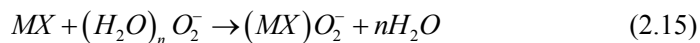
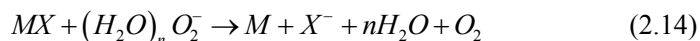
Thus hydrated protons $(\text{H}_2\text{O})_n\text{H}^+$ are formed with a variable number of water molecules depending on the temperature, the pressure and the humidity [139-142]. This water clusters form the so called reactant ion peak or RIP and are the source of the protons for ionizing the analytes. Other clusters as $(\text{H}_2\text{O})_n\text{NH}_4^+$ or $(\text{H}_2\text{O})_n\text{NO}^+$ can be formed by impurities contained in the synthetic air, which are produced by proton transfer and charge-exchange reactions. Peaks of these ions can be seen in mobility spectra as small ammonia cluster peaks (pre-RIP) before the RIP.

In addition to positive reactant ions, **negative ions** are also formed in an ion source principally through the attachment of a thermalized electron to molecular oxygen would be attached to sample molecules and form negative ions on different ways: electrophilic attachment, resonant attachment or dissociative attachment [143-146]. Charge transfer [135, 147-152] and proton abstraction [19, 153, 154] could also occur. Often, both positive and negative ions are formed. Limitations will come by the total number of ions available, which is realized by the reaction ion peak.

A negative ionization of the O_2 simultaneously takes place in the ionization chamber. An electron is attached to the oxygen leading to the formation of the negative O_2^- ion. Clusters with water are formed similarly to the positive ionization with a three-body collision [155, 156].



Negative product ions are formed from neutral sample molecules MX (like O_2 or H_2O or a neutral analyte M) due to charge transfer reactions and include dissociation electron attachments equation (2.14) and associative electron attachments according to equation (2.15).



Cluster of hydrated ions for these product ions are also known with the structures $\text{M}^-(\text{H}_2\text{O})_n$ and $(\text{M}-1)^-(\text{H}_2\text{O})_n$.

In addition to ^{63}Ni , tritium (T or H^3) may be used as a beta emitting ion source for IMS devices [26, 132, 157]. The beta particles (electrons) are emitted as a result of the following equation:



where the average kinetic energy of the electrons is 6.5 keV with a maximum energy of 18.6 keV. The radioactive half-life of tritium is approximately 12 years. Tritium poses fewer radiation hazards than ${}^{63}\text{Ni}$ due to the low energy beta radiation. Although the detailed ionization pathways are not completely understood, similar processes are supposed in comparison with ${}^{63}\text{Ni}$ ionization. Another radioactive isotope that has been used for IMS is americium-241 sources (Am^{241}) [158-160]. In contrast to the before mentioned isotopes, ${}^{241}\text{Am}$ is an alpha-emitting isotope and releases alpha particles and gamma rays forming ${}^{237}\text{Neptunium}$ according to Equation (2.17):



The energy of emitted alpha particles is above 5.4MeV with a short effective range. ${}^{241}\text{Am}$ sources are therefore suitable for small volume sources. The high-energy alpha particles collide with air constituents and form ions. Charge transfer reactions are believed responsible for forming product ions, though ionization pathways have not yet been fully described.

32
However, ionization in an R-APCI source is initiated by radioactive material which carries a safety issue and requires certificates and permissions to use according to the local safety regulations. Thus, a number of non-radioactive atmospheric pressure ionization techniques, have successfully been combined with IMS instrumentation.

Atmospheric Pressure Photoionization

The main alternative ionization techniques combined with IMS devices is atmospheric pressure photo ionization (APPI) [15, 161] based on ultraviolet light (UV) [26, 69, 149, 162-164].

The photoionization at ambient pressure (Atmospheric Pressure PhotoIonization, APPI) is based on the ionization of the sample with light, that higher is the frequency, greater will be the ionization energy. This light can be achieved through the use of gas-discharge lamps that have their maximum emission energy in the UV range, which generate light by sending an electrical discharge through an ionized gas. UV lamps emit photons from the inside gas when it is electrically excited with energy $E_\gamma = h\nu$, where h [$6.626 \cdot 10^{-34}$ J·s] is Planck's constant and ν [s^{-1}] is the frequency of the photon.

The ionization energy or ionization potential is the energy necessary to remove an electron from the neutral atom. Therefore, a UV emitting at an energy of $E_\gamma = 10.6$ eV

[165] can ionize all the molecules or compounds that have an ionization potential equal or less to this value, for example acetone ($IP_{Ac} = 9.73 \text{ eV}$ [166]) while air will not be ionized because its ionization potential is much higher: $IP(N_2) = 15.58 \text{ eV}$, $IP(O_2) = 14 \text{ eV}$ [166]. The energy that can provide this type of lamp ranges from 8.4 to 11.8 eV [165].

In contrast to chemical ionization with radioactive sources, PhotoIonization (PI) is said to be a primary ionization process without or with a very tiny amount of reactant ions and corresponding spectral peaks. Therefore, spectra are comparatively simple and the linear range of response curves, established by reactant ion concentration with radioactive sources, does not apply with PI sources. A complication with discharge lamps is the fixed operating lifetime for a lamp (with replacement costs), the additional power demand needed for the photo-discharge, and maintenance in cleaning the lamp window, which can be fouled with high vapor concentrations or complex mixtures, particularly containing substances of low vapor pressure.

Corona Discharge Atmospheric Pressure Chemical Ionization

Corona discharges atmospheric pressure chemical ionization (CD-APCI) provides gas phase ions that may resemble the reactant ion chemistry found in radioactive sources [15, 162, 167-173]. These ions are formed in the high electric field developed between a needle (or thin wire) and a metal plate or discharge electrode. Though other geometries and arrangements are possible, ions are formed in a comparatively stable electrical discharge in air at ambient pressure when voltage differences of 1 and 3 kV exist between the needle and plane, at spacing of 1 cm or so. Product ions may be formed via different processes due to the varying strength of the electric field around the corona needle. The high electric field near the corona needle ($\sim 10^6 \text{ V}\cdot\text{cm}^{-1}$) allows ion formation by electron transfer yielding gaseous electrons with a mean free path of $\sim 10^{-5} \text{ cm}$ and energy of 30 to 40 eV. These electrons can initiate ionization processes as known from electron impact ionization. At increased distance from the corona needle, the electric field strength decreases and photoionization and protontransfer reactions, as described with radioactive sources, can occur. The combination of these processes permits the detection of compounds (e.g., n-alkanes, saturated hydrocarbons) which are not detectable or weakly detectable with the other ionization techniques [121, 174]. These mixed mechanisms of ionization, and differences that arise through the formation of reactive gases including NO_x and ozone, complicate comparisons of response of CD sources with traditional ^{63}Ni sources. However, comparable response can be obtained when ventilation of neutrals is properly arranged or managed. As with other non-radioactive discharge methods, CD sources are disadvantaged practically by the additional requirements of power and maintenance.

Laser Desorption Ionization

When using a laser as ion source, two separate functions including desorption or vaporization of sample and the ionization of constituents in the sample vapors can be combined in a single component, is the so called laser desorption/ionization (LDI) [7, 175-184] . Also, each process may be used independently to process solids or ionize gases. While infrared rays are normally used for desorption of low-volatile substances, photons from the ultraviolet wavelengths are effective in the ionization of organic compounds. Solid-state lasers of Nd:YAG (neodymium-doped yttriumaluminum-garnet) provide a wavelength of 1064 nm (1.17 eV) from which 532 nm (2.33 eV), 355 nm (3.49 eV), and 266 nm (4.66 eV) can be produced with additional crystals. Improved selectivity of ionization can be approached with tunable lasers with wavelengths in the ultraviolet range and is accomplished with excimer lasers, dye lasers, and the combination of special techniques with various lasers. Though lasers have certain mechanical advantages over simple discharge lamps, there are also disadvantages of size and cost. The same limitation applies for matrix-assisted laser desorption/ionization (MALDI), which has recently been combined with IMS for the determination of biomolecules and polymers [182, 185-198].

Surface Ionization

A specialized ionization technique, the surface ionization [199-204], has been developed for selective response to compounds (M) with low ionization energies, which undergo dissociation by loss of hydrogen atoms or alkyl groups and electron transfer. In the source, molecules are brought in contact with a solid, where surface ionization principally to $[M - H]^+$ and $[M - R]^+$ arises. Additionally, $[M + H]^+$ ions can be formed, depending on the sample concentrations. The surface consists of single-crystal molybdenum, heated to 300 to 500°C. Contact or collision of molecules with this heated reactive surface results in electron loss and the formation directly of product ions. This ionization method does not have the broad applicability of a ^{63}Ni source but has specificity for certain functional groups, notably amines.

Electrospray Ionization

A last ion source included here has been used only in laboratory studies yet provides capabilities not found in any other method. In electrospray ionization (ESI), liquid sample is directly introduced into a drift tube through methods that are now well developed from advances in mass spectrometry [15, 205-221]. Gas-phase ions are formed by creating a fine aerosol of highly charged droplets in a high electric field of several thousand volts per cm. Subsequent and progressive loss of solvent in the aerosols leads to a gaseous product ions from substances with large molecular weights including biomolecules of 10,000 amu and greater.

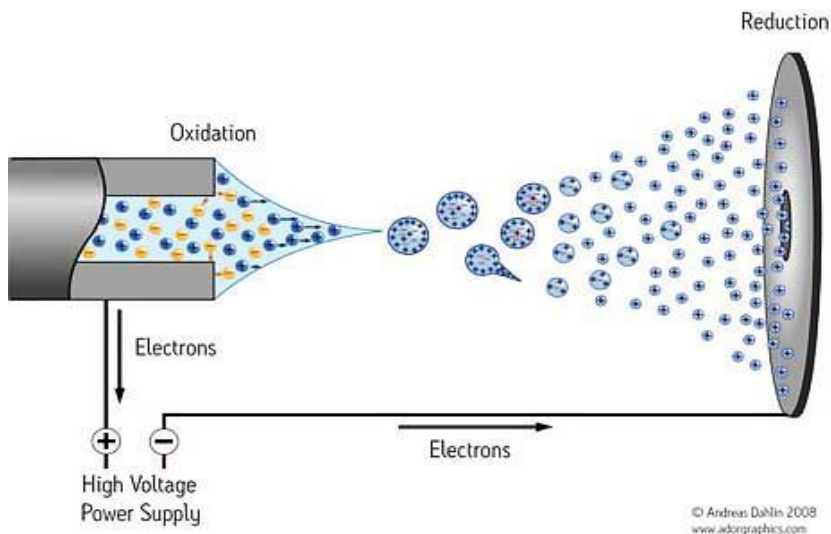


Figure 2-11: Electro spray Ionization (ESI) diagram [222]. After formation the ions are “dragged” through a potential gradient (an electric field) to the counter plate.

Electrospray ionization has been demonstrated with IMS analyzers in combination with mass spectrometry for environmental analyses of water samples for chemical warfare agents and their degradation products. In Figure 2-12 is shown a commercial IMS device with an ESI source [20]. Electro spray ionization is also used with mobility analyzers as an ion filter before mass spectrometry in commercial versions of high field mobility methods. In this application, the mobility analyzer behaves as a notch filter suppressing chemical noise and enhancing S/N (signal-to-noise ratio) for MS determinations.

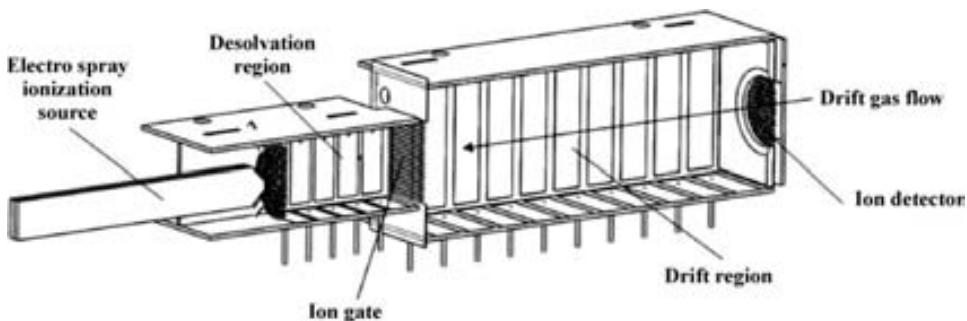


Figure 2-12: Excellims GA-2100 High Resolution Ion Mobility Spectrometer (HRIMS) fitted with an electro spray ionization (ESI) source [20].

2.2.c Drift region

The drift tube is the central component of an IMS. For conventional IMS the main function of the drift region is to separate the different components so they can be identified by the time they need to traverse this region. To do so, it is important to fix the temporal origin ($t = 0$) at which a sample of gas and ions are introduced in the drift region. The ion gate is this device.

Ion gates

The ion gate is the part of the IMS which allows the ion swarm into the drift region. There are two different systems of ion gates, The Bradbury-Nielson gate and the Tyndall gate. Both devices involve the creation of an electric field between two sets of thin wires interspersed and strung across the drift tube. The gates are open when the two sets are at the same potential of their location in the drift field, and are close when they have opposite potentials [223].

In the Bradbury-Nielson gate, which is the most common one and used in the IMS for this study, the ions are passed in a single plane of the drift field. The gate consists of a single grid of widely spaced wire, alternate wires being biased positive and negative to the gates' reference voltage (see Figure 2-13), creating an orthogonal gate field to the drift field [224, 225]. The gate field is usually three times the drift field, directing the ions into the wires where they are neutralized [223].

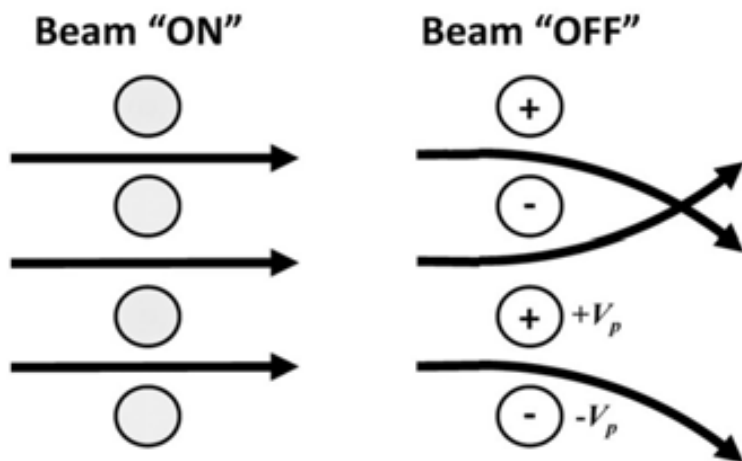


Figure 2-13: Schematic of a Bradbury-Nielson gate (BNG). A BNG consists of two interleaved and electrically isolated sets of wires. The charged particles are transmitted through the BNG when the two wire sets are at an equal potential (Beam "ON"). When voltages that are equal in magnitude and opposite in polarity ($\pm V_p$) are applied to the two wire sets, the charged particles are deflected (Beam "OFF"). Adapted from [225].

The Tyndall gate on the other hand consists of two independent wire grids separated by a short distance (≈ 1 cm) composed of finely spaced wires. The gate is closed by applying a voltage across the grids which reverses the drift field in the vicinity of the gates [223, 226].

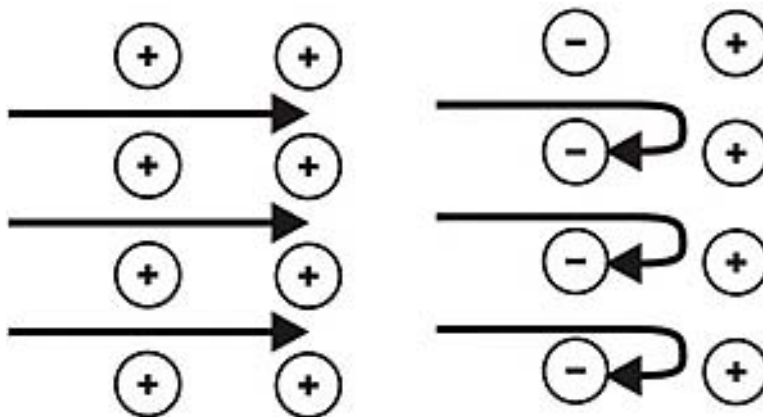


Figure 2-14: Schematic of a Tyndall gate (TG). A TG consists of two independent wire grids separated by a short distance (≈ 1 cm). LEFT) The gate is open when the two wire grids have the same voltage. RIGHT) The gate is closed by applying a voltage across the grids which reverses the drift field in the vicinity of the gates.

IMS Ion Dynamics

Ions moving in a gas-phase medium and in presence of an electric field E , are accelerated due to coulomb forces and slowed due to collisions with molecules of the gas medium. As a result, the ions move in average at a constant drift velocity v_d , proportional to the electric field and in the same direction [227].

The proportional factor is call mobility, K , and usually is expressed in $\text{cm}^2 \cdot \text{V}^{-1} \cdot \text{s}^{-1}$:

$$v_d = K \cdot E \quad (2.18)$$

Conventional IMS are operated for low electric fields ($E < 10,000 \text{ V} \cdot \text{cm}^{-1}$ or $E/N = 80 \text{ Td}$). The parameter E/N was introduced due to the need to extend the comparison of results. E/N is expressed in $\text{V} \cdot \text{cm}^2$, where N is the number density (the number of molecules per unit volume), but for convenience, it was resolved to adopt the unit Townsend: $1 \text{ Td} = 10^{-21} \text{ V} \cdot \text{m}^2$ [228, 229]. However it was demonstrated in the earliest studies of ions in gases at the beginning of 20th century [15, 230] that the mobility K is dependent on the energy obtained from the applied electric field by ions

between collisions. When E/N is small, energy acquired by the ion from the electric field is considered negligible because collisions with molecules of the supporting gas atmosphere will dissipate any field-acquired energy (i.e. K will not be influenced by the applied electric field at a given pressure, $K \neq K(E/N)$) [15]. The mobility coefficient will become dependent on the electric field (i.e. $K = K(E/N)$) with increasing values of E/N .

The force exerted by the electric field, with a negligible magnetic field, on a single ion is described by the Lorentz law:

$$F = qE \quad (2.19)$$

where F [N] is the force perceived by the ion with a charge q [C] being $q = ze$ where e is the elementary charge [1.602×10^{-19} C] and z [dimensionless] is the number of elemental charges. The force and the electric field are both vectors, so Equation (2.19) describes that the force has the same direction as the electric field.

Mobility is usually considered constant in front of E . That can be assumed to be true for almost all the practice cases, particularly in the design of conventional IMS. However, for high values of E , K varies.

The mobility K [$\text{cm}^2 \cdot \text{V}^{-1} \cdot \text{s}^{-1}$] and the diffusion coefficient D [$\text{cm}^2 \cdot \text{s}^{-1}$] of an ion are connected by the Nernst-Townsend-Einstein relationship [227]:

$$K = \frac{Dq}{k_B T} \quad (2.20)$$

where q [C] is the ion charge; k_B is the Boltzmann constant [$1,38065 \times 10^{-23}$ J·K⁻¹], and T is the gas temperature [K].

A molecule will diffuse differently in different media; hence D is a property of the pair of diffusing and media molecules. For diffusion in gases, D is determined by [227]:

$$D = \frac{3}{16} \left(\frac{2\pi k_B T}{\mu} \right)^{1/2} \frac{1}{N\Omega} \quad (2.21)$$

where N is the number density (the number of molecules per unit volume), $\mu = mM/(m+M)$ is the reduced mass of the pair of diffusing ion and carrier gas molecule (with respective masses of m and M), and Ω is the collision cross section (the first-order binary collision integral of the pair ion-neutral, from an infinite number of collision integrals defined in the transport theory).

Hence, the mobility of an ion also depends on Ω , according to the theory of Chapman-Enskog, we obtain the Mason-Champ equation:

$$K = \frac{3}{16} \left(\frac{2\pi}{\mu k_B T} \right)^{1/2} \frac{ze}{N\Omega} = K'_{ion} \frac{1}{N} \quad (2.22)$$

The mobility can be reduce to, showing that as in low electric fields it do not depend on E , it do depends on the number density (N). From Equation (2.18), it can be derived that for ions in a fixed E having a constant velocity v , the displacement L is proportional to time: $s = KEt$, so the drift time that an ion needs to pass through the drift region is proportional to the inverse of the mobility, and therefor of the inverse of E/N :

$$t_{ion} = \frac{1}{K'_{ion}} \frac{L}{E} = \frac{L}{K'_{ion}} \left(\frac{E}{N} \right)^{-1} \quad (2.23)$$

2.2.d Detector region

Usually the detector is a Faraday's plate combined with an aperture grid. Collision and annihilation of ions on the detector cause a current flow of nano- or pico-amps [8] which is amplified and converted into voltage. To maintain the spectral resolution in single-scan or single averaged spectral collection, an aperture grid must be placed at short distance, 1 to 4 mm, from the Faraday plate [8, 223, 231]. This provides a capacitive decoupling between the arriving ions and the detector. Without the aperture grid, the ion swarm will induce, by Coulomb attraction, a charge on the collector several millimeters prior to its arrival resulting in decreased signal intensity and peak broadening hence spectral resolution. In Figure 2-15 is shown how adding an Aperture Grid shields the ion collector from induced charges in the surface of the collector. Thus, an aperture grid prevents distortion or fronting of peaks and preserves resolution in a mobility spectrum. The size of both the aperture grid and detector affects sensitivity.

The signals are amplified and sent to a computer where the software records the data. The ion mobility spectrum is usually a plot of ion intensity current as a function of drift time that takes to an ion to reach the detector once has been opened the ion gate [110], as can be seen in Figure 2-16 [232].

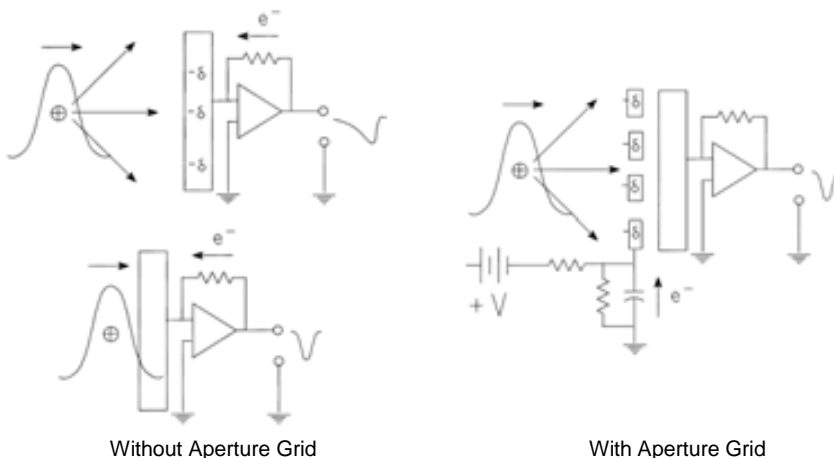


Figure 2-15: Illustrations of an ion cloud approaching and then hitting the ion collector of an ion mobility spectrometer. Without Aperture Grid, is shown the real (left top) and the expected (left bottom) ion cloud induction of charges. With Aperture Grid a solution to real ion cloud induction of charges is obtained. (left top) Real approach: shows that the ionic charge induces surface charge on the ion collector, and this surface charge is supplied by electron flow through the feedback resistor of the electrometer. (left bottom) Ideal approach: shows that electron flow again occurs through the feedback resistor as the ion cloud hits the ion collector, and that the electron flow is in the same direction as the induced current flow. (right) Solution with AG: shows how an aperture grid interposed between an approaching ion cloud and ion collector shields the ion collector from induced charge. A ballast capacitor is added to serve as a ready source of electrons that can flow into the aperture grid. Adapted from [233].

40

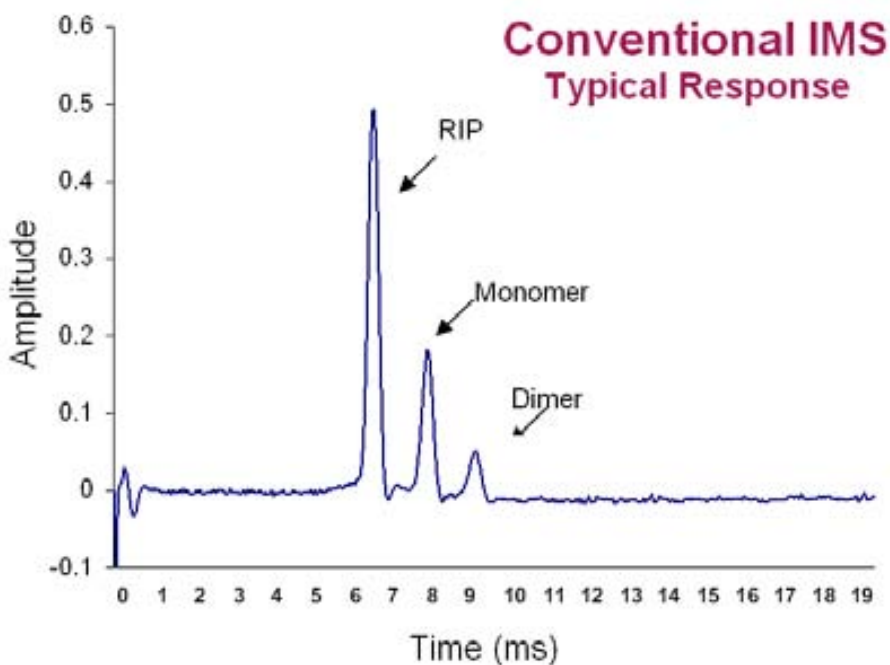


Figure 2-16: Schema of a typical IMS chromatogram showing the reactant ion peak (RIP), one monomer and one dimer. Adapted from [232].

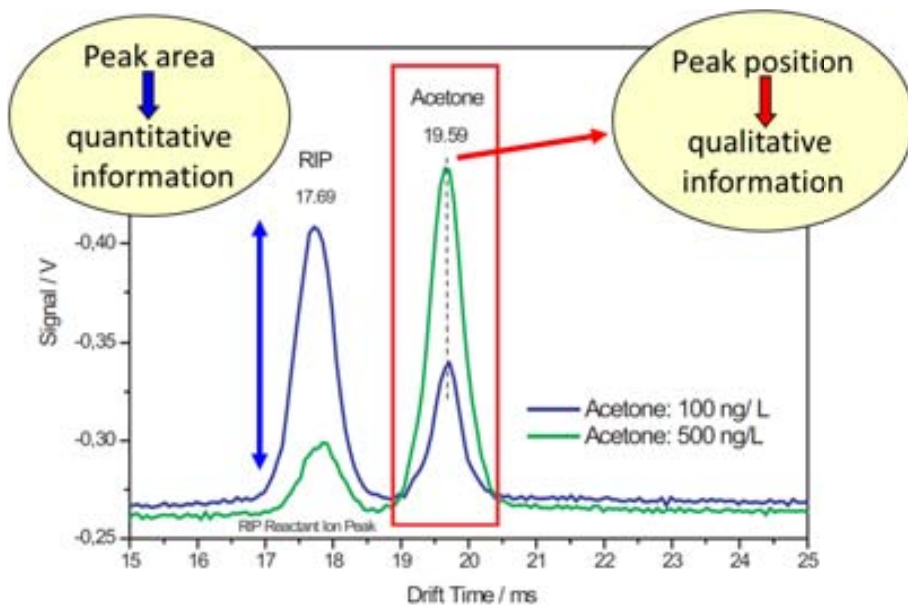


Figure 2-17: Ion mobility spectrum of positive ions of acetone in air using a ^{63}Ni -IMS device. Adapted from [234].

IMS chromatograms gives not only quantitative information (peak area is related to compound concentration) of the analyzed compounds, it gives also qualitative information (peak position is related to the compound shape and size because as drift time is related to K). Figure 2-17 shows two typical spectra obtained from a sample of acetone in air at concentrations of 100 and 500 ng/L [234]. The two peaks shown in Figure 2-17 corresponds to the presence of air (RIP: reactant ion peak) at 17.69 ms and the analyte acetone at 19.59 ms. The ionization of acetone is realized by charge transfer between the air ions and the acetone molecule. Thus, it is clear that with higher concentration of the analyte in air, the RIP will decrease and the acetone-related peak will increase. In general, the peak position is relevant to identification and the peak area is related to the concentration of the analyte. Peak areas are often calculated using Gaussian-Curve-Analysis procedures. It should be noted that IMS is most suitable for *trace* gas analysis [234].

2.2.e Hyphenated Methods with Ion Mobility Spectrometers

Ideally, different ions reach the detector (Faraday plate) totally separated, but this cannot be realized for complex samples due to that on complex ionization reactions (charge transfer) different molecules have similar values of K . Additionally compounds with a high proton affinity are being formed preferentially. This leads to a

lack of information about compounds with a low proton affinity. Also, humidity causes the major problem under atmospheric conditions due to cluster reactions between ions and water molecules, leading to significant changes of the spectra and to a decrease of sensitivity.

Vautz *et al.* studied how humidity affected the spectrum of a single compound [235]. Figure 2-18 presents the IMS spectra of α -pinene² for varying relative humidity. Beside the decrease of the peak height of the initial major peaks at 20.5 and 28.5 ms the formation of additional peaks with increasing relative humidity can be observed at 17.0, 22.0 and 32.0 ms drift time. Those additional peaks seem to be the result of the already mentioned cluster reactions in the presence of water molecules. They make the identification of the substance much more difficult, because the shape of the IMS spectra depends directly on the relative humidity. Furthermore, the increase of relative humidity leads to a decrease in the total signal area (up to 40%), thus decreasing the sensitivity of the IMS for increasing relative humidity.

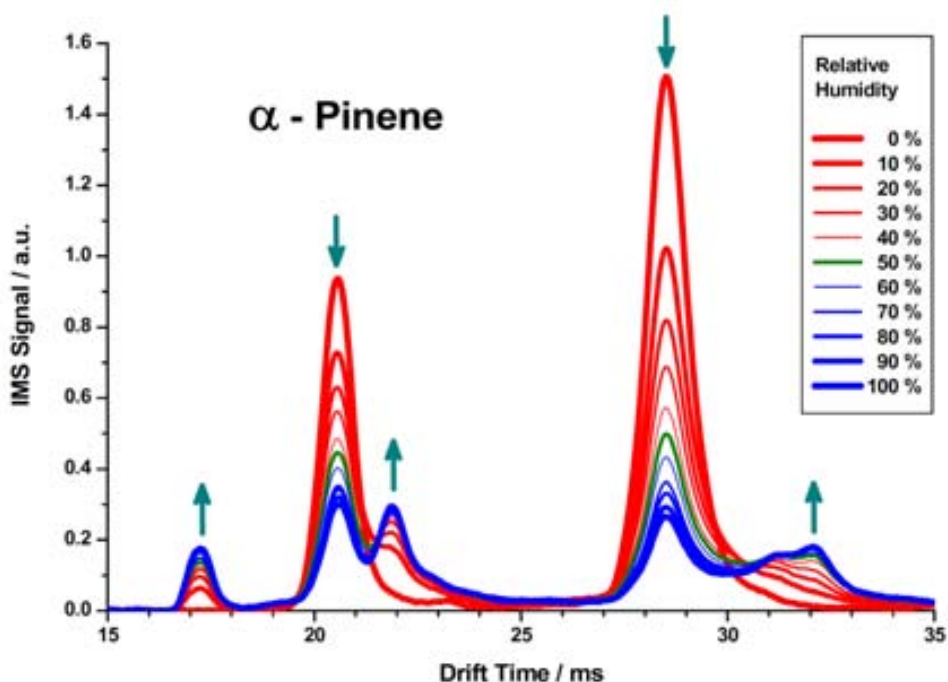


Figure 2-18: Ion mobility spectra of α -pinene using direct introduction of the analyte into the ionization chamber for 0% and 100 % relative humidity (RH) of the carrier gas with the analyte [235]. The spectra show the development of additional peaks for high relative humidity due to the formation of monomer and dimer ions. Significant changes can be observed already for low RH values.

² α -pinene is a compound present in essential oils of conifers, particularly pines, but can also be found in many orders of plants. Represents one of the major VOCs emitted into the air.

Real samples, gives complex IMS spectra's, and identification of analytes can be difficult or even impossible. To identify what compound you are detecting, two main strategies can be followed:

- 1) Pre-Separate the sample, so the obtained detection spectrum is less complex. This strategy, uses the combination of gas chromatograph (GC), as pre-separation, with IMS [236]. Recently, a variation of a capillary GC column – the multi-capillary column (MCC) – has successfully been used in combination with IMS for analysis of biological and medical samples (Figure 2-19) [36, 75, 237, 238]. Furthermore, this avoids negative effects from clustering in the ionization chamber when humid air is analyzed: Using pre-separation, the water molecules and the analyte molecules enter the ionization chamber successively. Therefore, relevant substances can be detected even in humid air up to 100% relative humidity without negative effects on the detection limits [235]. Hence, this technique is a very promising tool in VOC analysis in general, including breath analysis sampling where the content of humid air is really high [87].
- 2) Identify the compound when it is detected. This strategy uses the combination of a Mass Spectrometer (MS) as the detector part of the IMS. The set of IMS-MS instruments provide unambiguous identification of ions in a mobility spectrum and were commercially available since the 1970s but were mainly used for aqueous and solid samples like proteins, lipids, or alcohols and not for VOC applications. However, those instruments have predominantly been used only in research and development laboratory [239-241]. An excellent overview about different coupling technologies of IMS with MS has been given recently [241]. Up to now, applications for VOC analysis by IMS-MS instruments have been few because of very complex equipment's which are currently used in the laboratories only and not as portable analysis instruments.

pre-separation with MCC, the MCC-IMS

In IMS all ions will be created and diffused at the same time with the risk that, ions of different analytes, but with similar K , will reach the detector simultaneously. This problem can be largely overcome by pre-separating the different analytes. A way to achieve this, is coupling a gas chromatograph (GC) before the IMS itself, in which packed GC columns were soon replaced by multi-capillary columns (MCC), that can be understood as multiple gas chromatographs set together with short lengths (~cm) [242] in front of the GC lengths (~m) [243], with the advantage that it can process higher sample flows and obtained intensities than the a simple GC. The effect of the column is that different molecules need different time to pass through the capillaries, thus obtaining three dimensional ion spectra.

For direct analyte introduction, a significant decrease of the total number of ions in the range of 28–42% with increasing relative humidity was found by Vautz *et al.* [235], as seen in Figure 2-18. Simultaneously additional peaks in the spectra were formed, thus complicating the identification of the analytes. In case of pre-separation of the analyte, the spectra do not change with increasing relative humidity, due to the successive appearance of the analyte and the water molecules in the ionization chamber.

An example of a multi-capillary is found in Figure 2-19, for a 17 cm long weak polar multi-capillary column (MCC-OV5, Sibertech, Ltd., Novosibirsk, Russia) coupled to a ^{63}Ni -IMS. It is made by combining approximately 1,000 capillaries bundles from glass (see Figure 2-19A) each one of them with an inner diameter of $\sim 40\ \mu\text{m}$ and containing stationary phase film of $0.2\ \mu\text{m}$ thick. The total column diameter of 3 mm allows operation with a carrier gas flow up to 150 mL/min, which is the optimum flow rate for the IMS. In addition, the effective separation of water vapor is one major advantage of the MCC. Using other techniques like humidity sorbents or membrane separation units, some of the original analytes may be lost. The stationary phase of the non-polar OV5 phase is made with 5% diphenylpolysiloxane and 95% polydimethylsiloxane or PDMS.

Once pre-separated the sample it passes to the IMS (Figure 2-19B), and then integration of all the spectra over the retention time in minutes, a spectrum similar to that one obtained by sample introduction without MCC (Figure 2-19C) is the result.

The heating of the column is indispensable for the reproducibility of the chromatographic results [244]. To achieve comparable retention times the MCC is hold at 40°C (sometimes also 70°C are applied, but such effects will not be considered here more in detail) during analysis procedure. Once the different components of the sample are separated by their retention time in the multi-capillary column, they pass to the ionization region of the IMS.

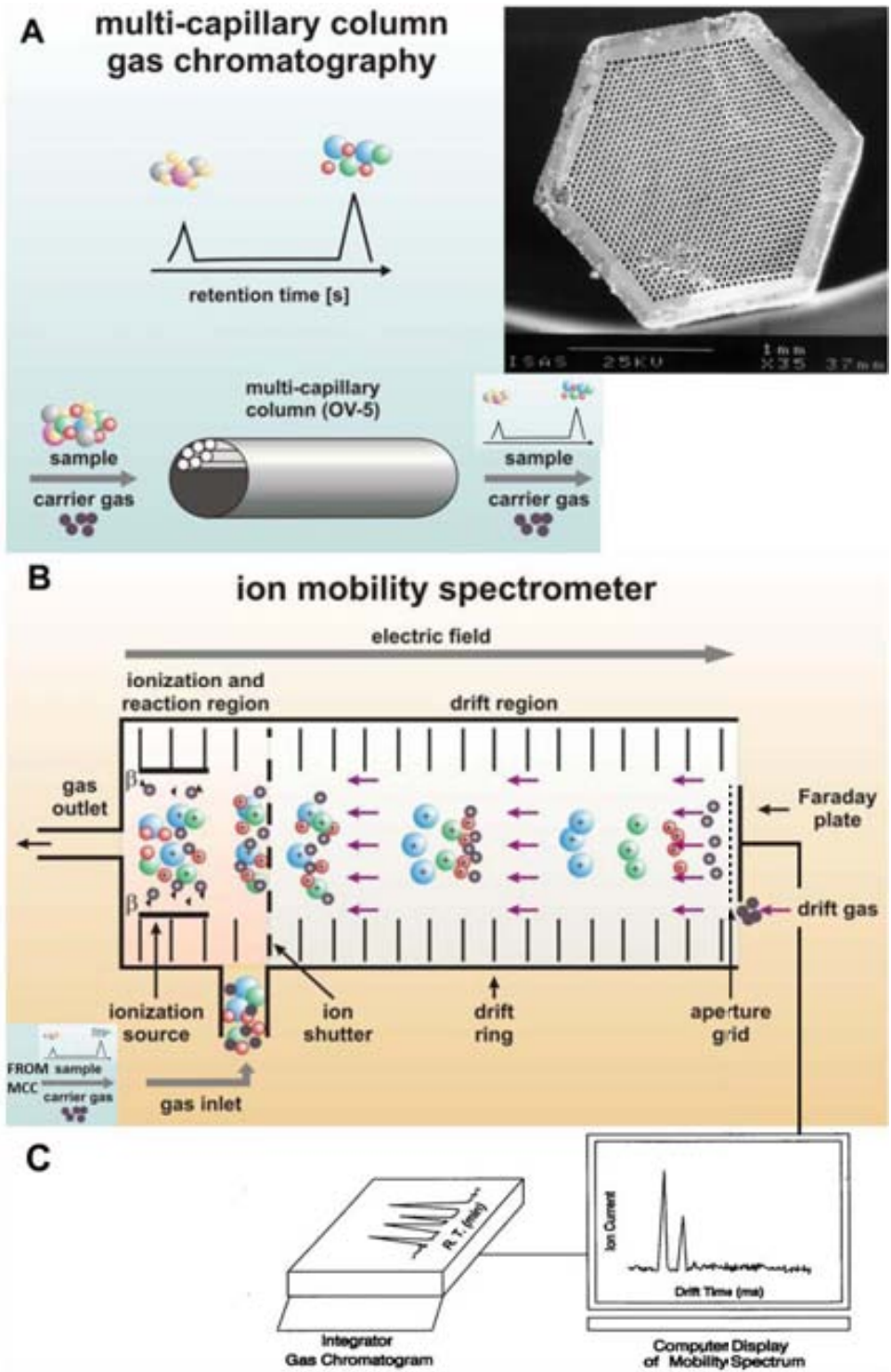


Figure 2-19: Overview of a multi-capillary column separation technique with a lateral section picture (A) coupled with an ion mobility spectrometer (B) and the data analysis (C). Adapted from [88], [150] and [244].

Mass Spectrometry as a Detector, the IMS-MS

Another way of ion determination is to identify the compound when it is detected. Mass Spectrometers (MS) are used as the detector part of an IMS. The name ‘mass spectrometry’ is an inaccurate term [245]. The mass is not what is measured; instead, mass spectrometry determines the mass-to-charge (m/z) ratio or a property related to m/z . A mass spectrum is a plot of ion abundance versus m/z , although in many cases the x -axis is labeled ‘mass’ rather than m/z .

The spectrum is presented in terms of Daltons (Da) per unit charge. So for example, benzene (molecular mass 78 g/mol), when ionized, can form an ion of the intact molecule at m/z 78 (the number of places after the decimal that can be determined depends on the type of mass analyzer and often just the integer mass is reported). However, the molecular weight is the molar mass of a compound and what is actually measured in a mass spectrometer are individual ions, and the true units of the measurement are kilograms per Coulomb.

Basically, any information gathered from a mass spectrometer comes from the analysis of gas-phase ions. There are three main components of a mass spectrometer: an ionization source, a mass analyzer and a detector (Figure 2-20).

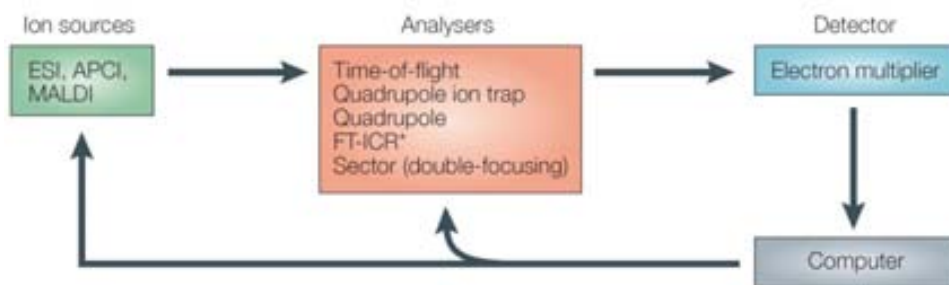


Figure 2-20: Basic components of a typical mass spectrometer [245]. *FT-ICR does not use an electron multiplier. APCI, atmospheric-pressure chemical ionization; ESI, electrospray ionization; MALDI, matrix-assisted laser desorption/ionization; FT-ICR, Fourier transform ion-cyclotron resonance.

The different types of mass analyzer measure ions in different ways. In most analytical measurements, two of the predominant figures of merit are accuracy and precision. It is important to note that an accurate measurement does not necessarily require a precise measurement and vice versa. In MS, the precision of the measurement is related to the resolution (that is, the ability to resolve two adjacent peaks). In general, resolution is defined as $m/\Delta m$, where m is the integer mass of the peaks being resolved and Δm is the mass difference between the two peaks. There are five principal types of mass analyzer in use today. These analyzers can be divided

into two groups: beam analyzers and trapping analyzers. In beam analyzers, the ions leave the ion source in a beam and pass through the analyzing field to the detector (Figure 2-21). In trapping analyzers, the ions are trapped in the analyzing field, after being formed in the analyzer itself or being injected from an external ion source (Figure 2-22).

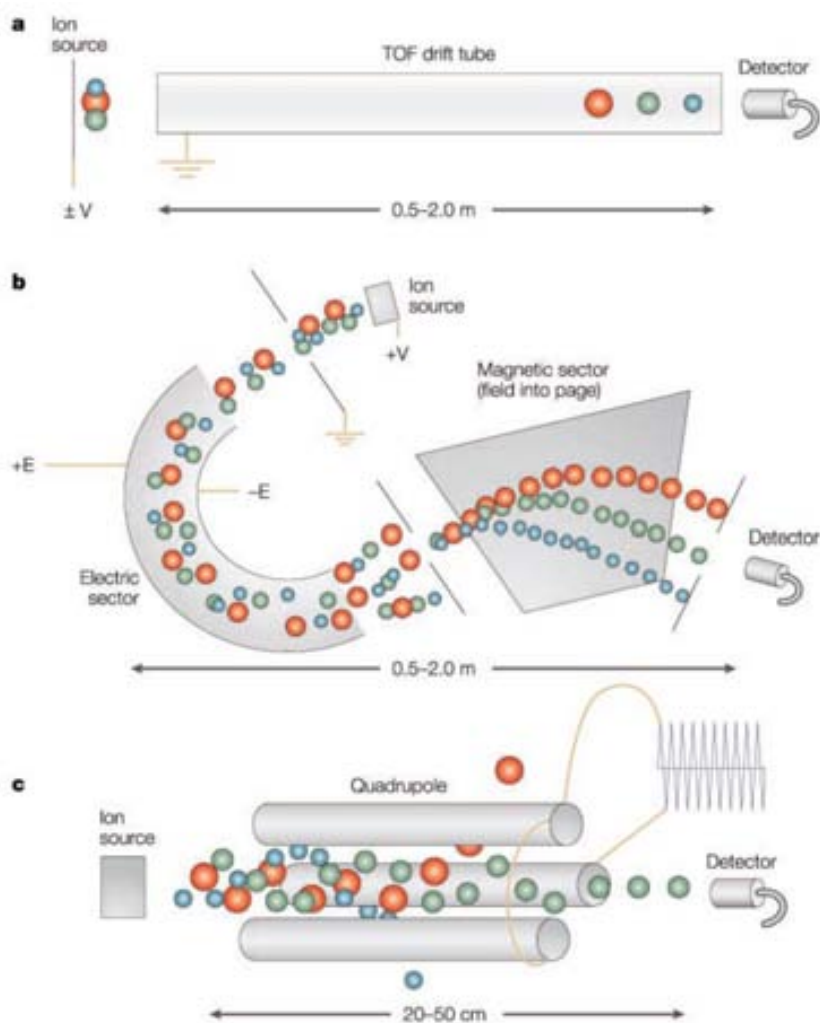


Figure 2-21: Diagrams of the common beam mass analyzers [245]. **a)** Mass analysis in time-of-flight (TOF) spectrometry is achieved because ions of different mass-to-charge (m/z) values have different velocities and therefore reach the detector at different times. **b)** A double-focusing analyzer provides direction focusing through both the electric and magnetic sectors. Ions with the same kinetic energy-to-charge ratio follow a common path through an electric sector, and ions can then be dispersed according to their momentum-to-charge ratio in a magnetic sector. Overall analysis according to m/z is achieved. **c)** In a quadrupole mass analyzer (top rod not shown), the correct magnitude of the radio frequency and direct current voltages applied to the rods allows ions of a single m/z to maintain stable trajectories from the ion source to the detector, whereas ions with different m/z values are unable to maintain stable trajectories.

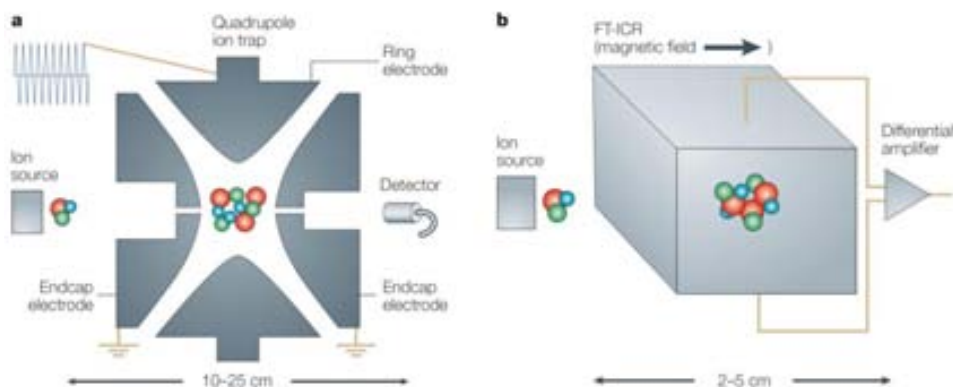


Figure 2-22: Diagrams of the common trapping mass analyzers [245]. **a)** Ions in a quadrupole ion trap maintain stable trajectories inside the device as a result of the application of a radio frequency voltage to the ring electrode. Mass analysis is achieved by making ion trajectories unstable in a mass-selective manner. **b)** Ions in an Fourier-transform ion-cyclotron resonance (FT-ICR) oscillate around the magnetic field at frequencies that are related to their mass-to-charge (m/z) scales. As the ions oscillate near the top and bottom metal plates of the cubic trapping cell, they induce an alternating current that can be measured and then related to their m/z . Note that whereas the FT-ICR cell is small, it is in a high magnetic field (typically a superconducting magnet), so the actual instrument size is large.

IMS instruments separate ions on the basis of size, mass, and charge, while MS determines the mass-to-charge (m/z) ratio or a property related to m/z . In IMS-MS instrumentation, ions are separated on the size-to-charge ratio in the IMS component and the mass-to-charge ratio in the MS component. A two-dimensional separation is obtained based on size and mass [241].

In Figure 2-23 is shown an IMS(tof)MS, which is commercially available from Waters company [246], is the traveling-wave ion mobility spectrometer described above. The commercial version is called the Synapt G2-S HDMS. From left to right the components are as follows: The ionization source is an electrospray source which is orthogonal to the ion path. Once ionized and desolvated, the ions are guided into a quadrupole mass spectrometer which can be operated as a mass filter. Mass-selected ions are then trapped prior to the ion gate of the IMS. Periodically the ions are gated into the mobility cell and separated as a function of mobility. The ion swarm exiting the ion mobility cell is then focused into the time-of-flight mass spectrometer for a two-dimensional analysis.

Ion transmission has been improved by implementing an electrodynamic ion funnel for their re-focusing into tight circular beams at the FAIMS-MS interface [247, 248]. Higher IMS resolving powers have allowed IMS-MS to be utilized in the analysis of isobaric species with minimal structural differences, including polymer subunits [249], cis-trans isomers [250], and diastereomers [251]. Such peak capacities are generally insufficient to separate all the components in complex samples. To increase the peak capacity of IMS-MS separations, a third dimension Liquid Chromatography

(LC) stage can be added. Figure 2-24 demonstrates the increased separation capability obtained when LC and IMS are coupled prior to the MS stage. IMS-MS spectra were summed across 10 s in three LC regions, corresponding to the elution of lysophospholipids (Figure 2 -24A), phospholipids (Figure 2 -24B), and triacylglycerides (Figure 2-24C).

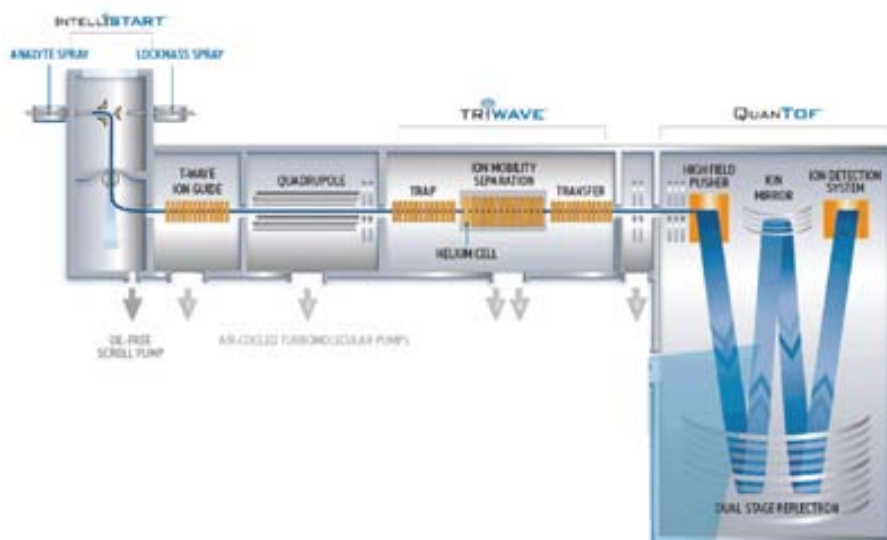


Figure 2-23: Schematic of an ambient-pressure IMS(tof)MS from Waters company [246].

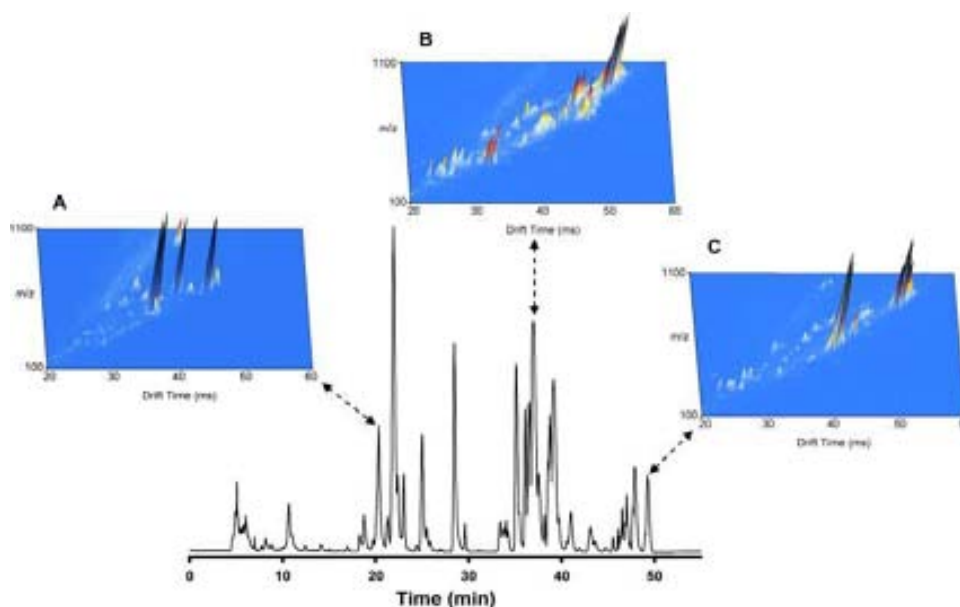


Figure 2-24. LC-IMS-MS analysis of a human total lipid extract [252]. A human plasma total lipid extract was analyzed by LC-IMS-MS utilizing a 50 min LC separation and a 98 cm IMS drift tube. To indicate the increased separation capability obtained with the combination of LC and IMS, IMS-MS spectra were summed across three 10 s regions (20.83–21.00 min; 37.00–37.17 min; and 49.17–49.33 min) of the LC separation, creating three-dimensional plots of m/z , drift time, and intensity.

2.2.f Data collection and treatment

The data recollected directly by an IMS is current versus drift time (Figure 2-16). The variable time can be rewritten to the inverse ion mobility

$$\frac{1}{K} = \left(\frac{V}{L^2} \right) \cdot t \quad (2.24)$$

where L [cm^{-1}] is the length of the drift tube. The mobility depends in turn on the temperature and pressure. The way to enabling comparisons between IMS data at different N is established by introducing the reduced mobility K_0 [$\text{cm}^2 \cdot \text{V}^{-1} \cdot \text{s}^{-1}$]:

$$K_0 = K \frac{P}{P_0} \frac{T_0}{T} = K \frac{N}{N_0} \quad (2.25)$$

where the mobility is normalized to pressure P and temperature T for the value for standard conditions for temperature and pressure (STP) from IUPAC definition [253]: $T_0 = 273.15$ K (0°C) and $P_0 = 760$ Torr; or to the gas number density $N_0 = 2.687 \times 10^{25}$ m^{-3} (the number of molecules per unit volume or the Loschmidt constant). STP usually is employed in reporting gas volumes, and for flow meters calibrated in standard gas volumes per unit time often refer to volumes at 298.15 K (25°C), not 273.15 K (0°C) [253].

In case of an IMS coupled with a MCC the result is shown as a function of the drift time (or inverse of the reduced ion mobility K_0) of the IMS and the retention time of the MCC [8, 85], as can be seen in Figure 2-25. The spectra are displayed in $1/K_0$ which is proportional to the drift time but normalized to the electric field, drift length, temperature, and pressure, and therefore represents the actual spectra resolution. Figure 2-25A shows exemplarily the topographic plot of positive ions of nonan-2-one [88]. The topographic plot is a three dimensional chromatogram that combines information about MCC retention time or RT [min], the drift time expressed as the inverse ion mobility $1/K_0$ [$\text{V} \cdot \text{s} \cdot \text{cm}^{-2}$] and the signal intensity [V] (after amplification and conversion from nA), indicated by different colors (*white* = zero, *blue* = low, *red* = medium, *yellow* = high). Extracted ion chromatograms of the nonan-2-one protonated monomer and proton-bound dimer (Figure 2-25B) reflect their formation during the ionization process that follows previous MCC separation. Additionally, the ion mobility spectrum (Figure 2-25C) is used to determine the characteristic $1/K_0$ for the proton-bound monomers and dimers. The reactant ion peak (RIP, $1/K_{0,RIP} = 0.485$ $\text{V} \cdot \text{s} \cdot \text{cm}^{-2}$) which is always occurring when ^{63}Ni is used as ionization source, can be detected at any MCC retention time, indicating detected reactant ions as products of ionized molecules of synthetic air, which are used for the ionization of analytes by charge transfer.

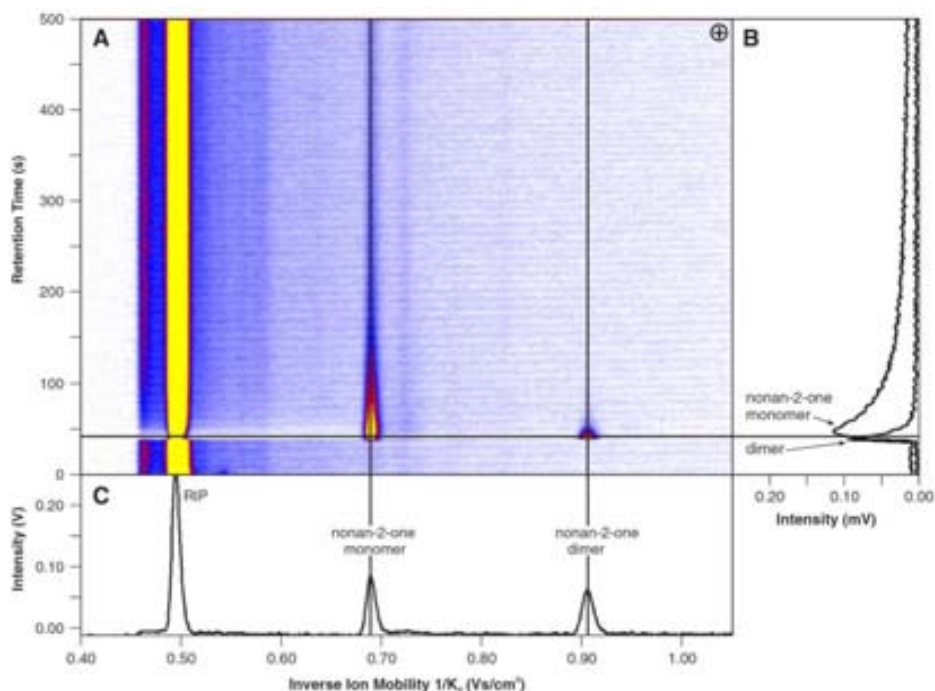


Figure 2-25: Example of MCC-IMS chromatograms for ~ 3 ppbv nonan-2-one [88]. This compound could be detected as proton-bound monomer and dimer ion as shown in the topographic plot. (A) is the that is Intensity vs. Retention Time and Inverse Ion Mobility $1/K_0$. The overlay of MCC chromatograms (Retention time vs. Intensity) from 0 to 500 s of the extracted proton-bound monomer ion at $1/K_{0,D} = 0.688 V \cdot s \cdot cm^{-2}$ and dimer ion at $1/K_{0,D} = 0.904 V \cdot s \cdot cm^{-2}$ of nonan-2-one are shown in (B). The IMS spectrum (Intensity vs. Inverse Ion Mobility $1/K_0$), reflecting the RIP, nonan-2-one proton-bound monomer and dimer at MCC $t_R = 38.9$ s is displayed in (C). Peak height/intensities are indicated by different colors (white zero, blue low, red medium, yellow high).

Resolution and Resolving power

In order to compare instrument performance between laboratories, resolving power or R_p [dimensionless] is often used and is defined as [254-258]:

$$R_p = \frac{t_d}{FWHM} = \frac{t_d}{w_{1/2}} \quad (2.26)$$

where t_d is the drift time of a peak, and FWHM or $w_{1/2}$ is the Full Width at Half of the Maximum of the peak of interest in the IMS spectrum, as can be seen in Figure 2-26. Resolving power provides a convenient method for comparing the relative ability of an IMS devices to separate closely spaced peaks but is calculated using a single peak in the spectrum.

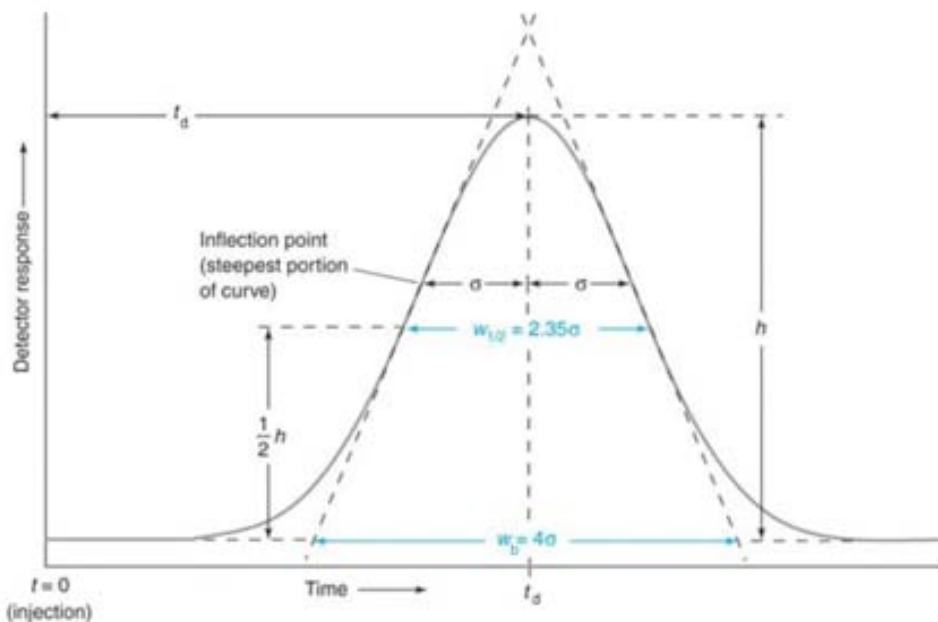


Figure 2-26: Response as a normal Gaussian peak. Are shown the drift time (t_d) at which the peak is detected, the standard deviation (σ), the peak height (h), the peak width at half-height ($w_{1/2}$), and the peak width at base (w_b) Lines drawn tangentially to the inflection points, intersect the signal baseline at the base width of the peak. Adapted from [258].

52

In Figure 2-26 shows how the width at half maximum ($w_{1/2}$) and at the base (w_b) can be calculated relating them to the standard deviation (σ):

$$w_{1/2} = 2\sqrt{2\ln 2} \sigma \approx 2.355 \sigma \quad (2.27)$$

$$w_b = 4 \sigma \quad (2.28)$$

If separation performance is being tested, **resolution** R [dimensionless] provides a direct measurement of peak-to-peak separation between two IMS peaks (Figure 2-27) and is defined as:

$$R = 2 \times \frac{|t_A - t_B|}{w_{b,A} + w_{b,B}} \quad (2.29)$$

where t_A , t_B are the drift times of the ions of interest, and $w_{b,A}$, $w_{b,B}$ are the peak widths in seconds at the base of the peak [258, 259]. This equation provides a method for comparing the relative ability of an IMS to separate closely related peaks.

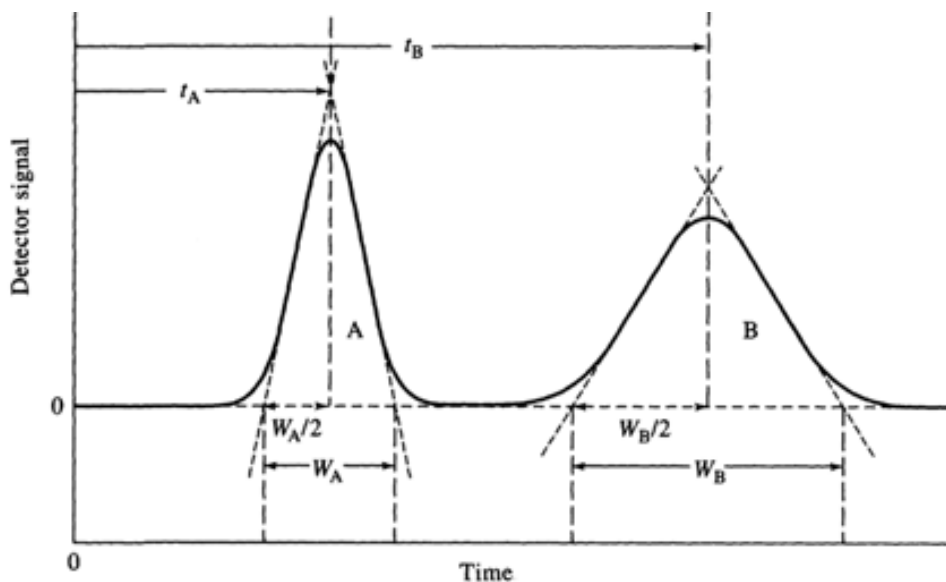


Figure 2-27: Separation of component peaks A and B. Are shown the drift times ($t_{A,B}$) at which the peaks are detected, and the peak widths at base ($w_{A,B}$). Lines drawn tangentially to the inflection points, intersect the signal baseline at the base width of the peak. Adapted from [258].

Aspect Ratio

A better way of describing peak quality is through his aspect ratio AR [260], or the ratio of the peak height h to the width at the base w_b :

$$AR = \frac{h}{w_b} \quad (2.30)$$

The taller and more narrow a peak (i.e., high aspect ratio), the easier it is to resolve it from a neighboring peak. However, the aspect ratio AR do not give the same information as the resolving power R_p . The AR allows to compare different peaks on the basis that their appearance at different values of time do not affect its shape. However the R_p takes into account the time when the peak appears assuming that in principle, as longer time takes to an ion to pass though the IMS its signal should be wider due to the diffusion mechanisms

Data treatment

Additional information from the obtained spectra can be extracted through Gaussian de-convolutions [261]. Gaussian de-convolution is a powerful tool for enhancing the amount of information which can be obtained from an IMS spectrum. In addition to increasing resolution of peaks in relatively pure samples, Gaussian de-convolution may be used to more accurately describe the ion molecule reactions which occur in a chemical system by isolating mixed dimer peaks from those dimers found in pure samples. Even the de-convoluted signal is not improved as the intensity is reduced, it is used to extract data from the peaks like the full width at half maximum (FWHM), and to identify the detected ions.

The parameters which affect the de-convolution are the FWHM data of the Gaussian used in the de-convolution, the degree of interpolation used, and the number of successive iterations used in the de-convolution. In an iteration a spectrum is convoluted by a Gaussian function. The spectrum to be convoluted is the original spectrum for only the first iteration. The new spectrum is subtracted from the original spectrum which entered the convolution iteration and a third spectrum, a difference spectrum, is created. The difference spectrum is then added to the original spectrum and a de-convoluted spectrum is obtained, completing the iteration. This de-convoluted spectrum is then used as the input to the next iteration, as necessary. An example a de-convoluted signal is shown in Figure 2-28 [262], where acetone raw or original spectrum and the de-convoluted signal for 200 iterations, a Gaussian FWHM of 18 with a factor of interpolation of 1 are shown.

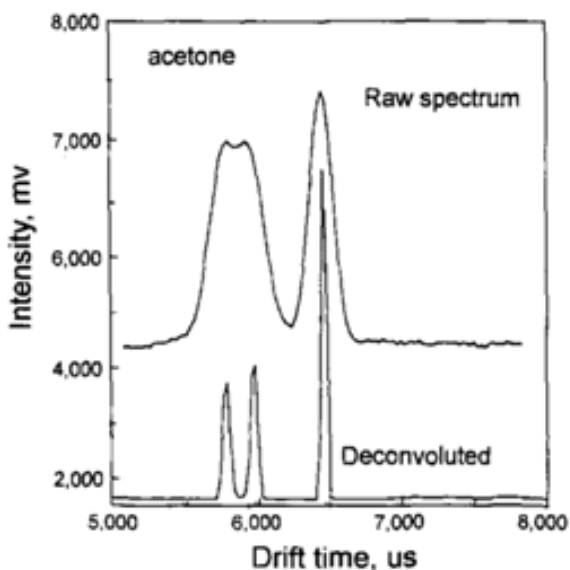


Figure 2-28: De-convolution of acetone spectrum. Spectrum was acquired on the Graseby “Scrubber CAM” at ambient temperature and concentration of ~10 ppb. Adapted from [262].

Temperature and pressure effects

Tabrizchi has done considerable work on the effect of temperature and pressure on mobility measurements and resolution [263].

Drift time varies linearly with pressure while it does not change linearly with temperature [263]. He attributed this different behavior to the different impact of temperature and pressure on the clustering reactions. In fact, temperature and pressure both affect the neutral density of the drift gas which leads to change in the collision frequency. However, temperature changes the identity of the ions through affecting the clustering equilibrium. Thus a non-linear behavior is observed for temperature but not for pressure.

Operating IMS at elevated temperature decreases the resolution, but improves de-clustering. Therefore, IMS is frequently operated at elevated temperature to assist in de-clustering and cleaning of the drift tube, even though some resolution is sacrificed. In contrast, negative ion mobility spectra are better resolved at elevated temperatures [256]. De-clustering (for negative ions) at elevated temperature leads to a change in the identities of the ions, which results in faster drift times.

The resolution of IMS is often described as diffusion limited resolution [264] because the broadening of the peaks is due to the diffusion of ions as they transverse the drift tube. Other factors that contribute to peak broadening include: (1) the initial pulse width and shape; (2) coulomb repulsion; (3) capacitive coupling between approaching ions and the collector plate; (4) field gradient uniformity, (5) temperature gradient; (6) gate depletion/dynamic leakage; (7) pressure fluctuations; and (8) ion-molecule reaction in the drift space [223]. Additional broadening has been attributed to the construction of the IMS drift tube and the parallelism (or lack) that exists between the aperture grid and ion collector. Still another is the so called distribution the electric field to bias the drift tube.

Temperature and pressure effects in ion separation can be described by the mobility dependence on the gas number density, N : $K(E/N)$ defined in Equations (2.39) and from Equations:

$$N = \frac{n}{V} N_A \quad (2.31)$$

$$\frac{n}{V} = \frac{p}{RT} \quad (2.32)$$

$$\frac{E}{N} = E \frac{RT}{pN_A} \quad (2.33)$$

The number density N [m^{-3}] can be found using Equation (2.31), where n/V [$\text{mol}\cdot\text{m}^{-3}$] is determined from the ideal gas law in Equation (2.32) and N_A [$6.022\times 10^{23} \text{mol}^{-1}$] is Avogadro's number. Also, p [Pa] is the pressure of the gas, V [m^3] is the volume of the gas, n [mol] is the amount of substance of gas (also known as number of moles), T [K] is the temperature of the gas and R [$8.314 \text{J}\cdot\text{K}^{-1}\cdot\text{mol}^{-1}$] is the ideal, or universal, gas constant, equal to the product of the Boltzmann constant [$1.38065 \times 10^{-23} \text{J}\cdot\text{K}^{-1}$] and the Avogadro number N_A .

From previous equations, it is determined that as temperature T increases, n/V decreases causing the number density to decrease and therefore the effective E/N to increase. In the other hand, it is determined that as pressure p increases, n/V also increases causing the number density to increase and therefore the effective E/N to decrease. To maintain balanced conditions for an ion of interest within the FAIMS device, temperature and pressure conditions must be constant.

In planar-FAIMS it has been shown that pressure variation of p-FAIMS peak positions may be eliminated by a rescaling of the coordinates, expressing both compensation and separation fields in Townsend units (electric field divided by density) [265]. At fixed temperature, Townsend-rescaled p-FAIMS spectra are independent of the drift gas pressure (see Figure 2-29a). In contrast, p-FAIMS spectra recorded at fixed pressure but varying temperature do not simplify in a similar way [266]. Even in terms of Townsend p-FAIMS spectra are distinguished for different bulk temperatures (see Figure 2-29b).

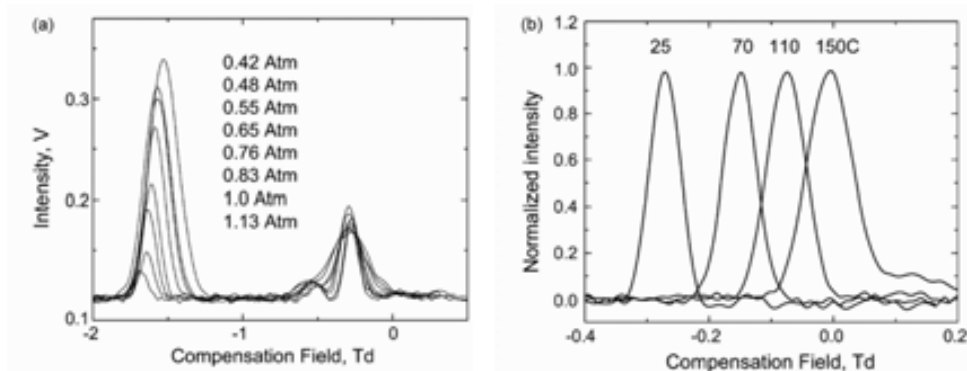


Figure 2-29: Positive p-FAIMS spectra of methyl salicylate ions at the same 100 Td filtering field, but with different drift gas pressures (a) and temperatures (b). Pressure does not affect the p-FAIMS spectrum scaled in Td units. Variation of peak position with temperature remains even after Townsend scaling. Adapted from [266].

Carrier Gas Composition:

The carrier gas used in IMS can dramatically affect separation. The composition and flow rate of carrier gas can be optimized for enhanced resolution. Adding trace quantities of vapors to ion mobility spectrometers to produce specific analytical effects was first utilized in 1978 by Kim *et al.* [267] added ammonia to the N₂ carrier gas to selectively ionize a series of amines. Later, Blyth [268] used acetone for the selective detection of chemical warfare agents and Spangler *et al.* [10] introduced the use of carbon tetrachloride for the selective detection of explosives. Eiceman *et al.* [269] selectively detected mixtures of volatile organic and organophosphorus compounds using acetone and dimethylsulfoxide reagent gases and also Meng *et al.* [270] used water, acetone, and dimethylsulfoxide reagent gases to provide specific ionization of indoor ambient atmospheres for volatile organic compounds. Puton *et al.* [130] reviewed the use of reagent gases and modifiers in IMS in negative and positive modes.

In most cases, when trace quantities of dopant vapors are added to IMS instruments, the purpose is to reduce ionization interferences and selectively ionize the target analytes of interest. When doping agents are introduced directly into the drift region of the mobility spectrometer rather than the ionization region, they modify mobilities through dynamic ion-molecule interactions as they drift through the carrier gas.

Common carrier gas compositions are N₂ and N₂/He combinations, but combinations of CO₂, SF₆, O₂, and N₂O have been used [271]. The mobility of ions varies with differing gas compositions. Blanc's law describes the mobility of an ion at low field in a gas mixture:

$$\frac{1}{K_{mix}} = \sum_i \frac{x_i}{K_i} \quad (2.34)$$

where K_{mix} is the mobility of an ion in the mixture of gas, x_i is the abundance of a gas and K_i is the mobility in the individual gas.

2.3 high Field Asymmetric waveform Ion Mobility Spectrometers

Miniaturization and system integration is a common development in almost every branch of technological industry. It promises numerous benefits like a reduced need of space, reduced use of resources and higher quantities coming along with mass-production. Miniaturization also enters the field of Ion Mobility Spectrometry. Portable Ion Mobility Spectrometers are commercially available from various companies [67, 272]. However, the size (> 35 cm) and the weight (> 1.9 kg) of these miniaturized IMS's units are still not handy to equip custom or police officials for daily usage of such devices.

In this scenario appeared a new miniaturized IMS but with a total different separation technique from the conventional IMS's, the high Field Asymmetric waveform Ion Mobility Spectrometer (FAIMS). In contrast to IMS, the FAIMS is a Radio Frequency (RF) filter and produces an added dispersive force which further enhances mobility differences. The FAIMS is different from the IMS in that the mobility of ions are measured according to the compensation voltage necessary to correct for the oscillatory path of the ion caused by the RF field. One of the main advantages that FAIMS has over IMS is that ions can be introduced into the sensor continuously whereas in IMS, ions are introduced in pulses. This allows for more continuous monitoring and sensing of biological samples when time plays a critical factor in a particular application. The FAIMS is less complex than the IMS, in part because it does not require the precise timing of ion travel. The continuous sensing property also simplifies the sample injection process so that samples can be injected in either a continuous or pulsed manner.

FAIMS, again, three main parts: (1) Ionization Region, where samples are ionized; (2) Filtering Region, where ions are separated due to their mobility; and (3) Detector Region, where ions reach the detector. The three regions of a FAIMS device can typically be considered independent. For example, a ^{63}Ni radioactive ionization source can be changed with an ultraviolet (UV) source without requiring a change to the filtering or detection regions. Ionization sources used in FAIMS are mostly the same than in IMS (see Section 2.2.b *Ionization region*). Also, detection can be equally accomplished through the use of a Faraday cup within the FAIMS device, or by passing the ions into a MS. Such changes, while not resulting in a distinctly new technique, will encounter benefits and drawbacks within a study. Similarly, modification of the filtering region will result in a change in performance. Since this region is so integral to FAIMS different filtering region designs are considered independently.

2.3.a Filtering Region electrodes design

The first FAIMS developed by Buryakov *et al.* in 1993 [110] employed planar electrodes (p-FAIMS). Sionex (Waltham, MA) currently manufactures FAIMS with a planar geometry as a stand-alone detector [273]. The dome cell geometry was developed in 1995 by Carnahan *et al.* [274], but is no longer commercially available. In 2004, Guevremont *et al.* [275] patented cylindrical FAIMS electrodes (c-FAIMS), which are currently commercially produced by Thermo-Fisher Scientific (San Jose, CA) as a separation device to be used in conjunction with a mass spectrometer [276]. The spherical cell design was proposed by Guevremont *et al.* [277] in 2004 but was never reduced to practice. Each FAIMS electrode geometry has their advantages and disadvantages in the optimization of resolution and ion transmission.

In general, planar geometries can have higher resolution, whereas cylindrical geometries can offer higher ion transmission [247]. Improved transmission in the cylindrical geometry is due to two-dimensional atmospheric pressure ion focusing caused by the non-uniform electric field created by the curved surface of the electrodes that facilitates focusing ions into the center of the analytical gap [278]. For those reasons, stand-alone FAIMS [115, 279] and GC-FAIMS [128, 280, 281] instruments use planar FAIMS designs. The need to convey ions from the atmospheric pressure in FAIMS to the MS vacuum makes cylindrical or spherical FAIMS with ion focusing more attractive for FAIMS-MS systems [282]. Therefore, the cylindrical FAIMS technology (c-FAIMS) is moving towards full integration into mass spectrometry for pharmaceutical [283] and protein conformer [284-286] analysis in a tandem FAIMS-MS. Instead, the planar FAIMS technology (p-FAIMS) has been concentrated on healthy risky volatiles [287-289], explosives [279, 290] and chemical warfare agents [291, 292] analysis.

Cylindrical FAIMS

The analytical gap in FAIMS analyzers is defined as the distance between electrodes, and in the case of cylindrical analyzers is determined by the difference in radii of the inner and outer electrode. The curvature of the cylindrical FAIMS is determined by the average of the radii, and is a critical factor in the resolution and ion transmission of a device. Gap dimensions of cylindrical FAIMS devices range from 1.5 to 3 mm [118].

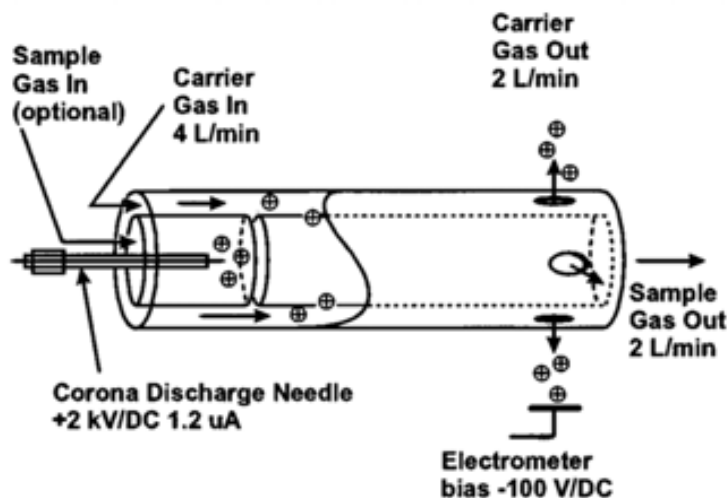


Figure 2-30: Cylindrical FAIMS device as taken from Purves *et al.* [293]. The two inner electrodes have lengths of 30 and 90 mm respectively and inner diameter of 12 mm and outer diameters of 14 mm. The outer electrode has a length of 125 mm, inner diameter of 18 mm and outer diameter of 20 mm. Ionization occurs within the smaller inner electrode

The electric field at any point between the electrodes can be calculated using Equation (2.35). V [V] is the applied voltage, r [Å] is the radius of the ion at any point between the electrodes, a [mm] is the radius of the center electrode, and b [mm] is the radius of the distance between the center of the inner electrode and inner surface of the outer electrode.

$$E_{r,cylindrical} = -\frac{V}{\ln\left(\frac{a}{b}\right)r} \quad (2.35)$$

It was discovered that upon applying the asymmetric waveform the ion intensity detected increased [293]. This initially unsuspected result was later attributed to a focusing effect due to the cylindrical geometry [116], which could counteract the typical loss of response due to ion diffusion. Due to the non-uniformity of the electric field in cylindrical electrodes, ion focusing can be achieved. Ions near the inner electrode are repelled to the center of the analytical gap, whereas ions near the outer electrode are pulled to the center of the analytical gap, as shown in Figure 2-31.

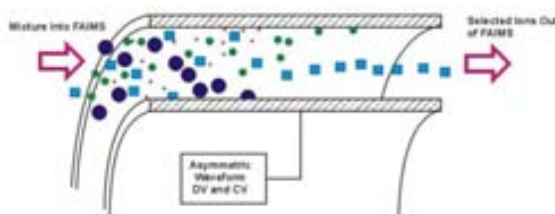


Figure 2-31: Ions separated between concentric cylinders of a FAIMS analyzer [294]. The transmitted ion is focused towards a fixed radial distance, and distributed around that distance through the effects of diffusion and space charge repulsion. The effect of the focus is exaggerated for clarity in this figure.

Species that are focused with one waveform polarity [also decided by the form of $K(E/N)$] are defocused with the opposite polarity. Covering both polarities means duplication of analyses, which halves the experimental duty cycle.

However, the use of curved surfaces to increase sensitivity compromises resolution [275]. Guevremont *et al.* theorized that curved surfaces focus ions with a wide range of mobility behavior, which decreases resolution and increases peak width [275]. As the radii decreases, focusing improves and ion intensity increases at the expense of resolution. Ions with very different mobility behavior can be focused together when utilizing curved electrodes. As the electrode curvature decreases, the focusing effect lessens and resolution improves at the expense of sensitivity. Without the curvature,

there is no focusing effect and ions with different mobility behavior can be distinguished. Therefore, as the electrode radii increases, resolution increases. Planar geometry electrodes have no curvature, thus they exhibit the maximum attainable resolution [275].

There are two differing designs for cylindrical FAIMS devices. The most common is referred to as the ‘Cigar’ type (Figure 2-32, [295]), and the newer version referred to as the ‘side-to-side’ type (Figure 2-33, [296]).

Cylindrical ‘Cigar’ FAIMS

The dome cell geometry was first proposed by Carnahan in 1995, but is not currently commercialized. The cylindrical design was later adapted by creating a dome end to the inner electrode Figure 2-32 also referred to ‘cigar’ type cylindrical FAIMS, this improved the interface with a MS orifice. As the name implies, ‘cigar’ type analyzers have a ‘cigar’ shaped inner electrode, with the inlet end being flat and the exit end having a rounded dome. The outer electrode is machined as a cylinder with a slightly larger diameter than the inner electrode to create a constant analytical gap. Ions are injected orthogonally to the ion exit through a small hole in the outer electrode, which can be held at ground or have a small dc potential applied to it, while the inner electrode is connected to the high amplitude asymmetric waveform and compensation voltage. ‘Cigar’ type analyzers differ from all other FAIMS analyzers in that the distance between the dome of the inner electrode and the ion exit of the outer electrode is variable and is an important tuning parameter for device optimization. Varying the gap between the inner electrode and ion exit causes significantly different relative intensities and changes in resolution.

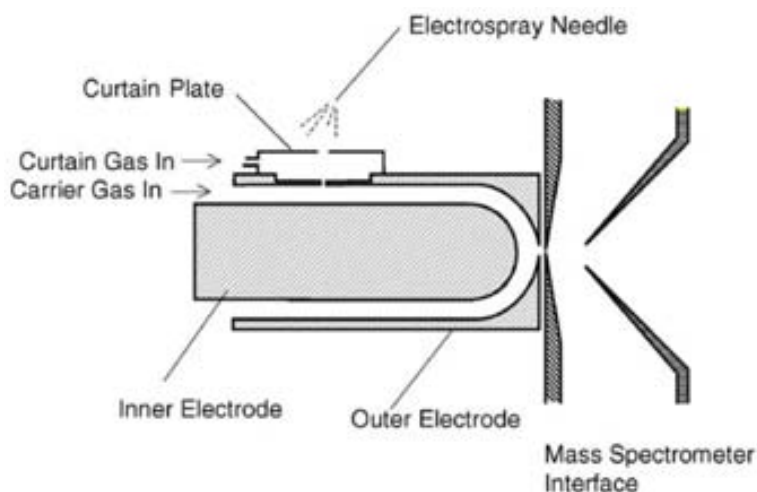


Figure 2-32: Domed cylindrical FAIMS device as taken from Guevremont *et al.* [295].

Modeling demonstrates that the ions are separated in the cylindrical portion and focused in the spherical portion [295]. The gap between the inner and outer electrode in the spherical portion is adjustable. A gap between 1.7 and 2.5 mm has been found to be optimal for most compounds. The gap between the inner and outer electrode on the cylindrical portion is 2 mm, so the electric field may differ between the cylindrical and spherical portion of the dome electrodes allowing enhanced resolution and transmission.

The strength of this design is its straightforward coupling to a MS, but there has since been theoretical investigations which conclude that planar FAIMS devices will result in a better selectivity, if the difficulties in coupling with a MS can be overcome [247].

Cylindrical 'side-to-side' FAIMS

The cylindrical geometry known as the 'side-to-side' FAIMS is currently commercialized by Thermo-Fisher Scientific and is sold as a separation device to be used in conjunction with a mass spectrometer [276]. Schematics of the cylindrical FAIMS filtering electrodes are shown in Figure 2-33.

Side-to-side type analyzers are simple devices, with cylindrical inner and outer electrodes, and an ion inlet in line with the ion outlet. Although the inlet and outlet are co-linear, there is no line-of-sight for the incoming ions, and the ions must travel a minimum of one half the circumference of the inner electrode to reach the outlet. As with the 'cigar' type analyzer, a high-amplitude asymmetric waveform and compensation voltage are applied to the inner electrode, while the outer electrode has only a dc bias voltage applied to assist in ion transmission into the mass analyzer. A feature of the 'side-to-side' device is the ability to heat the electrodes. Originally instituted to provide temperature stability, it was quickly observed that an increase in temperature resulted in improved resolution. The observed improvements in performance are due to improved ion droplet de-solvation and an increase in the E/N value.

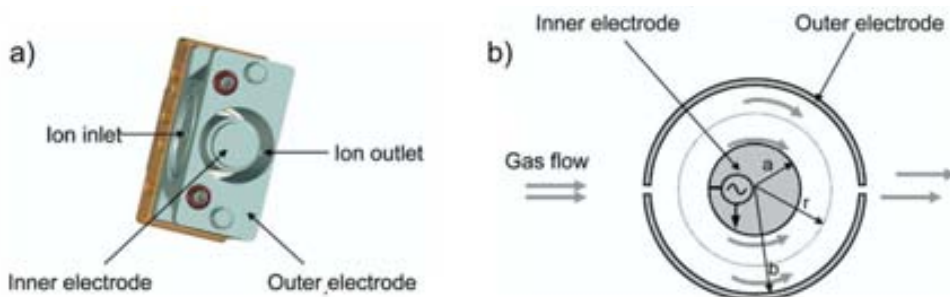


Figure 2-33: (a) Three-dimensional schematic of a 'side-to-side' FAIMS device, (b) cross section of the FAIMS device illustrating radial location, r , between the walls of the inner electrode, "a" and outer electrode "b." The asymmetric waveform is applied to the inner electrode. Adapted from [296].

Due to the curved electrodes used in cylindrical FAIMS the electric fields are inhomogeneous which results in a focusing effect [278]. This is both an advantage and limitation, as the focusing results in higher ion transmission than that of planar devices, but limits resolution. In cylindrical FAIMS all ions of a similar structure feel the effect of the inhomogeneous fields and are focused together; resulting in a smaller spacial distribution, and increased peak overlap relative to planar FAIMS. The focusing at atmospheric pressure in cylindrical FAIMS analyzers results in two advantages: 1) high voltages result in better focusing, resulting in an improvement in ion transmission at higher fields [116]; and 2) ions can be trapped at atmospheric pressure [116]. While these are major advantages over planar FAIMS, the relative difficulty in the manufacture of cylindrical devices, the large number of variables which must be optimized to specific analyses, and lower resolution of the cylindrical devices are limitations which have lead researchers to pursue planar FAIMS technology [247].

Spherical FAIMS

Guevremont *et al.* patented spherical electrodes in 2004, but the patent was never reduced to practice [277]. Spherical FAIMS electrodes were predicted to improve ion focusing because all ion path lengths are equidistant, and therefore all ions experience the same field and travel the same distance. With spherical geometry, ions can distribute uniformly around the inner electrode. On the other hand, in a cylindrical design, when ions spread out due to charge repulsion and diffusion they may take different paths along the inner electrode, causing peak broadening.

Furthermore, the radial field in the spherical geometry varies as a function of $1/r^2$, whereas the radial field in cylindrical cell only varies as a function of $1/r$, allowing improved ion focusing capabilities between spherical electrodes [277].

$$E_{r,spherical} = -\frac{V}{\left(\frac{1}{a} - \frac{1}{b}\right)r^2} \quad (2.36)$$

where V [V] is the voltage applied, a [mm] is the radius of the inner sphere, and b [mm] is the radius of the outer sphere. It has been hypothesized that the resolution obtained by spherical FAIMS electrodes would be poor because of the focusing effects caused by the curvature [275, 297]. By varying the radius of the spherical electrodes, it may be possible to alter resolution and sensitivity in this electrode design.

Hemispherical FAIMS Electrodes

In a spherical cavity, all ions encounter equidistant trajectories from ion inlet to outlet, increasing its focusing capabilities, transmission, and uniformly spaced ion density. Nevertheless, the design and construction of a spherical cell is a daunting task; the suspension of a central spherical electrode at the exact center of a spherical cavity while delivering several thousand volts of RF to the central electrode is extremely difficult.

Initial spherical designs failed to provide the precise, accurate, and rigid centering required of the center electrode. Therefore, a second design employed a hemispherical central electrode mounted within a hemispherical cavity, as shown in Figure 2-34. This design has shown to provide the advantages of a fully spherical cell while permitting rigid, accurate, and reproducible positioning of the electrodes.

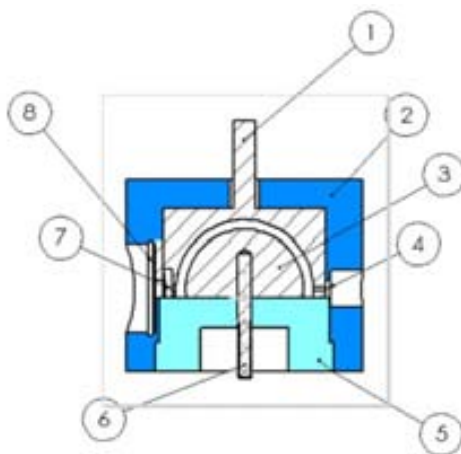


Figure 2-34: Schematic of hemispherical FAIMS electrodes [298]. (1) outer electrode, (2) outer housing, (3) inner electrode, (4) exit port, (5) base, (6) inner electrode connection, (7) entrance port, and (8) curtain plate.

The asymmetric waveform and the compensation voltage are applied to the inner electrode through the mounting screw that is threaded in the center of the electrode. The electric field in a hemispherical geometry can be calculated at any point within the analyzer region by using Equation (2.37), [298].

$$E_{r, \text{hemispherical}} = -\frac{V}{\left(\frac{1}{b} - \frac{1}{a}\right)r^2} \quad (2.37)$$

where V_a [V] is the applied voltage, a is the inner electrode radius, b is the outer electrode radius, r is position. The cylindrical cell, because of its curvature, is capable of focusing ions as described by Equation (2.36) in the cylindrical cell the field varies

non-linearly and is higher at the inner electrode than the outer. The hemispherical cell offers higher sensitivity than that of the cylindrical geometry because of its curvature in both directions. The ions that are located at various radial distances between the inner and outer electrode of the hemispherical cell will more effectively fall into the atmospheric pressure ion trapping region because the focusing decreases ion loss to the walls.

Planar FAIMS

Planar FAIMS electrodes, also known as flat plate electrodes, were first introduced in 1993 by Buryakov *et al.* [110]. The asymmetric waveform can be applied to either electrode, while the other is held at ground or a small bias. Shortly after the first published account of planar FAIMS, interest switched to cylindrical devices due to the higher ion transmission such devices offered. It was not until theoretical studies showed that resolution improved substantially with increasing electrode radius (to the limit that the radius is infinite) that interest was renewed in the simple planar FAIMS analyzer [247].

Planar analyzers consist of two flat parallel electrodes separated by an analytical gap through which ions are transported by gas flow perpendicular to the electric field (Figure 2-35). Analytical gaps range from 35 μm [299] to 2 mm [247] and electrode length ranges from 300 μm [299] to 50 mm [247]. In addition to the gap between electrodes and the length of the electrodes, the span (width) of the electrodes is an important parameter. To prevent ions from charging up the non-conductive surfaces which terminate the edges of the electrodes, the magnitude of the electrodes must be a minimum of 6 times the gap width.

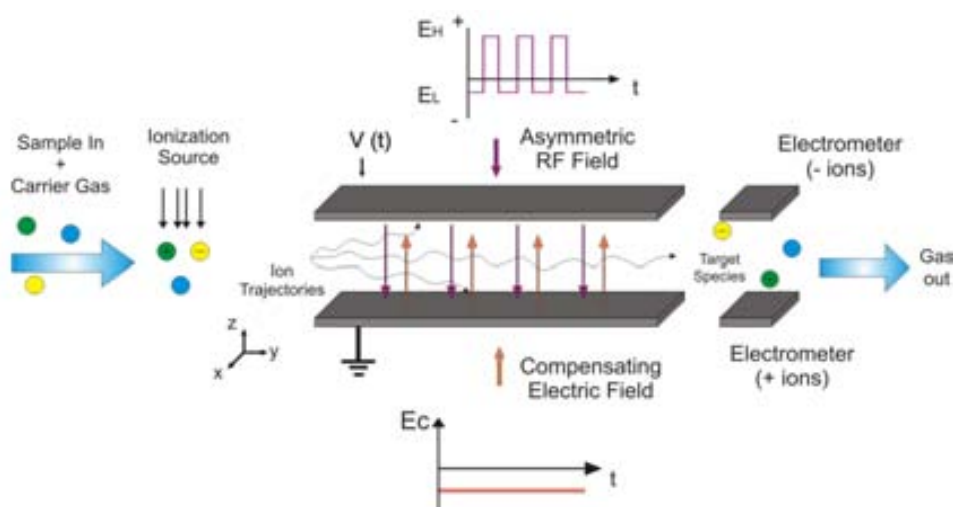


Figure 2-35: Schema of a planar high Field Asymmetric Ion Mobility Spectrometer or p-FAIMS.

The electric field between planar electrodes (E_{planar}) can be calculated using Equation(2.38), where V [V] is the applied voltage and g [mm] is the gap between the planar electrodes.

$$E_{planar} = -\frac{V}{g} \quad (2.38)$$

Asymmetric waveforms may be applied to electrodes, or sine waves maybe applied to each electrode independently and summed across the analytical gap to produce the desired waveform. Planar FAIMS has only two scan modes: either positive or negative scanning of the compensation voltage (CV). With only two modes of operation, all ions may be observed by scanning from negative to positive CV without changing the waveform polarity as would be necessary in cylindrical FAIMS.

The main advantage of the planar geometry is improved resolution. Resolving powers of 40 have been reported, and resolution improves as ion drift time increases [247]. Therefore, even ions with small variations in CV can be separated if the planar electrodes are long enough.

2.3.b FAIMS Ion Dynamics

The mobility K of an ion described by the Nernst-Townsend-Einstein relationship in Equation (2.20) and by the Mason-Champ theory in Equation (2.22) can be applied only for low E/N and need amendments at higher E/N . The mobility of an ion under the effects of high electrical fields can be expressed empirically by [227]:

$$K\left(\frac{E}{N}\right) = K_0 \times \left[1 + \alpha\left(\frac{E}{N}\right)\right] \quad (2.39)$$

where $K_0 = K(E)|_{E=0}$ is the mobility of the ion for a low electrical field as defined by Equation (2.22). The function $\alpha(E/N)$ takes account of the dependence of the ion mobility with the electrical field for a constant gas density, at ambient pressure and temperature. Equation (2.39) is derived using the approximation for little variations of α ($\alpha < 1$). In Figure 2-36 is shown a plots of the ratio $K/K_0 (= 1 + \alpha)$ vs. E/N . The term, $\alpha(E/N)$ can be negative, positive or null for an ion (indifferently of its polarity), as shown in Figure 2-36. The characteristic curves that allow a classification of ions as A, B or C type. For A type ions α increases as E/N increases, but for C type ions α decreases as E/N increases. For B type ions α initially increases as E/N increases and then decreases with further increase in E/N after reaching a maximum. This difference between types A and B is an artifact of the experimental limitation in the E/N range:

raising E will at some point reveal B-type for all A-type species. In contrast, C-type ions are truly distinct and cannot be similarly ‘converted’ [118]. From a physical point of view this different ion behaviors probably are all the same. That would correspond to an equation similar to the damped resonant systems that provide similar curves. Also $\alpha(E/N)$ describes the slope and the direction of the graph of $K(E)$ as a function of E/N . For physical reasons $K(E/N)$ must be always positive ($K > 0$), meaning that in any case alpha must be greater than -1. The experimental data gives values of alpha in the range [-0.01, +0.30].

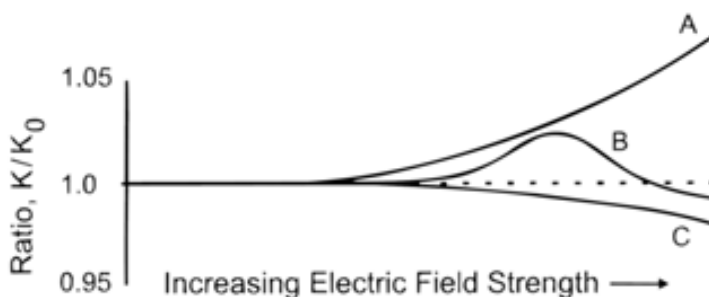


Figure 2-36: Classification of ion behavior in FAIMS. The mobility of type A ions increases at high fields, the mobility of type C ions decreases at high fields and the mobility of type B ions first increase before decreasing at even higher fields. Adapted from [116].

Usually, small and structurally stiff ions belong to type A, and large, flexible ions (e.g., proteins) belong to type C [271].

For low electric fields (< 30 Td, $\sim 7,500$ V/cm) the alpha values for every ion are similar, leading a constant mobility, this makes that for ions with a similar mobility K values. There is not a comprehensive model to explain such complex dependence of coefficient mobility against the electric field, there are just certain hypothetical models which are based on the Mason Schamp Equation (Eq.(2.22)).

The approximation for the function $\alpha(E/N)$ corresponds to a Taylor’s series, where for its definition it has to accomplish that it is equal to 0 for low E , and that it has to have the same value for E than for $-E$, so the terms of odd powers have to be zero, or almost their sum. $K(E/N)$ expanded into infinite series of powers of E/N , since only even powers may be present:

$$K\left(\frac{E}{N}\right) = K_0 \times \left(1 + \sum_{n=1}^{\infty} \alpha_{2n} \cdot \left(\frac{E}{N}\right)^{2n} \right) \quad (2.40)$$

All α_{2n} values may be positive and/or negative depending on the ion-neutral potential Φ among other factors. However, none is null and $\alpha(E/N)$ is never exactly zero, though can be near-zero over a broad range of E/N . The n coefficients could, in principle, be derived [227] from higher-order collision integrals of \mathcal{Q} using elaborated formalisms that will not be reported here.

Experimental measurements have shown that α_2 is three to five orders of magnitude smaller than one and α_4 is two orders of magnitude smaller than α_2 . So, in practice, with only two factors is enough to calculate the dependence of the mobility with the electric field.

$$K\left(\frac{E}{N}\right) = K_0 \times \left[1 + \alpha_2 \cdot \left(\frac{E}{N}\right)^2 + \alpha_4 \cdot \left(\frac{E}{N}\right)^4 + \dots \right] \quad (2.41)$$

For high electric fields in differential IMS, the velocity v [$\text{m}\cdot\text{s}^{-1}$] and the ions displacement s in the p-FAIMS sensor, only depends on mobility on z -axe, for y -axe v and s depend only of the drift gas flow, normally air or N_2 :

$$\mathbf{v} \begin{cases} v_x(t) = 0 & \text{except for} \\ & \text{diffusion} \\ v_y(t) = v_y(\text{carrier flow}) \\ v_z(t) = K\left(\frac{E(t)}{N}\right)E(t) = \frac{\partial z}{\partial t} \end{cases} \quad (2.42)$$

$$\int_{s_0}^{s_i} dz = \int_0^t K\left(\frac{E(t)}{N}\right)E(t) dt \quad (2.43)$$

$$\Delta s = K(0) \cdot \left[\int_0^t E(t) dt + \int_0^t \alpha\left(\frac{E(t)}{N}\right) \cdot E(t) dt \right] \quad (2.44)$$

The first term of Equation (2.44) does not take account of the differences of mobility due to electric field for the different ions and experimentally it is known that α_2 and α_4 are smaller than 1 [118, 227]. So, the only way to take advantage of the dependence of K with E is that the integral of E along t must be zero but not so E^3 and E^5 . That implies an asymmetric AC voltage.

Our focus will be on the form of $E(t)$, so it is convenient to normalize [291, 300, 301]:

$$E(t) = E_D F(t) \quad (2.45)$$

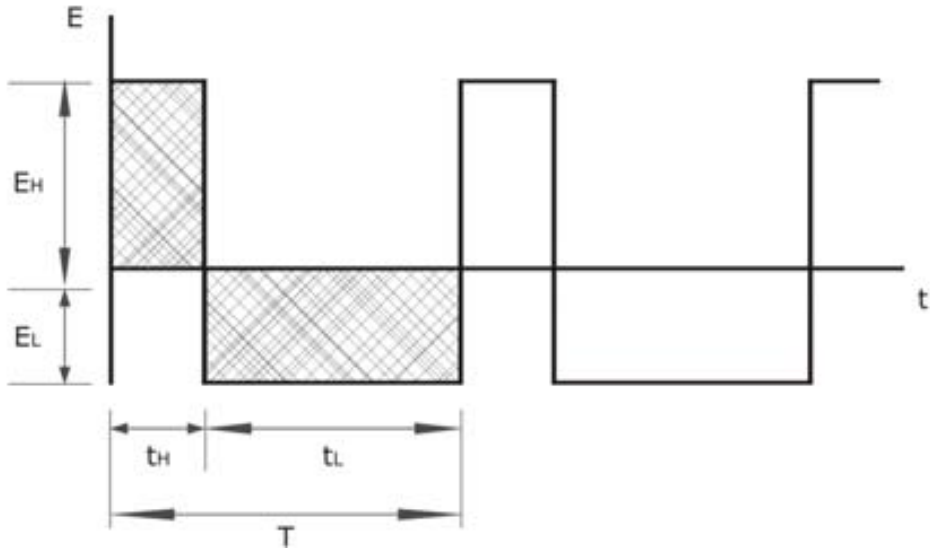


Figure 2-37: An idealized Rectangular asymmetric waveform which complies with the conditions required for use within a FAIMS system. The waveform has a period of T_w and is made from two regions, one of high field strength and the other of low field strength in the opposite polarity.

where E_D is the amplitude of $E(t)$ also called dispersion field, and $F(t)$ defines the profile.

To measure the difference between K at two values of E , one must send ions on paths where, for a period T of the asymmetric AC voltage, the first but not the second term on the right hand side of Equation (2.44) cancels. To understand the total transverse ion displacement across the filtering region the period of the asymmetric waveform (T) is defined. T is simply the time of the high and low field regions summed together, $T = t_H + t_L$ being t_H the time of the fraction of high voltage or field of the asymmetric waveform and, t_L the time of fraction of low voltage or field, as seen in Figure 2-37. The duty cycle D_T [dimensionless] of the asymmetric waveform is defined as a fraction of when the waveform is in the high field region with respect to the total waveform period:

$$D_T = \frac{t_H}{T} \quad (2.46)$$

Therefore, if the first term of Equation (2.44) is nullified, the displacement of ions in the z direction is:

$$\Delta s = K(0) \cdot \int_0^t \alpha \left(\frac{E(t)}{N} \right) \cdot E(t) dt \quad (2.47)$$

If we consider one period T , Equation (2.47) can be rewritten as:

$$\Delta s_{1T} = K(0) \cdot \int_0^T \alpha \left(\frac{E(t)}{N} \right) \cdot E(t) dt \quad (2.48)$$

$$\Delta s_{1T} = K(0) \cdot \int_0^{t_H} \alpha \left(\frac{E(t)}{N} \right) \cdot E(t) dt + K(0) \cdot \int_0^{t_L} \alpha \left(\frac{E(t)}{N} \right) \cdot E(t) dt \quad (2.49)$$

$$\Delta s_{1T} = K(0) \cdot \alpha \left(\frac{E_H}{N} \right) \cdot E_H \cdot t_H - K(0) \cdot \alpha \left(\frac{E_L}{N} \right) \cdot E_L \cdot t_L \quad (2.50)$$

$$\Delta s_{1T} = K_H \cdot E_H \cdot t_H - K_L \cdot E_L \cdot t_L = s_H - s_L \quad (2.51)$$

where the minus indicates the opposite direction in z of ions displacement s in one period T the gap; and s_H and s_L are the maximum and minimum transverse ion displacement during a period of the asymmetric waveform, respectively.

To nullify the first term of Equation (2.44), the integral of $F(t)$ in the range 0 to T , must nullify [291, 300, 301]:

$$\int_0^T F(t) dt = 0 \quad (2.52)$$

Equation (2.52) is trivially met when $F_+(t) = -F_-(t+T/2)$ for a square waveform. Formally, at least some odd momenta of $F_+(t)$ and $F_-(t)$ must be unequal [118]. An $F(t)$ that meets Equation (2.52) comprises two rectangular fragments [302-304], as seen in Figure 2-37. But this waveform does not consider engineering aspects. An exact rectangular profile cannot be implemented with electrical circuitry. All commercial and most research instruments thus far have used $F(t)$ based on harmonics: bisinuoidal, clipped-sinusoidal forms, etc. For a bisinuoidal $F(t)$, that is a sinusoidal plus its second harmonic phase-shifted by 90° :

$$F(t) = \frac{1}{f+1} \left[f \sin(\omega t) + \sin \left(2\omega t - \frac{\pi}{2} \right) \right] \quad (2.53)$$

where $\omega = 2\pi/t_C$ and f is the ratio of amplitudes of first and second harmonics varying from 0 to ∞ . Both $f=0$ and $f=\infty$ converts Equation (2.53) to a symmetric sinusoid, hence the separation is best at intermediate f where $F(t)$ is most asymmetric and emulates the rectangular $F(t)$ with $f=2$, therefore $f_{opt} = 2$ [116, 118]. In Figure 2-38 the waveforms generated by Equation (2.53) for some values of f are shown.

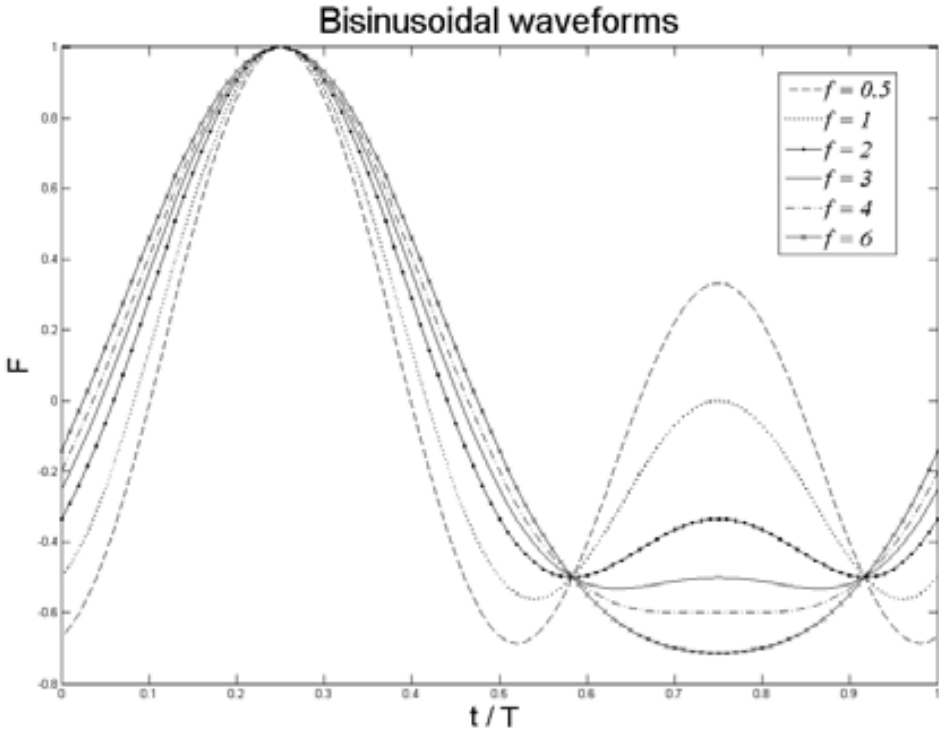


Figure 2-38: Bisinusoidal waveforms profile $F(t)$ with $f = 0.5, 1, 2, 3, 4$ and 6 [305].

Effective gap height

An important outcome of the equations describing ion displacement during an applied waveform is the appreciation of a new loss mechanism for the ions of interest. For detection an ion requires that the effective gap (g_{eff}) between electrodes is smaller than the physical gap (g) because the ions need enough space to oscillate with the dispersion field without striking the electrodes [301]. This effective gap height g_{eff} [mm] is equal to the gap height minus the maximum distance travelled by the ion of interest during a period of the asymmetric waveform:

$$g_{eff} = g - s_H \quad (2.54)$$

where s_H [mm] is the maximum transverse ion displacement during either region of the asymmetric waveform. It can be rewritten as

$$g_{eff} = g - \frac{V_H D_T K_H}{v \cdot g} \quad (2.55)$$

Considering that (i) the transverse ion displacement for the high field region is $s_H = K_H |E_H| t_H$; (ii) for a planar-FAIMS the maximum electric field strength is $E_H = V_H/g$ where V_H is the voltage of the idealized asymmetric waveform in the high field region; (iii) the frequency ν [s] of the applied asymmetric waveform is related to the period of the same waveform by the expression $T = 1/\nu$; and (iv) the duty cycle defined in Equation (2.46) as $D_r = t_H/T$.

This is a simplification of the real losses incurred through this mechanism since it is based upon an idealized waveform but it is something that affects FAIMS systems. This is particularly true for designs with a small gap height since any loss translates to a greater percentage loss than for larger sensors. It is an obvious conclusion to state that for maximum transmission of ions of interest through the filtering region g_{eff} should approximately equal g . From this treatment it appears that only benefits can result from increasing the frequency. However, a very rapidly changing waveform (between low and high fields) is a violent environment for a molecular-ion. FAIMS relies heavily on chemistry within the filtering region which can be affected by the limits imposed on interaction times through a change in frequency. An example of this would be the phenomena of clustering (see Section 2.3.c *Detection: Field strength effects: 5. Clustering and de-clustering of ions*).

FAIMS filtering using Compensation Field

If a DC voltage or ‘compensation voltage’ of intensity field E_C is superpose on $E(t)$ it will displace the ions by:

$$\Delta s_{1T} = \int_0^T K [E(t) + E_C] dt \quad (2.56)$$

Selected ions can be kept in the flowing gas by applying particular low DC field ($|E_C| < |E_L| \ll |E_H|$) between the filter electrodes. This DC voltage or compensation voltage (V_C) prevents the ion migration towards either electrode, also if the total oscillation of the ion is lower than the gap. Thus, a selected ion passes through the filter electrodes and reaches the detector being this V_C voltage a characteristic of each ion species, as is resumed in Figure 2-39.

For a given ionic species can be found the compensation field E_C in order to satisfy that ions are stable in the *gap* (pass through it), as [118]

$$\frac{E_c}{N} = -\sum_{n=1}^{\infty} \kappa_{2n} \left(\frac{E_D}{N}\right)^{2n+1} = -\kappa_2 \left(\frac{E_D}{N}\right)^3 - \kappa_4 \left(\frac{E_D}{N}\right)^5 - \dots \quad (2.57)$$

where κ_2 and κ_4 are defined by:

$$\begin{aligned}\kappa_2 &= -\alpha_2 \langle F_3 \rangle \\ \kappa_4 &= -\alpha_4 \langle F_5 \rangle + 3\kappa_2 \alpha_2 \langle F_2 \rangle\end{aligned}\tag{2.58}$$

where α_2 and α_4 are own values for each ion species, and the average values of the bisinusoidal function are [301]: $\langle F_2 \rangle = 0.833$, $\langle F_3 \rangle = 0.111$ and $\langle F_5 \rangle = 0.116$, where N [mol·m⁻³] is the number of molecules in the carrier gas.

Sweeping the compensation voltage produces a high-field equivalent of a mobility spectrum of the different ion species present in the gas stream. Plots of E_C/N versus E/N allow the extraction of α for a certain ion, because the compensation potential for a p-FAIMS was shown to be proportional to the cube of the dispersion potential with the proportionality constant containing ion specific information [306].

An important advantage of FAIMS is the possibility for separation of negative and positive ions simultaneously [15, 118], although, at the cost of increasing electronics [119]. All of the different atmospheric pressure ionization (API) methods used for the drift tube IMS instruments are applicable to FAIMS instruments as well. In addition, an advantage of μ IMSs, in comparison to conventional IMSs, is simplification of the analyzer construction, due to the elimination of ion shutters (ion gates) which are the most difficult component to produce, and also elimination of the aperture grids as the detector is placed parallel to the gas flow.

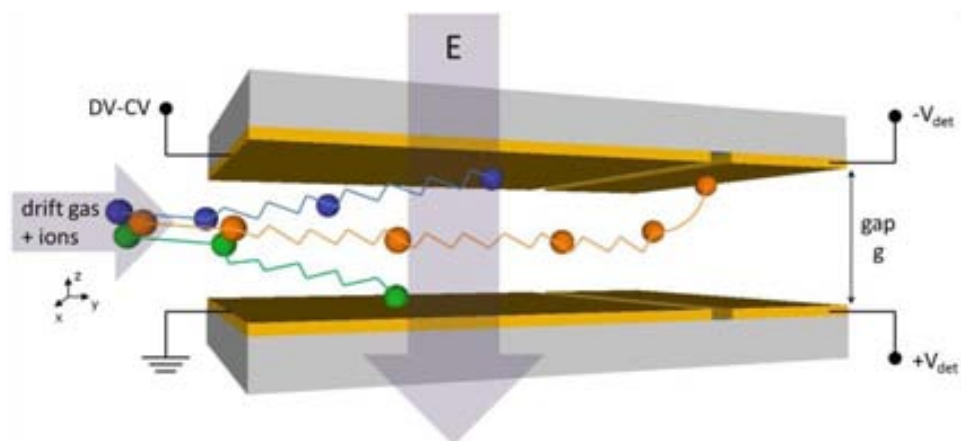


Figure 2-39: Ion trajectory “straightening” through the application of a DC compensation voltage to the ion filter electrodes.

2.3.c Detection

The most used detectors with FAIMS are, (again) faraday cups [307, 308], electrometers [115, 116], picoammeters [309] and also Mass Spectrometers [217, 293]. Sweeping the compensation voltage or CV, a spectrum can be drawn for a particular dispersion voltage or DV based on the trajectory of the ions through the sensor, as can be seen in Figure 2-40. Intensity results are either given in pA [304] other in V after having amplified and converted the intensity, currents of 10^{-11} A correspond to an amplification of 1 V [15]. Typical values for polyatomic ions in FAIMS are $\sim 10\text{--}100$ pA [310].

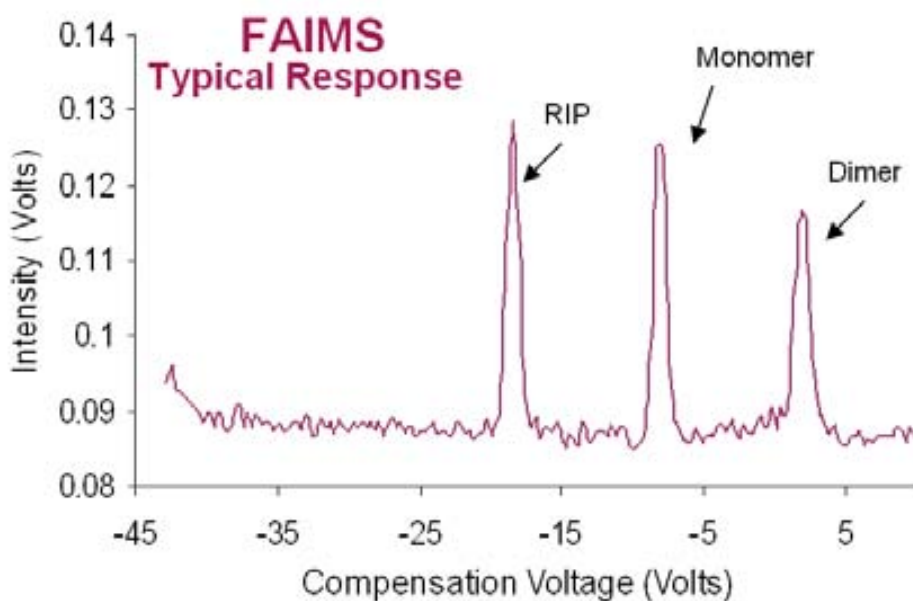


Figure 2-40: Schema of a typical FAIMS chromatogram showing the reactant ion peak (RIP), one monomer and one dimer. Adapted from [218].

Drift time

The drift time or residence time (t_{res}) is the time spent by an ion within the filtering region of a FAIMS device. The translational velocity of the ion through the filtering region is only dependent upon the magnitude of the carrier flow and the dimensions of the filtering region. All imposed electric fields are orthogonal to the translational component of the ion so drift time is independent of field and may be calculated through [118]:

$$t_{res} = \frac{gwl}{Q} = \frac{V_m}{Q} \quad (2.59)$$

Where V_m [mm³] is the volume of the filtering region, Q [mL·min⁻¹] is the volume flow rate and g [mm], w [mm] and l [mm] are the gap, width and length of the filtering electrodes, as defined in Figure 2-41.

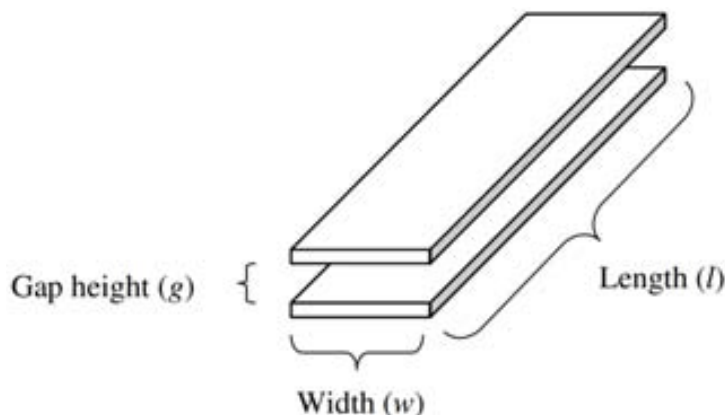


Figure 2-41: Dimensions of a FAIMS filtering region.

The greater the drift time the longer the ions will be subject to the filtering influence of the electric fields. Therefore as the drift time increases the resolution and selectivity of the FAIMS system increases. At the same time, increased drift allows for more random interactions (collisions) of ions with the neutral carrier gas, which leads to greater losses to an electrode. Consequently, there is typically an associated loss of sensitivity with increased selectivity.

Doped Gases

As in the conventional case, doped gases can be used to enhance the FAIMS spectrum obtained. For instance, a CV needed for a particular ion in N₂/O₂ can be calculated using Blanc's law [311]. However, other gas mixtures, such as CO₂/He, SF₆/He and He/N₂, deviate from Blanc's law at high fields and have much higher CVs than anticipated [271]. Higher CVs create more focusing due to higher fields and therefore are desired. It was determined that mixtures of gases that greatly varied in molecular weight and cross section, such as He and SF₆, deviated the most from Blanc's law [271].

Diffusional loss

Diffusion is the major loss mechanism for ions that have the correct mobility coefficient to traverse the FAIMS filtering region. The random interactions which ions experience with the neutral carrier flow can lead to the ions of interest reaching an electrode surface and neutralizing. The dimensionless diffusion loss D_{loss} is calculated through [301]:

$$D_{loss} = 1 - \exp\left(-\frac{\pi^2 k_B T K t_{res}}{e g_{eff}^2}\right) \quad (2.60)$$

This diffusion is dependent on a number of factors including, indirectly and directly, the geometry of the filtering region. With a value of zero being complete ion transmission and a value of unity meaning total signal loss. Figure 2-42 is constructed from Equation (2.60) assuming an ion mobility of $K = 2.30 \text{ cm}^2 \cdot \text{V}^{-1} \cdot \text{s}^{-1}$, corresponding to toluene monomer TH^+ .

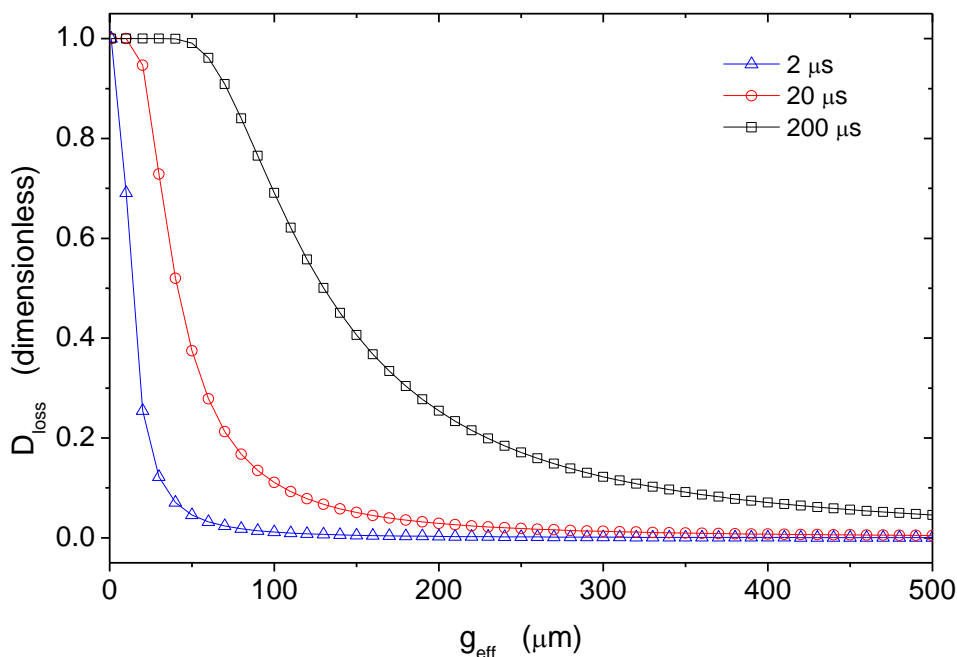


Figure 2-42: Diffusion loss at drift times of 2 μs (blue triangles), 20 μs (red circles) and 200 μs (black squares) as dependent on the effective gap.

Diffusion loss is of greater importance at low effective gap heights but the losses are reduced with a reduction in the drift time of ions within the filtering region. It becomes clear that the magnitudes of drift time and the effective gap height are important when considering diffusion loss. These two magnitudes are controlled through the geometry of the filtering region and the flow rate of the neutral carrier gas. The diffusion loss is proportional to the drift time and effective gap height through,

$$D_{loss} \propto \frac{t_{res}}{g_{eff}^2} \quad (2.61)$$

As the drift time is decreased, sensitivity will be closer to optimum; if the effective gap height is reduced, the losses due to diffusion will markedly increase as Equation (2.61) is sensitive through the g_{eff}^2 term. The effect of narrowing the effective gap height is not wholly detrimental since the drift time is reduced through Equation (2.59).

Space charge effect

The major cause for ion swarm broadening within a FAIMS system is thermal diffusion. A second reason for broadening is Coulomb repulsion of ions of like charge. This is known as the space charge effect. The magnitude of the space charge effect is proportional to the square of the charge density ρ [$C \cdot m^{-3}$]. When the charge density is too great, the repulsion of ions to the walls of the FAIMS sensor results in neutralization. The space charge effect therefore not only affects the resolution but also imposes a limit on the maximum current permissible. This limit is known as the charge capacity [118].

In traditional IMS devices space charge effects are normally surpassed by the larger effect of thermal diffusion [312]. With the development of FAIMS, greater duty cycles, smaller analytical volumes and improvements in ionization efficiencies space charge effects may become significant [118]. Ions in FAIMS experience directed drift, anisotropic diffusion, and Coulomb repulsion. The drift proceeds along E that is orthogonal to the electrodes (see Section 2.3.b *FAIMS Ion Dynamics: FAIMS filtering using Compensation Field*). Charge density can be reduced by streaming ions into multiple channels, since the repulsion is described by Coulomb's law:

$$F_C = \frac{1}{4\pi\epsilon_0} \frac{q^2}{r^2} \quad (2.62)$$

Where ϵ_0 [$8.85 \cdot 10^{-12} \text{ F} \cdot \text{m}^{-1}$] the electric permittivity of vacuum [166], r is the distance between ions, q is the ion charge [C] being $q = ze$ where e is the elementary charge [$1.602 \times 10^{-19} \text{ C}$] [166] and z is the number of elemental charges [dimensionless].

Figure 2-43a shows a simulated CV scan for a cylindrical FAIMS, where the traces show the residual ion density at 50 ms intervals up to 250 ms. At short drift times in the FAIMS analyzer the peaks are expected to be wider than the peaks at longer drift times. Figure 2-43b is a repeat of the calculations of Figure 2-43a, but with the addition of the effect of coulombic ion-ion repulsion. The ion-ion repulsion acts in a direction to expand the radial dimensions of the ion clouds, and as a result the ion cloud is more likely to be in contact with the electrodes and ion density decreases with time.

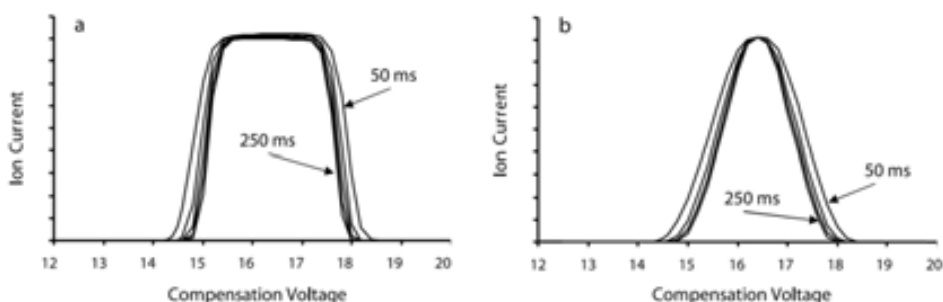


Figure 2-43: Calculated CV peak shapes based on drift times of 50 to 250 ms in a 0.8/1.0 cm radii cylindrical FAIMS. Calculated (a) without, and (b) with coulombic ion-ion repulsion. The ion cloud density was calculated at 50 ms intervals with ions having $K_0 = 1.7 \text{ cm}^2 \text{V}^{-1} \text{s}^{-1}$, $\alpha_2 = 7.984 \times 10^{-6} \text{ Td}^{-2}$, $\alpha_4 = 3.049 \times 10^{-10} \text{ Td}^{-4}$, (corresponding to bromochloroacetate anion or BCA^-) at $\text{DV} = 3,960 \text{ V}$ and CV from 12.6 to 19.8 V in 0.1 V increments. Adapted from [295].

Waveform frequency effects

Frequency enhances transmission but has no effect on ion separation, as suggested by Equation (2.55). This can be seen in Figure 2-44 shows average spectra of 20 scans for 2-pentanone monomer and dimer ions with hydrated protons at waveform frequencies of 0.6, 0.8, and 1.0 MHz at the same dispersion voltage of 690 V. Ion intensity is lower at reduced frequencies, and the width of the peak at full-width half-maximum for hydrated protons at $\text{CV} = 8.8 \text{ V}$ is $w_{1/2} = 0.68 \text{ V}$, and $R_p = 13$. At 1.0 MHz, the width of the peak increases to $w_{1/2} = 0.72 \text{ V}$, and $R_p = 12$.

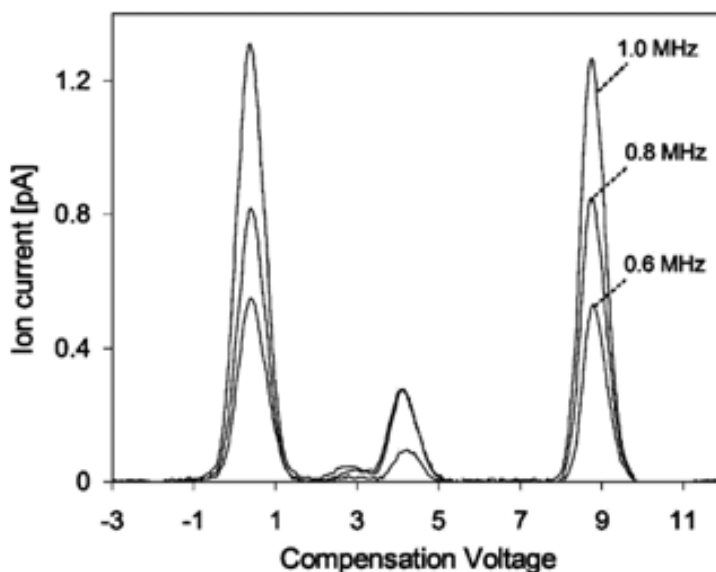


Figure 2-44: Differential mobility spectra for 2-pentanone protonated monomer and proton-bound dimer ions with hydrated protons obtained at frequencies of 0.6, 0.8, and 1.0 MHz [304].

Waveform shape effects

As pointed in the Section 2.3.b *FAIMS Ion Dynamics*, as seen in Equation (2.52) for an effective separation the integral of the waveform applied must be zero:

$$\int_0^{\tau} F(t) dt = 0 \quad (2.63)$$

A high number of waveforms accomplish this condition. In Figure 2-45 are shown the ideal rectangular waveform (Figure 2-45b) and the mostly used ones: the bisinusoidal (Figure 2-45a) that is a sinusoidal plus its second harmonic phase-shifted by 90° [118]; and the clipped-sinusoidal (Figure 2-45c) waveforms that is generated by clipping a single sinusoidal offset by a fixed DC voltage [291, 313]. Even though most FAIMS experiments have made use of the bisinusoidal waveform [116, 118, 314], theoretical studies have suggested that a rectangular waveform would be ideal for FAIMS analyses [303, 304, 310]. Analytical considerations show that rectangular waveforms may improve ion separation efficiency, resolution, and/or sensitivity as compared to sinusoidal waveforms [301, 310, 315, 316]. Unfortunately, practical use of electronics that deliver rectangular pulses for driving differential ion mobility separations has been hindered due to the excessive power load imposed by the system [304].

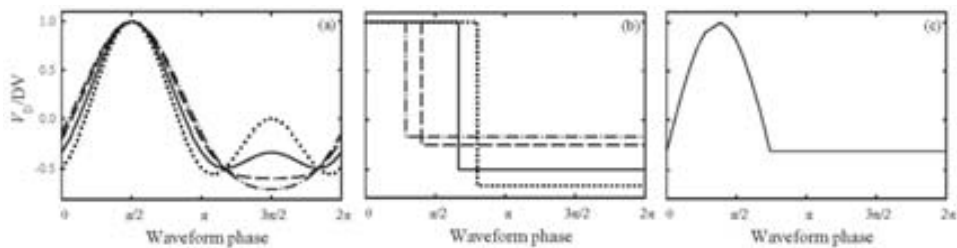


Figure 2-45: Asymmetric waveforms: (a) bisinusoidal from superpositions of a sinusoidal and scaled 2nd harmonic; (b) rectangular; and (c) clipped sinusoidal. In (a) and (b), the high-to-low coefficients f are: solid line–2, dash–4, dash dot–6, dotted–1.0 in (a) and 1.5 in (b). In (c), $f = 1.7$. Adapted from [310].

For each different waveform accomplishing equation (2.63), its portion of high electric field will be different, so the ions movement inside the filtering electrodes gap also will be different for each waveform, and therefore the detected compensation voltage. Prieto *et al.* [314] studied how the shape of the waveform applied affected to the compensation voltage for the bisinusoidal and the rectangular waveforms. Figure 2-46 shows CV as a function of DV for square and sinusoidal waveforms, with the bisinusoidal wave at 750 kHz and for a duty cycle of 33.3 %; and the square wave at three different frequencies (250, 333, and 500 kHz) all of them for a duty cycle of 25 %. Compensation voltages from each waveform considered differs 0.7 V for a dispersion field of 300 V to 1.0 V for a dispersion field of 350 V.

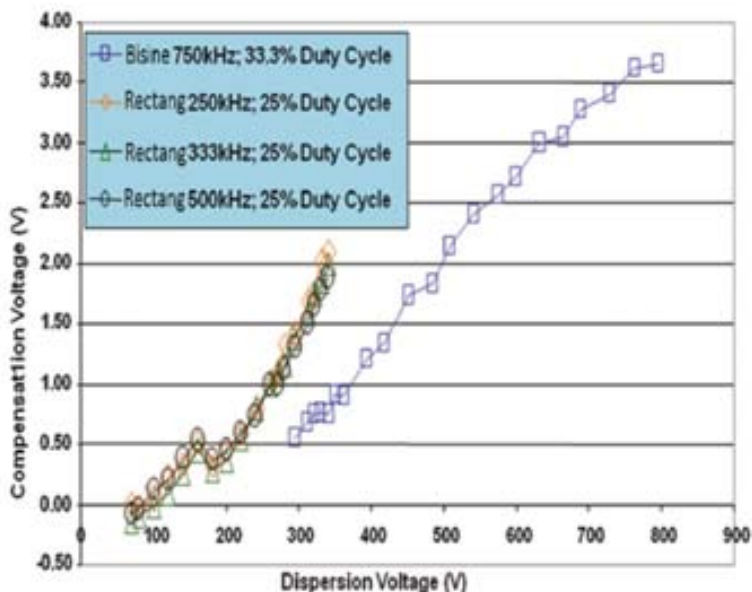


Figure 2-46: Graphs displaying behavior of CV as a function of DV. Adapted from [314].

Field strength effects

Nazarov *et al.* [265] presented five separate ways in which the field dependence of the mobility coefficient could be understood. Considering the consequence of separate effects upon the mobility coefficient is important as it is the principal magnitude that results in the separation of compounds within a FAIMS sensor. These mechanisms consider the carrier flow and applied asymmetric waveform. This section is intended as an introduction with a more in depth treatment provided later in the chapter for the most prevalent types of interaction.

1 Scattering through direct contact

Considering the ions and neutral carrier flow as rigid bodies has been the Standard approach to understanding mobility. This methodology is explored in greater detail within the Momentum transfer theory.

Collisions between ions and neutral molecules are considered the primary physical mechanism for interaction of ions within the filtering region. To investigate this interaction the theory of momentum transfer is applied [227]. The average velocity of ions can be described by the sum of three components, as described by:

$$\frac{1}{2}m\bar{v}^2 = \frac{1}{2}M\bar{V}^2 + \frac{1}{2}mv_d^2 + \frac{1}{2}Mv_d^2 \quad (2.64)$$

where v_d [$\text{m}\cdot\text{s}^{-1}$] is the drift velocity of the ions, m [uma] and \bar{v} [$\text{m}\cdot\text{s}^{-1}$] are the mass and average velocity of the ions respectively, and M [uma] and \bar{V} [$\text{m}\cdot\text{s}^{-1}$] are the mass and average velocity of the neutral molecules respectively.

The terms on the right hand side of Equation (2.64) represent real world observable magnitudes. The second term is the drift motion of ions while the third term is the random part of the field energy due to the effects of any collision that occurs. The velocity, and hence the kinetic energy, of the gas molecules is entirely due to thermal energy since they cannot be affected by an applied electric field, therefore the first term is only dependent upon the mass and velocity of the neutral gas and so is determined by the thermal environment and is equal to:

$$\frac{1}{2}M\bar{V}^2 = \frac{3}{2}k_B T \quad (2.65)$$

where k_B is the Boltzmann constant [$1,38065 \times 10^{-23} \text{ J}\cdot\text{K}^{-1}$], and T is the gas temperature [K].

2 Elastic scattering due to polarization interaction

As ions move through the carrier gas they can induce a dipole in the neutral species present. Interaction between ions and induced dipoles can then occur and is dependent upon an effective ion neutral cross section (Ω_{pol}). This cross section is dependent upon the relative velocities of the constituents, with the interaction becoming more likely if the constituents are moving slowly [227],

$$\Omega_{pol} \propto \frac{1}{\sqrt{\varepsilon}} \quad (2.66)$$

where ε [eV] is the energy of the ion. When the effective ion neutral cross section decreases to the geometric size of the constituents the effect through induced dipoles should no longer be in evidence and scattering through direct contact is dominant.

3. Resonant charge transfer

When ions are similar in structure to the neutral species present in the carrier flow the transfer of electrons can easily occur between the constituents. This happens very quickly and when it occurs an ion's velocity is lost. Charge transfer will therefore affect the drift velocity of an ion. Nazarov *et al.* [265] noted that the theory resulting from scattering through direct contact also describes the effects of resonant charge transfer.

82

4. Change in shape/identity of ion

High electric fields potentially have the energy to change the molecular conformation and dipole moments of species. Such changes to the shape of an ion are often abrupt as the energy imparted to the ion reaches a critical value. An example of this is the response from methyl salicylate given in Figure 2-47.

The response from all the reactant and product ions appears to be smooth and continuous except for the product ion peak in the negative polarity. The apparent break in the negative product ion peak was suggested as a consequence of the applied electric field changing the identity of the product ion. Through the use of a mass spectrometer this hypothesis was confirmed. The expected product ion was indeed changed through a proton abstraction as a consequence of heating of the ion [153, 265].

The electric field within the filtering region is increased through the voltage applied between the electrodes, but the voltage cannot be amplified ad infinitum since there will be a case where an arc will travel from one electrode to the other. Such an arc occurs when the medium between the electrodes exceeds its 'breakdown voltage'. At the breakdown point the voltage is too great for the supporting atmosphere (for a FAIMS system this will be the carrier gas) and the insulating medium becomes electrically conductive. This is described by Paschen's law [317]:

$$V_{BD} = \frac{B \cdot P \cdot g}{\ln(A \cdot P \cdot g) - \ln\left[\ln\left(1 + \frac{1}{\gamma}\right)\right]} \quad (2.67)$$

where V_{BD} [V] is the breakdown voltage, and A and B are constants dependent upon the identity of the carrier gas, being in air and at standard atmospheric pressure (101,325 Pa) $A = 11.25 \text{ m}^{-1} \cdot \text{Pa}^{-1}$ and $B = 273.77 \text{ V} \cdot \text{m}^{-1} \cdot \text{Pa}^{-1}$ [318], and $\gamma = 0.01$ [dimensionless] [318] is the secondary ionization coefficient and is defined as the net number of secondary electrons produced per incident positive ion, photon, excited particle, or metastable particle and is called the Townsend's secondary ionization coefficient. Paschen discovered that the breakdown voltage reaches a minimum value at a separation of several micrometers at atmospheric pressure [317]. When the electrode separation is reduced below several micrometers, the breakdown voltage and field increase rapidly.

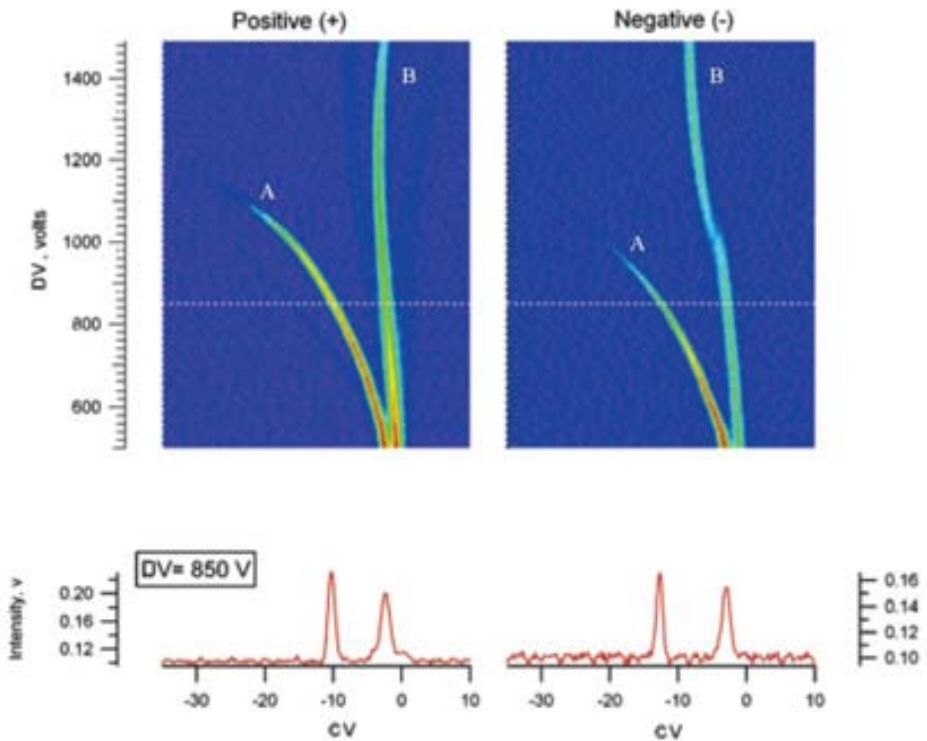


Figure 2-47: Dispersion voltage sweeps of methyl salicylate in positive and negative polarity. **A** are the reactant ions and **B** are the product ions. Adapted from [265].

A plot of the breakdown voltage as a function of the product of electrode separation and pressure, known as the Paschen curve, is given in Figure 2-48 [319]. Also is shown the breakdown field: $E_{BD} = V_{BD}/g$ [$V \cdot m^{-1}$]. To the left of the minimum breakdown voltage there are too few impacts of ionized molecules to achieve a regenerative avalanche breakdown unless the applied voltage increases. At the minimum breakdown voltage the electrostatic energy is most efficiently linked to the avalanche process. With regard to air at atmospheric pressure, Paschen's law does not describe the breakdown voltage well at gap heights below $10 \mu m$ [320, 321].

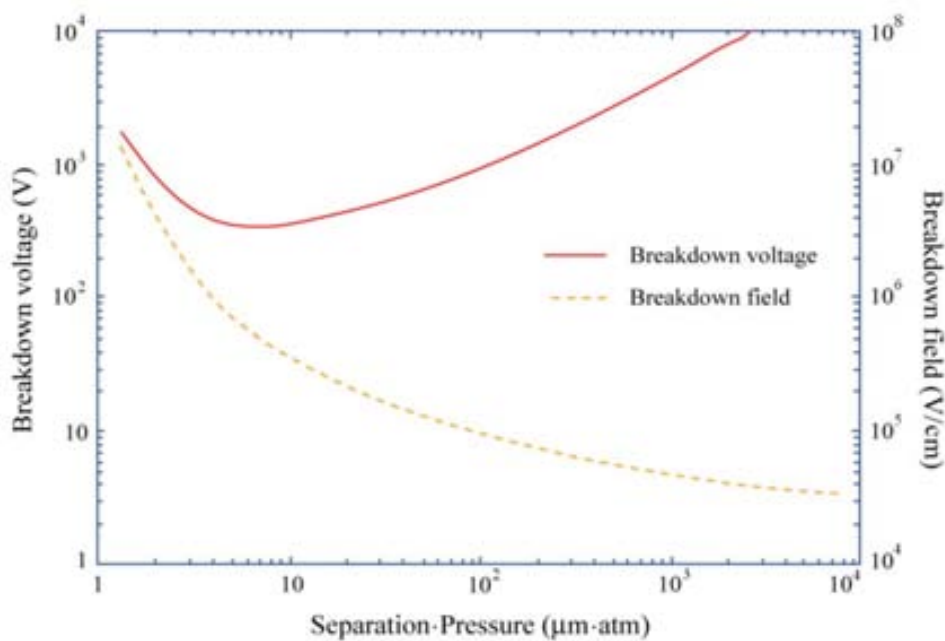


Figure 2-48: Breakdown voltage V_{BD} and Breakdown electric field E_{BD} against a range of separation (gap height or g) \times pressure for air [319].

As long as the maximum applied across a filtering region is below V_{BD} , decreasing the gap height enables ever greater electric fields to be imposed without risking an arc across the electrodes. A small gap height therefore enables greater electric fields with comparable resources to devices with larger geometry. While there is a trade-off attributable to reducing the gap height with regards to ion losses by diffusion (see *Section 2.3.c Detection: Doped Gases*) the breakdown voltage imposes an absolute maximum that the gap height can be increased.

5. Clustering and de-clustering of ions

While ions traverse the filtering region of a FAIMS sensor an asymmetric waveform is cycled. This results in the ions experiencing differing environments at different times. For instance, the low field portion of the waveform may be more conducive to the solvation of neutrals onto the molecular ion cluster. In Figure 2-49 is shown the clustering and de-clustering of ions. In contrast the high field portion may make the likelihood of such clustering unlikely. If this scenario were to occur an increase in the collision cross section would be expected in a low field but not in a high field. Such a change would affect the difference in mobility experienced by the ion throughout the waveform and result in a change of observed ion behavior. The effect would be dependent upon the chemical identity of the ions and available neutrals. Solvation is likely if the Gibbs energy of the solvated system is less than the case with no solvation [322].

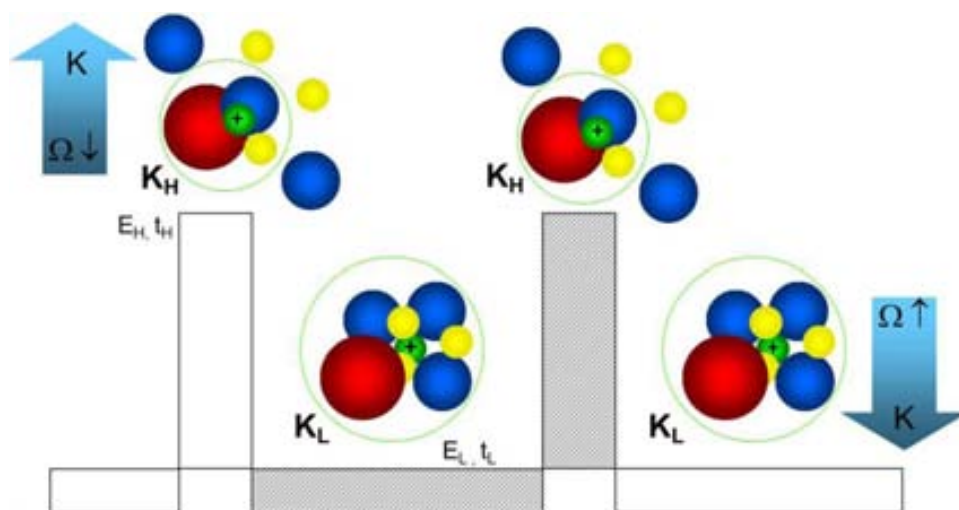


Figure 2-49: Model for positive alpha functions is illustrated above where an ion core is de-clustered at high field (E_H) and re-clustered at low field (E_L) when the ion is considered thermalized or thermally cool. At high field of E_H , ions are de-clustered leading to a decrease in Ω (represented by the faint circle around the ion cluster) and an increase in K . At low field of E_L , ions are re-clustered leading to an increase in Ω and a decrease in K . Adapted from [323].

The onset of clustering has been investigated by increasing the population of potential clustering neutrals. It was discovered that the onset of clustering occurred at a set-point which was dependent upon the concentration of potential clustering neutrals and the frequency of the asymmetric waveform [324]. The hypothesis of this 'solvent effect' has since been questioned by Shvartsburg [118]. The solvent effect appears to explain likely clustering behavior. It is suggested that the conflict within the literature can be settled with the inclusion of a term describing the rate that which collisions are

successful. This is present within the work by Eiceman and Kapras [15] but not Schvartsburg [118]. There have also been a number of studies investigating the possibility of exploiting clustering to better resolve separate ion species [259, 292, 324, 325].

Modifying the geometry of electrodes

The separation of ions within a FAIMS instrument is dependent upon several interconnected magnitudes. Some of these magnitudes, such as electric field, are varied as part of the normal operation and can easily be tailored within certain limits. One magnitude that affects all other considerations is that of electrode geometry and it cannot be changed following fabrication of a FAIMS system.

Modifying the width and length of the filtering region

If the gap (or analytical) height g [mm] is kept constant while the length l [mm] and width w [mm] (defined in Figure 2-41) are changed the position of resultant peaks with respect to CV remains unchanged. This is due to the ion's mobility coefficient being dependent upon the electric field experienced. In the case of a planar FAIMS device the electric field is applied orthogonally to the length and width of the filtering region and therefore is independent of the changing geometry.

86

Maintaining the gap height while length and width are changed will modify the drift times of ions in accordance with Equation (2.59). This can affect the sensitivity and resolution but not the CV position of ions.

Another consideration is that changing the length of the filtering region changes the angle of trajectory an ion has to possess for detection. A greater length would reduce the acceptance angle and hence reduce the FWHM. From geometric considerations the angle of acceptance is not linear with length and the rate of change decreases with increased length. More accurately the angle of acceptance γ is dependent upon the ratio of the gap height g with the length l of the filtering region:

$$\tan \gamma = \frac{g}{l} \quad (2.68)$$

Modifying the gap height of the filtering region

Narrowing the gap height of the filtering region decreases the volume. This leads to both an increase and decrease in the losses attributable to diffusion since both the drift time and effective gap height is reduced. This loss can be countered through an increase in frequency of the waveform (see *Section 2.3.b FAIMS Ion Dynamics: Effective gap height*). The net equilibrium will depend on the particular geometry.

Narrowing the gap height would lead to an increased maximum electric field. This would alter the CV position at which ions are observed. Additionally, more ions of incorrect mobility would be lost if the effective gap height is decreased. However, reducing the gap height also decreases the drift time of ions which affects their net separation. Furthermore, the angle of acceptance of ions through the filtering region is dependent upon the gap height as expressed through Equation (2.68).

Increasing the gap height while also decreasing the flow rate would improve sensitivity and resolution. However, through an increase in gap height an increase in the voltage across the filtering region would be required to maintain an equivalent electric field. There is a limit to the extent the voltage can be increased across the filtering region (beyond practical limitations) which is described by Paschen's law (Equation (2.67)).

Resolution and Resolving power

Resolving power and Resolution for a FAIMS device are defined similarly as for the IMS (Equations (2.26) and (2.29)), just replacing the drift time for the compensation voltage. Being in FAIMS the Resolving power R_p [dimensionless] of one peak and the Resolution R [dimensionless] between two neighboring peaks:

$$R_p = \frac{|CV|}{FWHM} \quad (2.69)$$

$$R = 2 \times \frac{|CV_A - CV_B|}{w_{b,A} + w_{b,B}} \quad (2.70)$$

where $|CV|$ [V] is the absolute value of the compensation voltage for a particular ion at maximum peak height, and FWHM [V] is the full width at half maximum height for this compensation peak [254, 257]. And CV_A , CV_B are the CV values for the ions of interest, and $w_{b,A}$, $w_{b,B}$ the peak widths in seconds at the base of the peak as defined in Section 2.2.f. Planar-FAIMS usually offer higher specificity and resolving power at the expense of lower transmission [300], while cylindrical-FAIMS offer greater transmission due to an electrostatic focusing effect at the expense of lower resolving power [115].

Miniaturization of analytical instruments enables portability for field and real-time applications. The potential, however, for gas-phase based IMS technology to produce efficient miniature IMS (<centimeter scale) instruments is limited due to the rapid diffusion of ions in gases. Nevertheless, several recent attempts have been made to miniaturize the IMS device [148, 163, 326-331]. Table 2-1 provides a list of IMS

instruments in order of drift length (L) or filtering region length along with the resolving power R_p and the R_p/L . One method to compare the efficiency of an IMS instrument is to use resolving power/length (R_p/L) [332]. Although different in design from the Babis *et al.* [326] drift tube, the Xu *et al.* drift tube [330] had a similar resolving power of about 10 with an R_p/L of about 3 cm^{-1} . As the length of an IMS is reduced, the primary limitation to resolving power is the limit on producing effective ion pulses to inject into the IMS. As the length of a gas phase IMS device is reduced, the optimal resolving power voltage decreases, decreasing the maximum resolving power possible [327, 333, 334].

Reference	Drift Length L (cm)	Resolving Power R_p	R_p/L (cm^{-1})
Kanu <i>et al.</i> [327]	6.8	14	2.1
Babis <i>et al.</i> [326]	4.65	15	3.2
Baumbach <i>et al.</i> [148]	3.9	17	4.3
Kang <i>et al.</i> [163]	3.8	4.2	1.1
Teepe <i>et al.</i> [328]	3.6	10	2.8
Pfeifer and Sanchez [329]	3.6	12	3.3
Xu <i>et al.</i> [330]	3.5	12	3.4
Zimmermann <i>et al.</i> [331]	1	2.4	2.4

Table 2-1. Characteristics of a selected Gas-Phase Miniaturized IMS Instruments.

References

1. Rontgen, W.C., *On a New Kind of Rays*. Science, 1896. **3**(59): p. 227-231.
2. Langevin, M.P., *Une formule fondamentale de théorie cinétique*. Annales de Chimie et de Physique, 1905. **8**(5): p. 245-288.
3. Langevin, M.P., *L'ionisation des gaz*. Annales de Chimie et de Physique, 1903. **7**(28): p. 289-384.
4. Cohen, M.J. and F.W. Karasek, *Plasma chromatograph - a new dimension for gas chromatography and mass spectrometry*. Journal of Chromatographic Science, 1970. **8**: p. 330-337.
5. Karasek, F.W., *Plasma chromatography*. Analytical Chemistry, 1974. **46**: p. 710A.
6. Carr, T.W., ed. *Plasma Chromatography*. 1984, Plenum Press: New York.
7. Lubman, D.M. and M.N. Kronick, *Plasma chromatography with laser-produced ions*. Analytical Chemistry, 1982. **54**: p. 1546-1551.
8. Borsdorf, H. and G.A. Eiceman, *Ion mobility spectrometry: Principles and applications*. Applied Spectroscopy Reviews, 2006. **41**(4): p. 323-375.
9. Yamaguchi, S., et al., *Detection performance of a portable ion mobility spectrometer with ^{63}Ni radioactive ionization for chemical warfare agents*. Forensic Toxicology, 2010. **28**(2): p. 84-95.

10. Spangler, G.E., J.P. Carrico, and D.N. Campbell, *Recent advances in ion mobility spectrometry for explosives vapor detection*. Journal of Testing and Evaluation, 1985. **13**: p. 234-240.
11. Guo, Y., M.Q. Lu, and Y.T. Long, *Ion mobility spectra of selected amines and their application in field testing with the use of a portable IMS device*. Field Analytical Chemistry and Technology, 1997. **1**(4): p. 195-211.
12. Hübner, T., C. Tiebe, and I. Stephan, *Detection of fungal infestations of wood by ion mobility spectrometry*. International Biodeterioration & Biodegradation, 2011. **65**(5): p. 675-681.
13. Eiceman, G.A., A.P. Snyder, and D.A. Blyth, *Monitoring of Airborne Organic Vapors using Ion Mobility Spectrometry*. International Journal of Environmental Analytical Chemistry, 1990. **38**(3): p. 415-425.
14. Eiceman, G.A., *Advances in Ion Mobility Spectrometry - 1980-1990*. Critical Reviews in Analytical Chemistry, 1991. **22**(1-2): p. 17-36.
15. Eiceman, G.A. and Z. Karpas, 2005, *Ion Mobility Spectrometry*. 2nd ed. Boca Raton: CRC Press.
16. Mäkinen, M.A., O.A. Anttalainen, and M.E.T. Sillanpää, *Ion Mobility Spectrometry and Its Applications in Detection of Chemical Warfare Agents*. Analytical Chemistry, 2010. **82**(23): p. 9594-9600.
17. Tuovinen, K., H. Paakkanen, and O. Hänninen, *Determination of soman and VX degradation products by an aspiration ion mobility spectrometry*. Analytica Chimica Acta, 2001. **440**: p. 151-159.
18. Mäkinen, M., M. Nousiainen, and M. Sillanpää, *Ion spectrometric detection technologies for ultra-traces of explosives: A review*. Mass Spectrometry Reviews, 2011. **30**(5): p. 940-973.
19. Ewing, R.G., et al., *A critical review of ion mobility spectrometry for the detection of explosives and explosive related compounds*. Talanta, 2001. **54**(3): p. 515-529.
20. Hilton, C.K., et al., *Improved analysis of explosives samples with electrospray ionization-high resolution ion mobility spectrometry (ESI-HRIMS)*. International Journal of Mass Spectrometry, 2010. **298**(1-3): p. 64-71.
21. Jiang, D., et al., *Research of IMS technology and its application in narcotic drugs and explosives detection*. Tongweisu, 2005. **18**(1-2): p. 51-54.
22. Räsänen, R.-M., et al., *Determination of gas phase triacetone triperoxide with aspiration ion mobility spectrometry and gas chromatography-mass spectrometry*. Analytica Chimica Acta, 2008. **623**(1): p. 59-65.
23. Eiceman, G.A., M.E. Fleischer, and C.S. Leasure, *Sensing of petrochemical fuels in soils using headspace analysis with photoionization-ion mobility spectrometry*. International Journal of Environmental Analytical Chemistry, 1987. **28**: p. 279-296.
24. Reategui, J. and T. Bacon, *Applications of ion mobility spectrometry in environmental monitoring of hazardous chemical vapors*. Analysis Division Symposium, 1991. **25**: p. 189-203.
25. Baumbach, J.I., et al., *Ion Mobility Sensor in Environmental Analytical-Chemistry - Concept and 1st Results*. International Journal of Environmental Analytical Chemistry, 1993. **52**(1-4): p. 189-193.
26. Leonhardt, J.W., W. Rohrbeck, and H. Bensch, *A high resolution IMS for environmental studies*. International Journal for Ion Mobility Spectrometry, 2000. **3**(1): p. 43-49.
27. Dwivedi, P., et al., *Electrospray ionization-ion mobility spectrometry: a rapid analytical method for aqueous nitrate and nitrite analysis*. Analyst, 2004. **129**(2): p. 139-144.
28. Li, F., et al., *Ion mobility spectrometer for online monitoring of trace compounds*. Spectrochimica Acta Part B: Atomic Spectroscopy 2002. **57**(10): p. 1563-1574.
29. Márquez-Sillero, I., et al., *Ion-mobility spectrometry for environmental analysis*. TrAC Trends in Analytical Chemistry, 2011. **30**(5): p. 677-690.
30. Tuovinen, K., H. Paakkanen, and O. Hanninen, *Detection of pesticides from liquid matrices by ion mobility spectrometry*. Analytica Chimica Acta, 2000. **404**(1): p. 7-17.
31. Tuovinen, K., et al., *Ion Mobility Spectrometric Monitoring of Phosdrin® from Foliage in Greenhouse*. AIHAJ - American Industrial Hygiene Association, 2001. **62**(1): p. 80-86.
32. Chaim, W., Z. Karpas, and A. Lorber, *New technology for diagnosis of bacterial vaginosis*. European Journal of Obstetrics Gynecology and Reproductive Biology, 2003. **111**(1): p. 83-87.

33. Baumbach, J.I. and M. Westhoff, *Ion mobility spectrometry to detect lung cancer and airway infections*. Spectroscopy Europe, 2006. **18**(6): p. 22-27.
34. Baumbach, J.I., et al., *Breath Discovery based on Ion Mobility Spectrometry and Classification and Differentiation Models for Lung Diseases*. Biomedizinische Technik, 2010. **55**(Suppl. 1).
35. Likar, M.D., et al., *Rapid identification and absence of drug tests for AG-013736 in 1 mg Axitinib tablets by ion mobility spectrometry and DART™ mass spectrometry*. Journal of Pharmaceutical and Biomedical Analysis, 2011. **55**(3): p. 569-573.
36. Ruzsanyi, V., et al., *Detection of human metabolites using multi-capillary columns coupled to ion mobility spectrometers*. Journal of Chromatography A, 2005. **1084**(1-2): p. 145-151.
37. Ells, B., et al., *Trace level determination of perchlorate in water matrices and human urine using ESI-FAIMS-MS*. Journal of Environmental Monitoring, 2000. **2**(5): p. 393-397.
38. Karpas, Z., et al., *Diagnosis of vaginal infections by ion mobility spectrometry*. International Journal for Ion Mobility Spectrometry, 2002. **5**(3): p. 49-54.
39. Krebs, M.D., et al., *Detection of Biological and Chemical Agents Using Differential Mobility Spectrometry (DMS) Technology*. IEEE Sensors Journal, 2005. **5**(4): p. 696-703.
40. Verbeck, G.F., et al., *A Fundamental Introduction to Ion Mobility Mass Spectrometry Applied to the Analysis of Biomolecules*. Journal of Biomolecular Techniques, 2002. **13**(2): p. 56-61.
41. Snyder, A.P., et al., *Correlation of mass spectrometry identified bacterial biomarkers from a fielded pyrolysis-gas chromatography-ion mobility spectrometry biodetector with the microbiological gram stain classification scheme*. Analytical Chemistry, 2004. **76**(21): p. 6492-6499.
42. Lokhnauth, J.K. and N.H. Snow, *Solid-phase micro-extraction coupled with ion mobility spectrometry for the analysis of ephedrine in urine*. Journal of Separation Science, 2005. **28**(7): p. 612-618.
43. Wang, Y., S. Nacson, and J. Pawliszyn, *The coupling of solid-phase microextraction/surface enhanced laser desorption/ionization to ion mobility spectrometry for drug analysis*. Analytica Chimica Acta, 2007. **582**(1): p. 50-54.
44. Lu, Y., R.M. O'Donnell, and P.B. Harrington, *Detection of cocaine and its metabolites in urine using solid phase extraction-ion mobility spectrometry with alternating least squares*. Forensic Science International, 2009. **189**(1-3): p. 54-59.
45. Jafari, M.T. and M. Javaheri, *Selective Method Based on Negative Electrospray Ionization Ion Mobility Spectrometry for Direct Analysis of Salivary Thiocyanate*. Analytical Chemistry, 2010. **82**(15): p. 6721-6725.
46. Fernández-Maestre, R. and H. Hill, *Ion mobility spectrometry for the rapid analysis of over-the-counter drugs and beverages*. International Journal for Ion Mobility Spectrometry, 2009. **12**(3): p. 91-102.
47. Vautz, W., J.I. Baumbach, and J. Jung, *Beer fermentation control using ion mobility spectrometry - Results of a pilot study*. Journal of the Institute of Brewing, 2006. **112**(2): p. 157-164.
48. Vautz, W., et al., *Ion mobility spectrometry for food quality and safety*. Food Additives and Contaminants, 2006. **23**(11): p. 1064-1073.
49. Bota, G.M. and P.B. Harrington, *Direct detection of trimethylamine in meat food products using ion mobility spectrometry*. Talanta, 2006. **68**(3): p. 629-635.
50. Vautz, W. and J.I. Baumbach, *Analysis of bio-processes using ion mobility spectrometry*. Engineering in Life Sciences, 2008. **8**(1): p. 19-25.
51. Menendez, M., et al., *Direct determination of volatile analytes from solid samples by UV-ion mobility spectrometry*. Journal of Chromatography A, 2008. **1215**(1-2): p. 8-14.
52. Raatikainen, O., et al., *Ion mobility spectrometry based gas detector MGD-1: applications to food process monitoring and food quality assessment*. International Journal for Ion Mobility Spectrometry, 2007. **10**(1): p. 38-43.
53. Raatikainen, O., et al., *Multivariate modelling of fish freshness index based on ion mobility spectrometry measurements*. Analytica Chimica Acta, 2005. **544**(1-2): p. 128-134.
54. Baumbach, J.I., *Process analysis using ion mobility spectrometry*. Analytical and Bioanalytical Chemistry, 2006. **384**(5): p. 1059-1070.
55. Trimpin, S., et al., *Resolving Oligomers from Fully Grown Polymers with IMS-MS*. Analytical Chemistry, 2007. **79**(21): p. 7965-7974.

56. Scott, C.D., et al., *Characterization of Large Fullerenes in Single-Wall Carbon Nanotube Production by Ion Mobility Mass Spectrometry*. The Journal of Physical Chemistry C, 2006. **111**(1): p. 36-44.
57. Trimpin, S. and D.E. Clemmer, *Ion Mobility Spectrometry/Mass Spectrometry Snapshots for Assessing the Molecular Compositions of Complex Polymeric Systems*. Analytical Chemistry, 2008. **80**(23): p. 9073-9083.
58. Song, J., et al., *High-Resolution Ion Mobility Spectrometry–Mass Spectrometry on Poly(methyl methacrylate)*. Angewandte Chemie International Edition, 2010. **49**(52): p. 10168-10171.
59. Verkouteren, J.R. and J.L. Staymates, *Reliability of ion mobility spectrometry for qualitative analysis of complex, multicomponent illicit drug samples*. Forensic Science International, 2011. **206**(1–3): p. 190-196.
60. Keller, T., et al., *Detection of methamphetamine, MDMA and MDEA in human hair by means of ion mobility spectrometry (IMS)*. International Journal for Ion Mobility Spectrometry, 1998. **1**(1): p. 38-42.
61. Keller, T., et al., *Ion mobility spectrometry for the detection of drugs in cases of forensic and criminalistic relevance*. International Journal for Ion Mobility Spectrometry, 1999. **2**(1): p. 22-34.
62. Rasulev, U.K., et al., *Atmosphere pressure surface ionization indicator of narcotics*. International Journal for Ion Mobility Spectrometry, 2001. **4**(2): p. 121-125.
63. Kudriavtseva, S., et al., *Detection of drugs of abuse in sweat using ion trap mobility spectrometry*. International Journal for Ion Mobility Spectrometry, 2004. **7**(2): p. 39-46.
64. Kanu, A.B. and H.H. Hill Jr, *Identity confirmation of drugs and explosives in ion mobility spectrometry using a secondary drift gas*. Talanta, 2007. **73**(4): p. 692-699.
65. Palmer, P.T. and T.F. Limerio, *Mass Spectrometry in the U.S. Space Program: Past, Present and Future*. American Society for Mass Spectrometry, 2001: p. 656-675.
66. Eiceman, G.A., et al., *Monitoring volatile organic compounds in ambient air inside and outside buildings with the use of a radio-frequency-based ion-mobility analyzer with a micromachined drift tube*. Field Analytical Chemistry and Technology, 2000. **4**(6): p. 297-308.
67. Smiths Detection. *CAM and IONSCAN*. [cited 2008 1st February]; Available from: <http://www.smithsdetection.com/>.
68. Harden, C.S., *Ion mobility spectrometry for detection of chemical warfare agents 1960's to the present*. International Journal for Ion Mobility Spectrometry, 2004. **7**(1): p. 30-37.
69. Li, F., et al., *UV-ion mobility spectrometer coupled to mass spectrometer*. International Journal for Ion Mobility Spectrometry, 2001. **4**(2): p. 100-103.
70. Bowers, W.D., et al., *Trace impurities in solvents commonly used for gas-chromatographic analysis of environmental-samples*. Journal of Chromatography, 1981. **206**(2): p. 279-288.
71. Eiceman, G.A., R.E. Clement, and F.W. Karasek, *Analysis of fly-ash from municipal incinerators for trace organic-compounds*. Analytical Chemistry, 1979. **51**(14): p. 2343-2350.
72. Schwarz, K., W. Filipiak, and A. Amann, *Determining concentration patterns of volatile compounds in exhaled breath by PTR-MS*. Journal of Breath Research, 2009. **3**: p. 1-15.
73. Webster, G., *Evolution of IMS technology within the Australian Customs Service*. International Journal for Ion Mobility Spectrometry, 2001. **4**(1): p. 65-66.
74. Kotiaho, T., F.R. Lauritzen, and H. Degn, *Membrane Inlet Ion Mobility Spectrometry for On-Line Measurement of Ethanol in Beer and in Yeast Fermentation*. Analytica Chimica Acta, 1995. **309**: p. 317-325.
75. Vautz, W. and J.I. Baumbach, *Exemplar application of multi-capillary column ion mobility spectrometry for biological medical purpose*. International Journal for Ion Mobility Spectrometry, 2008. **11**(1): p. 35-42.
76. Ruzsanyi, V., J.I. Baumbach, and G.A. Eiceman, *Detection of the mold markers using Ion Mobility Spectrometry*. International Journal for Ion Mobility Spectrometry, 2003. **6**(2): p. 53-58.
77. Prasad, S., et al., *Analysis of bacteria by pyrolysis gas chromatography-differential mobility spectrometry and isolation of chemical components with a dependence on growth temperature*. Analyst, 2007. **132**(10): p. 1031-1039.

78. Prasad, S., et al., *Analysis of bacterial strains with pyrolysis-gas chromatography/differential mobility spectrometry*. *Analyst*, 2006. **131**(11): p. 1216-1225.
79. Karpas, Z., et al., *Determination of volatile biogenic amines in muscle food products by ion mobility spectrometry*. *Analytica Chimica Acta*, 2002. **463**(2): p. 155-163.
80. Harrington, P.d.B., T.L. Buxton, and G. Chen, *Classification of Bacteria by Thermal Methylation Hydrolysis Ion Mobility Spectrometry Using SIMPLISMA and Multidimensional Wavelet Compression*. *International Journal for Ion Mobility Spectrometry*, 2001. **4**(2): p. 148-151.
81. Shnayderman, M., et al., *Species-Specific Bacteria Identification Using Differential Mobility Spectrometry and Bioinformatics Pattern Recognition*. *Analytical Chemistry*, 2005. **77**(18): p. 5930-5937.
82. Basanta, M., T. Koimtzis, and C.L.P. Thomas, *Sampling and analysis of Exhaled Breath on human subjects with thermal desorption Gas Chromatography-Differential Mobility Spectrometry*. *International Journal for Ion Mobility Spectrometry*, 2006. **9**(1): p. 45-49.
83. Westhoff, M., et al., *Differentiation of chronic obstructive pulmonary disease (COPD) including lung cancer from healthy control group by breath analysis using ion mobility spectrometry* *International Journal for Ion Mobility Spectrometry*, 2010. **13**(3-4): p. 131-139.
84. Vautz, W., et al., *Breath sampling control for medical application*. *International Journal for Ion Mobility Spectrometry*, 2010. **13**(1): p. 41-46.
85. Vautz, W., et al., *An Implementable Approach to Obtain Reproducible Reduced Ion Mobility*. *International Journal for Ion Mobility Spectrometry*, 2009. **12**: p. 47-57.
86. Perl, T., et al., *Determination of serum propofol concentrations by breath analysis using ion mobility spectrometry*. *British Journal of Anaesthesia*, 2009. **103**(6): p. 822-827.
87. Baumbach, J.I., et al., *Early detection of lung cancer: Metabolic profiling of human breath with ion mobility spectrometers*, in *Modern Biopharmaceuticals*, J. Knäblein, Editor 2005, Wiley-VCH Weinheim p. 1343-1358.
88. Jünger, M., B. Bödeker, and J.I. Baumbach, *Peak assignment in multi-capillary column - ion mobility spectrometry using comparative studies with gas chromatography - mass spectrometry for exhaled breath analysis*. *Analytical and Bioanalytical Chemistry*, 2010. **396**(1): p. 471-482.
89. Bessa, V., et al., *Detection of Volatile Organic Compounds (VOCs) in exhaled breath of patients with Chronic Obstructive Pulmonary Disease (COPD)*. *International Journal for Ion Mobility Spectrometry*, 2011.
90. Basanta, M., et al., *Non-invasive metabolomic analysis of breath using differential mobility spectrometry in patients with chronic obstructive pulmonary disease and healthy smokers*. *Analyst*, 2010. **135**(2): p. 315-320.
91. Hill, H.H., et al., *Ion Mobility Spectrometry*. *Analytical Chemistry*, 1990. **62**(23): p. 1201A-1209A.
92. Shvartsburg, A.A. and R.D. Smith, *Fundamentals of Traveling Wave Ion Mobility Spectrometry*. *Analytical Chemistry*, 2008. **80**(24): p. 9689-9699.
93. Smith, D., et al., *Deciphering drift time measurements from travelling wave ion mobility spectrometry-mass spectrometry studies*. *European Journal of Mass Spectrometry*, 2009. **15**(2): p. 113-130.
94. Giles, K., et al., *A method for direct measurement of ion mobilities using a travelling wave ion guide*. *International Journal of Mass Spectrometry*, 2010. **298**(1-3): p. 10-16.
95. Giles, K., et al., *Applications of a travelling wave-based radio-frequency only stacked ring ion guide*. *Rapid Communications in Mass Spectrometry*, 2004. **18**(20): p. 2401-2414.
96. Sacristan, E. and A.A. Solis, *A swept-field aspiration condenser as an ion-mobility spectrometer*. *IEEE Transactions on Instrumentation and Measurement*, 1998. **47**(3): p. 769-775.
97. Zimmermann, S., et al., *An ion-focusing aspiration condenser as an ion mobility spectrometer*. *Sensors and Actuators B: Chemical*, 2007. **125**(2): p. 428-434.
98. Kotiaho, T. and H. Paakkanen. 1996. *Method for measurement of analytes by ion mobility spectrometry*. US Patent: 9618893.
99. Zimmermann, S. and S. Barth, *A Miniaturized Ion Mobility Spectrometer for Detection of Hazardous Compounds in Air*. *IEEE Sensors Journal*, 2007: p. 1501-1504.

100. Knudsen, E. and S. Israelsson, *Mobilities of small ions in the atmospheric surface layer*. Pure and Applied Geophysics, 1975. **113**(1): p. 525-533.
101. Intra, P. and N. Tippayawong, *An overview of differential mobility analyzers for size classification of nanometer-sized aerosol particles*. Songklanakarin Journal of Science and Technology, 2008. **30**(2): p. 243-256.
102. Rus, J., et al., *IMS-MS studies based on coupling a differential mobility analyzer (DMA) to commercial API-MS systems*. International Journal of Mass Spectrometry, 2010. **298**(1-3): p. 30-40.
103. Hogan Jr, C.J. and J. Fernandez de la Mora, *Ion-Pair Evaporation from Ionic Liquid Clusters*. Journal of the American Society for Mass Spectrometry, 2010. **21**(8): p. 1382-1386.
104. Hogan Jr, C.J. and J. Fernandez de la Mora, *Tandem ion mobility-mass spectrometry (IMS-MS) study of ion evaporation from ionic liquid-acetonitrile nanodrops*. Physical Chemistry Chemical Physics, 2009. **11**(36): p. 8079-8090.
105. Hogan, C.J., et al., *Tandem Differential Mobility Analysis-Mass Spectrometry Reveals Partial Gas-Phase Collapse of the GroEL Complex*. The Journal of Physical Chemistry B, 2011. **115**(13): p. 3614-3621.
106. Santos, J.P., et al., *Performance evaluation of a high-resolution parallel-plate differential mobility analyzer*. Atmospheric Chemistry and Physics, 2009. **9**(7): p. 2419-2429.
107. Ioner (Ramem S.A.). *High Resolution IMS*. [cited 2013 30th May]; Available from: <http://www.ioner.eu/index.php/ion-mobility-spectrometer/hrims.html>.
108. Owlstone Nanotech INC, *Ion Mobility Mass Spectrometry: The Next Five Years*, 2012. Available from: http://www.owlstonenanotech.com/ultrafaims/imsms-news/ebook-next-5-years?utm_source=IMS-in-spain&utm_medium=blog-post&utm_campaign=IMSebook.
109. Vidal-de-Miguel, G., M. Macia, and J. Cuevas, *Transversal Modulation Ion Mobility Spectrometry (TM-IMS), A New Mobility Filter Overcoming Turbulence Related Limitations*. Analytical Chemistry, 2012. **84**(18): p. 7831-7837.
110. Buryakov, I.A., et al., *A New Method of Separation of Multi-Atomic Ions by Mobility at Atmospheric-Pressure Using a High-Frequency Amplitude-Asymmetric Strong Electric-Field*. International Journal of Mass Spectrometry and Ion Processes, 1993. **128**(3): p. 143-148.
111. Borsdorf, H. and T. Mayer, *Electric field dependence of ion mobilities of aromatic compounds with different ionic mass and different functional groups*. International Journal for Ion Mobility Spectrometry, 2010. **13**(3-4): p. 103-108.
112. Baumbach, J.I. and G.A. Eiceman, *Ion Mobility Spectrometry: Arriving On Site and Moving Beyond a Low Profile*. Applied Spectroscopy, 1999. **53**(9): p. 338A-355A.
113. Collins, D.C. and M.L. Lee, *Developments in ion mobility spectrometry-mass spectrometry*. Analytical and Bioanalytical Chemistry, 2002. **372**(1): p. 66-73.
114. Eiceman, G.A., *Ion-mobility spectrometry as a fast monitor of chemical composition*. TrAC Trends in Analytical Chemistry, 2002. **21**(4): p. 259-275.
115. Miller, R.A., et al., *A novel micromachined high-field asymmetric waveform-ion mobility spectrometer*. Sensors and Actuators B: Chemical, 2000. **67**(3): p. 300-306.
116. Guevremont, R. and R.W. Purves, *Atmospheric pressure ion focusing in a high-field asymmetric waveform ion mobility spectrometer*. Review of Scientific Instruments, 1999. **70**(2): p. 1370-1383.
117. Salleras, M., et al., *Electrostatic shutter design for a miniaturized ion mobility spectrometer*. Sensors and Actuators B: Chemical, 2006. **118**(1-2): p. 338-342.
118. Shvartsburg, A.A., 2009, *Differential Ion Mobility Spectrometry: Nonlinear Ion Transport and Fundamentals of FAIMS*. First ed. Boca Raton, FL: CRC Press.
119. Kolakowski, B.M. and Z. Mester, *Review of applications of high-field asymmetric waveform ion mobility spectrometry (FAIMS) and differential mobility spectrometry (DMS)*. Analyst, 2007. **132**(9): p. 842-864.
120. Arce, L., et al., *Sample-introduction systems coupled to ion-mobility spectrometry equipment for determining compounds present in gaseous, liquid and solid samples*. TrAC Trends in Analytical Chemistry, 2008. **27**(2): p. 139-150.
121. Borsdorf, H., et al., *Corona discharge ion mobility spectrometry of aliphatic and aromatic hydrocarbons*. Analytica Chimica Acta, 2000. **403**(1-2): p. 235-242.
122. Owlstone Nanotech INC, *Whitepaper - Generating Calibration Gas Standards with OVG-4 and Permeation Tubes*, v 1.0.

123. Borsdorf, H., et al., *Rapid on-site determination of chlorobenzene in water samples using ion mobility spectrometry*. *Analytica Chimica Acta*, 2001. **440**(1): p. 63-70.
124. Seto, Y., *Determination of volatile substances in biological samples by headspace gas chromatography*. *Journal of Chromatography A*, 1994. **674**(1-2): p. 25-62.
125. Karpas, Z., *Ion mobility spectrometry of aliphatic and aromatic amines*. *Analytical Chemistry*, 1989. **61**: p. 684-689.
126. Strachan, N.J.C., F.J. Nicholson, and I.D. Ogden, *An automated sampling system using ion mobility spectrometry for the rapid detection of bacteria*. *Analytica Chimica Acta*, 1995. **313**: p. 63-67.
127. Criado-García, L., et al., *A comparative study between different alternatives to prepare gaseous standards for calibrating UV-Ion Mobility Spectrometers*. *Talanta*, 2013. **111**(0): p. 111-118.
128. Nazarov, E.G., et al., *Miniature Differential Mobility Spectrometry Using Atmospheric Pressure Photoionization*. *Analytical Chemistry*, 2006. **78**(13): p. 4553-4563.
129. Jazan, E. and M. Tabrizchi, *Kinetic study of proton-bound dimer formation using ion mobility spectrometry*. *Chemical Physics*, 2009. **355**(1): p. 37-42.
130. Puton, J., M. Nousiainen, and M. Sillanpää, *Ion mobility spectrometers with doped gases*. *Talanta*, 2008. **76**(5): p. 978-987.
131. Eiceman, G.A. and J.A. Stone, *Ion mobility spectrometers in national defense*. *Analytical Chemistry*, 2004. **76**(21): p. 390A-397A.
132. Leonhardt, M.J., J.W. Leonhardt, and H. Bensch, *Mobilities of halogenated compounds*. *International Journal for Ion Mobility Spectrometry*, 2002. **5**(1): p. 43-46.
133. Bell, A.J., et al., *Studies on gas-phase positive ion-molecule reactions initiated by proton transfer to alcohols: the reactions of 2-methyl-2-propanol (t-butyl alcohol) with H₃O⁺ in a Fourier transform mass spectrometer (FTMS)*. *International Journal of Mass Spectrometry and Ion Processes*, 1997. **165-166**: p. 169-178.
134. Vandiver, V.J., C.S. Leasure, and G.A. Eiceman, *Proton affinity equilibria for polycyclic aromatic-hydrocarbons at atmospheric-pressure in ion mobility spectrometry*. *International Journal of Mass Spectrometry and Ion Processes*, 1985. **66**(2): p. 223-238.
135. Kim, S.H., K.R. Betty, and F.W. Karasek, *Plasma chromatography of benzene with mass identified mobility spectra*. *Analytical Chemistry*, 1978. **50**: p. 1784-1788.
136. Bell, A.J., et al., *Studies on gas-phase positive ion-molecule reactions of relevance to ion mobility spectrometry The reactions of 2-methyl-2-propanol (t-butyl alcohol) with protonated water clusters in an ion mobility system*. *International Journal of Mass Spectrometry and Ion Processes*, 1998. **173**(1-2): p. 65-70.
137. Giles, K. and E.P. Grimsrud, *The Kinetic Ion Mobility Mass-Spectrometer - Measurements of Ion Molecule Reaction-Rate Constants at Atmospheric-Pressure*. *Journal of Physical Chemistry*, 1992. **96**(16): p. 6680-6687.
138. Sahlstrom, K.E., W.B. Knighton, and E.P. Grimsrud, *Reaction of chloride ion with isopropyl bromide at atmospheric pressure by ion mobility spectrometry*. *Journal of Physical Chemistry A*, 1997. **101**(8): p. 1501-1508.
139. Eiceman, G.A., et al., *Positive Reactant Ion Chemistry for Analytical, High Temperature Ion Mobility Spectrometry (IMS): Effects of Electric Field of the Drift Tube and Moisture, Temperature, and Flow of the Drift Gas*. *International Journal for Ion Mobility Spectrometry*, 1998. **1**(1): p. 28-37.
140. Munro, W.A., C.L.P. Thomas, and M.L. Langford, *Characterisation of the Ion Mobility Spectrometric Behaviour of a Dinitrobutane Under Varying Conditions of Temperature and Concentration*. *Analytica Chimica Acta*, 1998. **375**: p. 49-63.
141. Lubman, D.M., *Temperature-Dependence of Plasma Chromatography of Aromatic-Hydrocarbons*. *Analytical Chemistry*, 1984. **56**(8): p. 1298-1302.
142. Bensch, H., *The RIP positions in dependence on the moisture*. *International Journal for Ion Mobility Spectrometry* 2002. **5**(1): p. 39-42.
143. Itoh, K., M. Nishikawa, and R. Holroyd, *Electron attachment to toluene in n-Hexane and 2,2-Dimethylbutane at high pressure*. *Journal of Chemical Physics*, 1993. **97**: p. 503-507.
144. Makela, J.M., et al., *Comparison of mobility equivalent diameter with Kelvin-Thomson diameter using ion mobility data*. *Journal of Chemical Physics*, 1996. **105**(4): p. 1562-1571.

145. Ewing, R.G., et al., *Ionization mechanisms of chlorinated ethanes with relevance to the production of molecular ion species*. International Journal for Ion Mobility Spectrometry, 2001. **4**(2): p. 1-4.
146. Tabrizchi, M. and A. Abedi, *A novel electron source for negative ion mobility spectrometry*. International Journal of Mass Spectrometry, 2002. **218**(1): p. 75-85.
147. Sielemann, S., et al., *Detection of trans-1,2-dichloroethene, trichloroethene and tetrachloroethene using Multi-Capillary Columns Coupled to Ion Mobility Spectrometers with UV-Ionisation Sources*. International Journal for Ion Mobility Spectrometry, 1999. **2**(1): p. 15-21.
148. Baumbach, J.I., S. Sielemann, and P. Pilzecker, *Coupling of Multi-Capillary Columns with two Different Types of Ion Mobility Spectrometer*. International Journal for Ion Mobility Spectrometry, 2000. **3**(1): p. 28-37.
149. Sielemann, S., et al., *Quantitative analysis of benzene, toluene, and m-xylene with the use of a UV-ion mobility spectrometer*. Field Analytical Chemistry and Technology, 2000. **4**(4): p. 157-169.
150. Karpas, Z., Y.F. Wang, and G.A. Eiceman, *Qualitative and quantitative response characteristics of a capillary gas-chromatograph ion mobility spectrometer to halogenated compounds*. Analytica Chimica Acta, 1993. **282**(1): p. 19-31.
151. Bell, S.E., et al., *Atmospheric-Pressure Chemical-Ionization of Alkanes, Alkenes, and Cycloalkanes*. Journal of the American Society for Mass Spectrometry, 1994. **5**(3): p. 177-185.
152. Bell, S.E., et al., *Atmospheric Pressure Chemical Ionization of Alkanes, Alkenes, and Cycloalkanes - ERRATUM*. Journal of the American Society for Mass Spectrometry, 1994. **5**(11): p. 1026-1026.
153. Eiceman, G.A., et al., *Atmospheric pressure chemical ionization of fluorinated phenols in atmospheric pressure chemical ionization mass spectrometry, tandem mass spectrometry, and ion mobility spectrometry*. Journal of the American Society for Mass Spectrometry, 1999. **10**(11): p. 1157-1165.
154. Daum, K.A., D.A. Atkinson, and R.G. Ewing, *The role of oxygen in the formation of TNT product ions mobility spectrometry*. International Journal for Ion Mobility Spectrometry, 2001. **4**(1): p. 179-180.
155. Cravath, A.M., *The rate of formation of negative ions by electron attachment*. Physical Review, 1929. **33**: p. 605-13.
156. Spangler, G.E. and C.I. Collins, *Reactant ions in negative ion plasma chromatography*. Analytical Chemistry, 1975. **47**: p. 393-402.
157. Leonhardt, J.W., *New detectors in environmental monitoring using tritium sources*. Journal of Radioanalytical and Nuclear Chemistry-Articles, 1996. **206**(2): p. 333-339.
158. Yun, C.M., Y. Otani, and H. Emi, *Development of unipolar ion generator - Separation of ions in axial direction of flow*. Aerosol Science and Technology, 1997. **26**(5): p. 389-397.
159. Paakanen, H., *About the applications of IMCELL™ MGD-1 Detector*. International Journal for Ion Mobility Spectrometry, 2001. **4**(2): p. 136-139.
160. Pfeifer, K.B., et al., *Development of Rolled Miniature Drift Tubes Using Low Temperature Co-Fired Ceramics (LTCC)*. International Journal for Ion Mobility Spectrometry, 2004. **7**(2): p. 47-53.
161. Laakia, J., et al., *Separation of Different Ion Structures in Atmospheric Pressure Photoionization-Ion Mobility Spectrometry-Mass Spectrometry (APPI-IMS-MS)*. Journal of the American Society for Mass Spectrometry, 2010. **21**(9): p. 1565-1572.
162. Borsdorf, H., E.G. Nazarov, and G.A. Eiceman, *Atmospheric pressure chemical ionization studies of non-polar isomeric hydrocarbons using ion mobility spectrometry and mass spectrometry with different ionization techniques*. Journal of the American Society for Mass Spectrometry, 2002. **13**(9): p. 1078-1087.
163. Kang, W.J., et al., *Miniaturized Ion Mobility Spectrometer (μ IMS) with UV-Lamp as a Photoionization Source*. International Journal for Ion Mobility Spectrometry, 2001. **4**(2): p. 108-111.
164. Vautz, W., S. Sielemann, and J.I. Baumbach, *Determination of terpenes in humid ambient air using ultraviolet ion mobility spectrometry*. Analytica Chimica Acta, 2004. **513**(2): p. 393-399.

165. Perkin Elmer Optoelectronics. *Low Pressure Gas Discharge Lamps for Photoionization Detectors*. [cited 2013 10th May]; Available from: www.perkinelmer.com/opto.
166. NIST. *Chemistry WebBook*. [cited 2013 18th March]; Available from: <http://webbook.nist.gov/chemistry>.
167. Hill, C.A. and C.L.P. Thomas, *A pulsed corona discharge switchable high resolution ion mobility spectrometer-mass spectrometer*. *Analyst*, 2003. **128**(1): p. 55-60.
168. Tabrizchi, M. and T. Khayamian, *Ion mobility spectrometry in helium with corona discharge ionization source*. *International Journal for Ion Mobility Spectrometry*, 2001. **4**(1): p. 52-56.
169. Xu, J., et al., *A Miniature Ion Mobility Spectrometer with a Pulsed Corona-Discharge Ion Source*. *International Journal for Ion Mobility Spectrometry*, 2001. **4**(1): p. 3-6.
170. Ross, S.K. and A.J. Bell, *Reverse flow continuous corona discharge ionisation applied to ion mobility spectrometry*. *International Journal of Mass Spectrometry*, 2002. **218**(2): p. L1-L6.
171. Hill, C. and C.L.P. Thomas, *Pulsed Corona Discharge: a Replacement for ⁶³Ni in Ion Mobility Sources?* *International Journal for Ion Mobility Spectrometry*, 2003. **6**(1): p. 4-8.
172. Borsdorf, H., J.A. Stone, and G.A. Eiceman, *Gas phase studies on terpenes by ion mobility spectrometry using different atmospheric pressure chemical ionization techniques*. *International Journal of Mass Spectrometry*, 2005. **246**(1-3): p. 19-28.
173. Tabrizchi, M. and A. Abedi, *Negative Corona Discharge Ionization Source for Ion Mobility Spectrometry*. *International Journal for Ion Mobility Spectrometry*, 2002. **5**(1): p. 51-54.
174. Borsdorf, H., et al., *Determination of n-alkanes and branched chain alkanes by Corona discharge ion mobility spectrometry*. *International Journal for Ion Mobility Spectrometry*, 1999. **2**(1): p. 9-14.
175. Eiceman, G.A., et al., *Laser desorption and ionization of solid polycyclic aromatic hydrocarbons in air with analysis by ion mobility spectrometry*. *Analytical Letters*, 1988. **21**(4): p. 539-552.
176. Phillips, J. and J. Gormally, *The laser desorption of organic molecules in ion mobility spectrometry*. *International Journal of Mass Spectrometry and Ion Processes*, 1992. **112**(2-3): p. 205-214.
177. Bowers, M.T., et al., *Gas-Phase Ion Chromatography: Transition Metal State Selection and Carbon Cluster Formation*. *Science*, 1993. **260**(5113): p. 1446-1451.
178. Jarrold, M.F. and J.E. Bower, *Mobilities of metal cluster ions: Aluminum and the electronic shell model*. *Journal of Chemical Physics*, 1993. **98**(3): p. 2399-2407.
179. Roch, T. and J.I. Baumbach, *Laser-based ion mobility spectrometry as an analytical tool for soil analysis*. *International Journal for Ion Mobility Spectrometry*, 1998. **1**(1): p. 43-47.
180. Illenseer, C. and H.-G. Löhmannsröben, *Investigation of ion-molecule collisions with laser-based ion mobility spectrometry*. *Physical Chemistry Chemical Physics*, 2001. **3**(12): p. 2388-2393.
181. Young, D., et al., *Laser desorption-ionization of polycyclic aromatic hydrocarbons from glass surfaces with ion mobility spectrometry analysis*. *Analytica Chimica Acta*, 2002. **453**(2): p. 231-243.
182. Weis, P., et al., *A time-of-flight, drift cell, quadrupole apparatus for ion mobility measurements*. *International Journal of Mass Spectrometry*, 2002. **216**: p. 59-73.
183. Beitz, T., et al., *Ion Mobility Spectrometric Investigation of Aromatic Cations in the Gas Phase*. *Journal of Physical Chemistry A*, 2006. **110**(10): p. 3514-3520.
184. Eiceman, G.A., et al., *Ion mobility spectrometry of gas-phase ions from laser ablation of solids in air at ambient pressure*. *Applied Spectroscopy*, 2007. **61**(10): p. 1076-1083.
185. von Helden, G., T. Wyttenbach, and M.T. Bowers, *Inclusion of a MALDI ion source in the ion chromatography technique: conformational information on polymer and biomolecular ions*. *International Journal of Mass Spectrometry and Ion Processes*, 1995. **146-147**(0): p. 349-364.
186. Lee, S., T. Wyttenbach, and M.T. Bowers, *Gas phase structures of sodiated oligosaccharides by ion mobility/ion chromatography methods*. *International Journal of Mass Spectrometry and Ion Processes*, 1997. **167-168**(0): p. 605-614.
187. Gidden, J., et al., *Poly (ethylene terephthalate) oligomers cationized by alkali ions: Structures, energetics, and their effect on mass spectra and the matrix-assisted laser desorption/ionization process*. *Journal of the American Society for Mass Spectrometry*, 1999. **10**(9): p. 883-895.

188. Gillig, K.J., et al., *Coupling High-Pressure MALDI with Ion Mobility/Orthogonal Time-of-Flight Mass Spectrometry*. Analytical Chemistry, 2000. **72**(17): p. 3965-3971.
189. Bramwell, C.J., et al., *Atmospheric Pressure Matrix-Assisted Laser Desorption/Ionization Combined with Ion Mobility Spectrometry*. International Journal for Ion Mobility Spectrometry, 2002. **5**(3): p. 87-90.
190. Tong, H., et al., *Solid phase microextraction with matrix assisted laser desorption/ionization introduction to mass spectrometry and ion mobility spectrometry*. Analyst, 2002. **127**(9): p. 1207-1210.
191. Ruotolo, B.T., et al., *Analysis of protein mixtures by matrix-assisted laser desorption ionization-ion mobility-orthogonal-time-of-flight mass spectrometry*. International Journal of Mass Spectrometry, 2002. **219**(1): p. 253-267.
192. Steiner, W.E., et al., *Atmospheric pressure matrix-assisted laser desorption/ionization with analysis by ion mobility time-of-flight mass spectrometry*. Rapid Communications in Mass Spectrometry, 2004. **18**(8): p. 882-888.
193. Eiceman, G.A., D. Young, and G.B. Smith, *Mobility spectrometry of amino acids and peptides with matrix assisted laser desorption and ionization in air at ambient pressure*. Microchemical Journal, 2005. **81**(1): p. 108-116.
194. McLean, J.A., et al., *Ion mobility-mass spectrometry: a new paradigm for proteomics*. International Journal of Mass Spectrometry, 2005. **240**(3): p. 301-315.
195. Dwivedi, P., A.J. Schultz, and H.H.H. Jr, *Metabolic profiling of human blood by high-resolution ion mobility mass spectrometry (IM-MS)*. International Journal of Mass Spectrometry, 2010. **298**(1-3): p. 78-90.
196. Harkness, K.M., et al., *Surface Fragmentation of Complexes from Thiolate Protected Gold Nanoparticles by Ion Mobility-Mass Spectrometry*. Analytical Chemistry, 2010. **82**(7): p. 3061-3066.
197. Jackson, S.N., et al., *Gangliosides' analysis by MALDI-ion mobility MS*. Analyst, 2011. **136**(3): p. 463-466.
198. Chen, L., et al., *Molecular dynamics and ion mobility spectrometry study of model β -hairpin peptide, trpz1l*. Journal of Physical Chemistry A, 2011. **115**(17): p. 4427-35.
199. Wu, C., et al., *Surface ionization ion mobility spectrometry*. Analytical Chemistry, 1999. **71**(1): p. 273-278.
200. Rasulev, U.K., U. Khasanov, and V.V. Palitcin, *Surface-ionization methods and devices of indication and identification of nitrogen-containing base molecules*. Journal of Chromatography A, 2000. **896**(1-2): p. 3-18.
201. Rasulev, U.K., *A Study of a Surface-Ionization Source for IMS*. International Journal for Ion Mobility Spectrometry, 2001. **4**(2): p. 13-16.
202. Vautz, W., et al., *Detection of emission from material surfaces using ion mobility spectrometry*. International Journal for Ion Mobility Spectrometry, 2004. **7**(1): p. 25-29.
203. Kanu, A.B., P.E. Haigh, and H.H. Hill, *Surface detection of chemical warfare agent simulants and degradation products*. Analytica Chimica Acta, 2005. **553**(1-2): p. 148-159.
204. Vautz, W., J.I. Baumbach, and E. Uhde, *Detection of emissions from surfaces using ion mobility spectrometry*. Analytical and Bioanalytical Chemistry, 2006. **384**: p. 980-986.
205. Beegle, L.W. and I. Kanik, *Electrospray Ionization High-Resolution Ion Mobility Spectrometry for the Detection of Organic Compounds, I. Amino Acids*. Analytical Chemistry, 2001. **73**(13): p. 3028-3034.
206. Ells, B., et al., *Detection of Nine Chlorinated and Brominated Haloacetic Acids at Part-per-Trillion Levels Using ESI-FAIMS-MS*. Analytical Chemistry, 2000. **72**(19): p. 4555-4559.
207. Matz, L.M. and H.H. Hill, *Evaluation of Opiate Separation by High-Resolution Electrospray Ionization-Ion Mobility Spectrometry/Mass Spectrometry*. Analytical Chemistry, 2001. **73**(8): p. 1664-1669.
208. Matz, L.M. and H.H. Hill, *Evaluating the Separation of Amphetamines by Electrospray Ionization Ion Mobility Spectrometry/MS and Chrage Competition within the ESI Process*. Analytical Chemistry, 2002. **74**(2): p. 420-427.
209. Srebalus Barnes, C.A., et al., *Resolving Isomeric Peptide Mixtures: A Combined HPLC/Ion Mobility-TOFMS Analysis of a 4000-Component Combinatorial Library*. Analytical Chemistry, 2001. **74**(1): p. 26-36.

210. Dion, H.M., L.K. Ackerman, and H.H. Hill, *Detection of inorganic ions from water by electrospray ionization-ion mobility spectrometry*. *Talanta*, 2002. **57**(6): p. 1161-1171.
211. Wittmer, D., et al., *Electrospray-ionization ion mobility spectrometry*. *Analytical Chemistry*, 1994. **66**(14): p. 2348-2355.
212. Guevremont, R., et al., *Combined Ion Mobility/Time-of-Flight Mass Spectrometry Study of Electrospray-Generated Ions*. *Analytical Chemistry*, 1997. **69**(19): p. 3959-3965.
213. Wu, C., et al., *Electrospray ionization high-resolution ion mobility spectrometry-mass spectrometry*. *Analytical Chemistry*, 1998. **70**(23): p. 4929-4938.
214. Asbury, G.R. and H.H. Hill Jr., *Negative Ion Electrospray Ionization Ion Mobility Spectrometry*. *International Journal for Ion Mobility Spectrometry*, 1999. **2**(1): p. 1-8.
215. Steiner, W.E., et al., *Electrospray ionization with ambient pressure ion mobility separation and mass analysis by orthogonal time-of-flight mass spectrometry*. *Rapid Communications in Mass Spectrometry*, 2001. **15**: p. 2221-2226.
216. Barnett, D.A., et al., *Tandem mass spectra of tryptic peptides at signal-to-background ratios approaching unity using electrospray ionization high-field asymmetric waveform ion mobility spectrometry/hybrid quadrupole time-of-flight mass spectrometry*. *Rapid Communications in Mass Spectrometry*, 2002. **16**(7): p. 676-680.
217. Gabryelski, W. and K.L. Froese, *Characterization of Naphthenic Acids by Electrospray Ionization High-Field Asymmetric Waveform Ion Mobility Spectrometry Mass Spectrometry*. *Analytical Chemistry*, 2003. **75**(17): p. 4612-4623.
218. Bathgate, B., E.C.S. Cheong, and C.J. Backhouse, *A novel electrospray-based ion mobility spectrometer*. *American Journal of Physics*, 2004. **72**(8): p. 1111-1118.
219. Tang, X.T., J.E. Bruce, and H.H. Hill, *Characterizing electrospray ionization using atmospheric pressure ion mobility spectrometry*. *Analytical Chemistry*, 2006. **78**(22): p. 7751-7760.
220. Khayamian, T. and M.T. Jafari, *Design for Electrospray Ionization-Ion Mobility Spectrometry*. *Analytical Chemistry*, 2007. **79**(8): p. 3199-3205.
221. Levin, D.S., et al., *Using a Nanoelectrospray-Differential Mobility Spectrometer-Mass Spectrometer System for the Analysis of Oligosaccharides with Solvent Selected Control Over ESI Aggregate Ion Formation*. *Journal of the American Society for Mass Spectrometry*, 2007. **18**(3): p. 502-511.
222. Waters Corp. *Common Ionization*. [cited 2013 31th May]; Available from: http://www.waters.com/waters/es_ES/Common-Ionization/nav.htm?cid=10073251.
223. St. Louis, R.H. and H.H. Hill, Jr., *Ion mobility spectrometry in analytical chemistry*. *Critical Reviews in Analytical Chemistry*, 1990. **21**: p. 321-355.
224. Bradbury, N.E. and R.A. Nielsen, *Absolute Values of the Electron Mobility in Hydrogen*. *Physical Review*, 1936. **49**: p. 388-393.
225. Yoon, O.K., et al., *Simple Template-Based Method to Produce Bradbury-Nielsen Gates*. *Journal of the American Society for Mass Spectrometry*, 2007. **18**(11): p. 1901-1908.
226. Tyndall, A.M., 1938, *The mobility of positive ions in gases*. First ed. Cambridge Physical Tracts, eds. M.L.E. Oliphant and J.A. Ratcliffe. Cambridge, UK: The University press.
227. Mason, E.A. and E.W. McDaniel, 1988, *Transport properties of ions in gases* New York: John Wiley & Sons Inc.
228. Huxley, L.G.H., R.W. Crompton, and M.T. Elford, *Letters to the Editor: Use of the parameter E/N*. *British Journal of Applied Physics*, 1966. **17**(9): p. 1237-1238.
229. The Editor, *Letters to the Editor: Use of the parameter E/N*. *British Journal of Applied Physics*, 1967. **18**(5): p. 691.
230. Thomson, J.J. and G.P. Thomson, 1928, *Conduction of electricity through gases*. Third ed. Cambridge, UK: University Press.
231. Stach, J. and J.I. Baumbach, *Ion Mobility Spectrometry - Basic Elements and Applications*. *International Journal for Ion Mobility Spectrometry*, 2002. **5**(1): p. 1-21.
232. Wallis, E., et al., *Effects of CO₂ in the Carrier Gas of a Differential Mobility Spectrometer*, in *16th annual conference on Ion Mobility Spectrometry*. 2007: Mikkeli, Finland.
233. Spangler, G.E., *Expanded theory for the resolving power of a linear ion mobility spectrometer*. *International Journal of Mass Spectrometry*, 2002. **220**(3): p. 399-418.

234. Baumbach, J.I., et al., *Metabolites in human breath: ion mobility spectrometers as diagnostic tools for lung diseases*, in *Breath Analysis for Clinical Diagnosis and Therapeutic Monitoring*, A. Anmann and D. Smith, Editors. 2005, World Scientific: Singapore. p. 53-66.
235. Vautz, W., et al., *Sensitive ion mobility spectrometry of humid ambient air using 10.6 eV UV-IMS*. International Journal for Ion Mobility Spectrometry, 2004. **7**(1): p. 3-8.
236. Kanu, A.B. and H.H. Hill, *Ion mobility spectrometry detection for gas chromatography*. Journal of Chromatography A, 2008. **1177**(1): p. 12-27.
237. Westhoff, M., et al., *Ion mobility spectrometry for the detection of volatile organic compounds in exhaled breath of patients with lung cancer: results of a pilot study*. Thorax, 2009. **64**(9): p. 744-8.
238. Westhoff, M., et al., *Ion mobility spectrometry in the diagnosis of Sarcoidosis: Results of a feasibility study*. Journal of Physiology and Pharmacology, 2007. **58**: p. 739-751.
239. Pringle, S.D., et al., *An investigation of the mobility separation of some peptide and protein ions using a new hybrid quadrupole/travelling wave IMS/oa-ToF instrument*. International Journal of Mass Spectrometry, 2007. **261**(1): p. 1-12.
240. Mukhopadhyay, R., *IMS/MS: its time has come*. Analytical Chemistry, 2008. **80**(21): p. 7918-7920.
241. Kanu, A.B., et al., *Ion mobility-mass spectrometry*. Journal of Mass Spectrometry, 2008. **43**(1): p. 1-22.
242. Perl, T., et al., *Alignment of retention time obtained from multicapillary column gas chromatography used for VOC analysis with ion mobility spectrometry*. Analytical and Bioanalytical Chemistry, 2010. **397**(6): p. 2385-2394.
243. SGE Analytical Science. *Effect of Column length*. [cited 2013 30th May]; Available from: <http://www.sge.com/support/training/columns/effect-of-column-length>.
244. Baumbach, J.I., *Ion Mobility Spectrometry coupled with Multi-Capillary Columns for Metabolic Profiling of Human Breath*. Journal of Breath Research, 2009. **3**: p. 1-16.
245. Glish, G.L. and R.W. Vachet, *The basics of mass spectrometry in the twenty-first century*. Nat Rev Drug Discov, 2003. **2**(2): p. 140-150.
246. Waters Corp. SYNAPT® G2-S. [cited 2013 16th May]; Available from: http://www.waters.com/waters/es_ES/SYNAPT-G2-S-HDMS/nav.htm?locale=es_ES&cid=134612511.
247. Shvartsburg, A.A., et al., *High-Resolution Field Asymmetric Waveform Ion Mobility Spectrometry Using New Planar Geometry Analyzers*. Analytical Chemistry, 2006. **78**(11): p. 3706-3714.
248. Anderson, G.A., A.A. Shvartsburg, and R.D. Smith. 2011. *Microchip and wedge ion funnels and planar ion beam analyzers using same*. US Patent: 8299443 B1.
249. Baker, E.S., et al., *Sequence dependent conformations of glycidyl methacrylate/butyl methacrylate copolymers in the gas phase*. International Journal of Mass Spectrometry, 2004. **238**(3): p. 279-286.
250. Bushnell, J.E., et al., *The Determination of Cis-Trans Conformations in Tetrahedral p-Phenylene Vinylene Oligomers*. The Journal of Physical Chemistry A, 2004. **108**(38): p. 7730-7735.
251. Baker, E.S., et al., *Diastereomer Assignment of an Olefin-Linked Bis-paracyclophane by Ion Mobility Mass Spectrometry*. Journal of the American Chemical Society, 2004. **126**(20): p. 6255-6257.
252. Metz, T.O., et al., *High-resolution separations and improved ion production and transmission in metabolomics*. TrAC Trends in Analytical Chemistry, 2008. **27**(3): p. 205-214.
253. IUPAC. *IUPAC Compendium of Chemical Terminology - the Gold Book*. [cited 2013 21st May]; Available from: <http://goldbook.iupac.org/index.html>.
254. Rokushika, S., et al., *Resolution measurement for ion mobility spectrometry*. Analytical Chemistry, 1985. **57**(9): p. 1902-1907.
255. Tabrizchi, M. and F. Rouholahnejad, *Pressure effects on resolution in ion mobility spectrometry*. Talanta, 2006. **69**(1): p. 87-90.
256. Tabrizchi, M., *Temperature effects on resolution in ion mobility spectrometry*. Talanta, 2004. **62**(1): p. 65-70.
257. Siems, W.F., et al., *Measuring the resolving power of ion mobility spectrometers*. Analytical Chemistry, 1994. **66**(23): p. 4195-4201.

258. Harris, D.C., 2011, *Quantitative Chemical Analysis*: W. H. Freeman
259. Rorrer III, L.C. and R.A. Yost, *Solvent vapor effects on planar high-field asymmetric waveform ion mobility spectrometry*. International Journal of Mass Spectrometry, 2011. **300**: p. 173-181.
260. Tarver, E.E., *External second gate, Fourier Transform ion mobility spectrometry: Parametric optimization for detection of weapons of mass destruction*. Sensors, 2004. **4**(1-3): p. 1-13.
261. Davis, D.M.H., C.S., et al., *Analysis of ion mobility spectra for mixed vapors using Gaussian deconvolution*. Analytica Chimica Acta, 1994. **289**: p. 263-72.
262. Bell, S.E., et al., *Qualitative and quantitative evaluation of deconvolution for ion mobility spectrometry*. Analytica Chimica Acta, 1995. **303**(2-3): p. 163-174.
263. Tabrizchi, M. and F. Rouholahnejad, *Comparing the effect of pressure and temperature on ion mobilities*. Journal Of Physics D-Applied Physics, 2005. **38**(6): p. 857-862.
264. Revercomb, H.E. and E.A. Mason, *Theory of plasma chromatography/gaseous electrophoresis. Review*. Analytical Chemistry, 1975. **47**(7): p. 970-983.
265. Nazarov, E.G., et al., *Pressure Effects in Differential Mobility Spectrometry*. Analytical Chemistry, 2006. **78**(22): p. 7697-7706.
266. Krylov, E.V., S.L. Coy, and E.G. Nazarov, *Temperature effects in differential mobility spectrometry*. International Journal of Mass Spectrometry, 2009. **279**(2-3): p. 119-125.
267. Kim, S.H., F.W. Karasek, and S. Rokushika, *Plasma Chromatography with Ammonium Reactant Ions*. Analytical Chemistry, 1978. **50**(1): p. 152-155.
268. Blyth, D.A., *A vapour monitor for detection and contamination control*. Proc. Int. Symp. on Protection against Chem. Warfare, 1983.
269. Eiceman, G.A., et al., *Enhanced selectivity in ion mobility spectrometry analysis of complex-mixtures by alternate reagent gas chemistry*. Analytica Chimica Acta, 1995. **306**(1): p. 21-33.
270. Meng, Q., Z. Karpas, and G.A. Eiceman, *Monitoring indoor ambient atmospheres for volatile organic compounds using an ion mobility analyzer array with selective chemical ionization*. International Journal of Environmental Analytical Chemistry, 1995. **61**(2): p. 81-94.
271. Shvartsburg, A.A., K. Tang, and R.D. Smith, *Understanding and Designing Field Asymmetric Waveform Ion Mobility Spectrometry Separations in Gas Mixtures*. Analytical Chemistry, 2004. **76**(24): p. 7366-7374.
272. GE Security. *Itemiser*. [cited 2010 1st February]; Available from: <http://www.gesecurity.com.au/documents/Itemiser.pdf>.
273. Eiceman, G.A., et al., *Micro-machined planar field asymmetric ion mobility spectrometer as a gas chromatographic detector*. Analyst, 2002. **127**(4): p. 466-471.
274. Carnahan, B.L. and A.S. Tarassov. 1995. *Ion Mobility Spectrometer*. US
275. Guevremont, R. and R. Purves. 2004. *FAIMS apparatus and method with ion diverting device* US Patent: 6,825,461.
276. Thermo Scientific. *FAIMS interface, product specifications*. [cited 2013 27th April]; Available from: http://www.thermo.com/eThermo/CMA/PDFs/Product/productPDF_55743.PDF.
277. Guevremont, R., R. Purves, and D.A. Barnett. 2004. *Spherical side-to-side FAIMS*. US Patent: 6,713,758.
278. Guevremont, R., et al., *Atmospheric pressure ion trapping in a tandem FAIMS-FAIMS coupled to a TOFMS: studies with electrospray generated gramicidin S ions*. Journal of the American Society for Mass Spectrometry, 2001. **12**(12): p. 1320-1330.
279. Eiceman, G.A., et al., *Differential mobility spectrometry of chlorocarbons with a micro-fabricated drift tube*. Analyst, 2004. **129**(4): p. 297-304.
280. Eiceman, G.A., et al., *Miniature radio-frequency mobility analyzer as a gas chromatographic detector for oxygen-containing volatile organic compounds, pheromones and other insect attractants*. Journal of Chromatography A, 2001. **917**(1-2): p. 205-217.
281. Kendler, S., et al., *Fragmentation pathways and mechanisms of aromatic compounds in atmospheric pressure studied by GC-DMS and DMS-MS*. International Journal of Mass Spectrometry, 2007. **263**(2-3): p. 137-147.
282. Guevremont, R., *High-field asymmetric waveform ion mobility spectrometry: A new tool for mass spectrometry*. Journal of Chromatography A, 2004. **1058**(1-2): p. 3-19.
283. Miller, R.A., et al., *A MEMS radio-frequency ion mobility spectrometer for chemical vapor detection*. Sensors and Actuators A: Physical, 2001. **91**: p. 301-312.

284. McCooney, M.A., et al., *Quantitation of Amphetamine, Methamphetamine, and Their Methylenedioxy Derivatives in Urine by Solid-Phase Microextraction Coupled with Electrospray Ionization-High-Field Asymmetric Waveform Ion Mobility Spectrometry-Mass Spectrometry*. Analytical Chemistry, 2002. **74**(13): p. 3071-3075.
285. Cui, M., L. Ding, and Z. Mester, *Separation of Cisplatin and Its Hydrolysis Products Using Electrospray Ionization High-Field Asymmetric Waveform Ion Mobility Spectrometry Coupled with Ion Trap Mass Spectrometry*. Analytical Chemistry, 2003. **75**(21): p. 5847-5853.
286. Guevremont, R. and B. Kolakowski, *Using FAIMS to increase selectivity for LC-MS analyses*. American Laboratory, 2005. **37**(13): p. 11-14.
287. Purves, R.W., D.A. Barnett, and R. Guevremont, *Separation of protein conformers using electrospray-high field asymmetric waveform ion mobility spectrometry-mass spectrometry*. International Journal of Mass Spectrometry, 2000. **197**: p. 163-177.
288. Purves, R.W., et al., *Elongated conformers of charge states +11 to +15 of bovine ubiquitin studied using ESI-FAIMS-MS*. Journal of the American Society for Mass Spectrometry, 2001. **12**(8): p. 894-901.
289. Venne, K., et al., *Improvement in Peptide Detection for Proteomics Analyses Using NanoLC-MS and High-Field Asymmetry Waveform Ion Mobility Mass Spectrometry*. Analytical Chemistry, 2005. **77**(7): p. 2176-2186.
290. Veasy, C.A. and C.L.P. Thomas, *Fast quantitative characterisation of differential mobility responses*. Analyst, 2004. **129**: p. 198-204.
291. Buryakov, I.A., *Qualitative analysis of trace constituents by ion mobility increment spectrometer*. Talanta, 2003. **61**: p. 369-375.
292. Eiceman, G.A., et al., *Separation of ions from explosives in differential mobility spectrometry by vapor-modified drift gas*. Analytical Chemistry, 2004. **76**(17): p. 4937-4944.
293. Purves, R.W., et al., *Mass spectrometric characterization of a high-field asymmetric waveform ion mobility spectrometer*. Review of Scientific Instruments, 1998. **69**(12): p. 4094-4105.
294. Guevremont, R., et al. *FAIMS webpage*. [cited 2013 31st May]; Available from: <http://www.faims.com/howpart2.htm>.
295. Guevremont, R. and R. Purves, *Comparison of experimental and calculated peak shapes for three cylindrical geometry FAIMS prototypes of differing electrode diameters*. Journal of the American Society for Mass Spectrometry, 2005. **16**(3): p. 349-362.
296. Barnett, D.A., et al., *Characterization of a Temperature-Controlled FAIMS System*. Journal of the American Society for Mass Spectrometry, 2007. **18**(9): p. 1653-1663.
297. Shvartsburg, A.A., et al., *Field Asymmetric Waveform Ion Mobility Spectrometry Studies of Proteins: Dipole Alignment in Ion Mobility Spectrometry?* The Journal of Physical Chemistry B, 2006. **110**(43): p. 21966-21980.
298. Bryant, J.G., et al., *Design and evaluation of a novel hemispherical FAIMS cell*. International Journal of Mass Spectrometry, 2010. **298**(1-3): p. 41-44.
299. Shvartsburg, A.A., et al., *Ultrafast Differential Ion Mobility Spectrometry at Extreme Electric Fields in Multichannel Microchips*. Analytical Chemistry, 2009. **81**(15): p. 6489-6495.
300. Krylov, E.V., *Comparison of the planar and coaxial field asymmetrical waveform ion mobility spectrometer (FAIMS)*. International Journal of Mass Spectrometry, 2003. **225**(1): p. 39-51.
301. Krylov, E.V., E.G. Nazarov, and R.A. Miller, *Differential mobility spectrometer: Model of operation*. International Journal of Mass Spectrometry, 2007. **266**(1-3): p. 76-85.
302. Krylov, E.V., *A method of reducing diffusion losses in a drift spectrometer*. Technical Physics, 1999. **44**(1): p. 113-116.
303. Krylov, E.V., *Pulse of special shapes formed on a capacitive load*. Instruments and Experimental Techniques, 1997. **40**: p. 628-631.
304. Papanastasiou, D., et al., *Differential Mobility Separation of Ions Using a Rectangular Asymmetric Waveform*. Journal of Physical Chemistry A, 2008. **112**(16): p. 3638-3645.
305. Cumeras, R., et al., *Modelling a P-FAIMS with multiphysics FEM*. Journal of Mathematical Chemistry, 2012. **50**(2): p. 359-373.
306. Spangler, G.E. and R.A. Miller, *Application of mobility theory to the interpretation of data generated by linear and RF excited ion mobility spectrometers*. International Journal of Mass Spectrometry 2002. **214**(1): p. 95-104.
307. Tang, F., et al., *Study on simulation and experiment of array micro Faraday cup ion detector for FAIMS*. Science China Technological Sciences, 2010. **53**(12): p. 3225-3231.

308. Tang, F., X.H. Wang, and L. Zhang, *Array micro Faraday cup ion current detector for FAIMS*. *Guangxue Jingmi Gongcheng/Optics and Precision Engineering*, 2010. **18**(12): p. 2597-2602.
309. Mabrouki, R., et al., *Improving FAIMS Sensitivity Using a Planar Geometry with Slit Interfaces*. *Journal of the American Society for Mass Spectrometry*, 2009. **20**(9): p. 1768-1774.
310. Shvartsburg, A.A., K. Tang, and R.D. Smith, *Optimization of the design and operation of FAIMS analyzers*. *Journal of the American Society for Mass Spectrometry*, 2005. **16**(1): p. 2-12.
311. Barnett, D.A., et al., *Evaluation of carrier gases for use in high-field asymmetric waveform ion mobility spectrometry*. *Journal of the American Society for Mass Spectrometry*, 2000. **11**(12): p. 1125-1133.
312. Spangler, G.E., *Space charge effects in ion mobility spectrometry*. *Analytical Chemistry*, 1992. **64**(11): p. 1312-1312.
313. Buryakov, I.A., *Ion current amplitude and resolution of ion mobility increment spectrometer (IMIS)*. *International Journal for Ion Mobility Spectrometry*, 2001. **4**(2): p. 112-116.
314. Prieto, M., et al., *Comparison of Rectangular and Bisinusoidal Waveforms in a Miniature Planar High-Field Asymmetric Waveform Ion Mobility Spectrometer*. *Analytical Chemistry*, 2011. **83**(24): p. 9237-9243.
315. Krylov, E.V., et al., *Selection and generation of waveforms for differential mobility spectrometry*. *Review of Scientific Instruments*, 2010. **81**(2): p. 024101-11.
316. Shvartsburg, A.A. and R.D. Smith, *Optimum Waveforms for Differential Ion Mobility Spectrometry (FAIMS)*. *Journal of the American Society for Mass Spectrometry*, 2008. **19**(9): p. 1286-1295.
317. Paschen, F., *Ueber die zum Funkenübergang in Luft, Wasserstoff und Kohlensäure bei verschiedenen Drucken erforderliche Potentialdifferenz*. *Annalen der Physik*, 1889. **273**(5): p. 69-96.
318. Bazelyan, E.M. and Y.P. Raizer, 1998, *Spark Discharge*, eds. B.R. CRC Press.
319. Livermore, C., *course materials for 6.777J / 2.372J Design and Fabrication of Microelectromechanical Devices*, Spring 2007, MIT OpenCourseWare(<http://ocw.mit.edu/>), Massachusetts Institute of Technology. Downloaded on [24 April 2013].
320. Hourdakis, E., B.J. Simonds, and N.M. Zimmerman, *Submicron gap capacitor for measurement of breakdown voltage in air*. *Review of Scientific Instruments*, 2006. **77**(3): p. 034702-4.
321. Hourdakis, E., G.W. Bryant, and N.M. Zimmerman, *Electrical breakdown in the microscale: Testing the standard theory*. *Journal of Applied Physics*, 2006. **100**(12): p. 123306-6.
322. Marcsis, Y., 1985, *Ion Solvation*: Wiley-Interscience.
323. Eiceman, G.A., et al., *Field Dependence of Mobility for Gas Phase Ions of Organophosphorus Compounds at Atmospheric Pressure with Differential Mobility Spectrometry and Effects of Moisture: Insights into a Model of Positive Alpha Dependence*. *International Journal for Ion Mobility Spectrometry*, 2003. **6**(2): p. 43-47.
324. Krylova, N., et al., *Effect of moisture on the field dependence of mobility for gas-phase ions of organophosphorus compounds at atmospheric pressure with field asymmetric ion mobility spectrometry*. *Journal of Physical Chemistry A*, 2003. **107**(19): p. 3648-3654.
325. Viitanen, A.K., et al., *Experimental study of the effect of temperature on ion cluster formation using ion mobility spectrometry*. *Atmospheric Research*, 2008. **90**(2-4): p. 115-124.
326. Babis, J.S., et al., *Performance evaluation of a miniature ion mobility spectrometer drift cell for application in hand-held explosives detection ion mobility spectrometers*. *Anal Bioanal Chem*, 2009. **395**: p. 411-419.
327. Kanu, A.B., M.M. Gribb, and H.H. Hill, *Predicting Optimal Resolving Power for Ambient Pressure Ion Mobility Spectrometry*. *Analytical Chemistry*, 2008. **80**(17): p. 6610-6619.
328. Teepe, M., et al., *Miniaturized ion mobility spectrometer*. *International Journal for Ion Mobility Spectrometry*, 2001. **4**(1): p. 60-64.
329. Pfeifer, K.B. and R.C. Sanchez, *Miniaturized Ion Mobility Spectrometer System for Explosives and Contraband Detection*. *International Journal for Ion Mobility Spectrometry*, 2002. **5**(3): p. 63-66.

330. Xu, J., W.B. Whitten, and J.M. Ramsey, *A Miniature Ion Mobility Spectrometer*. International Journal for Ion Mobility Spectrometry, 2002. **5**(2): p. 207-214.
331. Zimmermann, S., et al., *Miniaturized Low-Cost Ion Mobility Spectrometer for Fast Detection of Chemical Warfare Agents*. Analytical Chemistry, 2008. **80**(17): p. 6671-6676.
332. Lamabadusuriya, M.R., et al., *Ionization, Transport, Separation, and Detection of Ions in Non-Electrolyte Containing Liquids*. Analytical Chemistry, 2012. **84**(21): p. 9295-9302.
333. Mariano, A.V., W. Su, and S.K. Guharay, *Effect of Space Charge on Resolving Power and Ion Loss in Ion Mobility Spectrometry*. Analytical Chemistry, 2009. **81**(9): p. 3385-3391.
334. Davis, E.J., et al., *Improved Ion Mobility Resolving Power with Increased Buffer Gas Pressure*. Analytical Chemistry, 2012. **84**(11): p. 4858-4865.

[This page intentionally left blank]

Chapter

3

Micro
p-FAIMS
Modeling

Chapter 3: Micro p-FAIMS Modeling	105
3.1 Finite element methods (FEM).....	107
3.2 Model Definition	109
3.3 Fluid Dynamics	111
3.4 Electric Fields.....	114
3.5 Ion Concentration	119
3.6 Ion Detection	121
3.7 Modeled compounds.....	122
3.8 Simulation Results.....	124
3.8.a Carrier gas flow rate effects.....	124
3.8.b Electric Field study.....	128
3.8.c Ions differentiation	131
3.8.d Filtering Electrodes Length Dependence.....	144
3.9 Validation	146
Discussion and Summary	149
References	150

This chapter provides a description of the general features of working with COMSOL Multiphysics to simulate a micro planar high-Field Asymmetric Ion Mobility Spectrometer. Up to now, the simulation of micro planar FAIMS devices has not been widely reported, as far as we know.

When performing simulations, it is very important to choose the appropriate software. In our case, to simulate a micro planar high-Field Asymmetric Ion Mobility Spectrometer or p-FAIMS, there are three main phenomena: i) the flow of the carrier gas that transports the ions through the defined channel or drift tube; ii) the various electric fields that are applied to the filtering and detector electrodes; iii) the movement of ions influenced by the carrier gas and by the electric fields applied, also considering ion diffusion. This implies the need to work simultaneously with different physical phenomena. Therefore, we need a Multiphysics treatment.

Once chosen the modeling software (COMSOL Multiphysics) and defined the modules to be included for the full simulation of the p-FAIMS, it has been done a study to determine the influence of each considered phenomenon on the response of our device. In this way, we have evaluated the ions intensity at the detector varying: (i) the flow of the carrier gas from 500 to 2,250 sccm (standard centimeter cubic per minute); (ii) the electric fields applied, changing the frequency for a fixed field, and fixing the field and changing the frequency. Frequency ranges from 1.0 to 2.0 MHz, and fields from 60 to 90 Td; and (iii) the length of the filtering electrodes. Two different values have been considered in this case, 13 and 20 mm.

Compounds selected for the simulations are representative for security applications, for which the p-FAIMS is intended to be used. Ions studied include a chemical warfare agent or CWA simulant (dimethyl methyl phosphonate or DMMP that emulates gas sarin, in its positive monomer), two risky healthy volatile organic compound or VOC (2-propanone or acetone Ac in its positive dimer, and toluene T in its protonated monomer); and three explosives (2,4,6-trinitrotoluene or TNT, 2,4-dinitrotoluene or DNT, and 1,3,5-trinitrobenzene or TNB, all three in their negative monomers).

Special attention is paid to the behavior of each studied compound and to the possibility of differentiation compound mixtures through a board range of conditions. Finally a validation of the model is shown.

3.1 Finite element methods (FEM)

Finite element methods (FEM) are numerical techniques to solve partial differential equations (PDE's). An in-depth discussion of these numerical techniques remains beyond the scope of this work, but there are some excellent books on this topic [1-4].

There are much commercial software's based in FEM to simulate Multiphysics phenomena, such as: Abaqus, ANSYS, CFD-ACE+, CFD-fast, COMSOL, Fluent, LS-DYNA, Nastran and NEi OOFELIE. In these software packages, PDE's system is transformed into a linear system of equations (usually very large) for the stationary case equations or, for transient cases, in ordinary differential equation (ODE) generally solved using a finite difference method (FDM) in time.

The first step is to describe the domain geometry. Then this domain is discretized in much smaller subdomains, named finite elements [4]. The set of elements is called mesh. The vertex of such elements are called nodes, although there can be nodes outside the vertex. Nodes are very important in FEM because it is where the solution is computed for the different variables.

The dimension of the elements is directly related to that of the domain. There are different kinds of elements depending on their geometry. The simplest geometry in one dimension is the linear segment, in two dimensions the triangle, and in three dimensions the tetrahedron [5]. Figure 3-1 schematizes a simple domain where triangular elements are used to create the mesh.

After the nodes discretization and PDE's domain definition, the FEM will provide an approximate value of the real solution to each node, being the approach much better as more dense is the mesh.

It was decided to choose COMSOL Multiphysics [6] as simulation software from the ones available at the IMB-CNM (ANSYS Multiphysics and COMSOL Multiphysics), because it has a friendly graphical interface, and allows us to treat more intuitively the interaction between fluids and electric fields. Note that p-FAIMS simulation presented in this work using COMSOL Multiphysics software was not done before for this application.

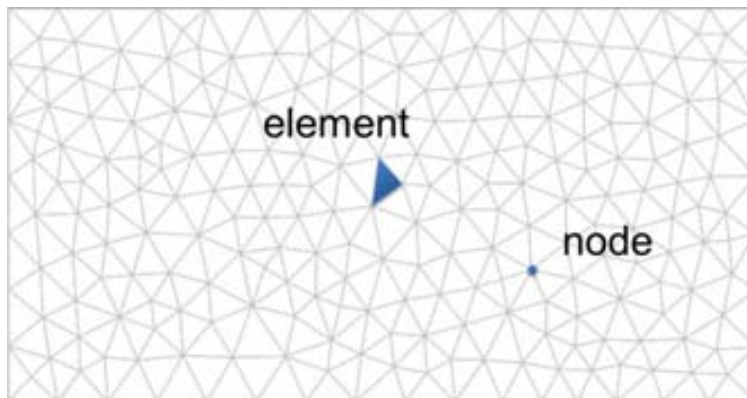


Figure 3-1: Schematic representation of a typical mesh for two dimensional domains. It uses triangular second order elements, with a node on each corner.

3.2 Model Definition

COMSOL Multiphysics software is used to simulate the behavior of different representative ions for security applications in a p-FAIMS. The software takes into account nonlinear combined effects of different forces and concentration gradients. Created model combines fluid dynamics, electric fields and transport of diluted species which have been found to be the most significant effects.

A 2D approximation of the p-FAIMS is done to reduce computation time and memory requirements, and considering that all the effects do not vary along the electrodes width, fixed at 5 mm. Simulations are realized considering two electrode regions as shown in the used geometry at Figure 3-2, for a fixed gap g of 0.5 mm:

- 1) *filtering electrodes* where the AC and DC voltages needed to filter the different ionic species are applied, of $l \times 5 \text{ mm}^2$. Being l [mm] the length of the filtering electrodes. As seen in Figure 3-2, the filtering electrodes are defined by boundaries 2 and 5. Filtering lengths studied in this work have been of 13 and 20 mm.
- 2) *detector electrodes* (charge collectors) of $5 \times 5 \text{ mm}^2$ that are placed 1 mm after filtering electrodes to collect ions and generate the p-FAIMS spectrum. In Figure 3-2 the filtering electrodes are defined by boundaries 8 and 9.

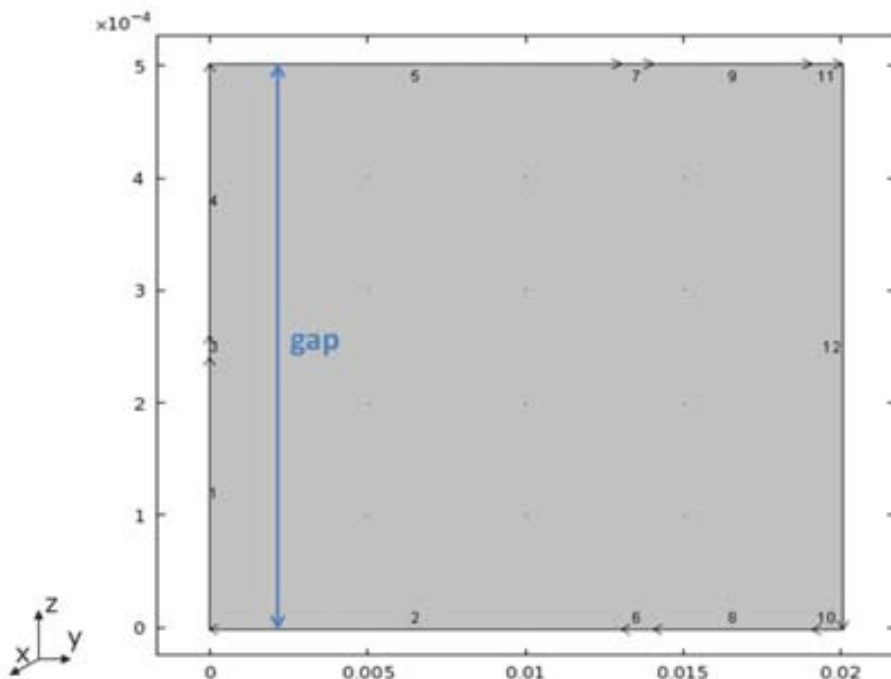


Figure 3-2: Schema of the simulated p-FAIMS. Numbers indicates the boundaries with which the domain is defined to establish the p-FAIMS geometry. Filtering electrodes length is 13 mm.

Carrier gas and ions enter the p-FAIMS from the left (boundaries 1, 3 and 4 from Figure 3-2), passes through the filtering electrodes and only ‘selected’ ions reach the detector electrodes. Ions are introduced from the center of the channel high at the beginning of the filtering electrodes with a spatial distribution specified as $\Delta z = 0.02$ mm and $\Delta y = 0.00$ mm (boundary 3 from Figure 3-2), while air gas flows over all the channel height (boundaries 1, 3 and 4 from Figure 3-2).

The domain division into finite elements (meshing) is adjusted in order to solve local electric field gradients or concentration gradients. It is always important to refine the mesh; that is, to define smaller mesh elements in those domains regions or points where one expects to find steeper gradients. In our case, as can be seen in Figure 3-3, in regions where concentration gradient is supposed to be higher as are near the detector electrodes and in the region where ions are introduced.

Models were performed using COMSOL Multiphysics 4.0a and earlier versions, and the used modules are summarized in Figure 3-4. Carrier gas velocity within the p-FAIMS has been calculated using the fluid flow module. Electric potentials on the p-FAIMS and detector electrodes are simulated using the AC/DC module.

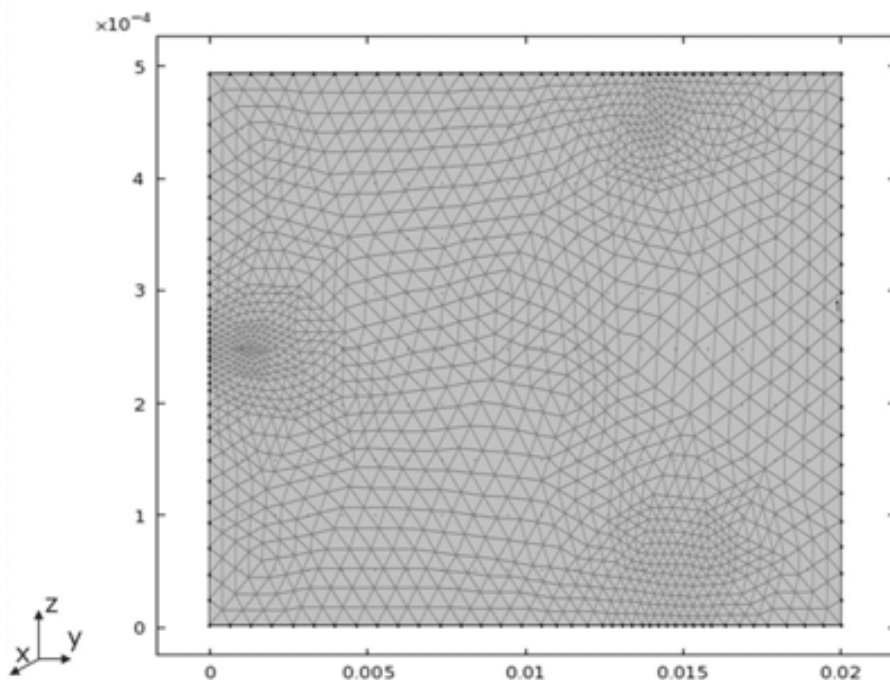


Figure 3-3: Used mesh in the simulated p-FAIMS. Filtering electrodes length is 13 mm.

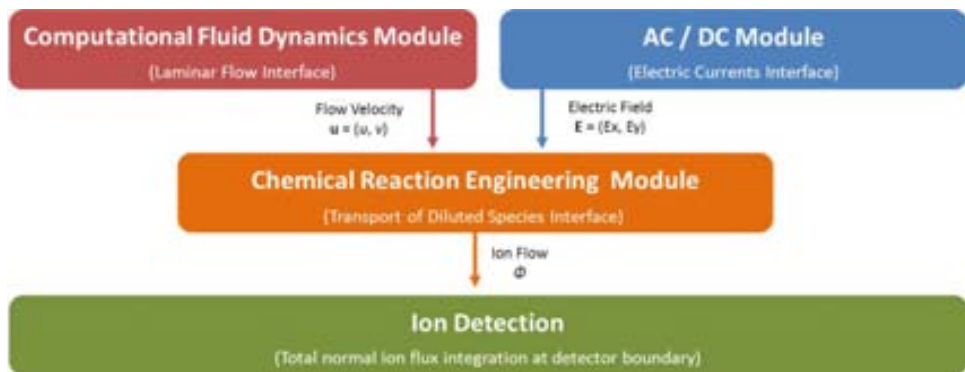


Figure 3-4: Block diagram of key computational steps involved in modeling p-FAIMS with COMSOL Multiphysics software.

For each specified time ($\sim 1\mu\text{s}$) COMSOL computes the fluid flow from Navier-Stokes equations and the electric currents in the device. Then, once having the solution of both modules, the local ion concentration is calculated with the chemical species transport module, which takes into account of ions behavior, including diffusion. Finally, ions that arrive to the detector are obtained evaluating the integral of the total normal ion flux over the detector boundary.

Modeled ions are analyzed once inside the p-FAIMS, and non-ionized molecules form part of the drift gas. To simplify numerical simulations, the following assumptions are made:

- All ions are singly charged, so $z = \pm 1$.
- The ions are free from clusters -from water vapor and nitrogen in the ionization process-
- Ions do not interact with one another, so that there are no interactions resulting from space charge: $R = 0 \text{ mol}\cdot\text{m}^{-3}\cdot\text{s}^{-1}$ as reaction rate expression for each ionic specie.
- Ions do not have dipolar moment, and therefore no polarization occurs, $P = 0 \text{ C}\cdot\text{m}^{-2}$.
- The type of ionization is not considered and ions are created immediately upon entering the analyzer.

3.3 Fluid Dynamics

The Single-Phase Flow Interface included in the CFD (computational fluid dynamics) Module of COMSOL Multiphysics software, incorporate several fluid flow physics interfaces. The various types of momentum transport that can be simulated include

laminar and turbulent flow, Newtonian and non-Newtonian flow, isothermal and non-isothermal flow, multiphase flow, and flow in porous media.

Gas flow in pipes or between parallel plates is in a laminar or turbulent regime that is determined by the dimensionless Reynolds number. In our case, for an inlet gas flow of $Q = 1 \text{ L}\cdot\text{min}^{-1}$, the Reynolds number obtained is $Re \sim 400$, this value is 10 times lower than the turbulence onset threshold ($Re \sim 4000$), so the gas flow can be considered laminar [7].

Therefore, we use the Laminar Flow Interface that has the equations, boundary conditions, and volume forces to model freely moving fluids using the Navier-Stokes equations, solving for the velocity field and the pressure.

When the temperature variations in a flow are small, a single-phase fluid can often be assumed incompressible; that is, density ρ [$\text{kg}\cdot\text{m}^{-3}$] is constant or nearly constant. For a constant ρ , the COMSOL Navier-Stokes equations solved are the momentum and the continuity equations:

$$\rho \frac{\partial \mathbf{u}}{\partial t} - \nabla \cdot \eta \nabla \mathbf{u} + \nabla \mathbf{u}^T + \rho \mathbf{u} \cdot \nabla \mathbf{u} + \nabla p = \mathbf{F} \quad (3.1)$$

$$\nabla \mathbf{u} = 0 \quad (3.2)$$

where ρ is the density [$\text{kg}\cdot\text{m}^{-3}$], \mathbf{u} is the velocity vector [$\text{m}\cdot\text{s}^{-1}$], η is the dynamic viscosity [$\text{Pa}\cdot\text{s}$], T is the temperature [K], p is the pressure [Pa] and \mathbf{F} is the volume force vector [$\text{N}\cdot\text{m}^{-3}$].

In Table 3-1 are listed the main physical properties of nitrogen and air [8, 9], that are used in the simulations done at ambient pressure and temperature ($P_{\text{amb}} = 101,325 \text{ kPa}$; $T_{\text{amb}} = 298,15 \text{ K}$), also including mean free path λ [nm], dielectric constant ϵ_r [dimensionless], electrical conductivity σ [$\text{S}\cdot\text{m}^{-1}$] and gas number density N [m^{-3}].

All studied compounds are simulated in nitrogen, but in the validation process has been taken into account experimental data from the literature, that was obtained in some cases in air.

	ρ ($\text{kg}\cdot\text{m}^{-3}$)	λ (nm)	ϵ_r	η ($\mu\text{Pa}\cdot\text{s}$)	σ ($\text{S}\cdot\text{m}^{-1}$)	N (m^{-3})
Nitrogen N₂	1.145	67.6	1.0005480	17.9	1×10^{-16}	2.5×10^{25}
Air (78.1% N₂ 20.9% O₂)	1.161	69.1	1.0005364	18.6	1×10^{-16}	2.7×10^{25}

Table 3-1: Physical properties of considered carrier gases at ambient pressure and temperature [8, 9].

Contour conditions used in Laminar Flow Interface for the carrier gas are shown in Figure 3-5. Carrier gas inlet is done through all the entry defined by boundaries 1, 3 and 4, while the carrier gas outlet is done through the output defined by boundary 10. The rest of the boundaries are considered as solid walls, and no slip condition is applied, that is, the fluid at the wall is not moving.

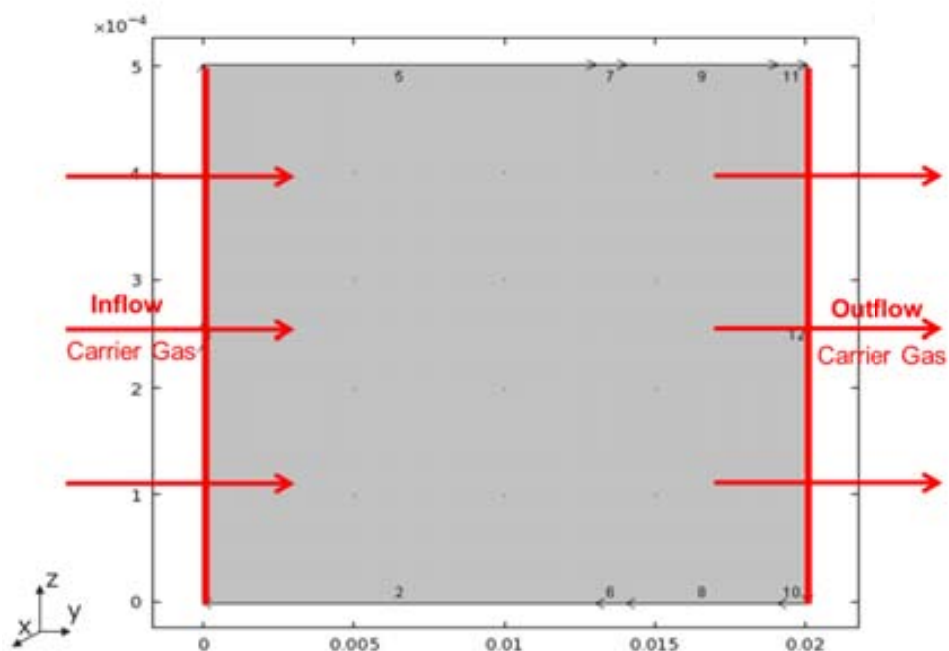


Figure 3-5: Schema of the Carrier Gas contour conditions in the simulated p-FAIMS.

In Figure 3-6 the modeled velocity field profile of nitrogen in the drift channel is shown and the graphic of the z -velocity of nitrogen is superimposed. It can be seen the laminar behavior of the carrier gas for a gas flow inlet of $Q = 1 \text{ L}\cdot\text{min}^{-1}$, with a maximum z -velocity of $10 \text{ m}\cdot\text{s}^{-1}$. This flow profile results in an increase of ion losses near the electrode region due to an increase in drift time of ions that is caused by the decrease in gas velocity from $10 \text{ m}\cdot\text{s}^{-1}$ (gap center) to zero (electrode surface) according to the parabolic profile.

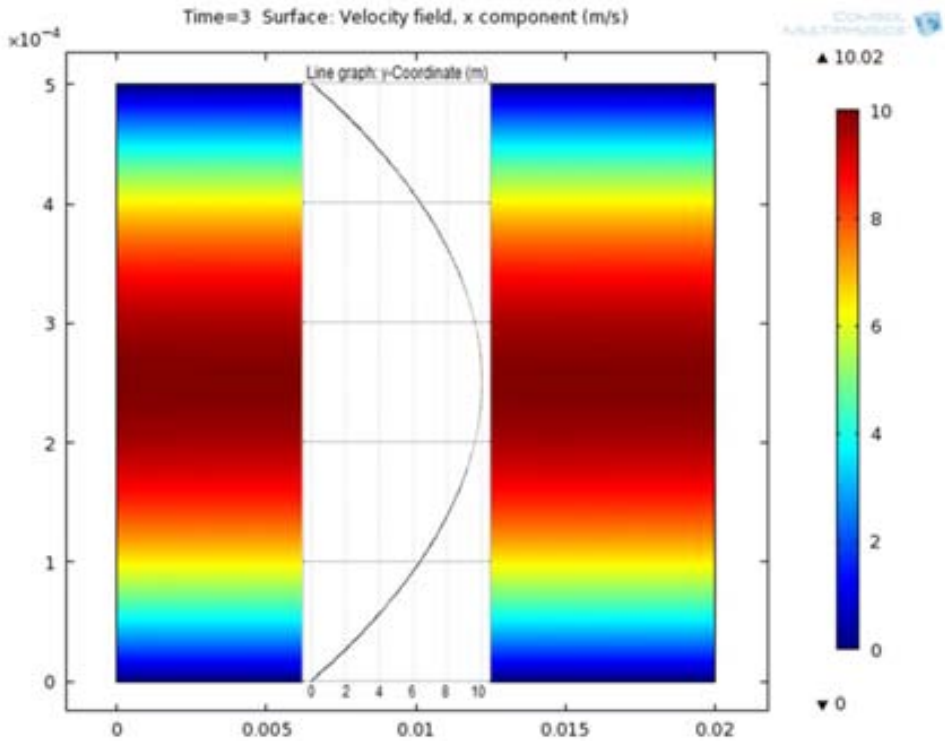


Figure 3-6: Velocity profile of nitrogen as carrier gas at the drift channel obtained with the Laminar Flow Interface for a gas flow inlet of $Q = 1 \text{ L} \cdot \text{min}^{-1}$. Superimposed is shown the laminar (parabolic) behavior of z-velocity of nitrogen in an arbitrary x. Filtering length is 13 mm.

3.4 Electric Fields

The Electric currents Interface included in the AC/DC Module of COMSOL Multiphysics software provides the equations, boundary conditions, and current sources to model steady electric currents in conductive media, solving for the electric potential.

Electric fields modeling are determined by the electrostatic equations. The **electric field** E [$\text{V} \cdot \text{cm}^{-1}$] is defined as the gradient of the electric potential V [V], applied between the electrodes:

$$E = -\nabla V \quad (3.3)$$

Combining this equation with the relationship $\mathbf{D} = \epsilon_0 \epsilon_r \mathbf{E} + \mathbf{P}$ between the electric displacement \mathbf{D} and the electric field \mathbf{E} , considering that ions do not have dipolar moment $\mathbf{P} = 0 \text{ C} \cdot \text{m}^{-2}$, and being ϵ_0 [$8.85 \cdot 10^{-12} \text{ F} \cdot \text{m}^{-1}$] the electric permittivity of

vacuum [9] and ϵ_r [dimensionless] the relative permittivity of the medium; COMSOL Electrostatics Interface uses Gauss's law to define the electric field as:

$$-\nabla \cdot \epsilon_0 \epsilon_r \nabla V = \rho \quad (3.4)$$

where ρ [$\text{C}\cdot\text{m}^{-3}$] is the space charge density defined as $\rho = F \sum_s z_s c_s$, where F

[96,485 $\text{C}\cdot\text{mol}^{-1}$] is the Faraday constant [9], z_s is the ionic charge of each ion s , and c_s is the concentration of each ion s . This term describes the Coulomb repulsion interaction of the ion with the electric field.

For in-plane 2D modeling, the Electric Currents Interface assumes a symmetry where the electric potential varies only in the y and z directions and is constant in the x direction. This implies that the electric field, \mathbf{E} , is tangential to the yz -plane. Given this symmetry, the equation is solved as in the 3D case. The interface solves the following equation where d [mm] is the thickness in the x direction:

$$-\nabla \cdot d \epsilon_0 \epsilon_r \nabla V = d \rho \quad (3.5)$$

The axisymmetric version of the Electric Currents Interface considers the situation where the fields and geometry are axially symmetric.

The total electric voltage applied at the filtering electrodes p-FAIMS $V_{\text{filtering}}$ [V] has been defined as:

$$V_{\text{filtering}} = DV - CV \quad (3.6)$$

where DV is the dispersion voltage [V], and CV is the compensation voltage [V]. The minus only indicates the voltages opposite direction.

A critical aspect of FAIMS operation is the asymmetric waveform used to characterize the ions. The ideal $DV(t)$ profile is a rectangular waveform, but in practice a rectangular waveform with sufficiently high frequencies and amplitudes are difficult to generate [10]. A ‘bisinusoidal’ profile produces experimentally very similar results [11, 12]. In this thesis, we used the bisinusoidal waveform to evaluate how it influences the ion motion through the drift channel (see Section 2.3.b *FAIMS Ion Dynamics*). The applied dispersion voltage DV also accomplish Equation (2.53) with $f = 2$ [13], being:

$$DV(t) = \frac{DV_i}{3} \left[2 \sin \omega t + \sin \left(2\omega t - \frac{\pi}{2} \right) \right] \quad (3.7)$$

where DV_i [V] is the amplitude of the dispersion voltage applied and ω [$\text{rad}\cdot\text{s}^{-1}$] is the angular frequency of the waveform. The compensation voltage CV is manually scanned. In Figure 3-7 is shown the dispersion voltage for a frequency of $\nu_D = 2.0$ MHz and a duty cycle of 30%. Also, DV satisfies the condition: $\int_T DV(t) dt = 0$, i.e. $E_H \times t_H + E_L \times t_L = 0$ for being an asymmetric waveform. Where E_H (E_L) is the maximum (minimum) dispersion field applied for a time t_H (t_L).

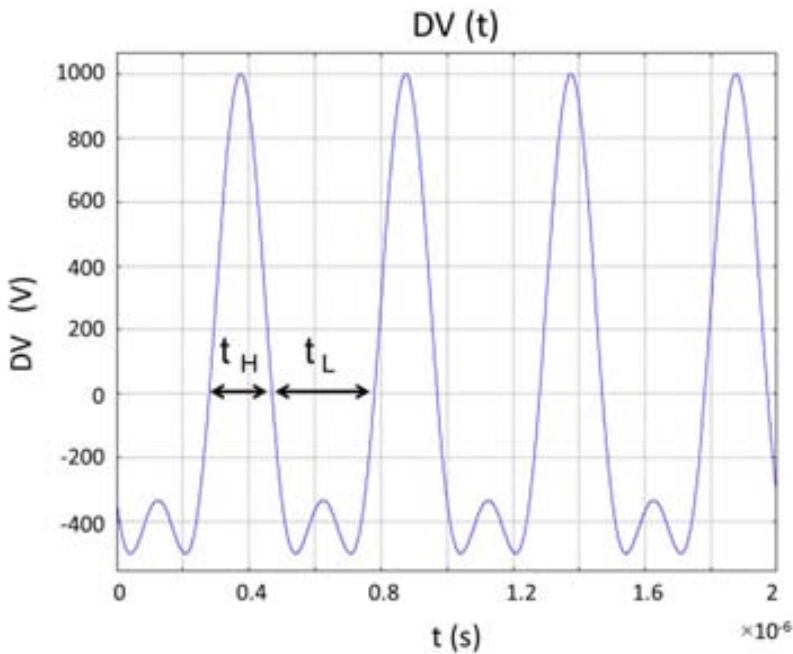


Figure 3-7: Dispersion voltage as applied to the modeled p-FAIMS with COMSOL Multiphysics software. Maximum dispersion voltage is applied for a time t_H , and the minimum dispersion voltage for a time t_L . $DV_i = 1,000$ V and $\nu_D = 2.0$ MHz.

It is needed to achieve a compromise between frequency, carrier gas flow and gap. A low frequency implies that the positive high-voltage V_H is applied for a longer time and ions will travel a longer distance toward the filtering electrodes during each period, and eventually they will be lost before reaching the detector.

Figure 3-8 shows the boundary conditions for the Electric Currents Interface used in the simulations. Filtering electrodes have two boundary conditions: (i) at the top

electrode (boundary 5) is applied the Electric Potential $V_{filtering} = DV(t) - CV$ (ii) the bottom electrode (boundary 6) is grounded (GND). Detector electrodes have the same boundary conditions but changed in sign, being the Electric Potential $V_{det} = +5$ V applied at the top electrode (boundary 8) and $-V_{det}$ at the bottom electrode (boundary 9). Detector electrodes have been biased with opposite signs to be able to detect either positive or negative ions. The rest of boundaries are considered as Electric Insulation boundaries, meaning that no electric current flows into the boundary $\mathbf{n} \cdot \mathbf{J} = 0$, being \mathbf{n} the normal vector from the boundary and \mathbf{J} the current density [$A \cdot m^{-2}$].

Figure 3-9 shows the obtained electric potential for a dispersion potential of $DV_i = 1,000$ V and for a frequency $\nu_D = 2.0$ MHz, being the filtering length of 13 mm. Images shown the change of the electric field in the zone between the end of filtering electrodes and the beginning of detector electrodes. The minimum electric potential obtained (Figure 3-9-TOP) is ~ 500 V, and the maximum electric potential (Figure 3-9-BOTTOM) is $\sim 1,000$ V, so the total amplitude of the dispersion voltage is 1,500 V. The simulated dispersion voltage has the behavior and amplitude expected. Also in Figure 3-9-MIDDLE is shown the electric potential close to the dispersion voltage value of zero ($DV(t) = 0$). Top detector electrode is biased at -5 V and bottom detector electrode is grounded.

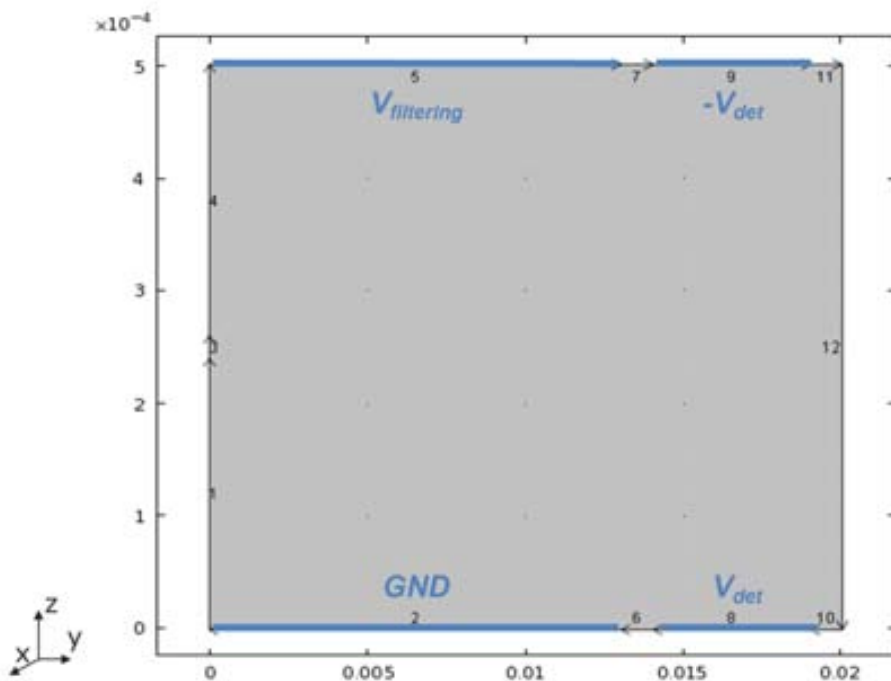


Figure 3-8: Schema of the Electric Field boundary conditions in the simulated p-FAIMS.

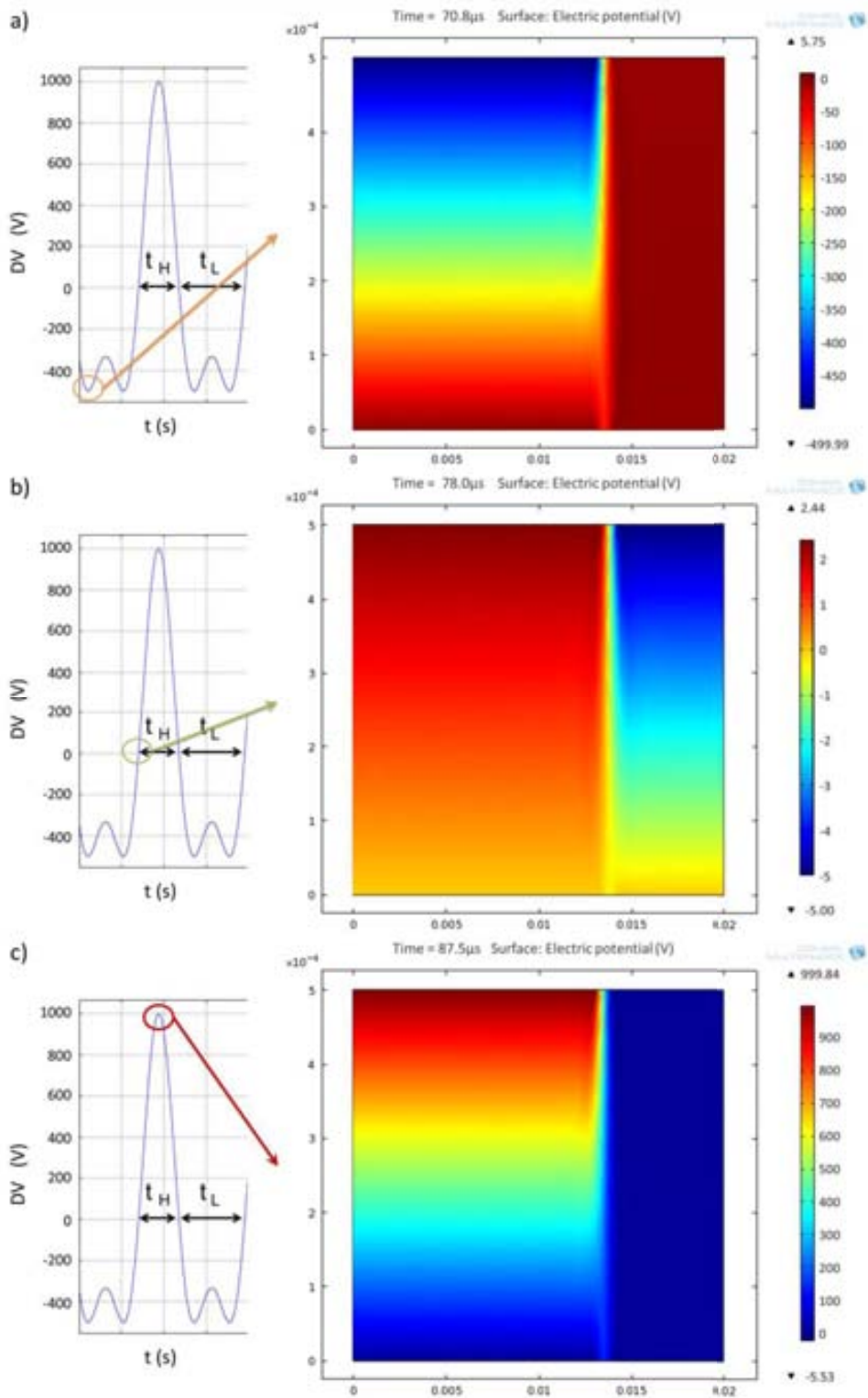


Figure 3-9: Obtained electric potentials for $DV_i = 1,000\text{V}$, $\nu_D = 2.0\text{ MHz}$, $CV = 0.0\text{V}$. a) Minimum electric potential; b) Electric potential for $DV(t) \sim 0$; and c) Maximum electric potential. Filtering length is 13 mm.

Results from FAIMS analysis are commonly graphed as ion current versus CV or ion current versus DV , but these voltages are not taking into account the carrier gas composition. For this study, CV and DV are normalized to the gas number density of the carrier gas and reported in units of Td. E/N is expressed in $V \cdot cm^2$, but for convenience, it was resolved to adopt the unit Townsend: $1 \text{ Td} = 10^{-21} V \cdot m^2$ [14, 15]. Therefore, the terms CV and DV are replaced with compensation electric field ($|E_C|/N$) and dispersion electric field ($|E_D|/N$), respectively.

3.5 Ion Concentration

The Transport of Diluted Species Interface included in the Chemical Species Transport Module of COMSOL Multiphysics software provides a predefined modeling environment for studying the transport of chemical species that can be directly coupled to any other physical process; such as fluid flow and electric fields in the studied case. The interface assumes that all species present are diluted and their concentration is small compared to the solvent.

A flow of charged ions subject to an electric field verifies the mass conservation law defined from Nernst-Planck equation that takes into account diffusion, convection and migration flows:

$$\nabla \cdot (-D\nabla c + \mathbf{u}c - z_{ion}Kc\nabla V) = R \quad (3.8)$$

where D is ion diffusion [$m^2 \cdot s^{-1}$], c is ion concentration [$mol \cdot m^{-3}$], z_{ion} is ion charge number [dimensionless], K is ion mobility coefficient [$cm^2 \cdot V^{-1} \cdot s^{-1}$], V [V] is the voltage affecting the ion, R [$mol \cdot m^{-3} \cdot s^{-1}$] is the reaction rate that is assumed to be zero -Ions do not interact with one another- and \mathbf{u} [$m \cdot s^{-1}$] is the fluid velocity vector in which ions are diluted in y and z directions $\mathbf{u} = (u_y, u_z)$. The total flow of the ionic specie is the electrokinetic flow Φ_{EK} , so previous equation is mass conservation for:

$\nabla \cdot \Phi_{EK} = 0$, where Φ_{EK} is the sum of:

$$\Phi_{EK} = \Phi_D + \Phi_C + \Phi_M \quad (3.9)$$

being,

- the **Diffusion flow** expressed by Fick's law:

$$\Phi_D = -D\nabla c \quad (3.10)$$

that takes into account ion random movements. Diffusion has been calculated using the Nernst-Townsend-Einstein relationship defined in Equation (2.20) as:

$$D = K \cdot \frac{k_B T}{q} \quad (3.11)$$

where K is the ion mobility [$\text{cm}^2/\text{V}\cdot\text{s}$], k_B is the Boltzmann constant [$1.38065 \times 10^{-23} \text{ J}\cdot\text{K}^{-1}$] [9], T is the temperature [K] set to 293.15 K (= 20°C) and q is the ion charge [C] being $q = ze$ where e is the elementary charge [$1.602 \times 10^{-19} \text{ C}$] [9] and z is the number of elemental charges [dimensionless].

- the **Convection flow**: $\Phi_C = \mathbf{u}c$, that takes account of gas drift velocity;
- the **Migration flow**: $\Phi_M = -z_{ion} Kc \nabla V$, that takes account of flow variations due to applied voltages.

Figure 3-10 shows the boundary conditions for the Transport of Diluted Species Interface used during simulations. Ions are introduced from the center of the channel high (boundary 3) with a spatial distribution specified as $\Delta z = 0.02 \text{ mm}$ and $\Delta y = 0.00 \text{ mm}$, for a concentration condition of $c = c_0$ for specie c . If more ionic species are considered, their concentrations are named as c_1, c_2, c_3 , etc. All modeled ions concentrations have been fixed to 1 ppm in the studied cases. COMSOL software parameter for the concentration, is the molar concentration, c_i [$\text{mol}\cdot\text{m}^{-3}$] defined as the amount of a constituent n_i [mol] divided by the volume V [m^3] of the mixture: $c_i = n_i/V$. To calculate the molar concentration, is used the ideal gas law at normal pressure and temperature (101,325 Pa and 298.15 K [9]): $pV = nRT$, where p [Pa] is the pressure of the gas, V [m^3] is the volume of the gas, n [mol] is the amount of the gas, T [K] is the temperature of the gas and R [$8.314 \text{ J}\cdot\text{K}^{-1}\cdot\text{mol}^{-1}$] is the ideal, or universal, gas constant, equal to the product of the Boltzmann constant [$1.38065 \times 10^{-23} \text{ J}\cdot\text{K}^{-1}$] and the Avogadro constant [$N_A = 6.02214 \times 10^{23} \text{ mol}^{-1}$]. Therefore, for an initial ion concentration of 1 ppm, the molar concentration in our case is $c_0 = 4.06 \times 10^{-5} \text{ mol}\cdot\text{m}^{-3}$. Boundaries 1, and 4 are set to $c = 0 \text{ mol}\cdot\text{m}^{-3}$, so no inflow of ions is allowed. In the rest of boundaries where the concentration of species is symmetric the concentration is set to $c = c_0$, meaning that in these boundaries is where the ion concentration can be calculated.

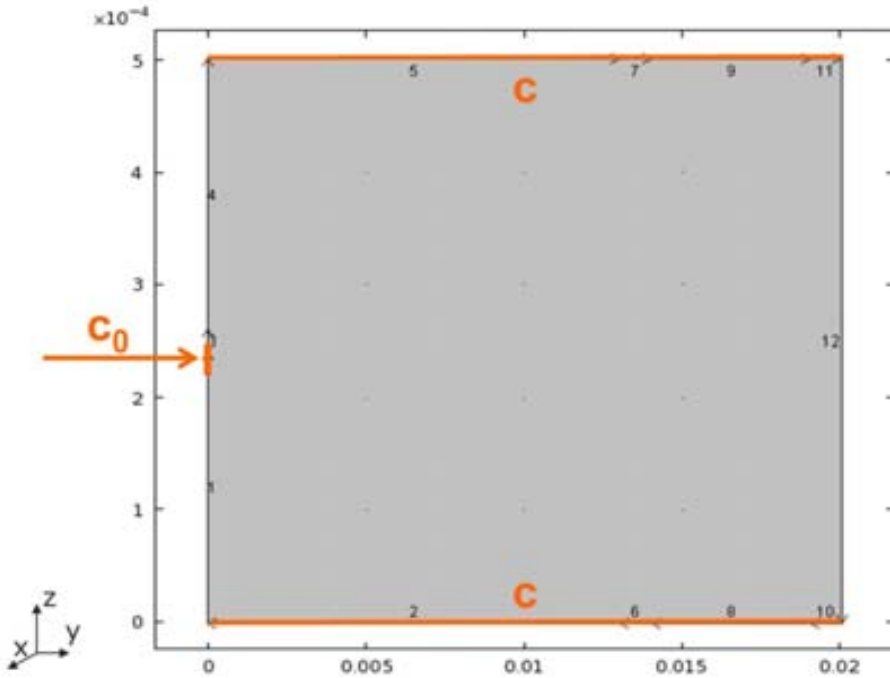


Figure 3-10: Schema of the Transport of Diluted Spices boundary conditions in the simulated p-FAIMS.

3.6 Ion Detection

The local concentration of ions within the drift region and its dependence from the parameters above mentioned allows computing the ion current at the detector. Integrating the normal component of ions flux per unit area A (mm^2) of the detector with normal vector \mathbf{n} yields the ion current [16]:

$$I = \int_A \mathbf{n} F z_{ion} \Phi_{EK} dA = \int_{x,y} \mathbf{n} F z_{ion} \Phi_{EK} dx dy \stackrel{2D \text{ approx}}{=} d \int_y F z_{ion} \Phi_{EK} dy \quad (3.12)$$

where F is the Faraday constant [$96,485 \text{ C}\cdot\text{mol}^{-1}$] [9]. Considering 2D simulations we assume that x -intensity is uniform for the whole detectors width d . This integral has been defined by ‘integration coupling variables’ option from the COMSOL software to the region where $\pm V_{det}$ is applied (see Figure 3-8, boundaries 8 and 9).

In Figure 3-11 is shown the COMSOL workbench for a simulation result of 1 ppm of toluene ions, when applying a dispersion field of $|E_D|/N = 80 \text{ Td}$ and a compensation field $|E_C|/N = 0.41$ ($CV = -5.1 \text{ V}$). A nitrogen flow of 1,000 sccm was considered.

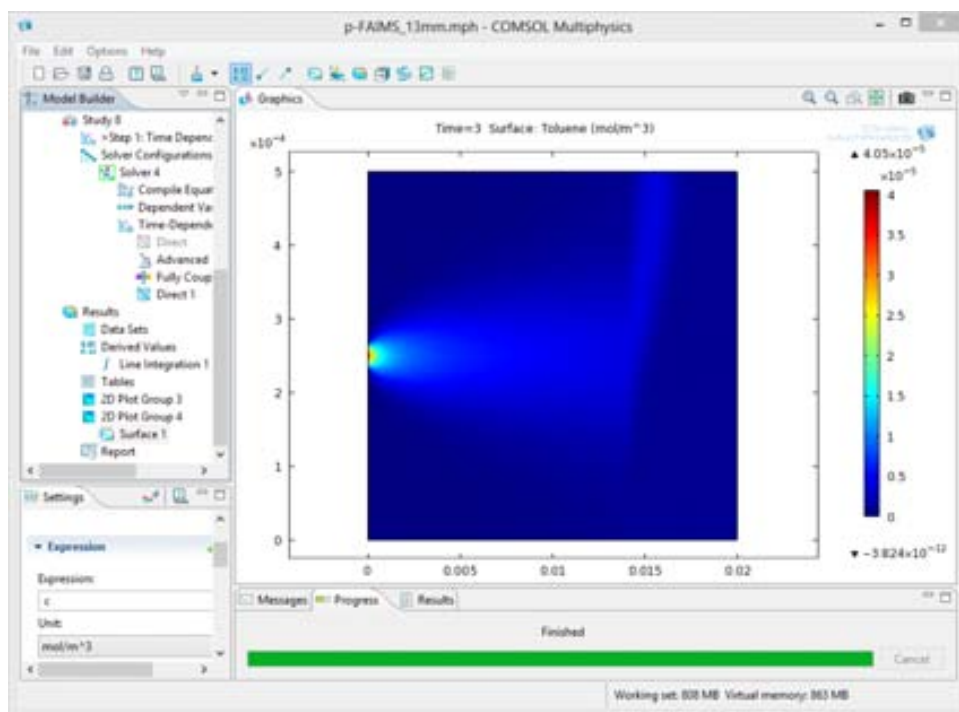


Figure 3-11: COMSOL workbench showing the simulation results for 1 ppm of toluene ions (surface, different tonalities of rainbow). Filtering electrodes length of 13 mm with a dispersion field of $|E_D|/N = 80$ Td and a flow of 1,000 sccm. Applied compensation field was $|E_C|/N = 0.41$ (CV = -5.1 V).

3.7 Modeled compounds

The objective of this study is to use FEM analysis with COMSOL Multiphysics to simulate a p-FAIMS for different types of ions of interest in security applications. Not all the chosen ions have been used for testing the micro p-FAIMS, it has only been tested for volatile organic compounds. Simulations have been done with experimental data available at the literature [11, 17-19], and the main properties needed: K_0 , α_2 and α_4 , are summarized in Table 3-2. Ions chosen had known α_2 and α_4 values and covered the A and B ion types (C type is not considered), and they have different charges: two of them are positive and three negative. We have chosen a chemical warfare agent (CWA) simulant, two healthy risky volatile organic compounds (VOC) and three explosives, being the ions included in this work:

- *CWA simulant*: dimethyl methyl phosphonate or DMMP that emulates gas sarin. It can be presented in proton-bound monomer and dimer form, but dimers are only formed in high concentrations, so in this work we will focus on the protonated positive monomer DMMPH^+ .

- *Volatile organic compounds-VOC's:*
 - 2-propanone or acetone Ac. It can be presented in proton-bound monomer and dimer forms; in industry can be present in high concentrations (TWA¹ = 500 ppm, STEL² = 750 ppm and CEILING³: 3,000ppm [20]), in this work we will focus on the protonated positive dimer Ac₂H⁺.
 - Toluene or T. It can be presented as ion T⁺ and also in proton-bound monomer form TH⁺; (TWA = 10 ppm, STEL = 150 ppm and CEILING = 500 ppm [21]). The most frequently observed ions in are the protonated monomers TH⁺ instead of the monomers T⁺, therefore, in this work we are going to focus on the protonated monomer TH⁺.
- *Explosives:* we have chosen to study the negative monomers of the three more representative explosives:
 - 2,4,6-trinitrotoluene or TNT: Its negative monomer ion formed by proton abstraction (TNT-H)⁻.
 - 2,4-dinitrotoluene or DNT: Proton abstraction ion (DNT-H)⁻.
 - 1,3,5-trinitrobenzene or TNB; Associative electron capture ion TNB⁻.

	Chemical	Ion Acronym	Ion m/z (amu)	K_0 ($\times 10^{-4}$ m ² ·V ⁻¹ ·s ⁻¹)	α_2 (Td ⁻²)	α_4 (Td ⁻⁴)	Ref.
CWA simulant	DMMP (monomer) C ₃ H ₉ O ₃ P	DMMPH ⁺	125	1.94	5.09 $\times 10^{-6}$	-1.58 $\times 10^{-10}$	[17]
VOC	2-propanone (dimer) C ₃ H ₆ O	Ac ₂ H ⁺	117	1.88	1.34 $\times 10^{-5}$	-1.77 $\times 10^{-9}$	[18]
	Toluene (monomer) C ₇ H ₈	TH ⁺	93	2.30	1.28 $\times 10^{-5}$	-8.2 $\times 10^{-10}$	[19]
Explosives	TNT (monomer) C ₇ H ₅ N ₃ O ₆	(TNT-H) ⁻	226	1.54	4.4 $\times 10^{-6}$	-2.7 $\times 10^{-10}$	[11]
	DNT (monomer) C ₇ H ₆ N ₂ O ₄	(DNT-H) ⁻	181	1.45	7.7 $\times 10^{-6}$	-4.2 $\times 10^{-10}$	[11]
	TNB (monomer) C ₆ H ₃ N ₃ O ₆	TNB ⁻	213	1.94	5.7 $\times 10^{-6}$	-3.0 $\times 10^{-10}$	[11]

Table 3-2: Parameters used in the simulations, for the representative chosen ions.

¹ TWA is a dose that should not be exceeded over either an 8-hour period.

² STEL is the Short Term Exposure Limit, which is a running 15-minute average concentration.

³ Ceiling is the concentration that should never be exceeded, even for one instant.

3.8 Simulation Results

This section will show the simulation results for the p-FAIMS in the conditions defined in the previous sections. First a study of the carrier gas flow rate effects in ions detection is shown. Next step was the study of effects of the electric field in the p-FAIMS, for which we varied the frequency and amplitude of the dispersion voltage applied. Then, we did a studio of ions differentiation for some combinations from the chosen ions. And finally, we studied the dependence of the ions signal with the filtering electrodes length l .

3.8.a Carrier gas flow rate effects

The significant ion losses and peak broadening caused by diffusion suggest that the drift time or residence time t_{res} [ms], that is the time that takes to an ion to pass through the filtering electrodes and then reach the detector, is a critical parameter that determines p-FAIMS resolution. For this reason, we studied the behavior of toluene monomer under different carrier gas flows ranging from 500 to 2,000 sccm (standard centimeter cubic per minute or $\text{cm}^3 \cdot \text{min}^{-1}$ at standard pressure and temperature, 101,325 kPa and 298,15 K [9]). The dispersion voltage DV and the frequency of oscillation were fixed for this study at $|E_D|/N = 80$ Td (DV = 1,000 V) and $\nu_D = 2.0$ MHz, being the compensation field $|E_C|/N = 0.41$ Td (CV = -5.1 V). Filtering electrode length considered was 13 mm, and study was done for an ion concentration of 1 ppm.

In Figure 3-12 are shown the results obtained for toluene monomer ions TH^+ diluted in nitrogen that moves in the y -direction with different flow rates. Contour lines of each plot indicate that diffusion effects are more relevant for lower flows since in this case there are more ions that collide with upper and lower boundaries. However, for higher flow rates there are fewer collisions in the filtering region and a greater number of ions reach the detector.

In order to quantify the amount of ions reaching the detector in each case, the peak intensities for toluene monomer ions as function of the compensation field $|E_C|/N$ was evaluated and results obtained are shown in Figure 3-13. As can be seen, the maximum of the signal intensity is the value taken for the compensation field of the compound. As the flow increases the peak height increases due to lower ion losses caused by diffusion, this means that resolution is increased for higher flows. The width of the peak should also be considered as it determines the selectivity or resolving power of the system when an ions mixture is considered; therefore the resolving power decreases for higher flows.

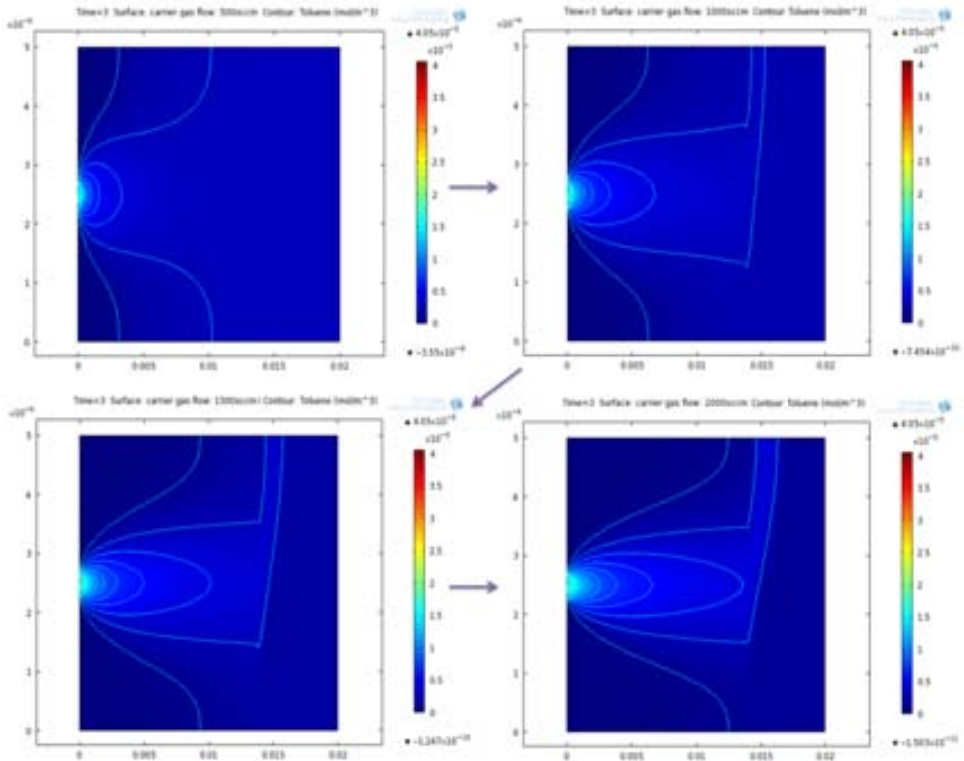


Figure 3-12: p-FAIMS simulation results for TH^+ ions diluted in nitrogen that moves in the y-direction with flow rates ranging from 500 to 2,000 sccm. $|E_D|/N = 80$ Td (DV = 1,000 V), $|E_C|/N = 0.41$ Td (CV = -5.1 V).

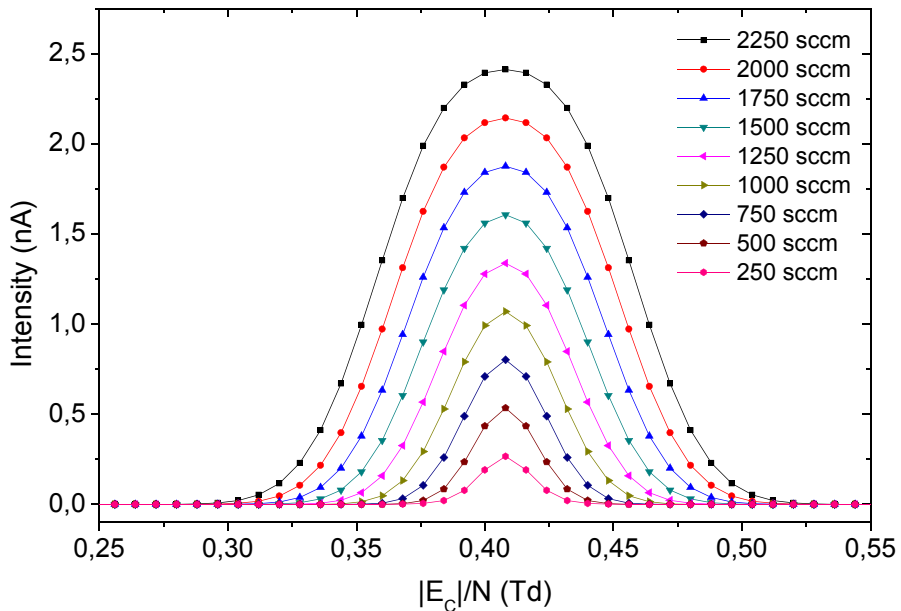


Figure 3-13: Signal intensities at the detector versus compensation voltages for different carrier gas flows. Simulation of toluene monomer TH^+ in the p-FAIMS. Filtering electrodes length is 13 mm, with $|E_D|/N = 80$ Td and $|E_C|/N = 0.41$ Td (CV = -5.1 V). Carrier gas flows in the range from 250 to 2,250 sccm.

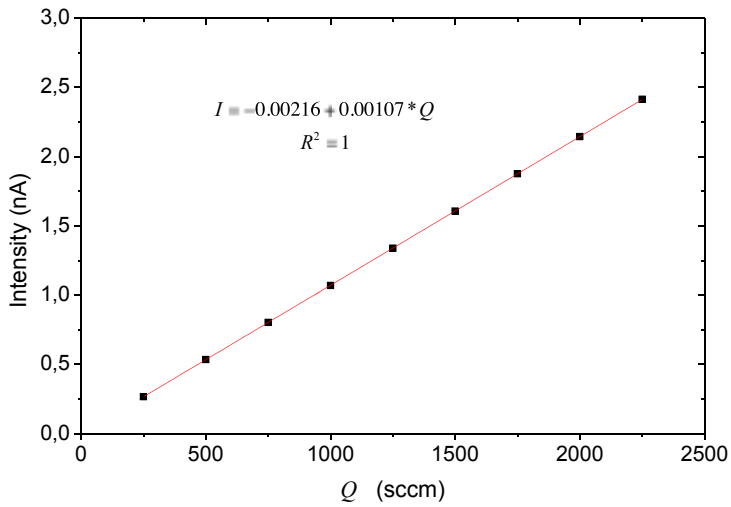


Figure 3-14: Maximum detector signal as a function of the carrier gas flow. Simulation of toluene monomer TH⁺ in the p-FAIMS. Filtering electrodes length is 13 mm, with $|E_D|/N = 80$ Td and $|E_C|/N = 0.41$ Td (CV = -5.1 V). Carrier gas flows in the range from 250 to 2,250 sccm.

The shape of the obtained signals are almost Gaussian, with an average adjust R-square of $R^2 = 0.998$. This means that the coulombic ion-ion repulsion is well defined in the simulations. In Figure 3-14 is shown the linear tendency of the maximum intensity for a concentration of 1 ppm of toluene ions as a function of the carrier gas flow in the range considered.

In Table 3-3 are listed the results for the carrier gas flow effects to 1 ppm of toluene monomer TH⁺ ions: maximum intensity I [nA]; the full width at half maximum (FWHM) or $w_{1/2}$ [Td] being calculated with a Gaussian de-convolution of the original signal; and the Resolving Power R_p [dimensionless] as defined in Section 2.3.c *Detection* as $R_p = |E_C/N|/w_{1/2}$, being the absolute value of the compensation field for the Toluene $|E_C/N| \sim 0.41$ Td.

Q (sccm)	I (nA)	$w_{1/2}$ (Td)	R_p
2,250	2.41	0.10	4.2
2,000	2.14	0.09	4.7
1,750	1.88	0.08	5.4
1,500	1.61	0.07	6.2
1,250	1.34	0.06	7.2
1,000	1.07	0.05	8.7
750	0.80	0.04	10.9
500	0.53	0.04	10.9
250	0.27	0.02	16.9

Table 3-3: Signal variations for Toluene monomer ions under different carrier gas flow conditions.

As commented previously, as the flow is increased the intensity is increased but also the peak width at half maximum, meaning that a decrease in the Resolving Power is obtained. Since the intensity of the signal and the resolving power have opposite response to the flow gas, one way to find a compromise value is multiplying both magnitudes and see if there is a maximum value. This was done for the toluene monomer TH^+ ions as shown in Figure 3-15. The curve obtained, showed that the product $I \times R_p$ increases for low carrier gas flows until they reach a ‘plateau’ at 1,000 sccm approx. from which the product $I \times R_p$ is almost saturated (~ 10 nA), so this flow is the one that we consider as the better for our purposes and will be used from now on, leading a reasonable resolving power (~ 8.7 for TH^+ ions), and signal intensity (~ 1.07 nA). Another way to find the suitable carrier gas flow is calculating the Aspect ratio AR as defined in Section 2.2.f *Data collection and treatment*: $AR = I_{max}/w_b$, being I_{max} the intensity at the compensation field, and w_b is the width at the base of the peak, also obtained with the de-convolution of the signals. The obtained AR plot is also shown in Figure 3-15. We can see that its behavior is the same that for the $I \times R_p$ curve. For high carrier gas flows, $I \times R_p$ and AR are increased while R_p/L is decreased, as the Resolving power is decreased (Table 3-3). And in opposite way for low carrier gas flows, for which the resolving power and R_p/L are increased while the $I \times R_p$ and AR are decreased. Therefore, both methods for calculating the optimum flow and resolving power are equivalent. The aspect ratio at 1,000 sccm for 1 ppm of toluene ions is ~ 15 nA/Td.

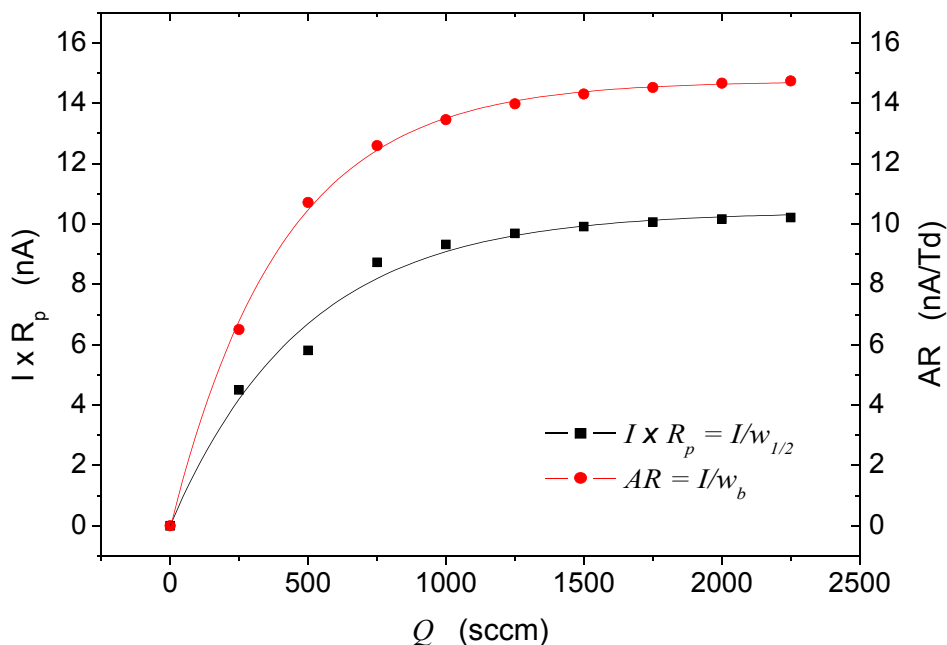


Figure 3-15: Product of the signal Intensity and the Resolving Power and of the Aspect Ratio as a function of the carrier gas flow, for 1 ppm of toluene monomer TH^+ ions. Filtering electrodes length is 13 mm.

Q (sccm)	$I \times R_p$ (nA)	w_b (Td)	AR (nA/Td)	R_p/L (cm ⁻¹)
2,250	10,2	0.16	14.7	3.3
2,000	10,2	0.15	14.7	3.6
1,750	10,1	0.13	14.5	4.1
1,500	9,9	0.11	14.3	4.7
1,250	9,7	0.10	14.0	5.6
1,000	9,3	0.08	13.4	6.7
750	8,7	0.06	12.6	8.4
500	5,8	0.05	10.7	8.4
250	4,5	0.04	6.5	13.0

Table 3-4: Signal variations for 1 ppm of Toluene monomer ions under different carrier gas flow conditions.

In Table 3-4 are listed the values obtained that configures Figure 3-15 for 1 ppm of toluene monomer TH⁺ ions and for different carrier gas flows Q [sccm]: $I \times R_p$ [nA]; the peak width at the base w_b [Td] being calculated with a Gaussian de-convolution of the original signal; the Aspect Ratio AR [nA/Td] and the relation of the Resolving power with the drift length or filtering electrodes length L [cm], R_p/L , is calculated with $L = 13$ mm. The R_p/L is used to make the results comparable to the obtained in the literature and previously showed in Section 2.3.c *Detection*.

For 1,000 sccm chose as optimum flow, the R_p/L is ~ 6.7 cm⁻¹, being a slightly better value (but of the same order of magnitude) than the available data in the literature ranging from 1.1 to 4.3 cm⁻¹.

The obtained intensity for 1 ppm is $I_{sim,1ppm} \sim 1.07$ nA. Papanastasiou *et al.* studied 0.15 ppm for the same flow condition but at a frequency of 1.0 MHz, obtaining an intensity value $I_{exp} \sim 1.30$ pA. Supposing linear variation with the concentration, for 0.15 ppm the intensity is reduced $I_{sim} \sim 1.61 \times 10^{-10}$ A. And considering that in the simulations were assumed that the entire sample is ionized, whereas Shvartsburg *et al.* [22] found that only a 3% of sample is ionized this leads a $I_{sim} \sim 4.83$ pA that is of the same order of the experimental value obtained in the literature.

3.8.b Electric Field study

Ions velocity in the z direction in the filter electrodes region is proportional to the electric field, as shown in Equation (2.42) from Section 2.3.b *FAIMS Ion Dynamics*, being the proportional factor the mobility coefficient $K(E/N)$.

The electric field study was done in two steps: (i) the study of the effect of changing the frequency having fixed the total electric field amplitude (the sum of the dispersion and compensation fields); and (ii) for a fixed frequency, it has been studied how changes the compensation field or E_C/N [Td] when changing the dispersion field

amplitude or E_{iD}/N [Td], being the compensation field defined as Equation (2.57) from Section 2.3.b *FAIMS Ion Dynamics*.

First we studied how varying the frequency for a fixed E_{iD} affects the movement of toluene monomer ions. Figure 3-16 shows the results obtained for a dispersion field of $|E_D|/N = 80$ Td, without compensation field $|E_C|/N = 0$ Td, and for two different frequencies ν_D : 1.0 and 2.0 MHz. For a better comprehension, results are shown as trajectories inside the first 3 mm of the filtering electrodes length instead of COMSOL figures. The y -axis velocity of ions does not change as expected. Only the paths in z -axis for each period, are larger as lower is the frequency, therefore more ions are lost to the walls of the p-FAIMS. This means that effective gap is also reduced as lower is the frequency, and the intensity measured will depend upon the frequency of the applied waveform. In our simulations no difference was found between 1 and 2 MHz due to the fact that ions are introduced just in the middle of the drift tube.

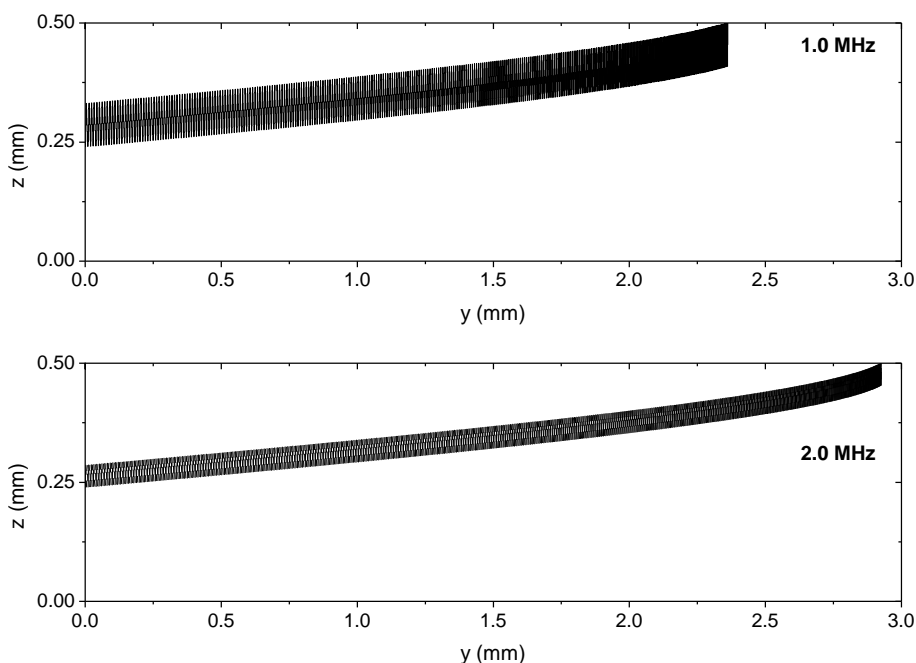


Figure 3-16: Toluene monomer pathways in between the filtering electrodes without applying a compensation field ($|E_C|/N = 0$ Td), for two dispersion fields $|E_D|/N$ of TOP) 60 Td and BOTTOM) 80 Td.

Next step is fixing the frequency and study how changes the compensation field of toluene monomer ions when changing the dispersion field amplitude or E_{iD}/N .

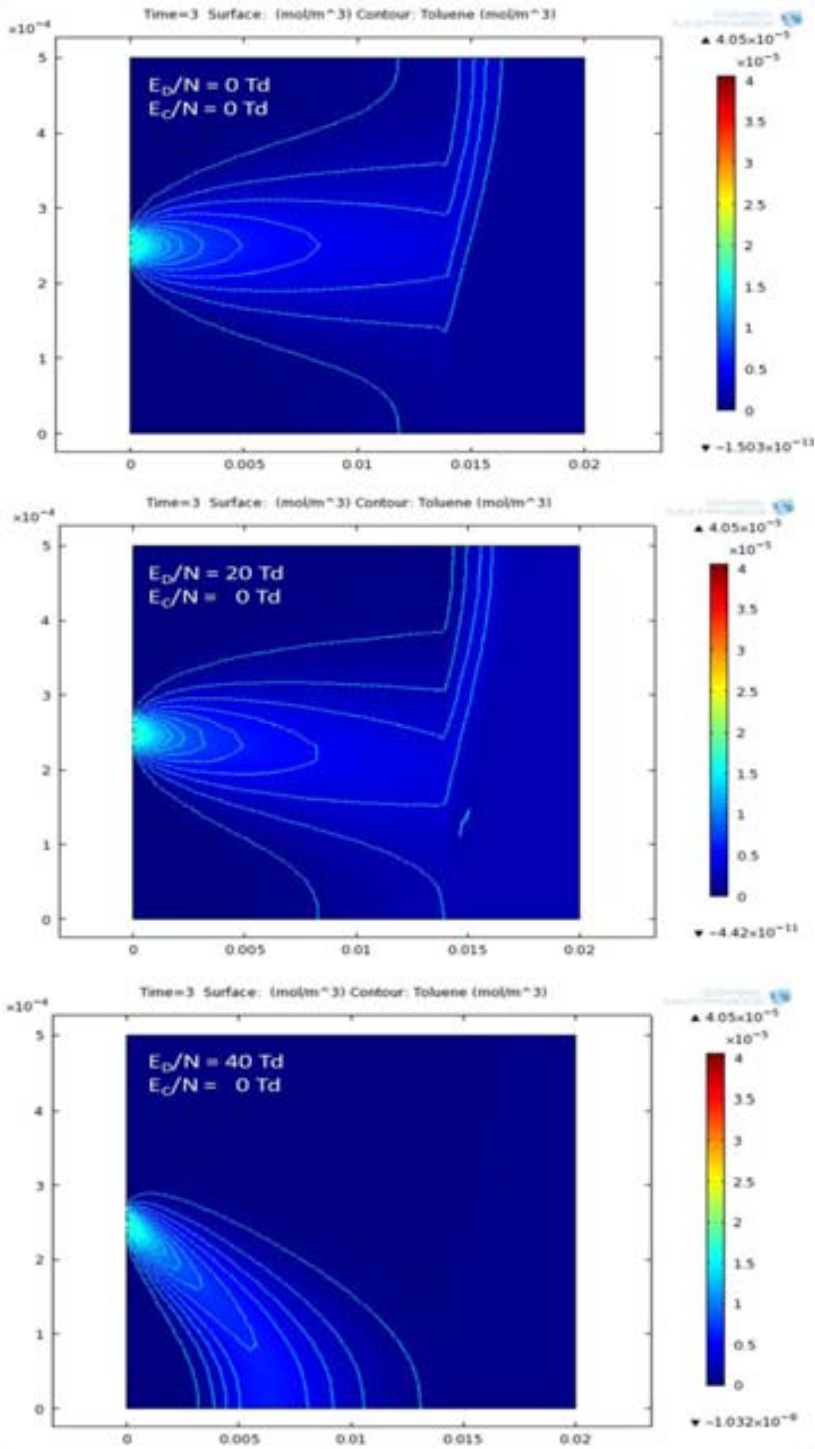


Figure 3-17: p-FAIMS simulation results at $|E_D|/N = 0, 20$ and 40 Td for 1 ppm of toluene monomer ions without compensation field. Frequency fixed at 2.0 MHz, and carrier gas flow of 2,000 sccm.

With this purpose the behavior of 1 ppm of toluene monomer ions inside the p-FAIMS was simulated for dispersion field amplitudes of 0 Td, 20 Td and 40 Td without compensation field. Results are shown in Figure 3-17, as can be seen the trajectory of ions is horizontally in the first case due to the absence of dispersion field, electric field influence begins for a 20 Td dispersion field and in this case a certain amount of ions is lost at the bottom boundary. For a dispersion field of 40 Td no ions reach the detector.

In Figure 3-18 are shown the results obtained for the compensation field at different dispersion fields. It can be seen the B type behavior of TH^+ ions, meaning that $|E_c|/N$ vs. $|E_d|/N$ curve increases until reaching a maximum and then decreases.

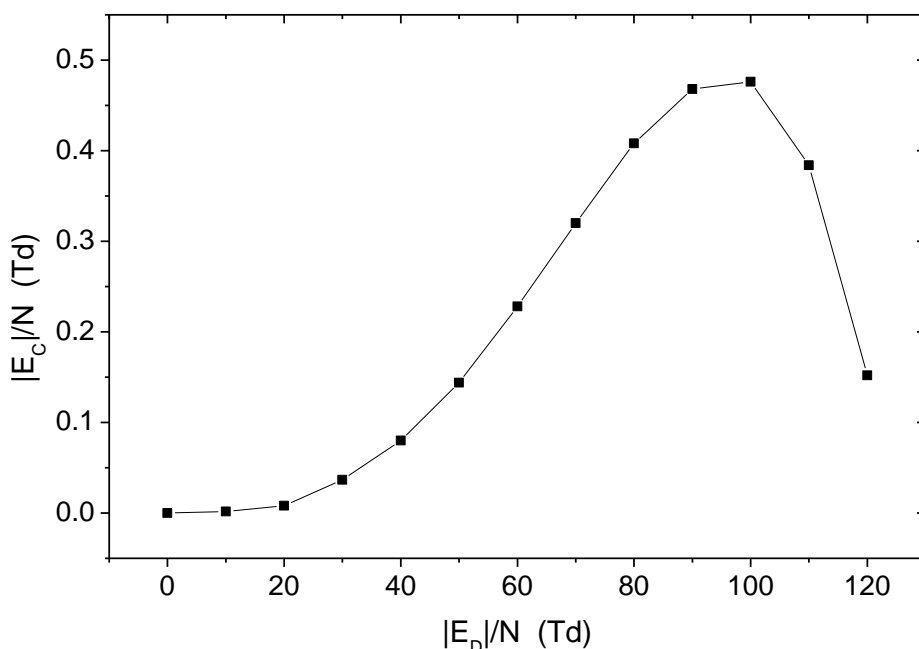


Figure 3-18: Obtained compensation fields for toluene monomer or TH^+ ions.

3.8.c Ions differentiation

Different combinations of compounds were studied in mixtures, but always for the same concentration of 1 ppm_v and flow of 1,000 sccm. Filtering length was 13 mm in all cases. Two studied mixtures were defined, trying to cover the major range of security compounds.

Mixture 1: one CWA (DMMP) with two VOC's (2-propanone and Toluene) and an Explosive (TNT)

Mixture 2: three Explosives (TNT, DNT and TNB)

Mixture 1: DMMP, 2-propanone, Toluene and TNT

For the first mixture, the modeled ions correspond to a chemical warfare agent simulant positive protonated ion monomer: DMMPH^+ that emulates gas sarin; two healthy risky volatile organic compounds: a positive protonated ion dimer, Ac_2H^+ and a positive protonated monomer ion TH^+ ; and an explosive negative monomer ion, the $(\text{TNT-H})^-$. Their main properties are summarized in Table 3-2.

The compensation fields versus dispersion field plots of the simulated compounds in nitrogen are shown in Figure 3-19. We should note that DMMPH^+ ions have a type A behavior, and that Ac_2H^+ , TH^+ and $(\text{TNT-H})^-$ ions have a type B behavior, which means that their curves increase until reaching a maximum and then decrease. Also we can see, that DMMPH^+ and $(\text{TNT-H})^-$ curves never crosses, and they can be discriminated better in a mixture as higher is the dispersion field applied, while Ac_2H^+ ions crosses both DMMPH^+ and $(\text{TNT-H})^-$ curves, at ~ 70 and ~ 80 Td respectively. Similarly to DMMPH^+ , TH^+ ions can be clearly distinguishable from Ac_2H^+ and $(\text{TNT-H})^-$ ions, instead TH^+ and DMMPH^+ ions curves can be distinguishable for a wide range of fields but their curves crosses at ~ 115 Td.

At intersection values, would not be possible to differentiate the ions if they have the same charge, but dual detection is expected for ions with opposite charges. But as much as $|E_D|/N$ differs, the separation of the Mixture-1 compounds is possible.

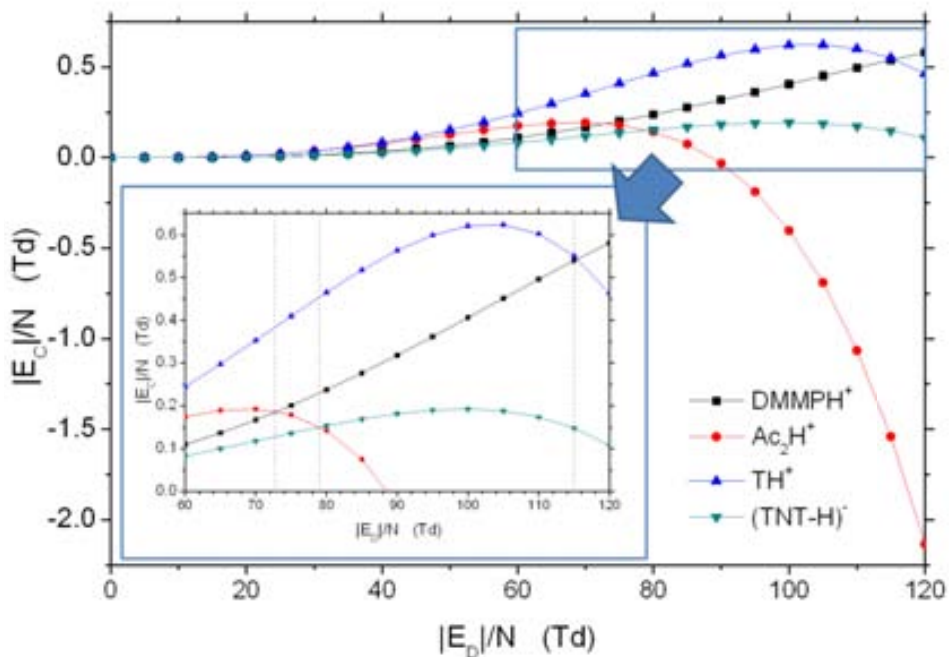


Figure 3-19: Compensation fields vs. dispersion fields for Mixture-1.

In Figure 3-20 is shown the distribution of concentration through the drift channel of ions of Ac_2H^+ and DMMPH^+ , for a dispersion field of $|E_D|/N = 70 \text{ Td}$ ($DV = 875\text{V}$), and for a compensation field of $(0.17 \text{ Td}, -2.1 \text{ V})$. As can be seen, an unsolved differentiation is obtained because both DMMPH^+ and Ac_2H^+ ions reach the detector at the same time and both have positive charges. DMMPH^+ ion concentration is shown as surface plot of different tonalities of rainbow, whereas Ac_2H^+ ion concentration is drawn as uniform coloring cyan lines, with a fixed 25 number of lines.

Experimentally it is widely used a dispersion field of 80 Td ($DV = 1,000 \text{ V}$) [23-26], so an accurate analysis will be done at this dispersion field.

For the positive mode, at $|E_D|/N = 80 \text{ Td}$, DMMPH^+ ions are detected at compensations fields of 0.22 Td (-2.8 V), Ac_2H^+ ions at 0.11 Td (-1.3 V), and TH^+ ions at 0.41 Td (-5.1 V). In Figure 3-21 and in Figure 3-22 are shown the COMSOL simulation results of DMMPH^+ concentration of for a $|E_D|/N = 80 \text{ Td}$ and for a compensation field of 0.22 Td (-2.8 V) with Ac_2H^+ and TH^+ ions, respectively. In both cases only the detection of DMMPH^+ ions is possible, so the differentiation of the compounds of Mixture-1 in positive mode is done.

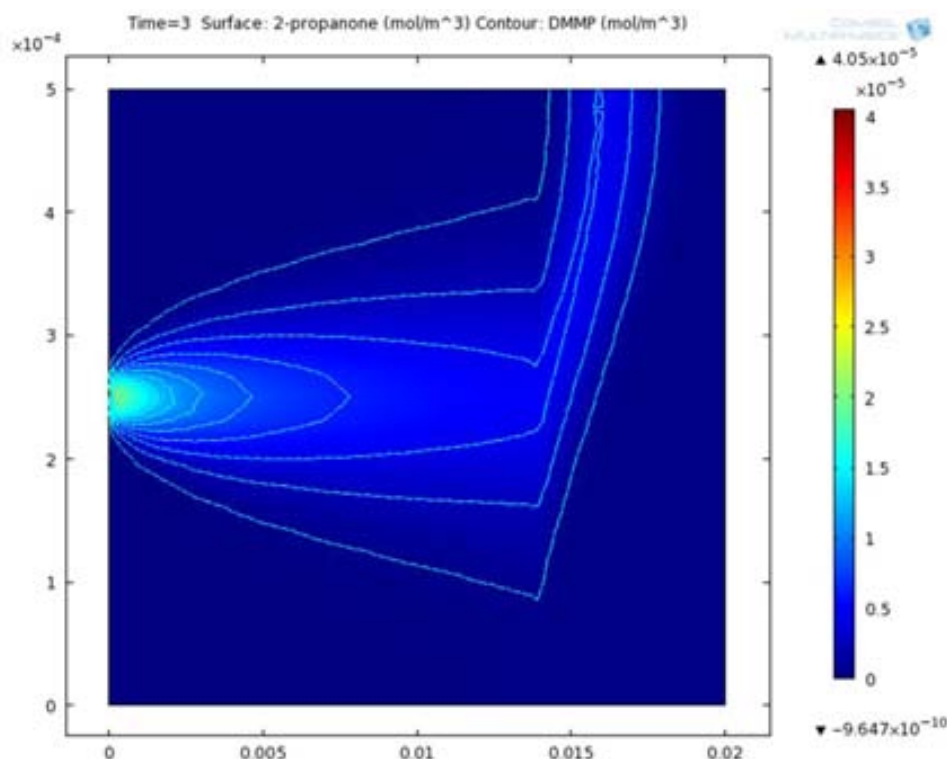


Figure 3-20: p-FAIMS simulation results at $|E_D|/N = 70 \text{ Td}$ ($DV = 875 \text{ V}$) and $|E_C|/N = 0.17 \text{ Td}$ (-2.1 V), for 2-propanone dimer or Ac_2H^+ ions (c, different tonalities of rainbow), and DMMP monomer or DMMPH^+ (c2, uniform coloring cyan lines).

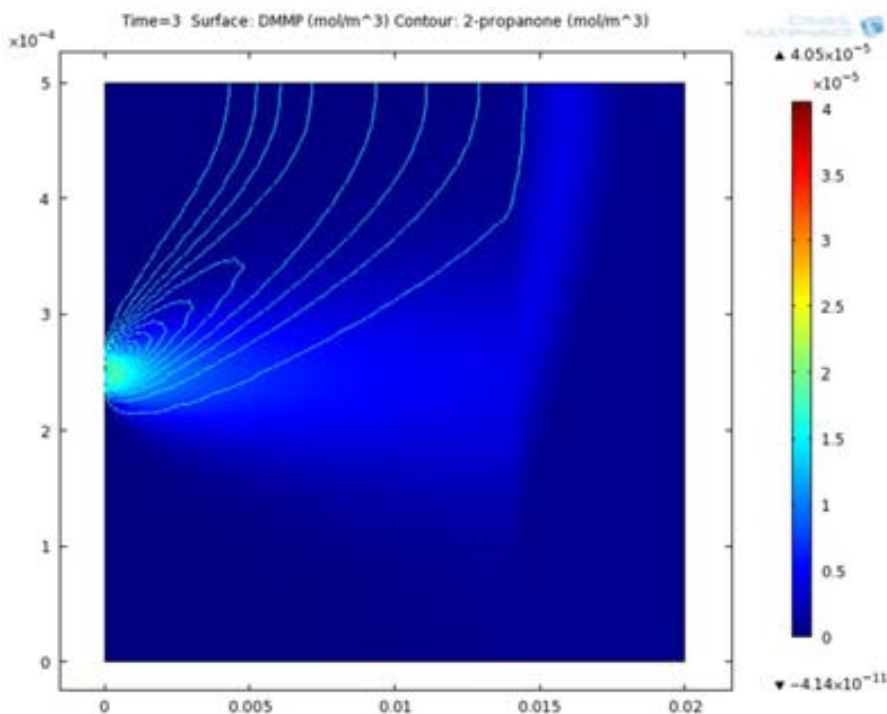


Figure 3-21: p-FAIMS simulation results at $|E_D/N| = 80$ Td for DMMPH⁺ ions (c, different tonalities of rainbow), and Ac₂H⁺ (c2, uniform coloring cyan lines), and for a compensation field of 0.22 Td (-2.8 V).

134

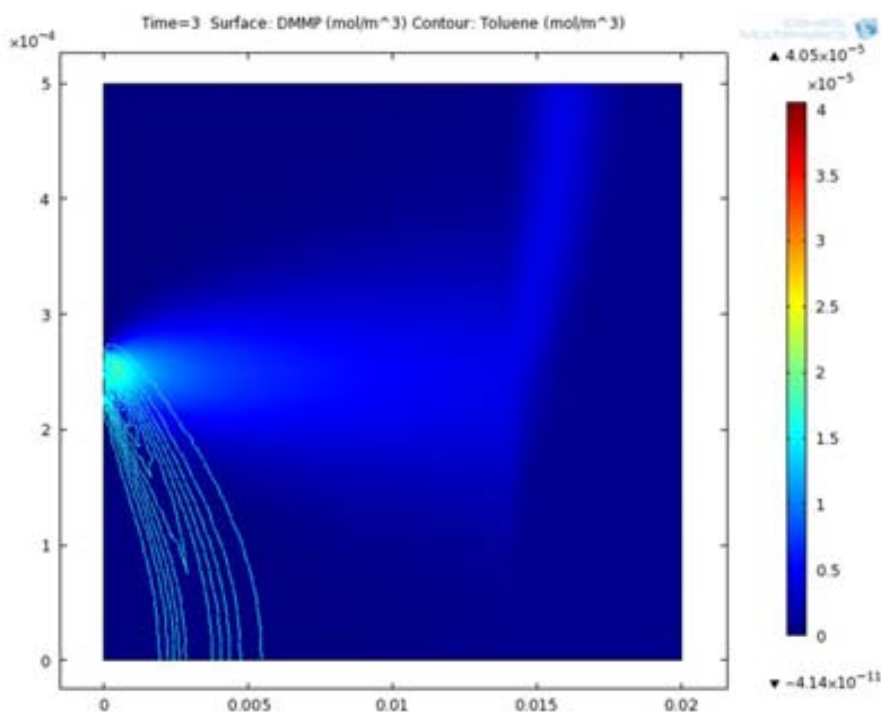


Figure 3-22: p-FAIMS simulation results at $|E_D/N| = 80$ Td for DMMPH⁺ ions (c, different tonalities of rainbow), and TH⁺ (c2, uniform coloring cyan lines), and for a compensation field of 0.22 Td (-2.8 V).

For the negative mode, at $|E_D|/N = 80$ Td, $(\text{TNT-H})^-$ ions are detected at a compensation field of 0.41 Td (-5.1 V). In Figure 3-23 is shown the distribution of concentration through the drift channel of Ac_2H^+ and $(\text{TNT-H})^-$ ions for a $|E_D|/N = 80$ Td and for a compensation field of 0.13 Td (-1.6 V) that is a mid-value of their respective compensation fields of 0.11 Td (-1.3 V) and 0.15 Td (-1.9 V). Both types of ions can be detected simultaneously measuring the current and obtaining a dual detection of ions. Positive charged ions are collected at the negative detector biased electrode while the negative charged ions are collected at the positive detector biased electrode. Ac_2H^+ ion concentration is shown as surface plot of different tonalities of rainbow, whereas $(\text{TNT-H})^-$ ion concentration is drawn as uniform coloring cyan lines, with a fixed number of lines of 25. The $(\text{TNT-H})^-$ ions are slightly drawn to the upper detector electrode, this means that a signal overlapping from $(\text{TNT-H})^-$ and Ac_2H^+ ions is expected.

In Figure 3-24 is shown the COMSOL simulation of the concentration of DMMPH^+ for a $|E_D|/N = 80$ Td and for a compensation field of 0.22 Td (-2.8 V) with $(\text{TNT-H})^-$. Only the detection of DMMPH^+ ions is possible, due to the fact that their compensation fields are really different. The same happens for TH^+ ions.

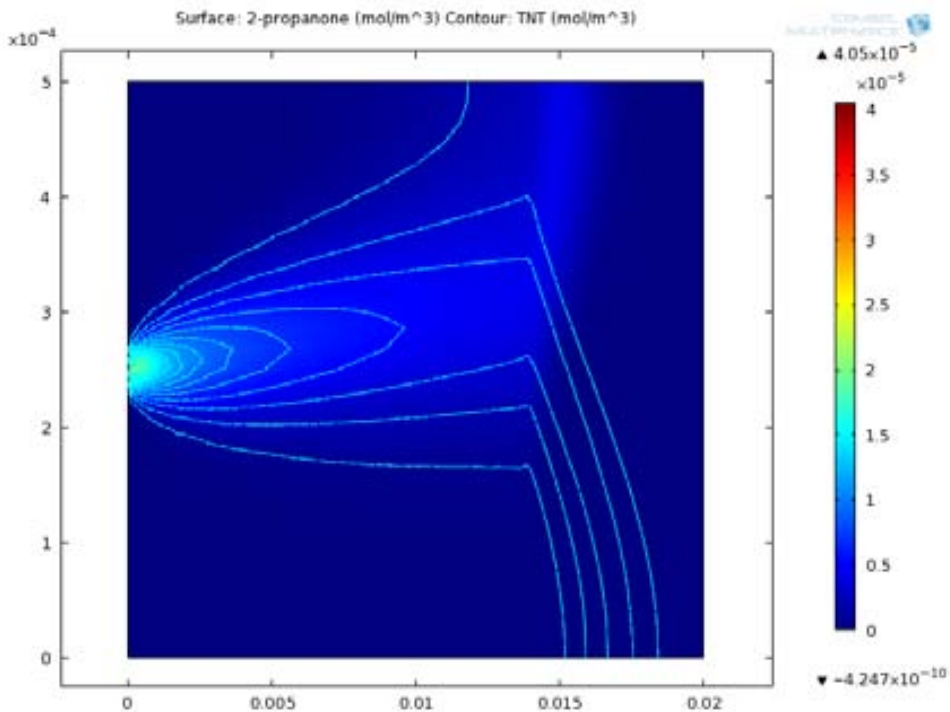


Figure 3-23: p-FAIMS simulation results at $|E_D|/N = 80$ Td for Ac_2H^+ ions (c, different tonalities of rainbow), and $(\text{TNT-H})^-$ (c2, uniform coloring cyan lines), and for a compensation field of 0.13 Td (-1.6 V).

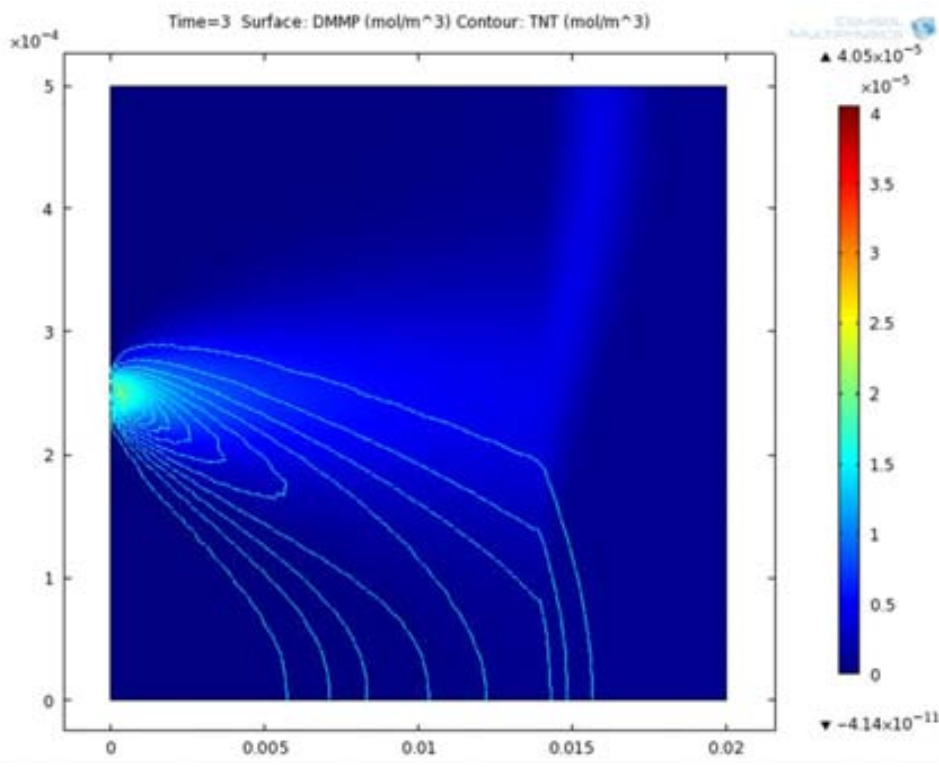
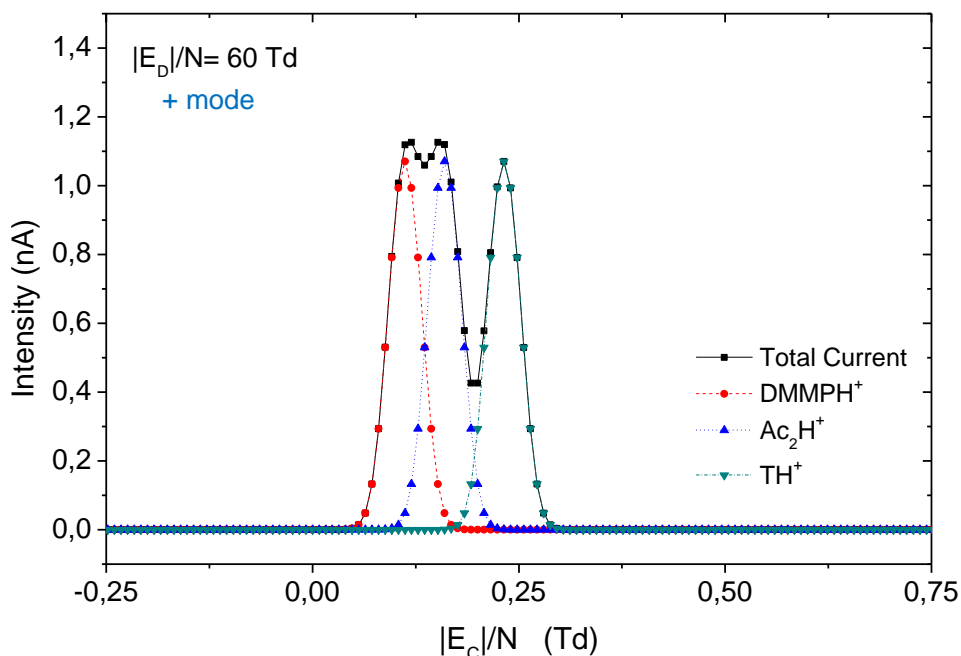


Figure 3-24: p-FAIMS simulation results at $|E_D|/N = 80$ Td for DMMPH⁺ ions (c, different tonalities of rainbow), and (TNT-H)⁻ (c2, uniform coloring cyan lines), and for a compensation field of 0.15 Td (-1.9 V).

Now we will obtain the chromatograms for the Mixture-1 at different dispersion fields: 60, 70, 80 and 90 Td. Results will be shown as compensation field in Td, and compensation voltage CV in V.

60 Td

In Table 3-5 are listed the results for Mixture-1 compounds at a dispersion field of 60 Td (750 V). In Figure 3-25 is shown the obtained chromatogram for a $|E_D|/N = 60$ Td (DV = 750 V), for the positive mode, meaning that only positive ions are detected. Also the de-convoluted ions signals (in order) are: DMMPH^+ (0.11 Td, -1.4 V), Ac_2H^+ (0.16 Td, -2.0 V) and TH^+ (0.23 Td, -2.9 V). Peaks of DMMPH^+ and Ac_2H^+ are overlapped but can be noted that there are two near peaks. The maximum intensity obtained is higher where 2-propanone and DMMP ions are overlapped (~ 1.13 nA), while for toluene the intensity is 1.07 nA, as in the de-convoluted signals of DMMP and 2-propanone ions. For the negative mode result at the dispersion voltage of 60 Td, only $(\text{TNT-H})^-$ monomer ions are detected (0.08 Td, -1.0 V) and its maximum intensity is also 1.07 nA.



137

Figure 3-25: Obtained and de-convoluted p-FAIMS chromatograms for the positive mode at $|E_D|/N = 60$ Td (CV = 750 V) for DMMPH^+ , Ac_2H^+ and TH^+ ions.

	Ion Acronym	$ E_C /N$ (Td)	CV (V)
+ mode	DMMPH^+	0.11	-1.4
	Ac_2H^+	0.16	-2.0
	TH^+	0.23	-2.9
- mode	$(\text{TNT-H})^-$	0.08	-1.0

Table 3-5: Obtained compensation voltages for Mixture-1 compounds at a dispersion field of 60 Td (750 V).

Moving to $|E_D|/N = 70$ Td ($DV = 875$ V) as seen in Figure 3-26, the obtained signal does not show two different compounds at ~ 0.16 Td, but once de-convoluted is noted the near values of the compensation fields: DMMPH⁺ (0.16 Td, -2.0 V) and Ac₂H⁺ (0.17 Td, -2.1 V). TH⁺ (0.32 Td, -4.0 V) ions are clearly differentiated. De-convoluted ions order is the same than in the 60Td condition: DMMPH⁺, Ac₂H⁺ and TH⁺. Obtained intensity, is almost twice where 2-propanone and DMMP ions are overlapped (~ 2.06 nA), while for toluene the intensity is 1.07 nA, as in the de-convoluted signals of DMMP and 2-propanone ions. In the negative mode at 70 Td only TNT monomer ions are detected at 0.12 Td (-1.5 V). In Table 3-6 are listed the results for Mixture-1 compounds at a dispersion field of 70 Td (875 V).

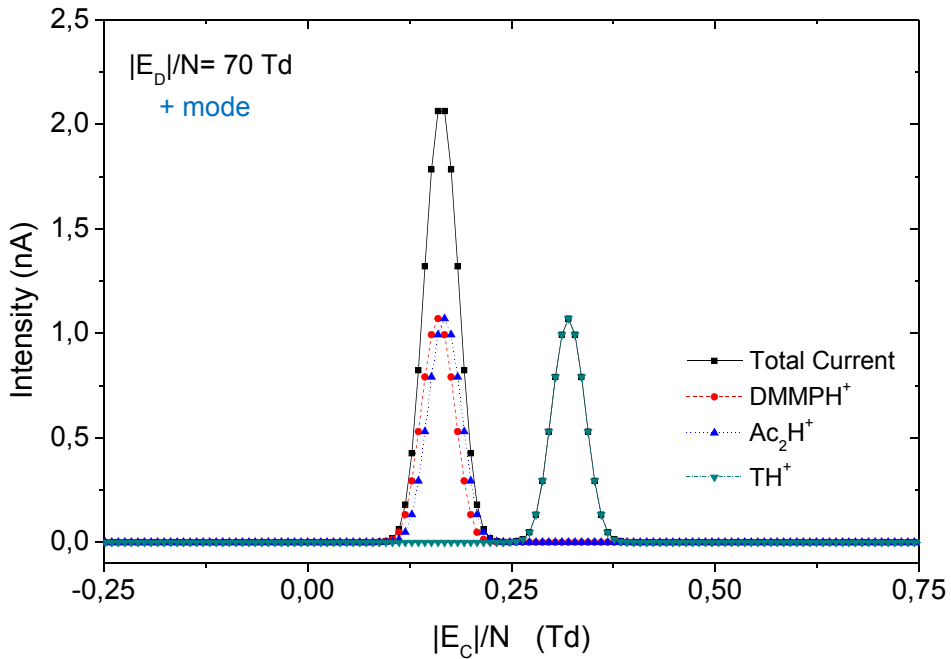


Figure 3-26: Obtained and de-convoluted p-FAIMS chromatograms for the positive mode at $|E_D|/N = 70$ Td ($DV = 875$ V) for DMMPH⁺, Ac₂H⁺ and TH⁺ ions.

	Ion Acronym	$ E_C /N$ (Td)	CV (V)
+ mode	DMMPH ⁺	0.16	-2.0
	Ac ₂ H ⁺	0.17	-2.1
	TH ⁺	0.32	-4.0
- mode	(TNT-H) ⁻	0.12	-1.5

Table 3-6: Obtained compensation voltages for Mixture-1 compounds at a dispersion field of 70 Td (875 V).

80 Td

For a higher dispersion field, $|E_D|/N = 80$ Td ($DV = 1,000$ V) in Figure 3-27 can be seen the de-convoluted ions signals for Ac_2H^+ at 0.11 Td (-1.3 V) and DMMPH^+ at 0.22 Td (-2.8 V) that are just tailoring overlapped, and TH^+ at 0.41 Td (-5.1 V). The order of the ions has changed, now: Ac_2H^+ , DMMPH^+ and TH^+ instead of DMMPH^+ , Ac_2H^+ and TH^+ as was in 60 and 70 Td. In the negative mode at 80 Td where only TNT monomer ions are detected at 0.15 Td (-1.9 V), its value has increased respect from the 70 Td value. Obtained intensities are in all cases of 1.07 nA. In Table 3-7 are listed the results for all Mixture-1 compounds at a dispersion field of 80 Td.

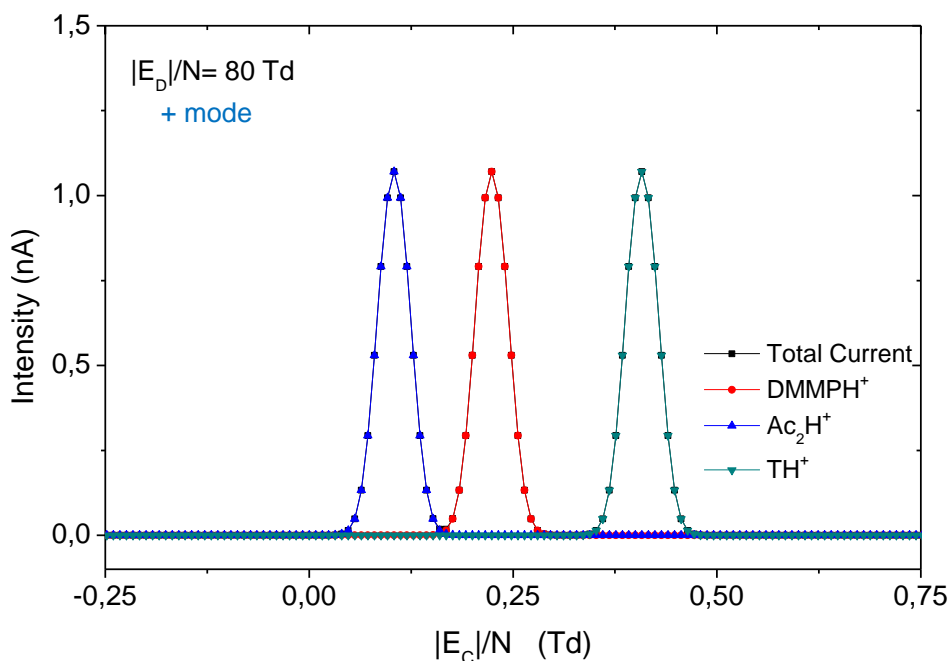


Figure 3-27: Obtained and de-convoluted p-FAIMS chromatograms for the positive mode at $|E_D|/N = 80$ Td ($DV = 1,000$ V) for DMMPH^+ , Ac_2H^+ and TH^+ ions.

	Ion Acronym	$ E_C /N$ (Td)	CV (V)
+ mode	DMMPH^+	0.22	-2.8
	Ac_2H^+	0.11	-1.3
	TH^+	0.41	-5.1
- mode	$(\text{TNT-H})^-$	0.15	-1.9

Table 3-7: Obtained compensation voltages for Mixture-1 compounds at a dispersion field of 80 Td (1,000 V).

90 Td

Finally in Figure 3-28 is shown the obtained chromatogram for $|E_D|/N = 90$ Td ($DV = 1,125$ V), where ions are clearly differentiated: DMMPH^+ (0.29 Td, -3.7 V), Ac_2H^+ (0.09 Td, -1.1 V) and TH^+ (0.47 Td, -5.9 V) compensation fields are different enough to be fully differentiated. The order of the ions is the same than in 80 Td. In the negative mode at 90 Td where only TNT monomer ions are detected (0.18 Td, -2.2 V), its value has increased respect from the 80 Td value. Obtained intensities are in all cases of 1.07 nA. In Table 3-8 are shown the results for all Mixture-1 compounds at a dispersion field of 90 Td.

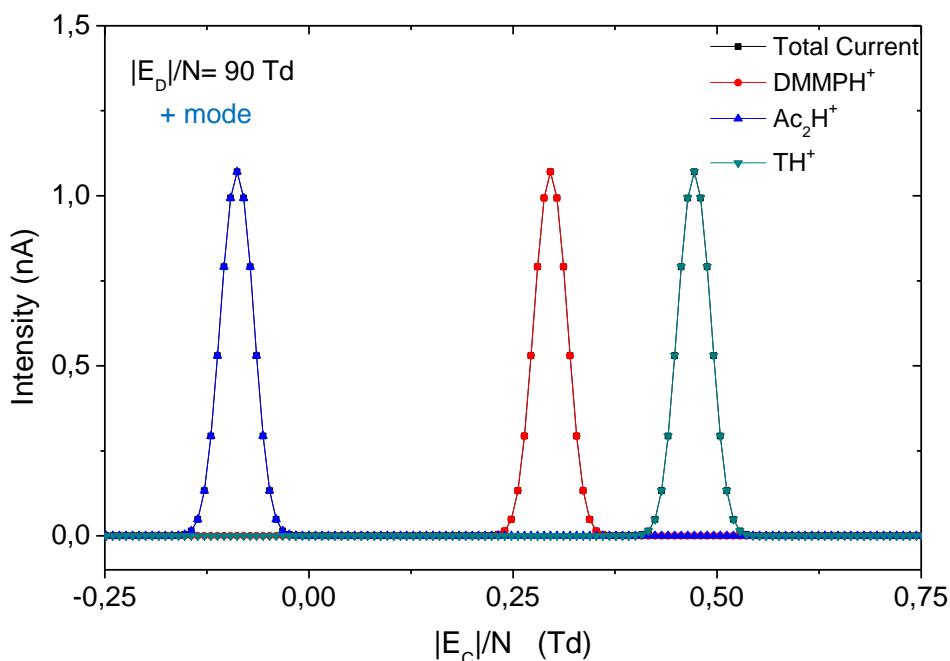


Figure 3-28: Obtained and de-convoluted p-FAIMS chromatograms for the positive mode at $|E_D|/N = 90$ Td ($DV = 1,125$ V) for DMMPH^+ , Ac_2H^+ and TH^+ ions.

	Ion Acronym	$ E_C /N$ (Td)	CV (V)
+ mode	DMMPH^+	0.29	-3.7
	Ac_2H^+	-0.09	+1.1
	TH^+	0.47	-5.9
- mode	$(\text{TNT-H})^-$	0.18	-2.2

Table 3-8: Obtained compensation voltages for Mixture-1 compounds at a dispersion field of 90 Td (1,125 V).

Those results clearly show the A or B type of the α -function for the simulated compounds. This means that compensation fields for A type ions would increase (DMMPH⁺ case) as dispersion field increase, while for B type ions would increase after reaching a maximum and then, decrease (Ac₂H⁺ case) when dispersion field increases.

Mixture 2: Explosives: TNT, DNT and TNB

For the second mixture, the modeled ions correspond to vapor phase compounds of three explosives: 2,4,6-trinitrotoluene monomer ion or (TNT-H)⁻; 2,4-dinitrotoluene monomer ion or (DNT-H)⁻; and 1,3,5-trinitrobenzene monomer ion or TNB⁻ in nitrogen ambient. Their main properties are summarized in Table 3-2, all the ions considered in this mixture are negative, and they would be detected in the negative mode.

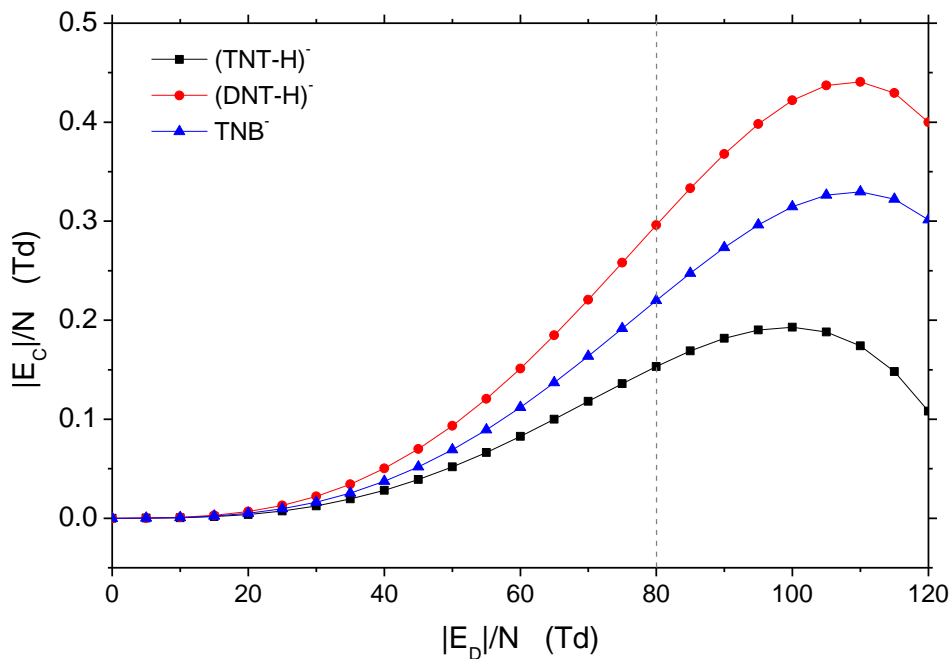


Figure 3-29: Compensation fields vs. dispersion fields for Mixture-2.

As the dispersion voltage is increased, the compensation voltages needed to pass ions through the drift tube are also increased up to a maximum from which, there is an inversion in slope, at $|E_d|/N = 100$ Td (DV = 1,250 V) for (TNT-H)⁻, and $|E_d|/N = 110$ Td (DV = 1,375 V) for (DNT-H)⁻ and TNB⁻ ions as can be seen in

Figure 3-29. These behaviors correspond to the so-called B type ions. For low RF electric fields $|E_D|/N < 30$ Td –equivalent to an electric field of $7,500 \text{ V}\cdot\text{cm}^{-1}$ for a gap of 0.5 mm– there is no dependence of mobility with electric field, therefore $CV \sim 0$ V for all ions, and in this case ions are not differentiated. Instead, for $30 < |E_D|/N \leq 120$ Td ions of Mixture-2 are clearly differentiated. Simulation is focused on a dispersion field of 80 Td, at which all three explosives should be clearly differentiated, as seen in Figure 3-29.

Results will be shown as compensation field in Td, and compensation voltage or CV in V. At $|E_D|/N = 80$ Td ($DV = 1,000$ V), $(\text{TNT-H})^-$ ions are detected at 0.15 Td (-1.9 V), $(\text{DNT-H})^-$ ions at 0.27 Td (-3.4 V), and TNB^- ions at 0.21 Td (-2.6 V). In Figure 3-30 and in Figure 3-31 are shown the COMSOL simulation results of the concentration of $(\text{TNT-H})^-$ for a $|E_D|/N = 80$ Td and for a compensation field 0.15 Td (-1.9 V) with $(\text{DNT-H})^-$ and TNB^- ions, respectively. In both cases the detection of $(\text{TNT-H})^-$ ions is possible, but whereas $(\text{TNT-H})^-$ ions and $(\text{DNT-H})^-$ ions can be clearly differentiated at this dispersion field, part of the TNB^- ions are slightly drawn to the low detector electrode, this means that a signal overlapping from $(\text{TNT-H})^-$ and TNB^- ions is expected. In Table 3-7 are listed the results for Mixture-2 compounds at a dispersion field of 80 Td.

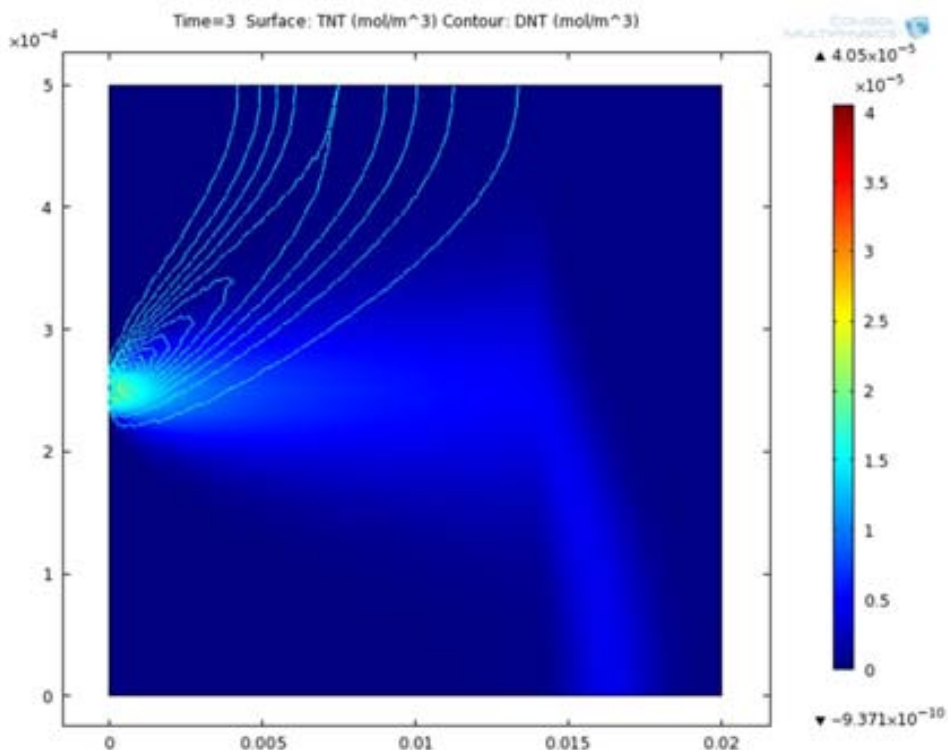


Figure 3-30: p-FAIMS simulation results at $|E_D|/N = 80$ Td for $(\text{TNT-H})^-$ ions (c, different tonalities of rainbow), and $(\text{DNT-H})^-$ (c2, uniform coloring cyan lines), and for a compensation field of 0.15 Td (-1.9 V) for which only $(\text{TNT-H})^-$ detection is obtained. Differentiation is achieved.

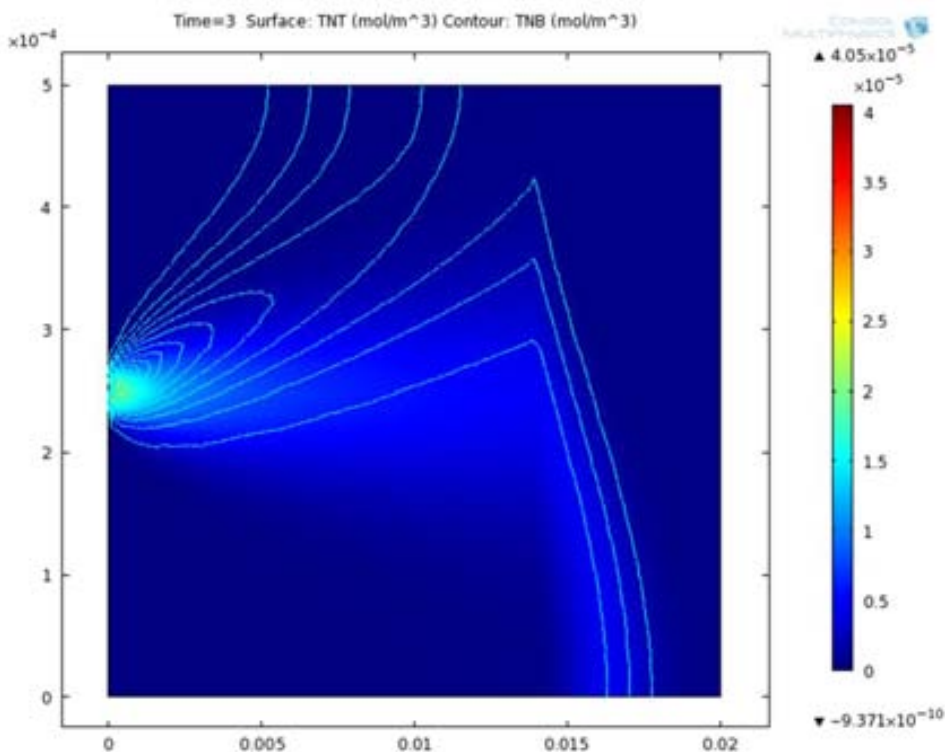


Figure 3-31: p-FAIMS simulation results at $|E_D|/N = 80$ Td for (TNT-H)⁻ ions (c, different tonalities of rainbow), and TNB⁻ (c2, uniform coloring cyan lines), and for a compensation field of 0.15 Td (-1.9 V) for which only (TNT-H)⁻ detection is obtained. Only partially differentiation is achieved.

	Ion Acronym	$ E_C /N$ (Td)	CV (V)
- mode	(TNT-H) ⁻	0.15	-1.9
	(DNT-H) ⁻	0.27	-3.4
	TNB ⁻	0.21	-2.6

Table 3-9: Obtained compensation voltages for Mixture-2 compounds at a dispersion field of 80 Td (1,000 V).

Obtained signal for Mixture-2 compounds at a dispersion field of 80 Td is shown in Figure 3-32, where is also shown the de-convoluted chromatogram. Peaks of (TNT-H)⁻ and TNB⁻ are overlapped but can be noted that there are two near peaks. Obtained maximum intensity is higher where TNT and TNB ions are overlapped (~1.09 nA), while for DNT the intensity is 1.07 nA.

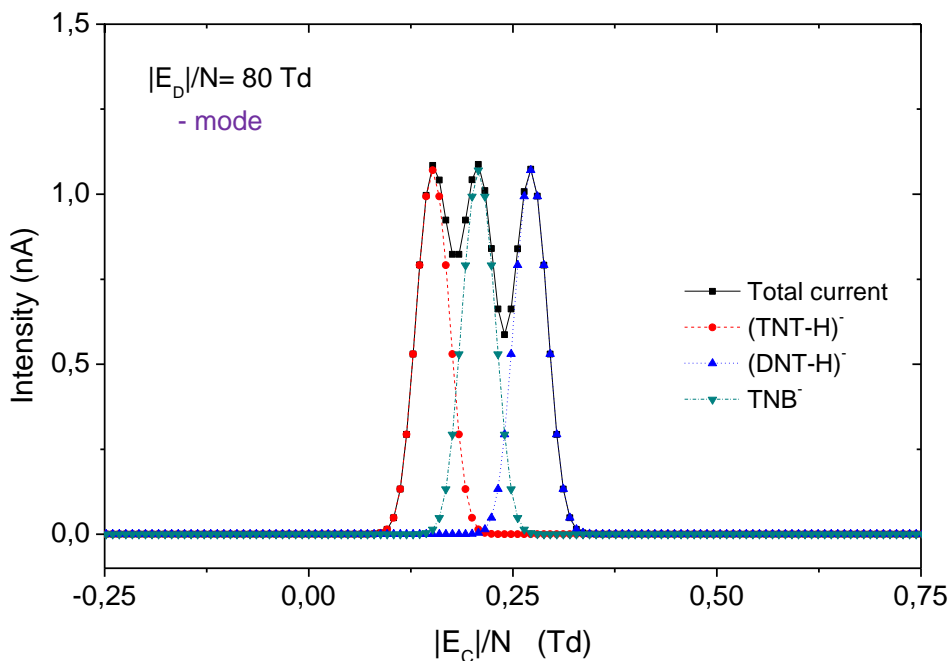


Figure 3-32: Obtained intensities (Total current) and de-convoluted chromatograms for a dispersion field of 80 Td for Mixture-2: (TNT-H)⁻, (DNT-H)⁻ and TNB⁻.

3.8.d Filtering Electrodes Length Dependence

Until now we have studied how the carrier gas flow and the electric field affects the ion motion through the drift tube. If we vary the length of the filtering electrodes, and consequently the length of the drift tube, the movement of the ions due to the carrier gas and the electric field will be the same, but you can detect more or less ions depending on the length because always some un-compensated ions can reach the detector but their quantity decreases for longer drift tubes as more ions will be lost in the walls. That is to say, an enlargement of the drift tube results in a decrease of the peak width of the characteristic chromatogram of the ions without affecting the signal intensity. In this way resolution and resolving power of the device are improved if the tube is longer.

In this work, to determine how the length of the filtering electrodes affects to the ions detected, two lengths were studied: 13 and 20 mm. The dispersion field applied was $|E_D|/N = 60$ Td ($DV = 750$ V) with $\nu_D = 2.0$ MHz, and for a carrier gas flow of 1,000 sccm, values considered suitable as DMMPH⁺ and Ac₂H⁺ ions are overlapped for a tube length of 13 mm. A complete $|E_C|/N$ scan was obtained for a mixture of both compounds for the two different lengths considered and the improvement due to the enlargement of the tube is shown in Figure 3-33.

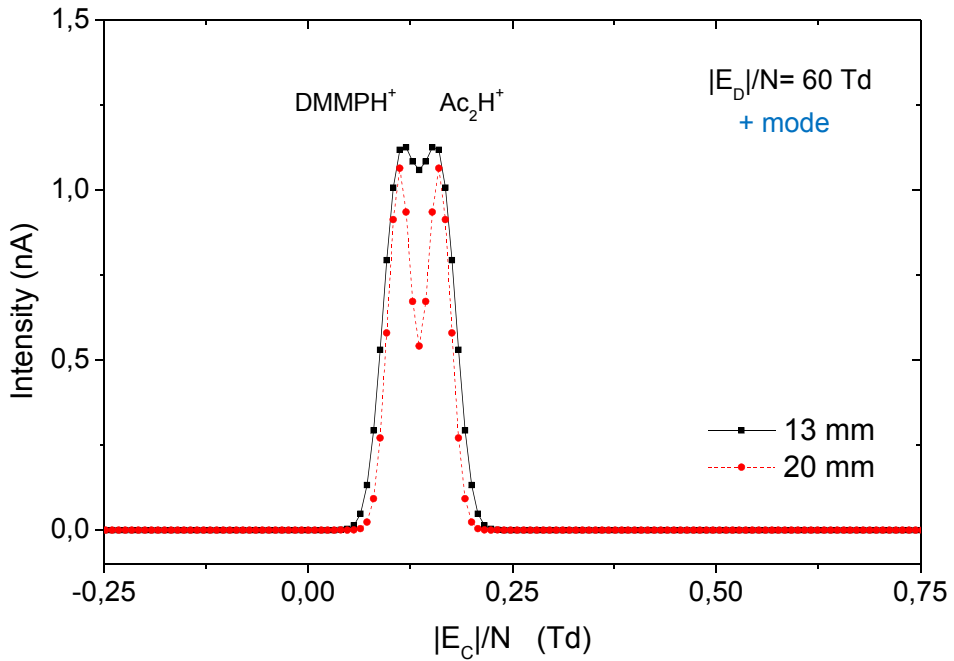


Figure 3-33: Obtained intensities for a mixture of 1 ppmv of DMMPH⁺ and 1 ppmv of Ac₂H⁺, at a carrier gas flow of 1,000 sccm, and at $|E_D|/N = 60$ Td ($DV = 750$ V). Two filtering lengths of 13 and 20 mm are considered.

Resolution and Resolving Power are improved for a length of 20 mm. Resolution is calculated using Equation (2.70) (Section 2.3.c *Detection: Resolution and Resolving power*), and Resolving Power using Equation (2.69), but both equations are calculated for compensation fields instead that for compensation voltages, as:

$$R = 2 \times \frac{\left| \left(\frac{E_C}{N} \right)_A - \left(\frac{E_C}{N} \right)_B \right|}{w_{b,A} + w_{b,B}} \quad (3.13)$$

$$R_p = \frac{|E_C/N|}{w_{1/2}} \quad (3.14)$$

where $(E_C/N)_{ion}$ [Td] are the compensation fields for the ions of interest, $|E_C/N|$ [V] is the absolute value of the compensation voltage for a particular ion at maximum peak height. The $w_{b,ion}$ [Td] are the peak width at the base of the peak, and $w_{1/2}$ [Td] is the full width at half maximum height of the peak, as defined in Section 2.2.f *Data collection and treatment*.

In Table 3-10 are summarized the obtained resolution R [dimensionless], resolving power R_p [dimensionless], and the ratio R_p/L [cm^{-1}]. The resolution obtained for the 20 mm long drift tube ($R_{20\text{mm}} = 0.94$) is a 27 % higher than the one obtained for 13 mm ($R_{13\text{mm}} = 0.68$). Also the peak width at half height ($w_{1/2}$) is reduced from 0.05 Td (0.6 V) for 13 mm to 0.03 Td (0.4 V) for 20 mm, meaning that increasing the filtering length narrowing peaks are obtained. Due to their dependence on compensation field value, resolving power is lower for DMMPH⁺ ions ($|E_C/N| = 0.11$ Td, -1.4 V) than Ac₂H⁺ ($|E_C/N| = 0.16$ Td, -2.0 V). The ratio R_p/L is used to be able to compare results obtained to the ones found in the literature and previously showed in Section 2.3.c *Detection*. As can be seen in the Table 3-10, those results have the same order of magnitude than data reported by other authors for R_p/L that ranges from 1.1 to 4.3 cm^{-1} (Section 2.3.c *Detection: Resolution and Resolving Power*).

Ion Anronym	L (cm)	w_b (Td)	$w_{1/2}$ (Td)	R	R_p	R_p/L (cm^{-1})
DMMPH ⁺	13	0.08	0.05	0.68	2.3	1.8
	20	0.06	0.03	0.94	3.2	1.6
Ac ₂ H ⁺	13	0.08	0.05	0.68	3.5	2.7
	20	0.06	0.03	0.94	4.7	2.4

Table 3-10: Obtained parameters for DMMPH⁺ and Ac₂H⁺ ions considering two different lengths of the drift tube.

Improving resolution, means that compounds would be less or non-overlapped, and therefore, selectivity is improved. So as the compounds we want to detect have relatively near compensation fields the best option is to fabricate longer filtering electrodes.

3.9 Validation

Once the major factors that affects the ion motion and transmission in the drift channel have been studied (carrier gas flow, electric fields and filtering electrodes length), next step is to validate our simulations.

As the main result obtained from simulations is the compensation field of each ion we will focus our validation in this value. Studied ions are reported for different experimental conditions and their compensation field values can be found in the literature [11, 17-19, 27-29].

In Table 3-11 are summarized the main experimental parameters used by different authors that affects compensation field. For this reason carrier gas flow, dispersion field frequency and filter electrodes length are not included.

Ion Acronym	Carrier gas	Carrier gas Temperature	FAIMS gap	Ref.
DMMPH ⁺	Air	60°C	0.5 mm	[17, 27]
Ac ₂ H ⁺	Air	60°C	0.5 mm	[18]
TH ⁺	N ₂	100°C	Not provided	[19, 28]
(TNT-H) ⁻	Air	25°C	Coaxial FAIMS	[11, 29]
(DNT-H) ⁻	Air	25°C	Coaxial FAIMS	[11, 29]
TNB ⁻	Air	25°C	Coaxial FAIMS	[11, 29]

Table 3-11: Operative conditions for the considered ions available in the literature.

In Table 3-12 are listed the experimental available compensation fields and voltages CV_{exp} as well as the obtained ones in the simulations CV_{sim} for DMMP monomer ions for which five dispersion fields have been considered. Higher discrepancies are observed for lower dispersion field values whereas for higher dispersion fields results are nearly the same.

Ion Acronym	E_D/N (Td)	DV (V)	$[E_C/N]_{exp}$ (Td)	$[E_C/N]_{sim}$ (Td)	CV_{exp} (V)	CV_{sim} (V)
DMMPH ⁺	78	1050	0.29	0.21	-4.0	-2.9
	85	1150	0.36	0.26	-4.8	-3.6
	93	1250	0.40	0.32	-5.4	-4.3
	100	1350	0.42	0.38	-5.7	-5.1
	107	1450	0.43	0.43	-5.9	-5.8

Table 3-12: Comparison of Compensation Voltages from experimental values from the literature and Simulation Values for DMMPH⁺ [27].

In Table 3-13 are listed the experimental available compensation fields and voltages CV_{exp} as well as the obtained ones in the simulations CV_{sim} for volatile organic ions. For the only available data for the 2-propanone dimer ions at 67 Td [18], the CV_{sim} slightly differs from CV_{exp} . For Toluene ions five dispersion fields have been found in the literature, the gap of the p-FAIMS used is not provided directly but as electric field values are given the comparison has been possible. Both, experimental and simulated values are very close for this compound excepting only for the higher dispersion field although measurements were performed at 100 °C.

Ion Acronym	E_D/N (Td)	DV (V)	$[E_C/N]_{exp}$ (Td)	$[E_C/N]_{sim}$ (Td)	CV_{exp} (V)	CV_{sim} (V)
Ac_2H^+	67	900	0.15	0.17	-2.0	-2.3
	40	500	0.10	0.08	-1.2	-1.0
TH^+	56	700	0.19	0.19	-2.4	-2.4
	72	900	0.43	0.34	-5.4	-4.2
	88	1100	0.56	0.46	-6.9	-5.8
	104	1300	0.68	0.45	-8.5	-5.7

Table 3-13: Comparison of Compensation Voltages from experimental values from the literature and Simulation Values for 2-propanone and toluene [18, 28].

In the case of explosive ions data corresponding to field compensation values are reported but a coaxial FAIMS has been used to do the experiments. Since radius of coaxial electrodes are provided we have started calculating the effective field applied but for the value obtained (20Td's) no compensation is needed in our case. Negative compensation field values have been found for dispersion fields higher than 120 Td's but no agreement with results reported was found. We conclude that for this case is not possible to compare the results due to the lack of enough reported data.

It has to be taken into account that our simulations do not consider interaction between ions. And, that the simulated asymmetric waveform and the experimental applied ones was not exactly the same. These two factors could contribute to some observed discrepancies between experimental obtained values and simulation ones. Nevertheless results obtained are in good agreement with the experimental ones when comparison is possible.

Discussion and Summary

In this chapter, the modeling of a micro p-FAIMS has been presented. COMSOL Multiphysics used to perform a full physical phenomenon p-FAIMS modeling is done in the present thesis, including the ions movements due to the carrier gas flow, and the electric fields applied considering the ions diffusion. This has implied the need of a Multiphysics treatment.

A 2D approximation has been done to reduce computation time and memory requirements, it has been considered that all the effects do not vary along the electrodes width. The gap has been fixed to 0.5 mm. The compounds to be simulated have been chosen as representative compounds used in security applications, for which is intended to be used the p-FAIMS final device. Ions studied included a chemical warfare agent or CWA simulant (dimethyl methyl phosphonate or DMMP that emulates gas sarin, in its positive monomer), two risky healthy volatile organic compound or VOC's (2-propanone or acetone Ac in its positive dimer, and toluene in its proton bound monomer form); and three explosives (2,4,6-trinitrotoluè or TNT, 2,4-dinitrotoluene or DNT, and 1,3,5-trinitrobenzene or TNB, all three in their negative monomers).

The studio of the carrier gas flow rate effects for Toluene ions, showed that peak width and intensity increases as the flow was increased. Increasing intensity means increasing sensitivity, but increasing peak width means decreasing selectivity. Therefore a compromise must be found. To find the optimum carrier gas flow can be used the product $I \times R_p$ or the Aspect Ratio, both lead a curve that has a plateau, being the gas flow of 1,000 sccm the chosen as optimum value. Obtained intensities for concentrations of 1 ppm at the optimal flow are of the same order of the experimental values reported in the literature.

The studio of the Electric Field for Toluene ions showed that for a fixed dispersion field, varying the frequency affects the ions transmission and therefore the intensity, while compensation field remains unchanged. For a fixed frequency, it has been studied how changed the compensation field versus the dispersion field, obtaining that compensation fields values obtained with COMSOL simulations are very close for this compound excepting only for the higher dispersion field. The validation of the compensation field obtained for 2-propanone ions has also been done, but for the case of explosive compounds not available data has been found in the literature to allow corroboration.

Different combinations of compounds have been studied in two different mixtures, one including DMMP, 2-propanone, Toluene and TNT; and the other three Explosives (TNT, DNT and TNB). Each compound has a characteristic E_C/N vs. E_D/N curve, being two compounds distinguishable under certain conditions if at that point the curves do not cross, and the separation is better the more remote they are.

The dependence of the filtering electrodes length has been studied for two different values of 13 and 20 mm. The main result is that the quantity of un-compensated ions that reach the detector decreases for longer drift tubes as more ions will be lost in the walls. For this reason, there are narrower peaks at the detector and resolution is increased for longer electrodes length.

Simulations showed that p-FAIMS simulation could be achieved with COMSOL software and that it is a good platform for this kind of application as simulation validation is coherent with the experimental values found in the literature.

Further simulations of the micro p-FAIMS device with COMSOL Multiphysics should include a 3D simulation, the study of more geometric parameters affecting the ions detection like the gap variation and the distance between filtering and detection electrodes, also detector electrodes length and ions interactions.

References

1. Hughes, T., 2000, *The Finite Element Method: Linear Static and Dynamic Finite Element Analysis* Courier Dover Publications.
2. Zienkiewicz, O.C., 1974, *Finite element method* Springer.
3. Zienkiewicz, O.C. and R.L. Taylor, 2005, *The Finite Element Method for Solid and Structural Mechanics* Elsevier.
4. Zienkiewicz, O.C., R.L. Taylor, and J.Z. Zhu, 2005, *The Finite Elements Method: Its Basis and Fundamentals*: Elsevier.
5. Zimmerman, W.B.J., 2004, *Process Modelling and Simulation With Finite Element Methods*: World Scientific.
6. COMSOL AB. [cited 2013 20th March]; Available from: <http://www.comsol.com>.
7. Shvartsburg, A.A., K. Tang, and R.D. Smith, *FAIMS Operation for Realistic Gas Flow Profile and Asymmetric Waveforms Including Electronic Noise and Ripple*. Journal of the American Society for Mass Spectrometry, 2005. **16**(9): p. 1447-1455.
8. CRC, 2008, *Handbook of chemistry and physics : a ready-reference book of chemical and physical data*. 89th ed., eds. C.T. Francis. Boca Raton, Florida.
9. NIST. *Chemistry WebBook*. [cited 2013 18th March]; Available from: <http://webbook.nist.gov/chemistry>.
10. Guevremont, R. and R.W. Purves, *Atmospheric pressure ion focusing in a high-field asymmetric waveform ion mobility spectrometer*. Review of Scientific Instruments, 1999. **70**(2): p. 1370-1383.
11. Buryakov, I.A., *Qualitative analysis of trace constituents by ion mobility increment spectrometer*. Talanta, 2003. **61**: p. 369-375.
12. Shvartsburg, A.A., K. Tang, and R.D. Smith, *Optimization of the design and operation of FAIMS analyzers*. Journal of the American Society for Mass Spectrometry, 2005. **16**(1): p. 2-12.
13. Shvartsburg, A.A., 2009, *Differential Ion Mobility Spectrometry: Nonlinear Ion Transport and Fundamentals of FAIMS*. First ed. Boca Raton, FL: CRC Press.
14. Huxley, L.G.H., R.W. Crompton, and M.T. Elford, *Letters to the Editor: Use of the parameter E/N*. British Journal of Applied Physics, 1966. **17**(9): p. 1237-1238.
15. The Editor, *Letters to the Editor: Use of the parameter E/N*. British Journal of Applied Physics, 1967. **18**(5): p. 691.

16. Barth, S., W. Baether, and S. Zimmermann, *System Design and Optimization of a Miniaturized Ion Mobility Spectrometer Using Finite-Element Analysis* Sensors Journal, IEEE, 2009. **9**(4): p. 377-382.
17. Krylova, N., et al., *Effect of moisture on the field dependence of mobility for gas-phase ions of organophosphorus compounds at atmospheric pressure with field asymmetric ion mobility spectrometry*. Journal of Physical Chemistry A, 2003. **107**(19): p. 3648-3654.
18. Krylov, E., et al., *Field dependence of mobilities for gas-phase-protonated monomers and proton-bound dimers of ketones by planar field asymmetric waveform ion mobility spectrometer (PFAIMS)*. Journal of Physical Chemistry A, 2002. **106**(22): p. 5437-5444.
19. Shvartsburg, A.A., et al., *High-Resolution Field Asymmetric Waveform Ion Mobility Spectrometry Using New Planar Geometry Analyzers*. Analytical Chemistry, 2006. **78**(11): p. 3706-3714.
20. ACGIH® (American Conference of Governmental Industrial Hygienists), 2010, *The Threshold Limit Values (TLVs®) and Biological Exposure Indices (BEIs®)* 1330 Kemper Meadow Drive, Cincinnati, OH 45240-4148. Printed in the United States.
21. Occupational Safety & Health Administration (United States Department of Labor). 2013; Available from: http://www.osha.gov/dts/chemicalsampling/data/CH_272200.html.
22. Shvartsburg, A.A., K. Tang, and R.D. Smith, *Modeling the resolution and sensitivity of FAIMS analyses*. Journal of the American Society for Mass Spectrometry, 2004. **15**(10): p. 1487-1498.
23. Nazarov, E.G., et al., *Pressure Effects in Differential Mobility Spectrometry*. Analytical Chemistry, 2006. **78**(22): p. 7697-7706.
24. Miller, R.A., et al., *A novel micromachined high-field asymmetric waveform-ion mobility spectrometer*. Sensors and Actuators B: Chemical, 2000. **67**(3): p. 300-306.
25. Eiceman, G.A., E.G. Nazarov, and R.A. Miller, *A micro-machined ion mobility spectrometer-mass spectrometer*. International Journal for Ion Mobility Spectrometry, 2000. **3**(1): p. 15-27.
26. Borsdorf, H., E.G. Nazarov, and R.A. Miller, *Time-of-flight ion mobility spectrometry and differential mobility spectrometry: A comparative study of their efficiency in the analysis of halogenated compounds*. Talanta, 2007. **71**(4): p. 1804-1812.
27. Karpas, Z., et al., *Models on Ion Heating and Mobility in Linear Field Drift Tubes and in Differential Mobility Spectrometers*. International Journal for Ion Mobility Spectrometry, 2004. **7**(1): p. 70-80.
28. Veasy, C.A. and C.L.P. Thomas, *Fast quantitative characterisation of differential mobility responses*. Analyst, 2004. **129**: p. 198-204.
29. Buryakov, I.A., *Ion current amplitude and resolution of ion mobility increment spectrometer (IMIS)*. International Journal for Ion Mobility Spectrometry, 2001. **4**(2): p. 112-116.

[This page intentionally left blank]

Section 2:

Ion Mobility

Spectrometry

Applications

[This page intentionally left blank]

Chapter

4

p-FAIMS
Security
Applications

Chapter 4: p-FAIMS Security Applications	155
4.1 Device design and assembly	157
4.1.a Ionization method	157
4.1.b Glass-Silicon-Glass Design	163
4.1.c PCB-PMMA-PCB Design	172
4.2 Measurements set-up	176
4.2.a The gas supply system	176
4.2.b Experimental set-up	177
4.3 p-FAIMS Characterization	181
4.3.a Electrodes biasing	181
4.3.b Detection without High Field	188
4.3.c Detection of Toluene Ions with RF field	198
Discussion and Summary	202
References	204

The development of the planar high Field Asymmetric Ion Mobility Spectrometer (p-FAIMS) has involved the use of techniques that were not present in the know-how of the research group. For this reason, a huge effort in the design of the device, and in the technological steps involved in its fabrication, has been done. Also, the assembling of the set-up for experimental measurements, the gas supply system design, and finally the characterization of the p-FAIMS has been made.

This chapter provides a summary of the different designs and materials considered for the p-FAIMS implementation: Glass-Si-Glass and PCB-PMMA-PCB structures; the technological tasks done for each one and the solving strategies that have led to it. UV photoionization has been chosen as ionization method for safety reasons in all cases.

4.1 Device design and assembly

FAIMS analyzers may be constructed in many configurations, with only two major requirements: 1) A gap between two electrodes, across which a time-dependent asymmetric waveform is applied; 2) A force which transports the ions through the analyzer toward the detector. These minimum requirements for a feasible design leave a great deal of flexibility in terms of filtering electrodes shape and spacing, length, and materials used. Unfortunately, there is no single elegant solution available which simultaneously provides good resolution as well as optimum ion transmission. As is typical of scientific instruments, high resolution results in low signal intensity so that the key is to find a compromise in terms of overall performance. This is further complicated by the need of build the design using the available fabrication techniques.

4.1.a Ionization method

The chosen ionization method has to be taken into account both for the device design and also for the encapsulation. In this work, the used ionization method has been non-radioactive, as a radioactive source needs specific safety issues and requires certificates and permissions according to the local safety regulations. From the ones pointed in the Section 2.2.b *Ionization region*, the used method in this thesis has been a UV photoionization, as it does not require special safety license, it can ionize a wide variety of compounds in the gas-phase and taking advantage that the UV spectrum is comparatively simpler than the one with radioactive sources, resulting in an enlarged range of quantitative response. Other non-radioactive sources for gas-phase have some drawbacks that make them unsuitable for our requirements: 1) Corona Discharge Atmospheric Pressure Chemical Ionization can generate electrons with an energy of 30 to 40 eV, meaning that both nitrogen and oxygen will be ionized, and therefore clustering will be obtained; and 2) Laser Desorption Ionization having the disadvantages of size and cost.

Photo-ionization lamp

Two different UV-lamps of 10.6eV have been considered, the first one a FK-794U from Perkin Elmer Optoelectronics [1] and the second one CDL 1021-0X from ACI Analytical Control Instruments GmbH [2] that is also provided with a power supply. In Figure 4-1 they can be seen both discharge lamps.

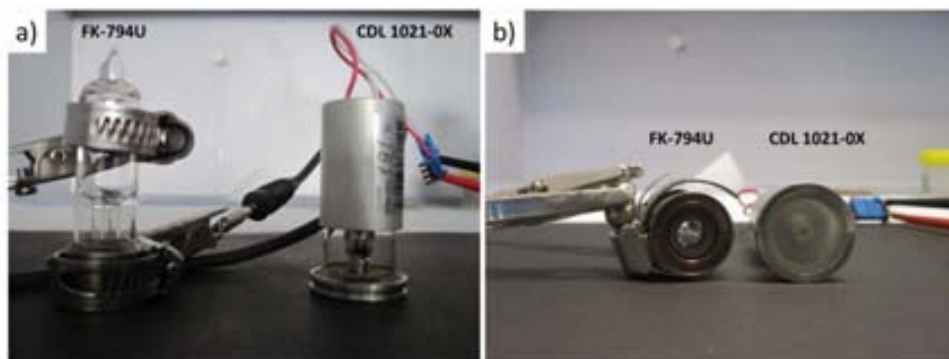


Figure 4-1: Used UV Discharge lamps FK-794U from Perkin Elmer Optoelectronics [1] and CDL 1021-0X from ACI Analytical Control Instruments GmbH [2] in a) vertical position, and b) horizontal position.

In low pressure gas discharge lamps, a glow discharge excites the natural resonance frequency of the fill gas, thus producing special emission lines down to short wave cut-off of the window material. The spectral output of the lamp is determined by the fill gas and the transmission characteristic of window material. The gases used most frequently are xenon (8.4eV, sapphire window), krypton (10 eV or 10.6 eV, MgF₂ window), and argon (11.7 eV, LiF window). The wavelength (in meter) and the eV rating are associated through Planck's constant. Both studied discharge lamps are filled with Krypton having an ionization energy of 10.6 eV. The gas discharge is confined within the lamp, as can be seen in Figure 4-2a, showing a zoom in Figure 4-2b of the UV-lamp from Analytical Control Instruments GmbH.

A power supply and a series resistor power the lamp. Lamp operation occurs when the breakdown threshold of the fill gas is exceeded. The series resistor limits the current of the lamp to a reasonable operating level. In Figure 4-3 are shown the considered lamps lighted on, seen in vertical and horizontal positions. The needed voltage to turn on the FK-794U from Perkin Elmer Optoelectronics is 1,100 V and needs 300 V to maintain it turned on, being used a Keithley 2410 High Voltage SourceMeter that is a 20W instrument that sources and measures voltage from $\pm 1\mu\text{V}$ to $\pm 1,100\text{V}$ and current from $\pm 50\text{pA}$ to $\pm 1\text{A}$ [3]. For the CDL 1021-0X lamp from ACI Analytical Control Instruments GmbH the needed ignition voltage is 450 V and needs 210 V to be maintained lighted on, however it was delivered with a power

supply that only needs 5 V to light on the UV lamp and 2.6 V to maintain it turned on, so using the power supply, a Keithley 2400 SourceMeter that is a 20W instrument that allows sourcing and measuring voltage from $\pm 1\mu\text{V}$ to $\pm 200\text{V}$ DC and current from $\pm 50\text{pA}$ to $\pm 1\text{A}$ [4] can be used.

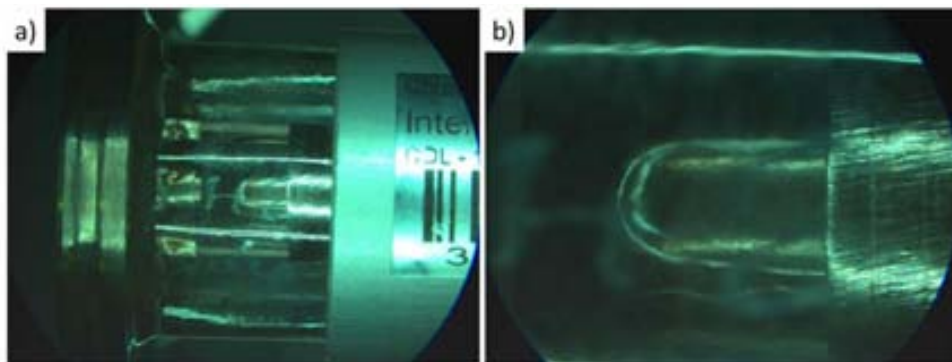


Figure 4-2: Details from the UV-lamp CDL 1021-0X from ACI Analytical Control Instruments [2]. a) the gas discharge is confined within the lamp; and b) a zoom of the confined gas zone. Photography's taken with a magnifying glass with a coupled camera.

As can be seen in Figure 4-3a, the FK-794U UV-lamp has a big window but the spot exit of the light is smaller than the one for the CDL 1021-0X that is also uniform along the entire window of 2 mm. Due to their bigger spot light and to the low power requirements to turn on the lamp, thanks to the power supply delivered with the lamp we have chosen the CDL 1021-0X one from ACI Analytical Control Instruments GmbH to ionize our samples.

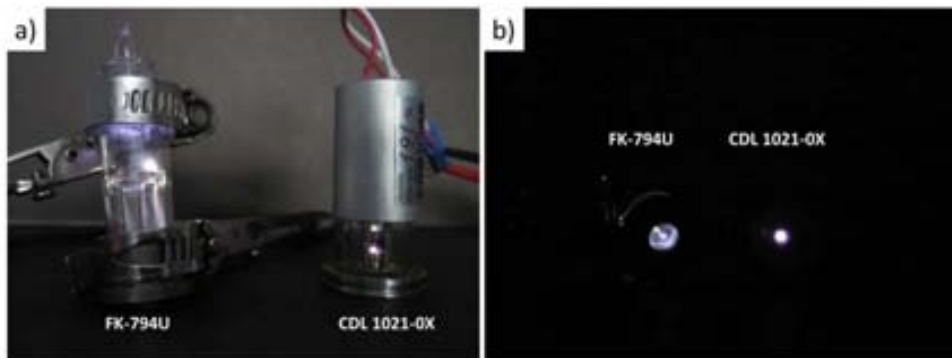


Figure 4-3: Lightened Discharge lamps from Figure 4-1. a) vertical and b) horizontal positions.

UV-lamp test

To check if our UV-lamp ionizes any gas a simple device was developed. It consists of a T-shaped copper and two copper concentric tubes assembled as can be seen in Figure 4-4. The UV-lamp is placed very close to the gas inlet and parallel to the gas flow inside the copper tubes. Some holes have been drilled in the lower diameter copper piece to ensure the flow of gas in the area between the concentric tubes. Thus, if the gas is properly ionized electric current may be measured between the two tubes.

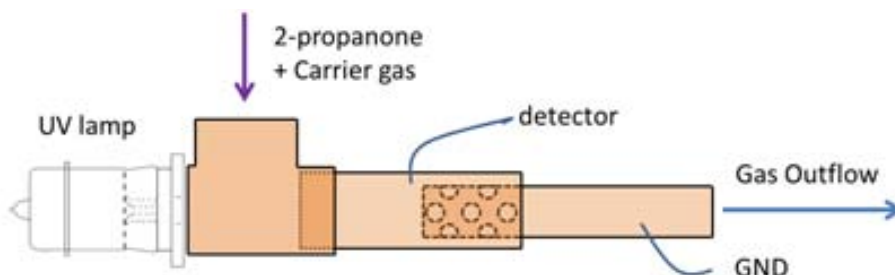


Figure 4-4: Schema of the UV-lamp test, showing the assembly of a UV lamp, the gas entrance and outflow, and the used copper pieces.

The middle piece of copper was used as detector and biased at V_{det} while the drilled piece was grounded. The measurement instrument used was a Keithley 6487 Picoammeter/Voltage Source With eight current measurement ranges that can measure currents from 20 fA to 20 mA [5]. The voltages needed to turn on and maintain lighted the UV lamps were provided by a Keithley 2400 SourceMeter [4]. In Figure 4-5 is shown the experimental set-up to test the UV lamp.

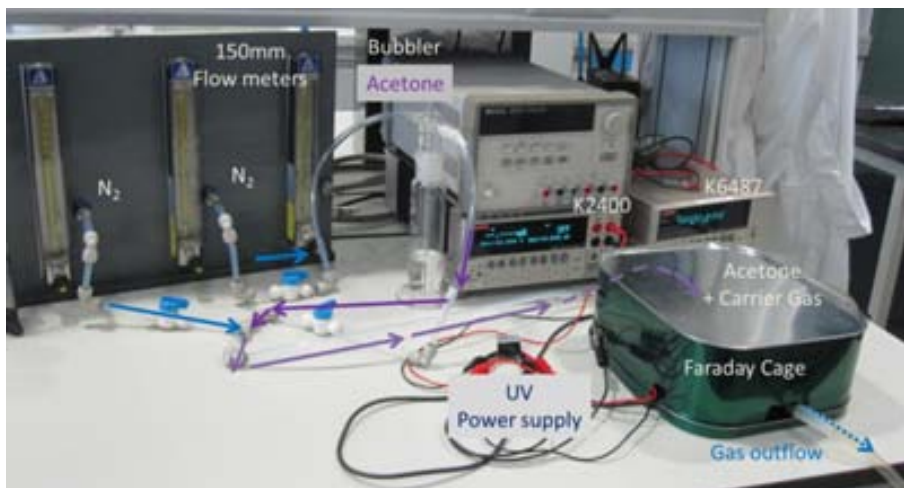


Figure 4-5: Set-up used for the UV lamp test.

The device was placed inside a Faraday Cage to avoid electric interferences. 2-propanone or acetone placed in a 125 mL bubbler from ALCO [6] was chosen for the test as it was easy to handle using home-made gas lines, nitrogen used as carrier gas was controlled with single tube flow meters of 150 mm with CVTM Valve from Aalborg [7].

To calculate the flow in a single tube 150 mm flowmeter, the equivalent air flow capacity Q_{air} at Standard Conditions (STP) is calculated as:

$$Q_{air} = \left(G \times \frac{T}{T_0} \times \frac{p_0}{p} \right)^{1/2} \times Q_{gas} \quad (4.1)$$

where Q_{gas} is the maximum flow of metered gas, G is the specific gravity of metered gas ($G_{air} = 1.000$, $G_{nitrogen} = 0.96724$), and T_0 and p_0 are the temperature and pressure at Standard Conditions (STP) ($T_0 = 273.15$ K, $p_0 = 101,325$ Pa). At a laboratory room of $T = 22^\circ\text{C}$ and being the pressure fixed to $p = 1$ atm = 101,325 Pa with a pressure regulator installed in the laboratory, the flow obtained at a reading of 100 mm is $Q_{air} \sim 1711$ sccm, being sccm a standard centimeter cubic per meter (at $T = 298.15$ K and $p = 101,325$ Pa for mass-flows [8]). In Figure 4-6 is shown the correlation of flows versus the scale reading for the single tube flowmeters used. Experimentally, a volume of 2 mm of Nitrogen was used to transport acetone from the bubbler to the device, after diluting in 100 mm of Nitrogen, leading a total flow of 1,750 sccm.

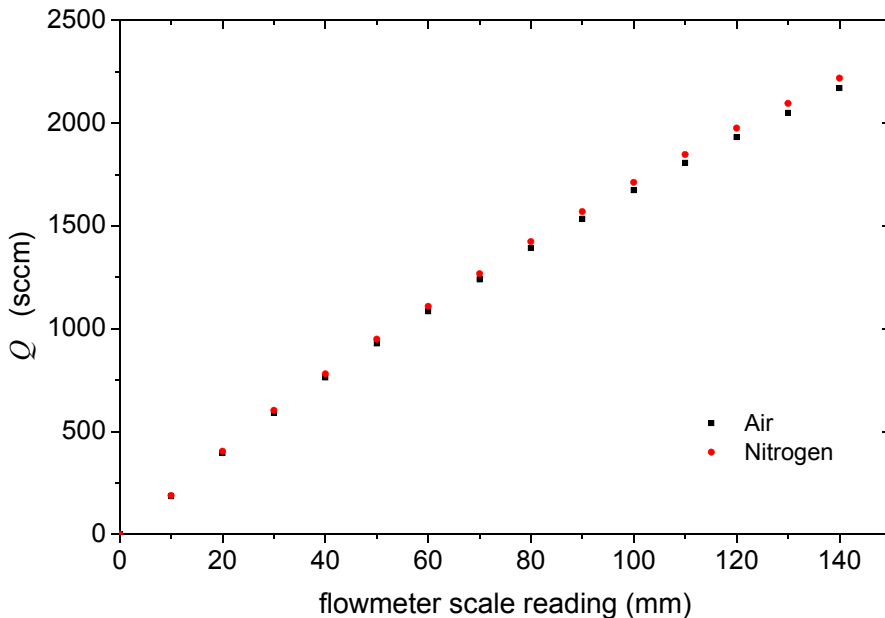


Figure 4-6: Single Tube Flowmeter of 150 mm from Aalborg [7] scale readings correspondence with flow in sccm, at center of the float for air and nitrogen.

A PhotoIonization Detector or PID was placed at the exit outside of the Faraday cage to ensure that 2-propanone passes through the copper device, and also to have an approximate lecture of the concentration of 2-propanone. The used PID is a portable Handheld VOC Monitor, the miniRAE 3000 from RAE Systems [9] that can measure VOC's up to 15,000 ppm with a response time of 3 s.

Lightning of the UV lamp was done with a LabView Graphical Interface named *UV_ACI.vi* and detailed in [Annex 4-1](#). Instrumentation controlling and data recording were also done with the LabView program *pA_UV-lamps-test.vi* that is detailed in [Annex 4-2](#).

Results of the UV lamp test are shown in Figure 4-7 for the positive mode (positive ions are detected when detector is biased in a negative voltage) having the UV lamp on and off.

Total acquisition time has been 60 s and the inflow of acetone has been on for 10 s. It can be seen that when the UV lamp was turned on acetone was measured, while when the UV lamp was turned off the acetone was not detected, so our UV lamp CDL 1021-0X from ACI Analytical Control Instruments GmbH is able to ionize the acetone. The acetone reaches saturation at $I_{\text{sat}} = (0.101 \pm 0.001)$ nA, for an estimated concentration of 1,500 ppm and a total flow of 1,750 sccm.

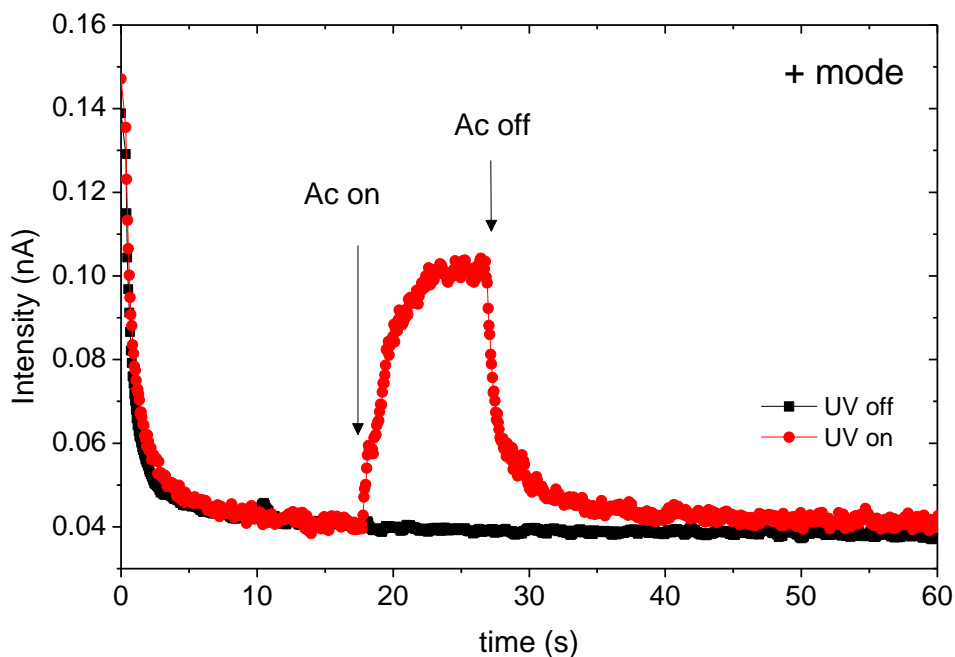


Figure 4-7: Intensities obtained during the UV lamp test. 2-propanone was measured when lamp was on for a detector voltage of -4V (+ mode).

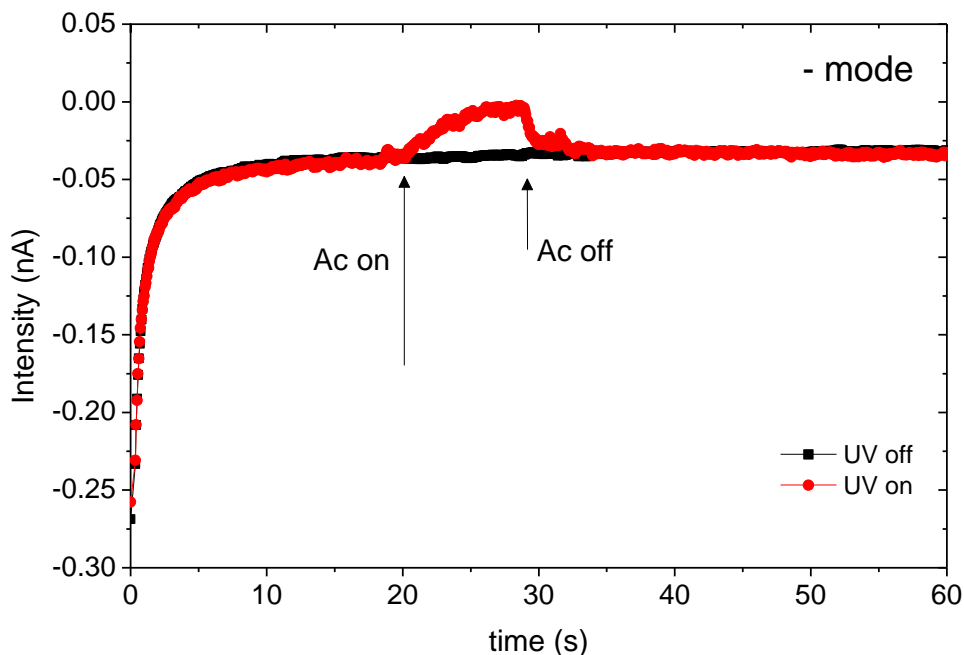


Figure 4-8: Intensities obtained during the UV lamp test. 2-propanone was measured when lamp was on for a detector voltage of +4V (- mode).

In Figure 4-7 results obtained are also shown for the negative mode (negative ions were detected when detector was biased in a positive voltage) having the UV lamp on and off. Total acquisition time has been 60 s and the inflow of acetone has been on for 10 s as in the previous case. Also, only when UV lamp was turned on acetone was detected. In this case the acetone reaches saturation at $I_{\text{sat}} = (-0.005 \pm 0.001)$ nA, for an estimated concentration of 1,500 ppm and a total flow of 1750 sccm. Signal detected for the negative mode was lower due to recombination of positive acetone ions with negative molecules present in the carrier gas, so the net amount of negative ions was decreased as seen in Figure 4-8.

4.1.b Glass-Silicon-Glass Design

The first p-FAIMS developed consisted of a Glass-Silicon-Glass (GL-Si-GL) sandwich design, as seen in Figure 4-9. It consists of two pieces of Pyrex one of them with a hole to allow the UV light reaches the gas, that contain the device electrodes. Among the Pyrex pieces there are two silicon strips that define the channel through which the gas passes. Both Pyrex and silicon strips are 0.5 mm thick

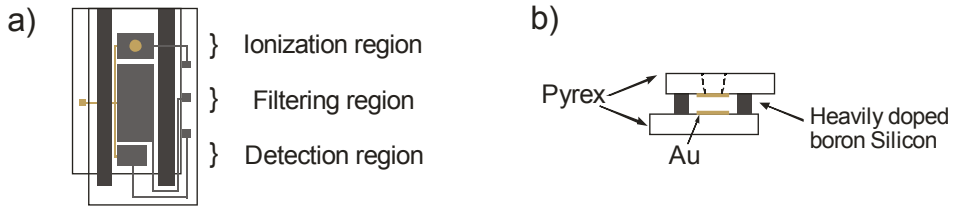


Figure 4-9: Schema of the p-FAIMS device for the GL-Si-GL configuration: a) top view; and b) front view.

The main steps for obtaining the p-FAIMS consist of drilling a through hole in the Pyrex, definition of the device electrodes, anodic bonding of Pyrex with silicon strips, electrical connection, and packaging. Below are discussed each one in detail highlighting the problems found during the fabrication process.

Pyrex used is Pyrex® 7740 Borosilicate Glass (SiO_2 80.6%, B_2O_3 13.0%, Na_2O 4.0%, Al_2O_3 2.3%, others 0.1%) [10] as it is a standard glass used for anodic bonding.

1. Pyrex wafer through hole

Different ways to do the through hole in the Pyrex wafer were considered. Pyrex® 7740 Borosilicate Glass etching is a difficult process due to that it is not pure silicon oxide and the other components present have different etch rates in the etching solutions.

HF-based wet etching

The first technique considered to have a through hole in the Pyrex piece was by an HF-based chemical etching (Hydrofluoric acid), as HF is a highly corrosive acid, capable of dissolving many materials, especially oxides and glass [11].

The regions that should not be etched need a masking layer, Photoresist is usually used for this purpose in microelectronics but to obtain structures deeper than $5\ \mu\text{m}$ it does not withstand because long etch times are required (glass etch rate is $\sim 5\ \mu\text{m}/\text{min}$). Thus an alternative masking must be used. Among the materials available in IC-technology only a few can withstand hydrofluoric acid. For this reason, in this thesis, a two etch step process has been used defining first a through hole in a Silicon wafer by KOH etching, then this Silicon wafer was anodic bonded to the Pyrex wafer to act as a mask and, finally the assembly was etched in the HF-based solution.

The main steps involved in this process are summarized in Figure 4-10.

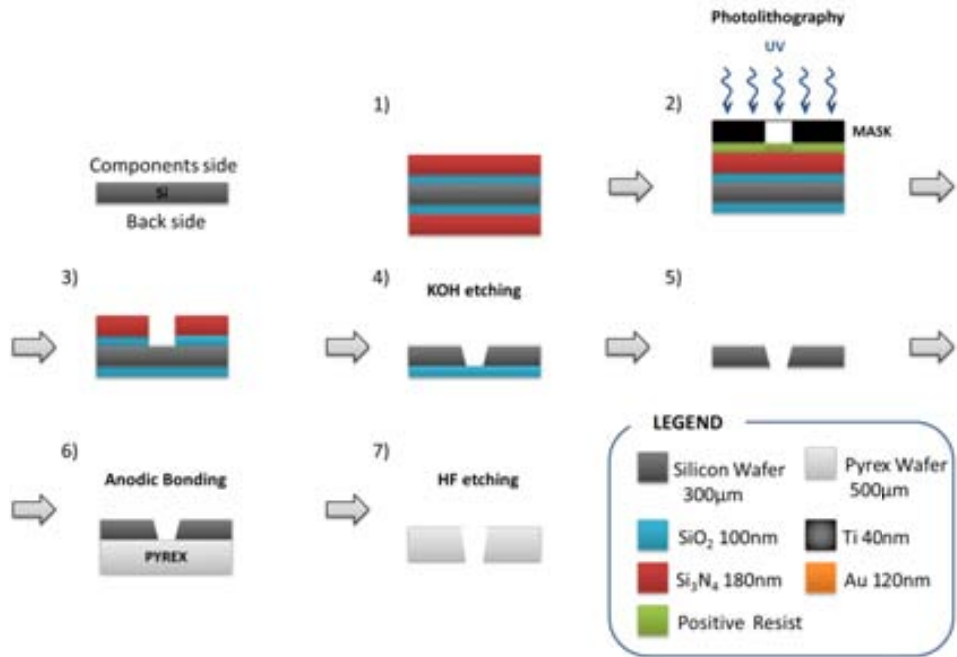


Figure 4-10: Main steps in the Pyrex through hole definition by HF etching.

Clean Room processes involved in Figure 4-10:

- 1) Growth of 100 nm thick thermal SiO₂ on a 300 µm thick, double side polished 4 inch (1 inch = 2.54 cm) silicon wafer. This was followed by a deposition of LPCVD (Low-pressure chemical vapor deposition) Si₃N₄ 180 nm thick.
- 2) Photolithography of the components side to define the through holes region.
- 3) Silicon Nitride and silicon dioxide etching in the through holes region.
- 4) Wet KOH anisotropic etching to define the through hole in the silicon wafer.
- 5) Removing of the protective SiO₂ layer.
- 6) Anodic bonding of the patterned silicon wafer with a Pyrex® 7740 Borosilicate Glass wafer.
- 7) HF etching (Hydrofluoric acid) at 49% diluted in water to through hole the Pyrex® 7740 Borosilicate Glass wafer. Removing of the silicon mask wafer.

In figure 4.4 is shown a 2 × 2 mm² through hole drilled with this technique in a Pyrex® 7740 Borosilicate Glass wafer. As can be seen a poor definition of the etched structure was obtained, also surface roughness was increased and a significant amount of defects was present probably due to the composition of the glass, especially to the aluminum oxide content.

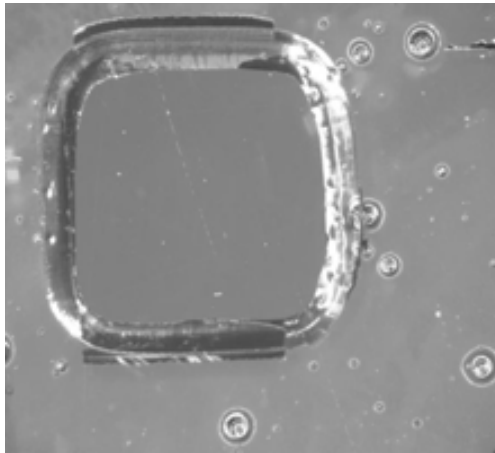


Figure 4-11: Through hole drilled in a Pyrex® 7740 Borosilicate Glass wafer with an HF-based solution etching.

Deep-RIE

The second considered way to have a through hole in a Pyrex® 7740 Borosilicate Glass wafer was by Deep reactive ion etching (DRIE), which is a highly anisotropic etch process used to create deep penetration, steep-sided holes and trenches in wafers/substrates, typically with high aspect ratios [11]. A schema of the involved steps is shown in Figure 4-12.

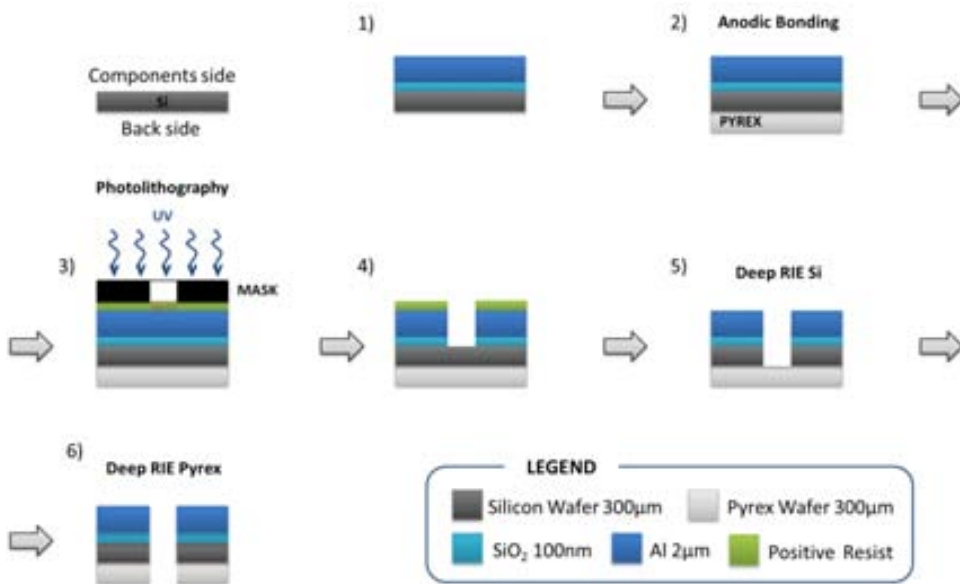


Figure 4-12: Main steps in the Pyrex through hole definition by DRIE etching.

Clean Room processes involved in Figure 4-12:

- 1) Growth of 100 nm thick thermal SiO₂ and deposition of 2 μm of Al on a 300 μm thick, double side polished 4 inch silicon wafer.
- 2) Anodic bonding of the silicon wafer with a Pyrex® 7740 Borosilicate Glass wafer.
- 3) Photolithography to define in the Aluminum and SiO₂ the through holes region.
- 4) Wet etchings of Aluminum and SiO₂ layers.
- 5) Deep RIE of 300 μm of silicon.
- 6) Deep RIE of Pyrex wafer.

The etch rate of Pyrex was very slow (calculated as 0.033 μm/min), this fact makes the use of this technique unfeasible and this approximation for the through hole was not continued.

Powder blasting

The third technique considered to have a through hole in a Pyrex® 7740 Borosilicate Glass wafer Pyrex piece was powder blasting. Powder blasting feature size accuracy is about 25 μm. The realization of 2 mm round through holes by this method process was ordered to the Micronit Microfluidics company [12].

Figure 4-13 shows a microscopic picture of one of the powder blasted through holes. The desired diameter of 2 mm is shown.

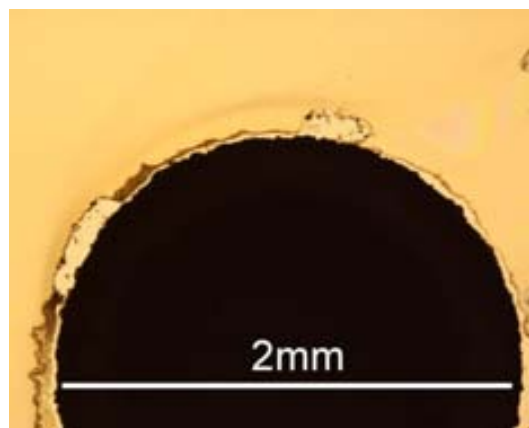


Figure 4-13: Microscope picture of a through hole done with Powder blasted process from Micronit Microfluidics company.

Once received the Pyrex wafers with the through round holes, the micro-fabrication of top and bottom part of p-FAIMS device begin.

2. Definition of the electrodes of the p-FAIMS device

Once we already had the through holed Pyrex wafers, next step was the patterning of the p-FAIMS electrodes. Gold was used for this purpose and a thin Chrome layer was used to improve gold adhesion to the Pyrex. The use of lift-off and traditional etching had been evaluated to define the structures (Process sequences are shown in Figure 4-14 and Figure 4-15. Best results were obtained using traditional etching process.

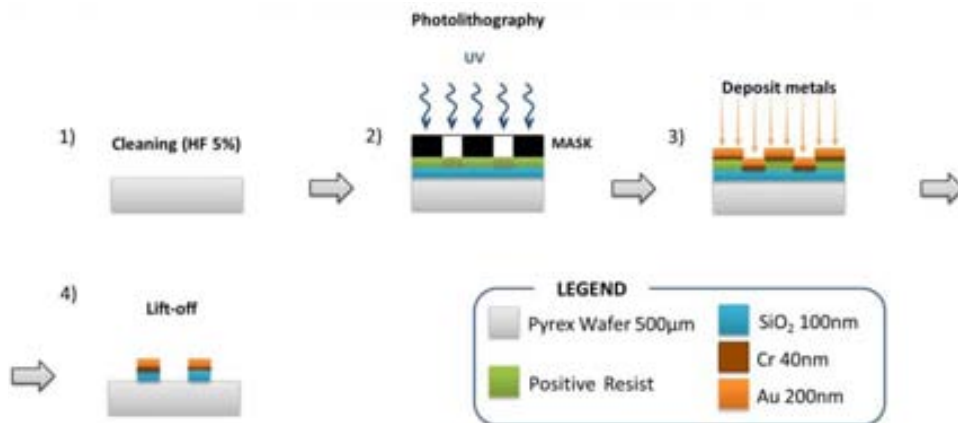


Figure 4-14: Lift-off process sequence.

Clean Room steps involved in Figure 4-14:

- 1) Cleaning and preparation of the substrate.
- 2) Photolithography to define the structures in the sacrificial layer (HIPR-6512 resist).
- 3) Deposition of metals: 40 nm of Cr and 200 nm of Au.
- 4) Lift-off of the deposited metals placed on the resist surface.

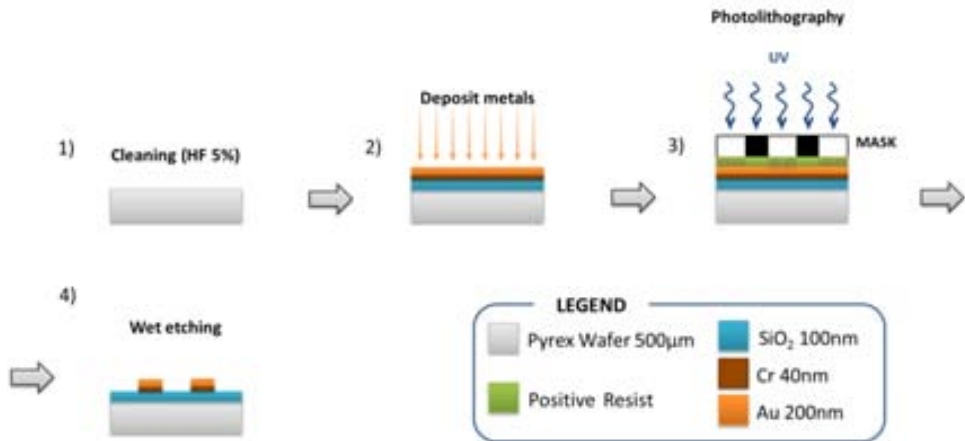


Figure 4-15: Traditional etching process sequence.

Clean Room processes involved in Figure 4-15:

- 1) Cleaning and preparation of the substrate.
- 2) Deposition of metals: 40 nm of Cr and 200 nm of Au.
- 3) Photolithography to define the structures in the resist masking layer.
- 4) Wet Au and Cr etching.

Figure 4-16 shows some pictures of the results obtained using traditional etching process. The structures were well transferred and no visible damages were found. Different p-FAIMS configurations have been studied.

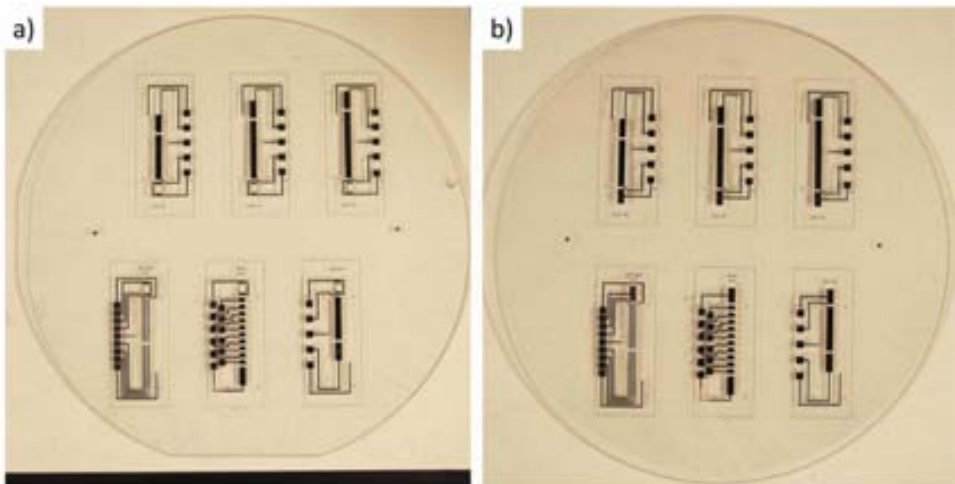


Figure 4-16: Pictures of the obtained p-FAIMS pieces for GL-Si-GL configuration.

Once we defined the electrodes into the Pyrex wafers, next step was dicing the p-FAIMS units and doing the anodic bonding with the silicon strips to have the final sandwich-like structure GL-Si-GL.

3. Anodic bonding: Sandwich-like configuration.

Some inconvenient with the anodic bonding of the silicon strips (2 mm × 25 mm) with the top and bottom parts of the p-FAIMS made on Pyrex® 7740 Borosilicate Glass were found. After ensuring that Pyrex and silicon strips were clean, process were done in two steps, in the first one silicon strips were anodic bonded to a Pyrex piece, and then the assembly must be bonded to the other Pyrex piece. In some cases good results were obtained during the first bonding process, but during the second process the parts that had a already bonded were separated again. As can be seen in Figure 4-17, the color of the image is not uniform in the areas where the anodic bonding has been performed indicating that the process were not worked in a proper way. Probably the cause of the poor performance obtained for the anodic bonding is related with the increased roughness of Pyrex due to the sand blasting process and with an unsuitable charge migration during the second process.

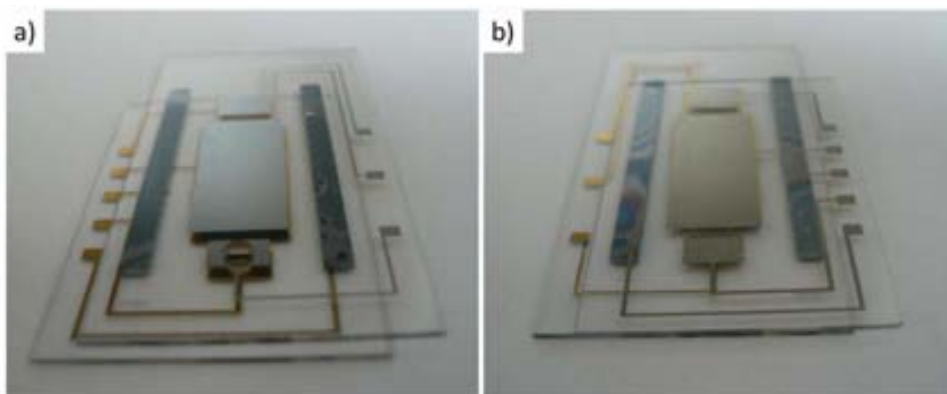


Figure 4-17: Pictures of a p-FAIMS device with GL-Si-GL configuration after anodic bonding: a) top view with the through hole; and b) bottom view.

Some alternatives to take under consideration include the use of adhesives although in this case there are some drawbacks as the gap is increased, the process becomes manual and results vary from one process to another.

4. Wire welding and packaging

To have a good electrical wire welding a conductive epoxy was used to prevent the removing of the metal in the connection area of the p-FAIMS, results obtained can be seen in Figure 4-18.



Figure 4-18: p-FAIMS device in the GL-Si-GL configuration with electrical wires.

The first attempt for the packaging of the p-FAIMS device in the GL-Si-GL configuration was mechanized from Teflon® blocks [13], as can be seen in Figure 4-19. Teflon® was chosen for its chemically inert properties.



Figure 4-19: Packaging of the p-FAIMS device in the GL-Si-GL configuration with mechanized Teflon®.

The major problem found using this packaging was the gas leaks as the structure do not seal properly. Due to the large number of problems encountered, some of them unresolved it was decided to completely change the strategies involved in the implementation of the device.

4.1.c PCB-PMMA-PCB Design

In this new approach it was decided to replace the Pyrex wafers for printed circuit boards (PCB's) thus obtaining a more robust device.

The electrodes of the p-FAIMS were defined in the printed circuit boards; and one of the plates was a 2 mm drilled hole to allow the UV light pass through. Between the two PCB's placed in a sandwich-like configuration is inserted a Polymethyl methacrylate (PMMA) piece with a channel mechanized on it.

Printed circuit boards were fabricated in the *Laboratori de Sistemes Electrònics* from the *Institut de microelectrònica de Barcelona* IMB-CNM. In Figure 4-20 is shown the p-FAIMS device using this configuration. A detail of the p-FAIMS electrodes from the top and bottom PCB pieces is shown in Figure 4-20a, where also the PMMA mechanized channel can be seen.

UV electrodes placed around the drilled hole could be polarized to decrease ion losses in the ionization region. UV electrodes are splitted, the UV-gate electrode with dimensions $2.0 \times 10.0 \text{ mm}^2$ (Figure 4-20a) can be used to allow or not the pass of the ions to the filtering region, and the UV-back with dimensions $4.5 \times 10.0 \text{ mm}^2$ separated 0.8 mm from UV-gate used to decrease ion losses in the ionization region. The width of the UV electrodes is designed to ensure that all formed ions are directed to the filtering electrodes. Positioned 1 mm after the UV-gate electrodes, there are the filtering electrodes with dimensions $18.0 \times 4.0 \text{ mm}^2$, being separated 1 mm from the detector electrodes of $5.0 \times 4.0 \text{ mm}^2$. Gas inflow is placed at 22 mm from the UV-ionization hole, to ensure a laminar gas flow along the channel, while the gas outflow is just at the end of the detection region. The PMMA gas channel has dimensions of $58.5 \times 6.0 \text{ mm}^2$, with a height of 1 mm. The full system dimensions are $64.0 \times 45.0 \text{ mm}^2$.

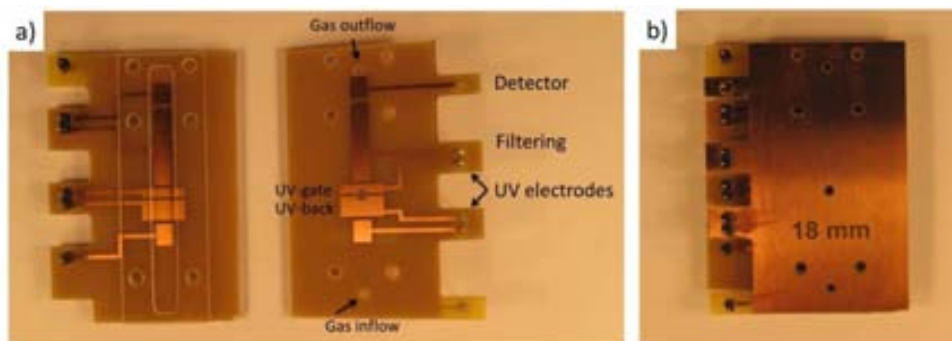


Figure 4-20: p-FAIMS device using the PCB-PMMA-PCB configuration: **a)** detail of the top and bottom PCB electrodes that configures the p-FAIMS device, showing also the PMMA mechanized channel that is resting in the bottom PCB piece; and **b)** top view of the sandwich-like.

In figure (Figure 4-20b) it is shown the top view of the sandwich-like, as can be seen there is a copper layer on it that can be grounded and became a Faraday cage avoiding external interferences during the measurements. The copper layer is also present in the bottom part not showed.

Figure 4-21 is shown a detailed schema of the p-FAIMS with PCB-PMMA-PCB configuration. The top and bottom parts can be grounded and became a Faraday Cage.

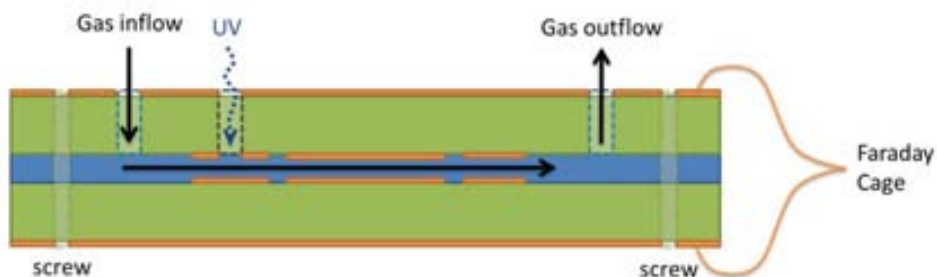


Figure 4-21: Detail of the PCB-PMMA-PCB configuration.

As stated previously, the PMMA piece that defines the channel has a thickness of 1 mm. Ideally would have been to have a p-FAIMS gap of 0.5 mm, but as seen in the Section 2.3.c *Detection: Modifying the geometry of electrodes* the gap increase would mean that the dispersion field (high voltage) needed will have to be also increased proportionally to have the equivalent electric field.

One of the major issues of the p-FAIMS is the gas introduction to the device, and also obtaining a packaging system without leaks. This problem was solved using the Plastic Laser-sintering system EOS FORMIGA P 100 (Germany) of the IMB-CNM, which has a very fast prototyping capacity from CAD files being its resolution ~ 0.1 mm. The used material is Fine Polyamide PA 2200 for EOSINT P.

In Figure 4-22 is shown the general schema of the designed packaging for our p-FAIMS. The top piece contains the fluidic connections as well as the housing of the UV-lamp. The bottom piece, made of PMMA due to its low cost and easy processing, only has the screw positions, and between them the PCB-based p-FAIMS device is placed. All the pieces involved are assembled by pressure as PCB is a robust material unlike the Pyrex. A home-made O-ring (toric joint) is used to seal the UV-lamp with the polyamide piece. A torically thread of 1.5 mm with a glue based on cyanoacrylate from Epidor [14] were used to fabricate the exact diameter for the used O-ring.

Figure 4-23 shows the different pieces of the p-FAIMS system packaging.

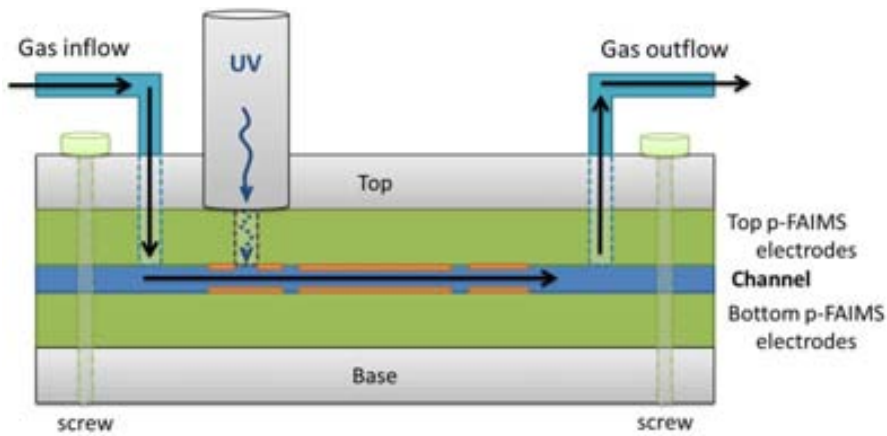


Figure 4-22: Schema of the p-FAIMS device in the PCB-PMMA-PCB configuration.

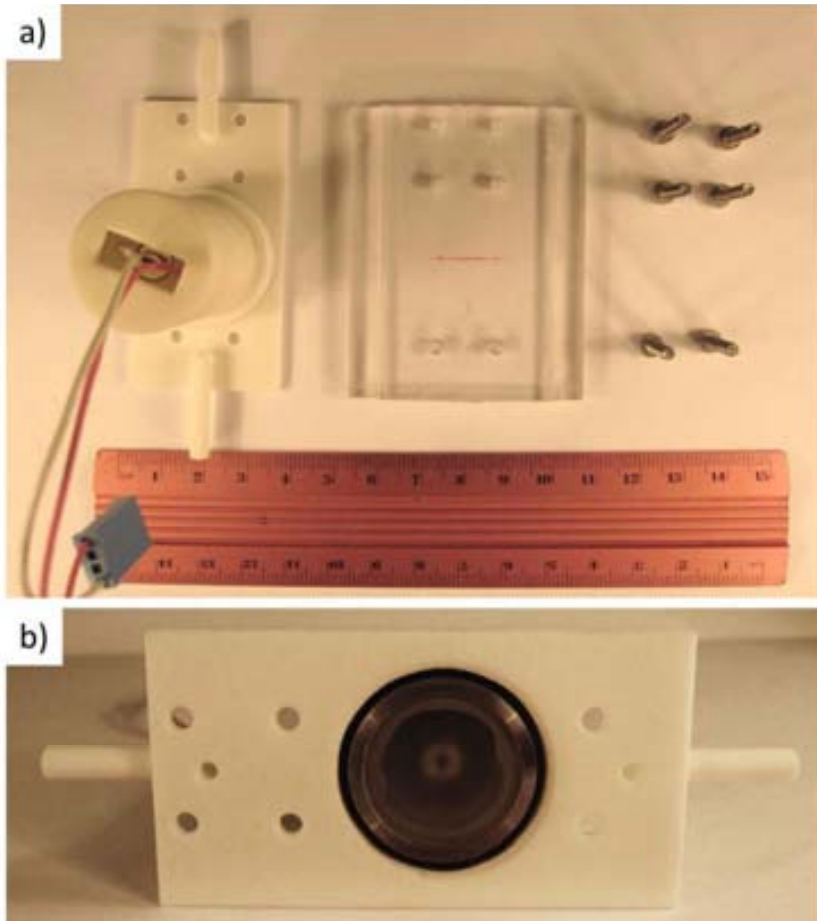


Figure 4-23: Packaging pieces for the PCB-PMMA-PCB p-FAIMS configuration. **a)** top piece housing the UV-lamp and gas connections prototyped with EOS Formiga P 100, and a bottom piece fabricated with PMMA using a milling machine. **b)** detail of the UV-lamp CDL 1021-0X from ACI Analytical Control Instruments GmbH, placed in the encapsulation system fabricated with the FORMIGA prototyping system. An O-ring is used to seal the UV-lamp with the polyamide piece.

Figure 4-24 shows a picture of the packaged p-FAIMS device. A proper sealing of the system was proved passing nitrogen through the p-FAIMS channel and adding water with soap in the joints. No bubbles were seen, so the sealing was satisfactory. Also with this prototype, as pressure is used as sealer (with screws) we have eliminated the problems found in the previous GL-Si-GL configuration during the anodic bonding assembly.

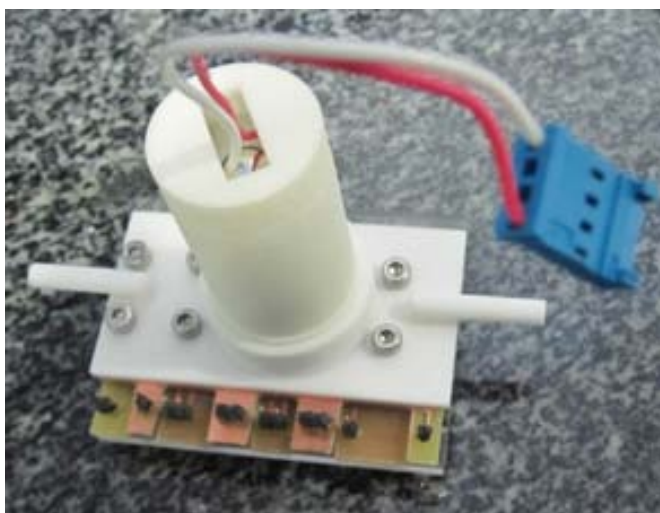


Figure 4-24: Picture of the packaged p-FAIMS device in the PCB-PMMA-PCB configuration.

Figure 4-25a shows the top part of the p-FAIMS (with the through hole) screwed on the polyamide piece, to allow the pass of the UV-light. As can be seen in Figure 4-25b with the UV lamp on, the through hole drilled is placed in the correct location.

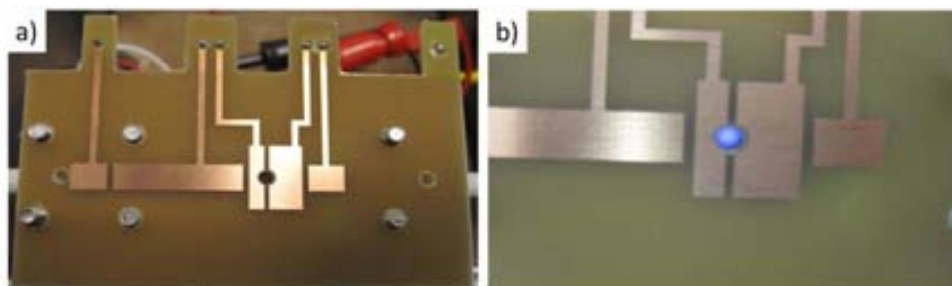


Figure 4-25: Pictures of the a) Top part of the p-FAIMS piece; and b) Detail of the top part showing the UV-lamp lightened and being correctly aligned with the drilled hole of the PCB.

4.2 Measurements set-up

In this section a summary of the chosen instrumentation to operate with the p-FAIMS device, the UV-lamp chose and the gas supply system used is done.

4.2.a The gas supply system

The gas supply system showed in Figure 4-26 was designed and installed in the *Institut de microelectrònica de Barcelona* IMB-CNM. It consists of a container with space for two gas cylinders placed outside the IMB building (Figure 4-26a). The gas lines go from the gas cylinders to the laboratory (Figure 4-26b) where are connected to pressure regulators. Gases are controlled with a home-made mass flow system. Nitrogen was chosen as carrier gas for the p-FAIMS device and is supplied by a general line in the laboratory; while toluene that was chosen as sample gas because it is a volatile organic compound used in security applications and would be a good testing gas for other devices developed in the research group, is supplied by Praxair with a concentration of 200 ppm (diluted in synthetic air) and is placed in the gas cylinders container. Toluene has the chemical formula C_7H_8 (CAS number 108-88-3), with a molecular weight of ~ 92 amu, and has an ionization energy of 8.8 eV [15] that allows its ionization with the UV-lamp as the required energy is lower than 10.6 eV.

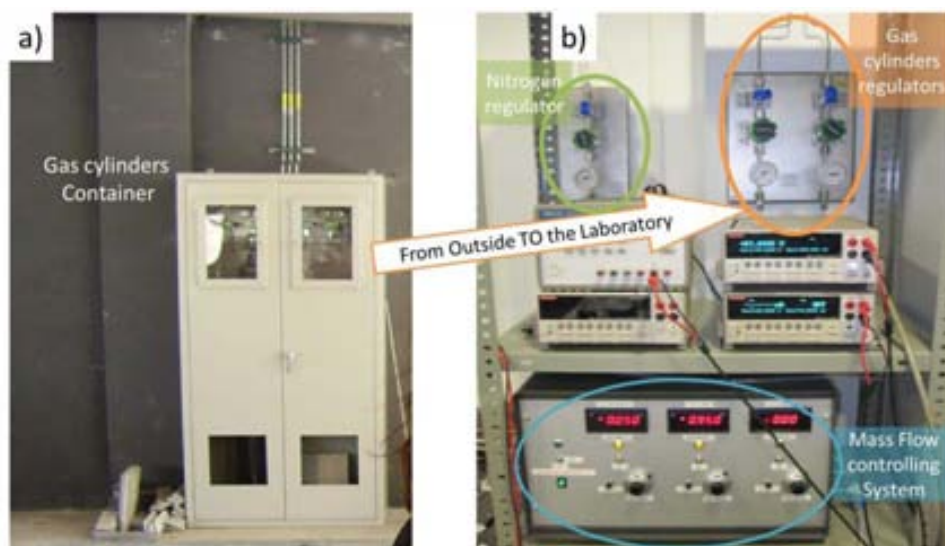


Figure 4-26: Gas supply system installed in the IMB-CNM facilities: a) Gas cylinders container placed outside the building, with space for two gas cylinders; b) Laboratory gas lines connections with pressure regulators, being also shown the general nitrogen line regulator and the mass flow controlling system.

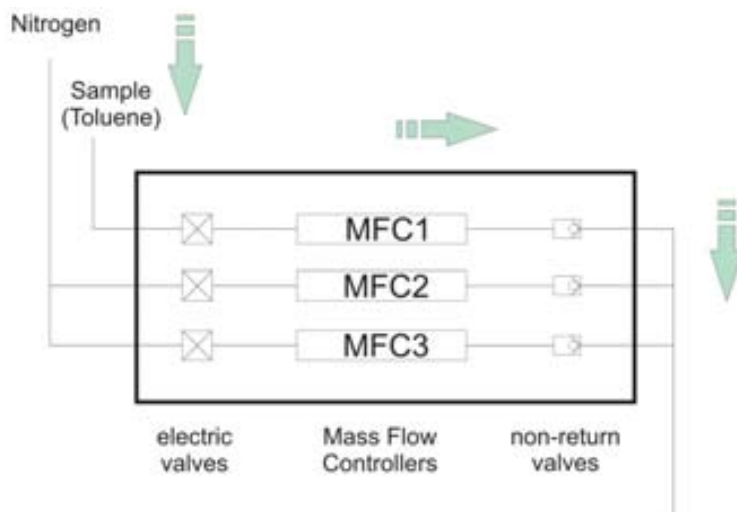


Figure 4-27: Schema of the Mass Flow Controlling system, as is used in p-FAIMS characterization.

In Figure 4-27 is shown a schema of the mass flow controlling system as they would be used for the p-FAIMS characterization. The system consist of three independent lines, each one with an electrical valve followed by a mass flows controller (Brooks 5850E from Brooks Instrument [16]) named as MFC#, and finally with a non-return valve. The first mass flow controller (MFC1) has a maximum mass flow of 50 sccm, while the other two (MFC2, MFC3) have a maximum mass flow of 1,000 slpm (standard liter per minute). All three MFC's can operate at pressures up to 104 bar (1 bar = 101,325 Pa = ambient pressure), and with ambient temperature operating from 5 to 65°C. During the p-FAIMS characterization, the used pressure and temperature have been the standard ambient temperature and pressure ($T_{\text{amb}} = 20^{\circ}\text{C} = 273.15^{\circ}\text{K}$, $p_{\text{amb}} = 101,325 \text{ Pa}$).

4.2.b Experimental set-up

Figure 4-28 shows the needed experimental set-up for the p-FAIMS device characterization.

Four different voltage suppliers provide the needed voltages to operate, including: a) two Keithley 2400 SourceMeter (allows sources and measures voltage from $\pm 1\mu\text{V}$ to $\pm 200\text{V}$ DC and current from $\pm 50\text{pA}$ to $\pm 1\text{A}$) [4] that are used one to turn on the UV-lamp CDL 1021-0X from ACI and the other one to scan the compensation voltage in the filtering region of the p-FAIMS; b) a Hewlett Packard (now Agilent) E3631A triple-output power supply [17] that offers three independent outputs: 0 to 6 V/5A, 0 to +25V/1A and 0 to -25V/1A (the 6 V output electrically isolated from the $\pm 25 \text{ V}$

supply to minimize any interference between circuits under test), this voltage source is used for the UV-gate, UV-back and the Detector voltage (V_{det}); c) a Keithley 2410 High Voltage SourceMeter (allows sources and measures voltage from $\pm 1\mu V$ to $\pm 1,100V$ and current from $\pm 50pA$ to $\pm 1A$) [3], that is used to provide the high voltages (HV) needed for the HV operating.

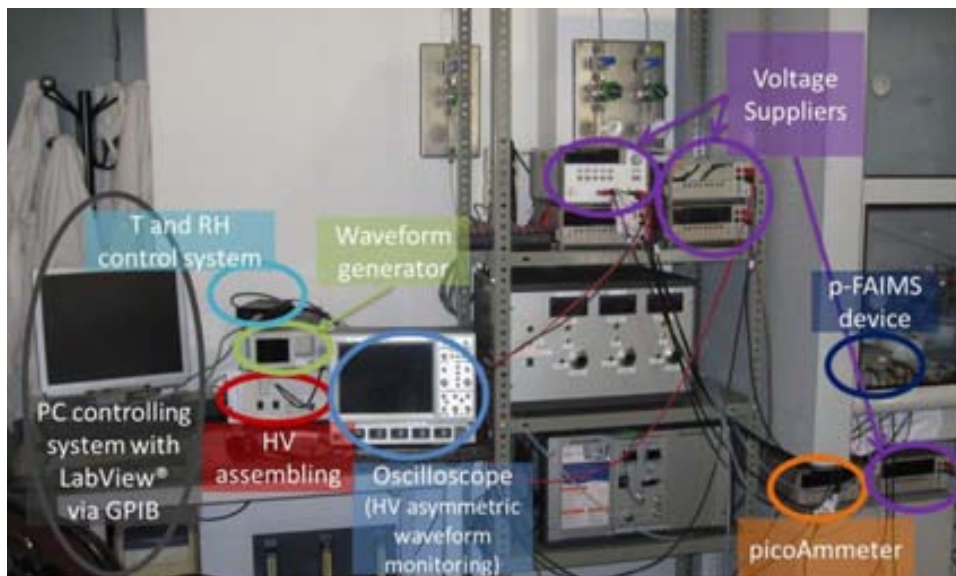


Figure 4-28: Experimental set-up, emphasizing the instrumentation used.

A waveform generator from Tabor Electronics WW1071 [18] is used to generate the bisinusoidal waveform, as it has an equation editor that allows nonstandard waveforms to be generated. To have the desired waveform but with HV, a DEI PVX-4140 (Pulse Output of 0 to $\pm 3,500 V$, with rise and fall Times $\leq 25 ns$, with pulse repetition frequency $> 30 KHz$, protected against arcs, shorts and load transients and also provides voltage and current monitor outputs) [19] is used, as it takes the HV inputs and the low voltage waveform and returns the HV waveform. To monitor the HV output voltage (monitoring signal is 1,000 times lower than the output signal), is used an oscilloscope WaveRunner 44 Xi-A from Teledyne LeCroy (400 MHz, 4 Channels, 5 GS/s, 12.5 Mpts/Channel with 10.4" Color Touch Screen Display) [20]. A personal computer is used to generate the desired waveform using the supplied ArbConnection software via a GPIB interface, showing in Figure 4-30 the wave composer and its editor for a bisinusoidal waveform.

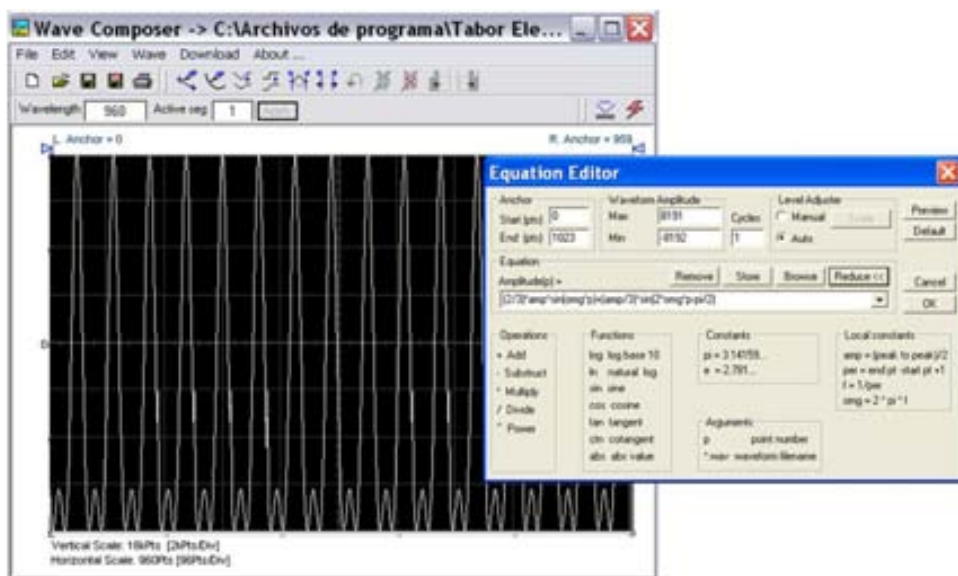


Figure 4-29: Wave Composer from the ArbConnection software of the Tabor Electronics WW1071 waveform Arbitrary Generator remote control [18]. Bisinusoidal waveform is shown.

To have a proper control of the temperature (T) and the relative humidity (RH) in the p-FAIMS, an evaluation Kit EK-H4 from Sensi rion A G [21] has been used with a Humidity and Temperature sensor SHT71 (operating ranges 0 – 100 %RH and -40 – 125°C, with an accuracy of $\pm 3\%$ RH and $\pm 0.3^\circ\text{C}$). Relative humidity is the ratio, often expressed as a percentage, of the partial pressure of water in the atmosphere at some observed temperature, to the saturation vapor pressure of pure water at this temperature [8]. A personal computer is used to save and view the data using the supplied EK-H4 Viewer software via USB, as shown in Figure 4-30 for data taken at the exit of the p-FAIMS as is shown in detail in the superimposed picture.

The used detector is a Keithley 6487 PicoAmmeter/Voltage Source (measure currents from 20 fA to 20 mA, at speeds up to 1000 readings per second, and source voltage from 200 μV to 505 V) [5]. Figure 4-31 shows general schemas of the input cable of the Keithley 6487 picoAmmeter, a triaxial cable (Figure 4-31a) and Figure 4-31b-c shows the typical measurement shielding. A noise shield (Figure 4-31b) is used to prevent unwanted signals from being induced on the picoammeter input. Typically, the noise shield is connected to the picoammeter input LO, as shown previously in Figure 4-21 for the faraday cage. Additionally, Figure 4-31c shows an added safety shield connected to earth ground and Model 6487 chassis. This type of shielding should be used whenever hazardous voltages will be present in the test circuit. As it is going to be our case (we want to use high voltages $\sim 1,000$ V), an extra safety box is added.

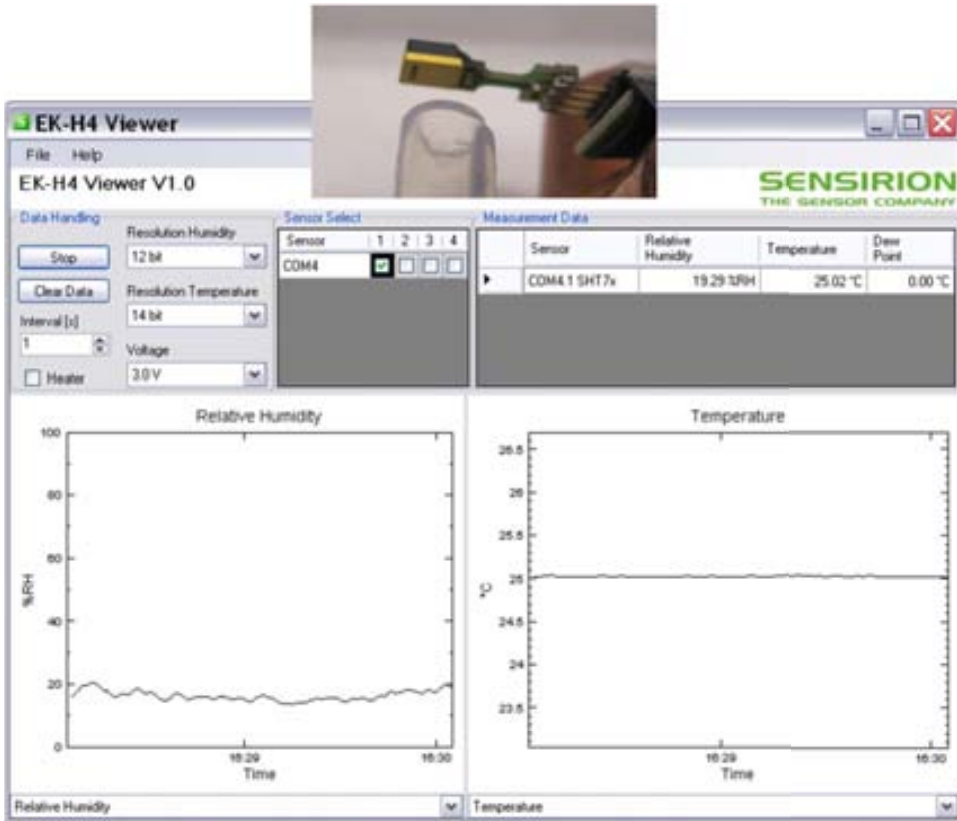


Figure 4-30: EK-H4 viewer software for the T&RH sensors SHT71 from Sensirion [21]. Data was taken at the exit of the p-FAIMS, as shown in the superimposed picture.

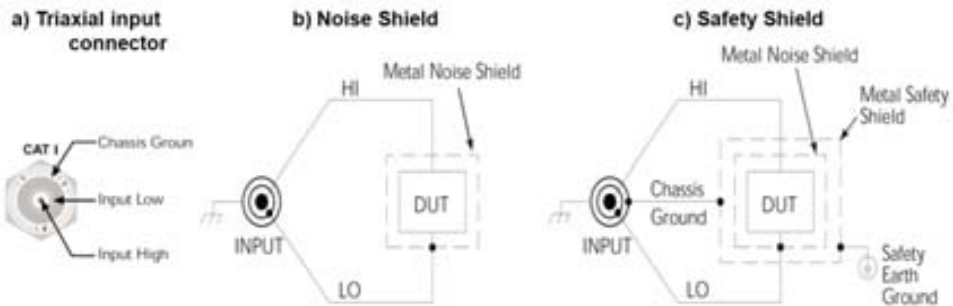


Figure 4-31: Schemas of Keithley 6487 picoAmmeter a) input triaxial cable; b) noise shield used to prevent unwanted signals from being induced on the picoAmmeter input. c) safety shield connected to earth ground and Model 6487 chassis.

Figure 4-32 shows the p-FAIMS inside the safety shield box. Connection cables including the one for the UV-lamp, the gas connections and the Temperature and humidity sensor are shown. Using a personal computer with Labview® via a G-PIB interface can be controlled the picoAmmeter, the compensation voltage scan and the dispersion voltage (HV).

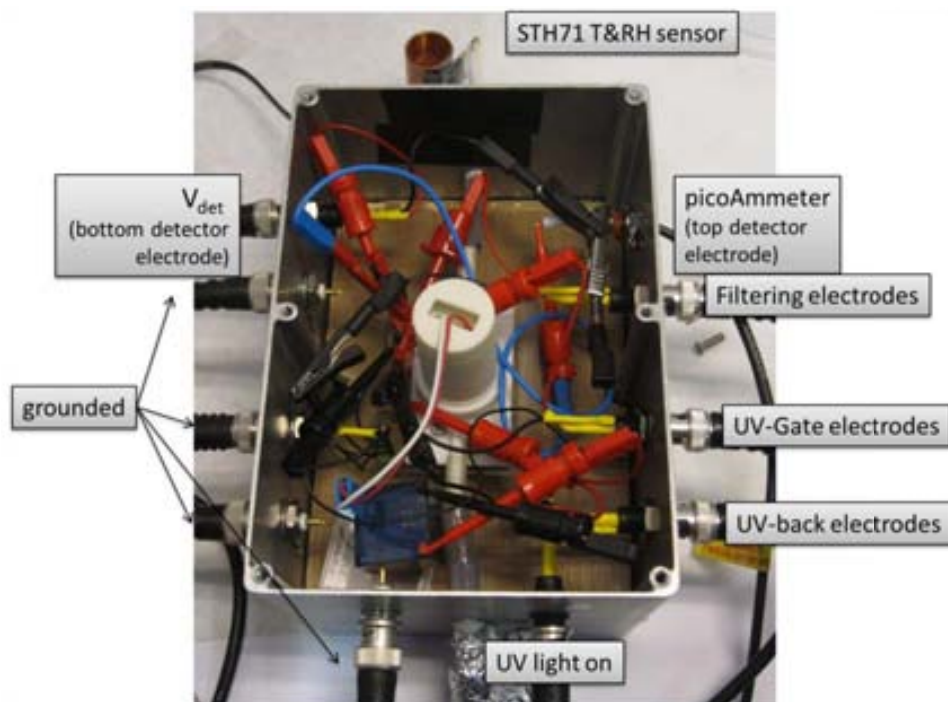


Figure 4-32: p-FAIMS device with connections, inside its safety shield box. Gas connections and temperature and humidity sensor are also shown.

4.3 p-FAIMS Characterization

In this section the characterization of the p-FAIMS device using the PCB-PMMA-PCB configuration is presented. Different experimental conditions affecting the signal obtained are studied. When errors are presented, they are calculated using the propagation of uncertainty as detailed in [Annex 4-3](#).

4.3.a Electrodes biasing

First of all, we measured the signal intensity in each pair of electrodes that compose the p-FAIMS structure to have an idea of how many ions were lost during their flight to the detector electrodes. Electrodes used for detection in each case was set to +5 V,

while setting the rest of electrodes to 0 V (no compensation –CV– or dispersion voltages –DV– were applied). Measurements were taken continuously with the LabView program *pAcontinuous.vi* that is detailed in Annex 4-4. 2-propanone at a concentration ~ 1,000 ppm in a total flow of 1,800 sccm was used for this test. First measurements were done in the UV-gate electrodes; then in the Filtering electrodes placed 3 mm from the UV-lamp; and finally in the Detector electrodes placed 22 mm from the UV-lamp. Table 4-1 shows a resume of the obtained results for each pair of electrodes considered. The intensity values showed are the mean of 10 measurements. As expected, as far as we measure from the ionization region where the UV lamp is placed less intensity is obtained, due to the ion losses in the walls and to their recombination and neutralization. In Figure 4-33 the ions intensity versus the distance between the UV lamp and the measurement electrodes is showed.

Electrodes	Area (mm ²)	Intensity (nA)
UV-gate	20.0 ± 0.1	5.5486 ± 0.0660
Filtering	72.0 ± 0.1	2.7924 ± 0.0626
Detector	20.0 ± 0.1	0.1506 ± 0.0062

Table 4-1: Intensities obtained in each pair of electrodes (non DV or CV applied).

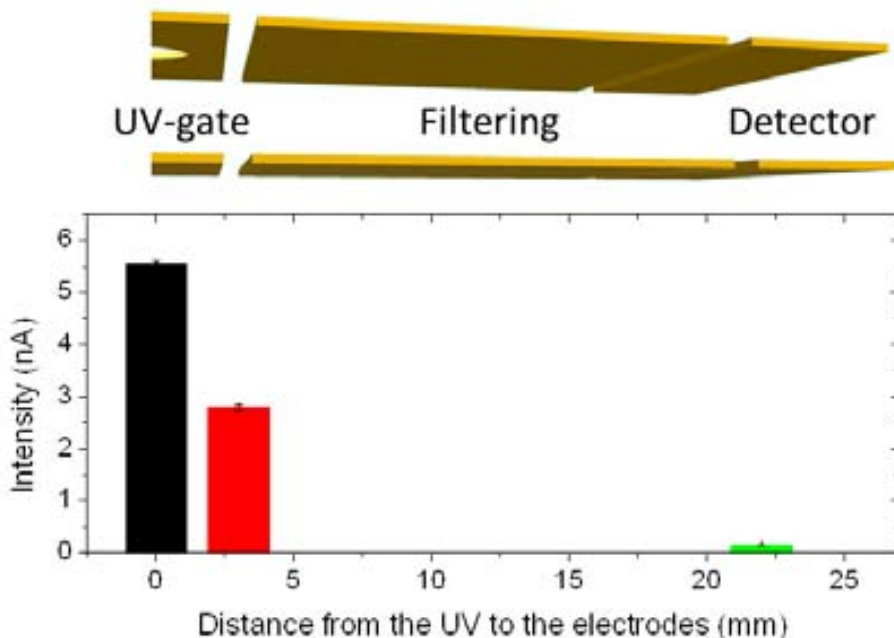


Figure 4-33: Intensity dependence with the distance of the electrodes for 1,000 ppm of 2-propanone.

Once proved the detection of 2-propanone, we shift to toluene using the experimental set-up shown in Figure 4-28 as it is more appropriate to make an accurate control of gas concentrations. At this time we were able to detect different concentrations of toluene in the detector electrodes, for the test no DV or CV were applied in the filtering region. Detector voltage was set to +5 V. Measurements were taken continuously with the LabView program *pAcontinuous.vi* that is detailed in Annex 4-4. Figure 4-34 shows the results obtained for a total flow of 50 sccm, and four different concentrations of toluene. As the concentration increased, also the intensity increased, up to a saturation value of 0.1298 ± 0.0060 nA for 200 ppm. This saturation value is slightly different from the obtained in the previous section for 2-propanone, but the total flow was better controlled in the case of toluene detection. Cleaning with nitrogen was done after each concentration measured, showing that intensity recovers its initial value.

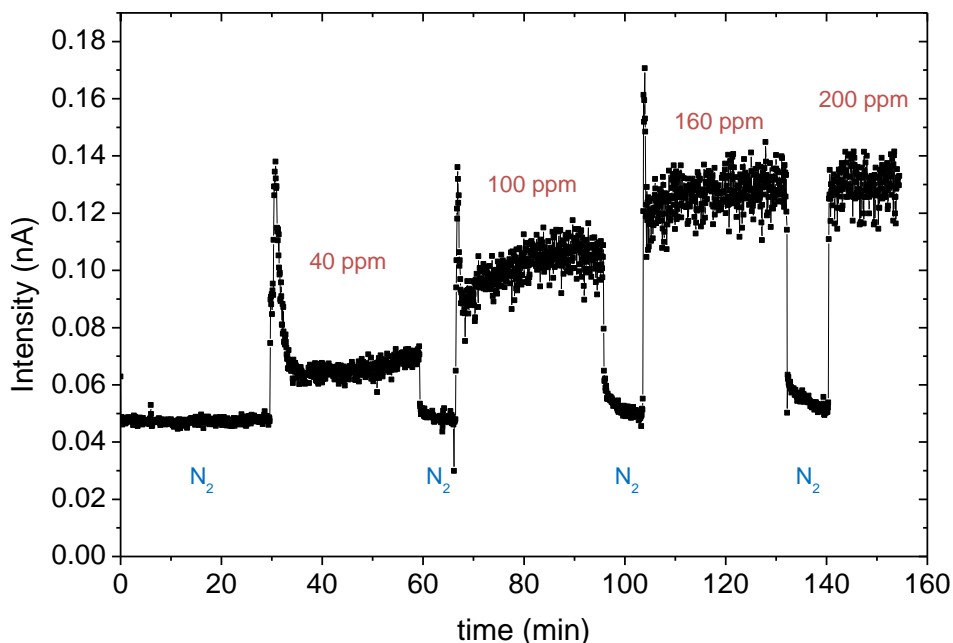


Figure 4-34: Obtained intensity at the filtering detector for different concentrations of toluene ions.

Detection of Toluene Ions with Compensation Voltage Scan

Once proved the detection of toluene in the detector electrodes, next step was to introduce the compensation voltage (no DV was applied). UV-gate and UV-back were set to 0 V, and detector voltage was set to +5 V. Measurements were taken with the LabView program *pA-VcScan.vi* that is detailed in Annex 4-5. Mass flow MFC1

was used for toluene control (50 sccm) while the other two mass flows, MFC2 and MFC3 (1 slm), were used to control nitrogen that was used as carrier gas. To measure 1 ppm of toluene, initially it was tried to use the same flow rate than in the previous section (50 sccm) but no signal was obtained. After a substantial increase of the flow up to 1,000 sccm, toluene ions were detected as is shown in Figure 4-35. Compensation voltage (CV) was scanned from -20 V to +20 V with a step of 0.1 V. Obtained intensity was $I = 1.27$ pA, having a full width at half of the maximum (FWHM) of $w_{1/2} = 1.0$ V. Measurement was centered at $CV = 0.0$ V because no dispersion field was applied, when the CV is higher or lower than zero, ions were attracted to the filtering electrodes where they were neutralized and lost. As can be seen the intensity signal is in the range of pA. When doing a CV scan (without DV) the ions are deviated to the filtering electrodes if the $CV \neq 0.0$ V, so the elapse of time at which they are compensated is very low and few ions would be detected.

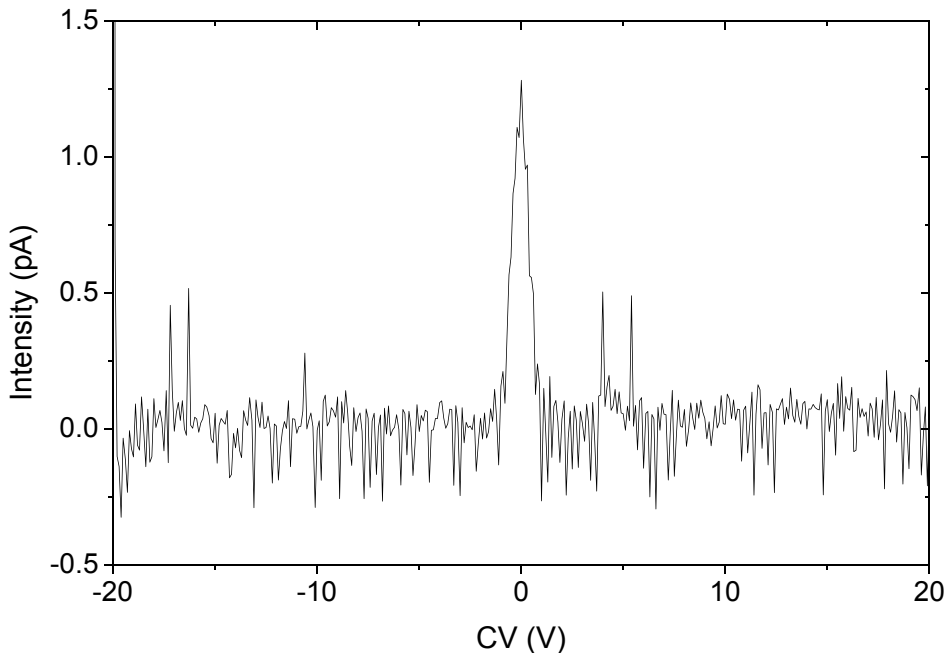


Figure 4-35: p-FAIMS spectrum for 1 ppm of toluene, in a total flow of 1,000 sccm.

Having the results in function of the compensation electric field E_C/N (-0.8 to +0.8 Td), leads that the obtained full width at half maximum was 0.05 Td (0.63 V) while for the simulation result at the same flow rate it was of 0.04 Td (0.50 V), so the measured value with is slightly higher than result obtained in the simulation. The obtained intensity in the simulations was $I_{sim} = 1,07$ nA for 1 ppm of toluene at

1,000 sccm for a gap of 0.5 mm. The gap variation from 0.5 mm in the simulated to 1 mm in the experimental case, contributes to the difference between intensity values obtained. Also, while in the simulations were considered that all ions are ionized, in the experimental case only up to a 3% of the sample is ionized (for a 0.5 mm gap) as seen previously.

UV-gate operation

The UV-gate electrode was studied. A scan of compensation voltage (no DV was applied) was used for this studio, and detector voltage was set to +5 V. First it was polarized from zero to negative values, so it was expected a decrease of the amount of toluene ions (TH^+) detected, because positive ions would be attracted to the UV-gate electrodes where they are neutralized. This test has been done for 1 ppm of toluene in a total flow of 1,000 sccm. Figure 4-36 shows the results for having the UV-gate at 0 V (normal operation), at -5 V for which the intensity was reduced to the half, and at -10 V for which value was not clear, as the obtained ‘peak’ has the same range than the noise. In Table 4-2 are summarized the obtained intensities for the UV-gate studio at negative voltages. Decreasing the UV-gate enough positive ions do not enter into the filtering region.

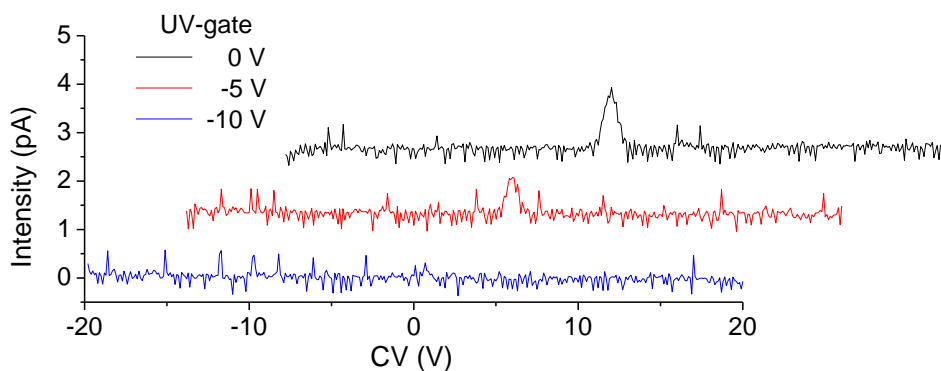


Figure 4-36: UV-gate studio for negative voltages.

UV-gate Voltage (V)	Intensity (pA)
0	1.28 ± 0.17
-5	0.63 ± 0.17
-10	0.15 ± 0.17

Table 4-2: Obtained intensities in the UV-gate studio for negative voltages.

A similar studio was done biasing positively the UV-gate, in this case it is also expected a decrease of the amount of toluene ions (TH^+) detected, because as they have opposite charges ions would be repelled from the UV-gate. 1 ppm of toluene in a flow of 1,000 sccm was tested in this studio. Figure 4-37 shows the results for having the UV-gate at 0 V (normal operation), at +5 V for which the intensity was slightly reduced, and at +10 V for which the intensity was reduced to the half. In Table 4-3 the obtained intensities for the UV-gate studio at positive voltages are summarized. Increasing the UV-gate, the amount of ions introduced that enter into the filtering region was decreased but not stopped.

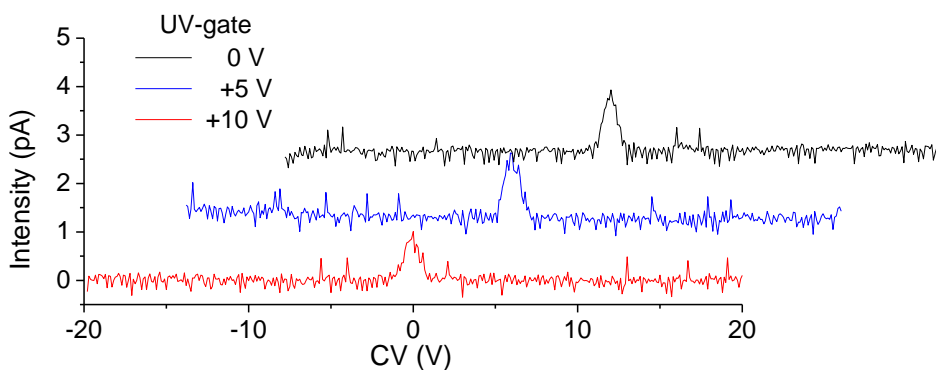


Figure 4-37: UV-gate studio for positive voltages.

UV-gate Voltage (V)	Intensity (pA)
0	1.28 ± 0.17
+5	1.17 ± 0.17
+10	0.66 ± 0.17

Table 4-3: Obtained intensities in the UV-gate studio for positive voltages.

Figure 4-38 shows a summary of the obtained results in the UV-gate studio. No toluene was detected having the UV-gates biased at -10 V or lower voltages, it can also be seen that the response obtained at -5 V and +10 V was almost the same so increasing the UV-gate voltage to 20 V or more, the same effect of non-toluene detection would be obtained. The difference between applying a positive or a negative UV-gate voltage is due to the fact that toluene ions are not ‘ideally’ spherical charges, and it would ‘feel’ the electric field in a different manner. Figure 4-39 show images of the toluene molecule without (Figure 4-39a) and with (Figure 4-39b) the electrostatic potential surface. Even though the surface is from the molecule and not from the ionized toluene, it gives an idea of how the electric potential is distributed.

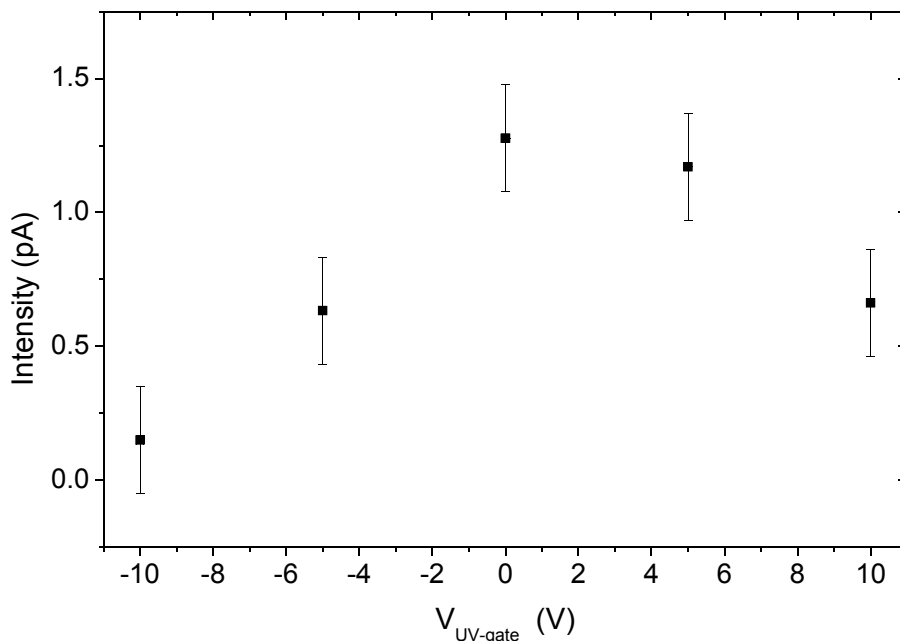


Figure 4-38: Resume of the results of the UV-gate operation studio.

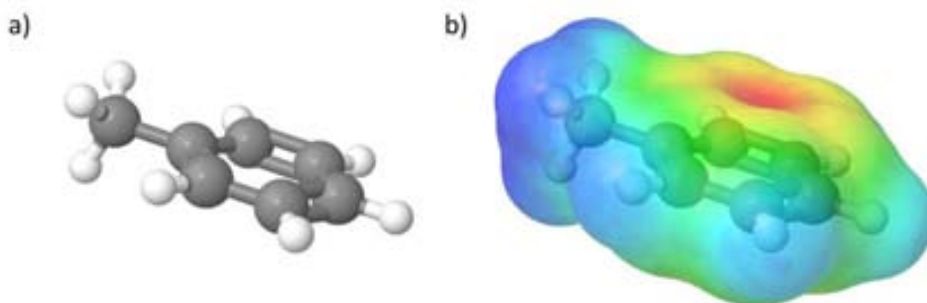


Figure 4-39: Structure of: a) toluene molecule; b) surface view of the electrostatic potential of the toluene molecule onto the solvent excluded surface, based on a probe of radius 1.4 Å. Regions of negative potential are shown in red, positive in blue. Adapted from [22].

Changing the detector polarity

Once proved the detection of toluene ions in positive mode ($V_{det} = +5V$) we move to negative mode ($V_{det} = -5V$). No peak is expected in the negative mode as toluene only is ionized as positive cations [23], being the main ion the monomer TH^+ . In Figure 4-40 are shown the results for both detector polarities. A little peak was obtained in the negative mode, with an intensity of $I_{exp_neg} = -0.4$ pA. This peak must be due to some impurities present in the carrier gas flow, which are recombined with the electron lost in the ionization of toluene.

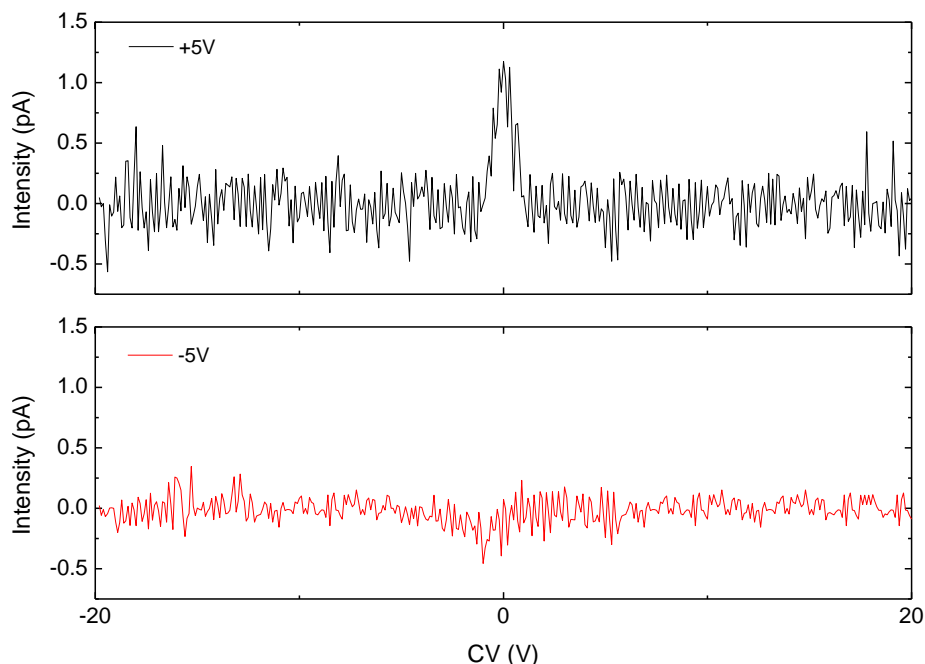


Figure 4-40: Obtained intensities of 1 ppm of toluene at 1,000 sccm changing the detector polarity.

From this point, always UV-gate will be grounded and detection will be done in positive mode for the measurements.

4.3.b Detection without High Field

Repeatability

Once seen that 1 ppm of toluene ions could be detected, we proved the repeatability of the results. Figure 4-41 shows the obtained p-FAIMS spectrums for 1 ppm of toluene, in a total flow of 1,000 sccm for 10 consecutive measurements. Between measurements cleaning with nitrogen was done for 1 min. Obtained mean value of the intensity was 1.28 ± 0.17 pA.

Once seen its continuous repeatability, we focus on its repeatability over time. Figure 4-42 shows the obtained p-FAIMS spectrums for 1 ppm of toluene, for a total flow of 1,000 sccm corresponding to 5 measurements made on five consecutive days. Obtained mean value of the intensity was (1.31 ± 0.22) pA that is very similar to the mean value obtained for the ten consecutive measurements with the p-FAIMS device.

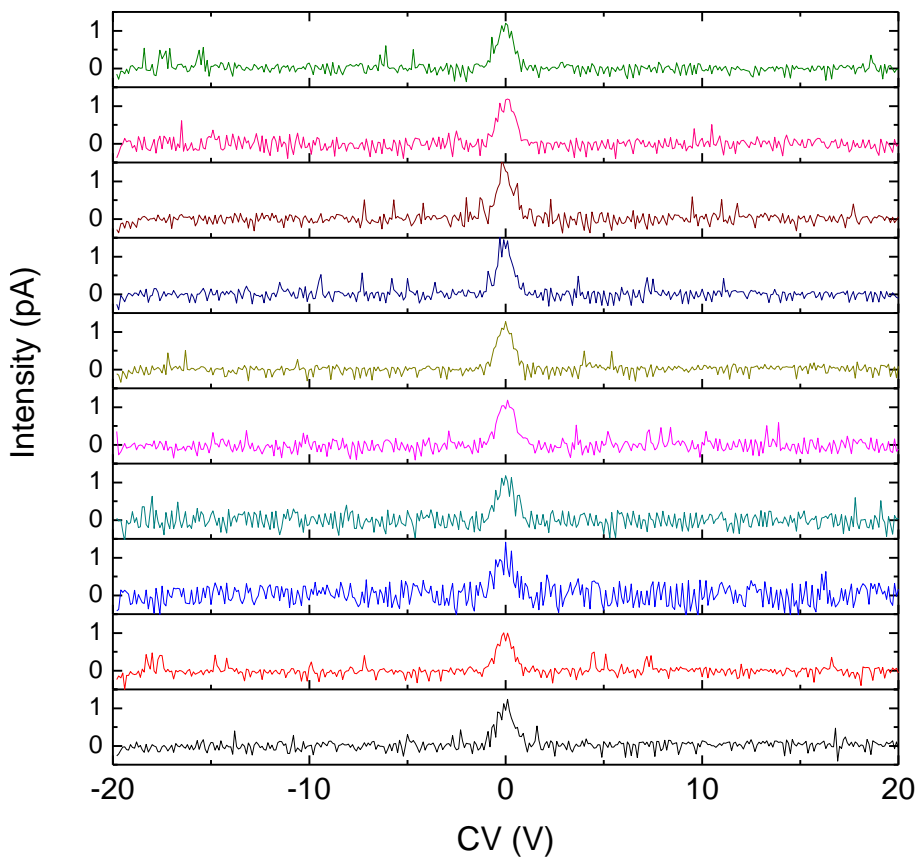


Figure 4-41: Stacked p-FAIMS spectra for 1 ppm of toluene, in a total flow of 1,000 sccm for 10 consecutive measurements.

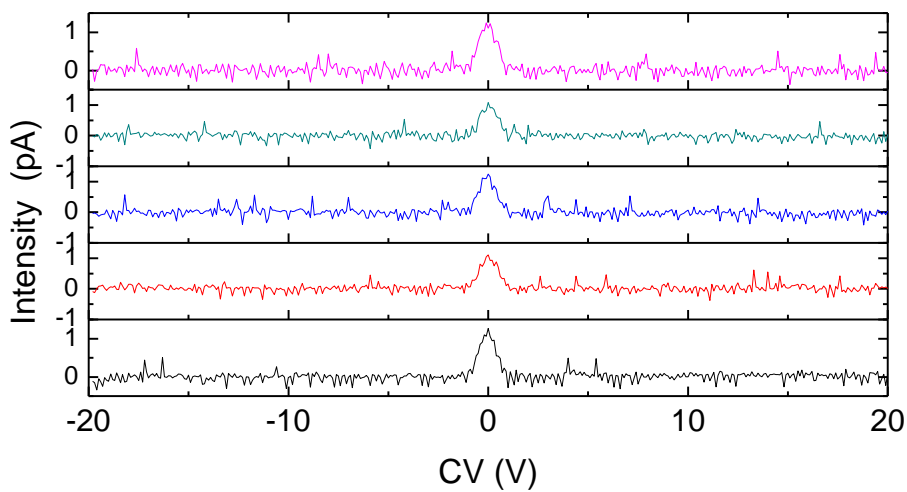


Figure 4-42: Stacked p-FAIMS spectra for 1 ppm of toluene, in a total flow of 1,000 sccm corresponding to 5 measurements made on consecutive days.

Concentration variations

Once proved the detection of 1 ppm, different concentrations were tested. Figure 4-43 shows the results obtained for toluene ranging from 1 to 10 ppm in a total flow of 1,000 sccm. Obtained intensity is clearly increased with increasing the toluene concentration.

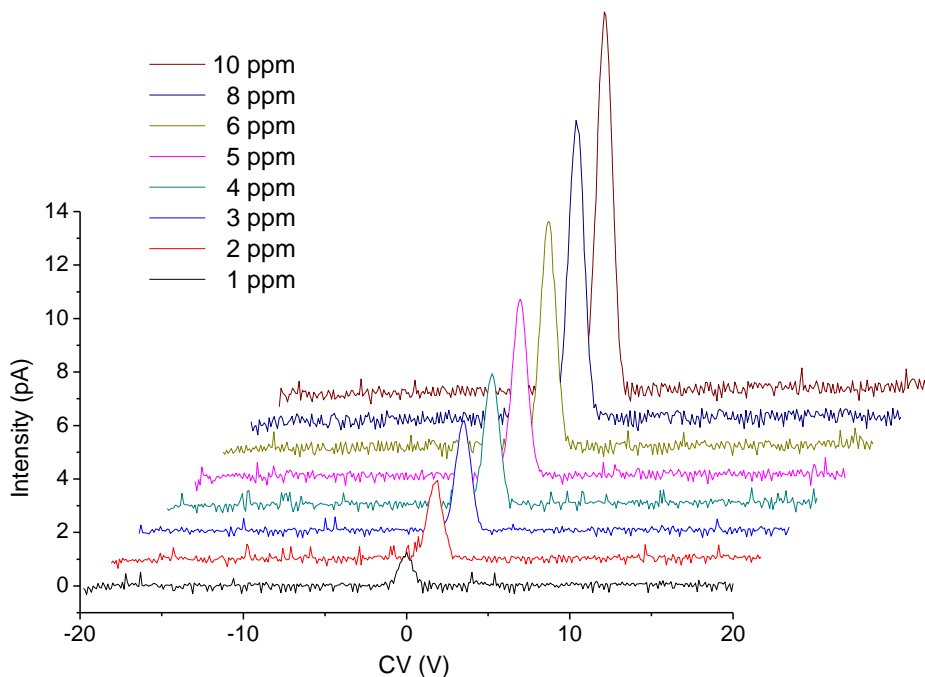


Figure 4-43: p-FAIMS spectrums for toluene with increasing concentration from bottom to top, from 1 to 10 ppm. Total flow is 1,000 sccm.

The peak heights and areas showed in Figure 4-43 are plotted in Figure 4-44 versus toluene concentration and appear linear over the range of concentrations tested.

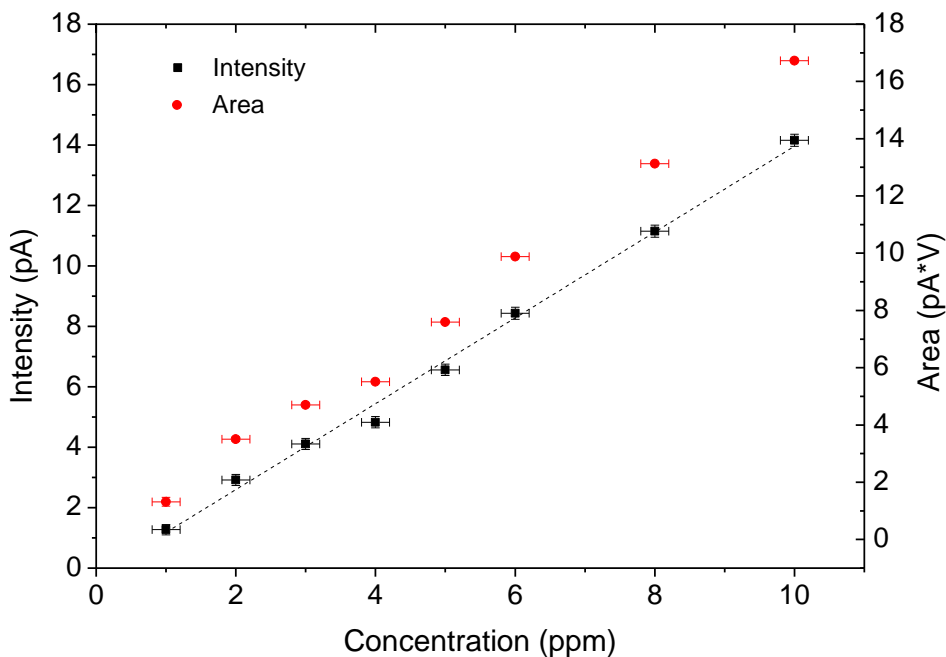


Figure 4-44: Toluene peak intensity and area dependence on concentration, for 1 to 10 ppm at 1,000 sccm.

Once studied the concentration in the ppm's range, we moved down to the ppb's range, specifically from 200 ppb to 1 ppm also for a total flow of 1,000 sccm. As can be seen in Figure 4-45, detection was obtained for all the studied concentrations but in the case of 200 ppb, obtained intensity was in the range of the noise signal.

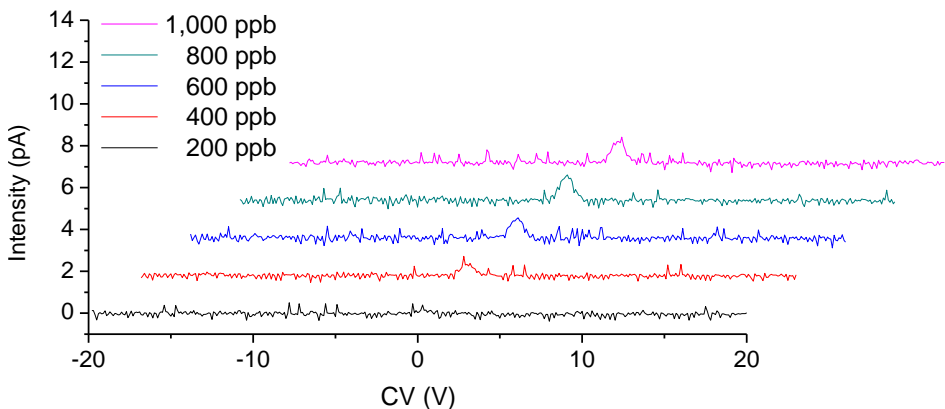


Figure 4-45: p-FAIMS spectra for toluene with increasing concentration from bottom to top, from 200 ppb to 1 ppm. Total flow is 1,000 sccm.

The peak heights found in the tests and showed in Figure 4-45 are plotted in Figure 4-46 as a function of concentration for clarity, as can be seen throughout the range of 200 ppb to 1 ppm also a linear variation of the intensity with concentration was obtained.

The analysis done confirms that the p-FAIMS spectrum has a linear intensity dependence on concentration also below 1 ppm. This result is in concordance with the one obtained by Miller *et al.* [24] for the ppb range, being linear with concentration when using a UV-ionization source (Figure 4-47a) instead of non-linear when a radioactive source was used (Figure 4-47b).

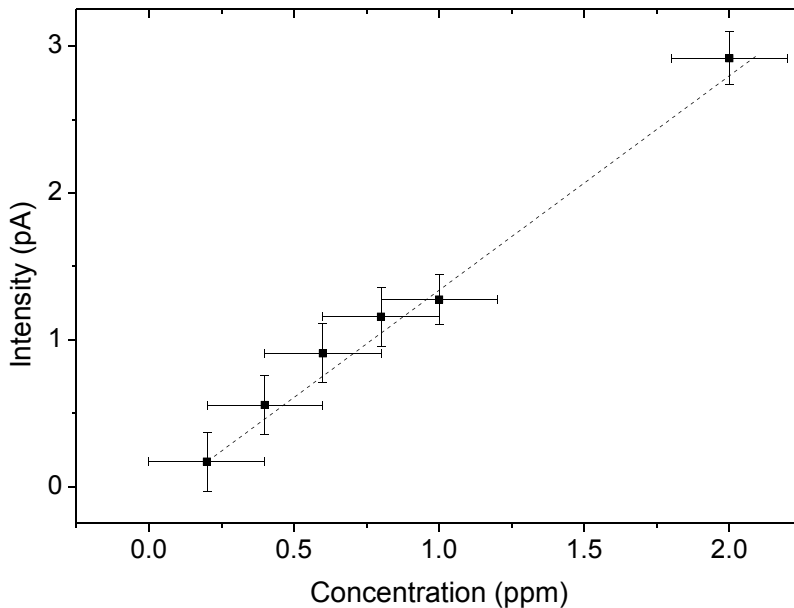


Figure 4-46: Toluene peak intensity dependence on concentration, for 200 ppb to 1 ppm at 1,000 scfm.

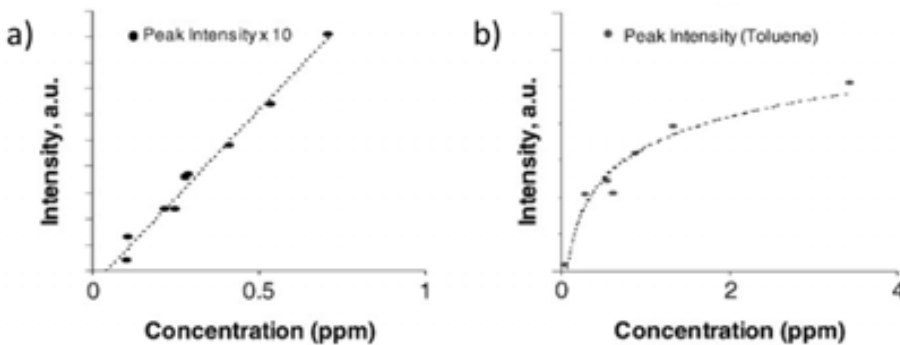


Figure 4-47: Concentration dependence of a FAIMS response for toluene in air with different ion sources: a) UV ionization source; b) Radioactive americium source with 1 μCi activity. Adapted from [24].

The limit of detection LOD in our case is 200 ppb, as it is the minimum concentration of toluene that our mass-flows system can provide, but intensities found for this concentration were in the same range as the noise signal. Anyway, a slight decrease of the noise was obtained by decreasing the voltage step of the compensation scan. Figure 4-48 shows two measurements done for 200 ppb of toluene at 1,000 sccm, for a step of 0.1 V (the one used until now) and for a step of 0.05 V. For a lower step voltage, the noise is reduced and basing upon signal to noise calculations LOD is estimated at 100 ppb. The LOD obtained is from the same range than reported [25].

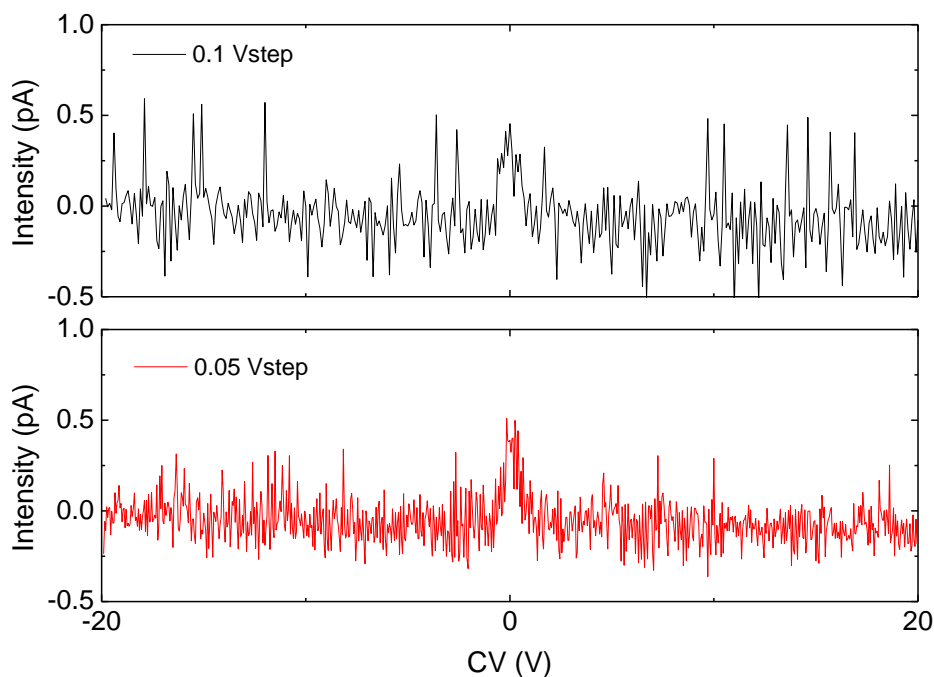


Figure 4-48: Obtained intensities for different V_{step} voltages for 200 ppb of toluene in a total flow of 1,000 sccm.

Figure 4-49 shows a detail of the obtained peaks for toluene concentrations from 200 ppb to 10 ppm in a total flow of 1,000 sccm. As the concentration is increased the peak width is also increased, as shown in Figure 4-50. For low concentrations the associated error is much bigger than for high concentrations. This is in part, due to the associated error of the home-made mass-flow system (0.2 ppm).

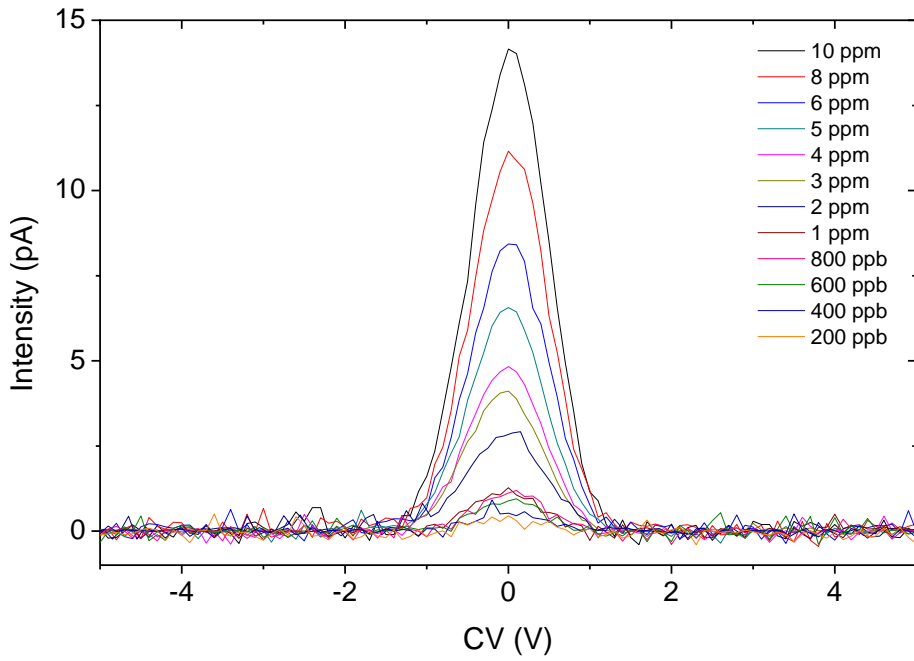


Figure 4-49: Obtained intensities for different toluene concentrations on p-FAIMS spectrums. Total flow was 1,000 sccm.

194

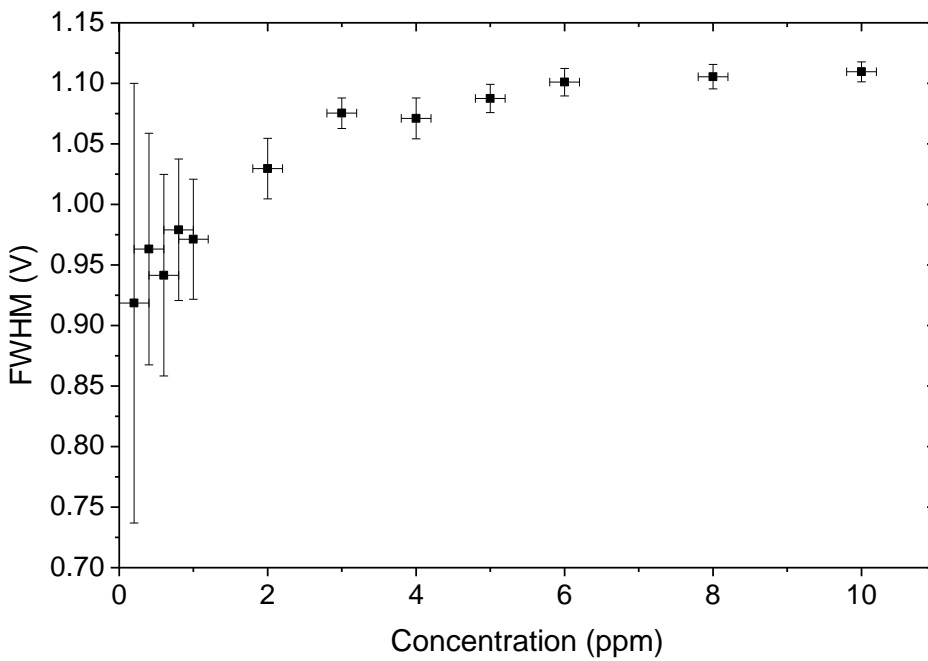


Figure 4-50: Toluene peak widths at half maximum, for different toluene concentrations. Total flow was 1,000 sccm.

Carrier Gas Flow Dependence

Next step was the study of the intensity dependence with carrier gas flow. Figure 4-51 shows the obtained results for 1 ppm of toluene in a total flow ranging from 250 to 2,000 sccm. It can be seen that as the flow is increased, the intensity obtained for 1 ppm is also increased.

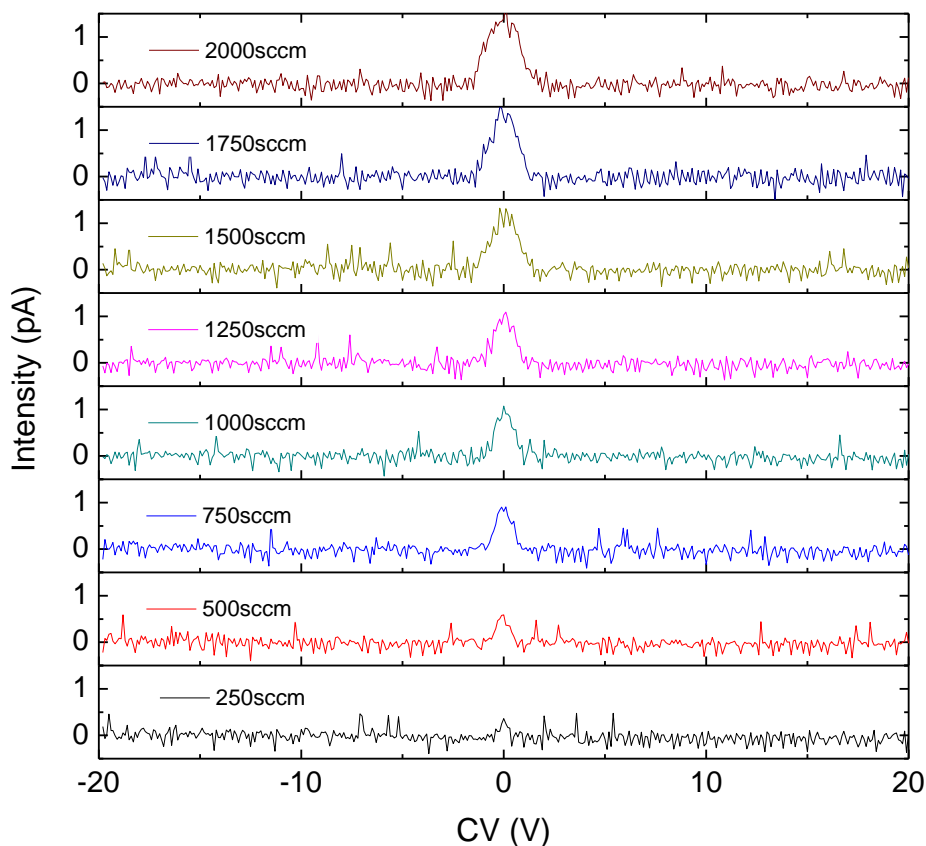


Figure 4-51: p-FAIMS spectra for toluene for 1 ppm with increasing total flow from 250 to 2,000 sccm.

The peak heights showed in Figure 4-51 are plotted in Figure 4-52 as a function of total flow for clarity, a linear relation was obtained. This result is in agreement with simulation results presented in Section 3.8.a *Carrier gas flow rate effects*.

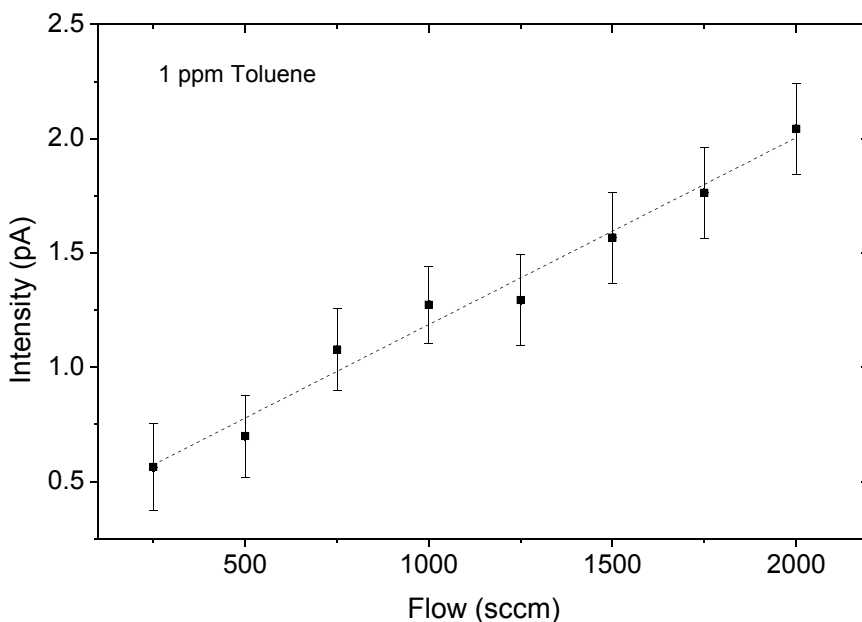


Figure 4-52: Toluene peak intensity dependence on total flow from 250 to 2,000 sccm, for 1 ppm.

We can calculate from the results obtained the Aspect ratio (AR) defined previously in Section 2.2. *fD ata col lection and t reatment* in equation (2.30) as: $AR = h/w_b$, where h is the peak height and w_b is the width at the base that is related with the standard deviation (σ) by equation (2.28) as $w_b = 4\sigma$. Figure 4-53 shows the aspect ratio results for a toluene concentration of 1 ppm in different carrier gas flows ranging from 250 to 2,000 sccm. The Aspect ratio curve is increased for low carrier gas flows until finding a ‘plateau’, so the flow associated is the considered one as the optimum.

Obtained ‘plateau’ is at 1,000 sccm, being the same value obtained in the Simulation, but the value of the $AR_{exp} \sim 0.7 \text{ pA/V} \sim 18 \text{ pA/Td}$ while the aspect ratio from simulations was $AR_{sim} \sim 15 \text{ nA/Td}$. Considering that only the 3% of the sample is ionized as seen previously, it is seen that there is a factor 10 between them that is believed to be due to the gap difference from 0.5 mm in the simulations to the 1 mm in the experimental p-FAIMS device.

The obtained intensity for 1 ppm was $I_{sim,1ppm} \sim 1.07 \text{ nA}$. Papanastasiou *et al.* studied 0.15 ppm for the same flow condition but at a frequency of 1.0 MHz, obtaining an intensity value $I_{exp} \sim 1.30 \text{ pA}$. Supposing linear variation with the concentration, for 0.15 ppm the intensity is reduced $I_{sim} \sim 1.61 \times 10^{-10} \text{ A}$. And considering that in the simulations are assumed that the entire sample is ionized, whereas [26] found that only a 3% of sample is ionized this leads a $I_{sim} \sim 4.83 \text{ pA}$ that is of the same order of the experimental value obtained in the literature.

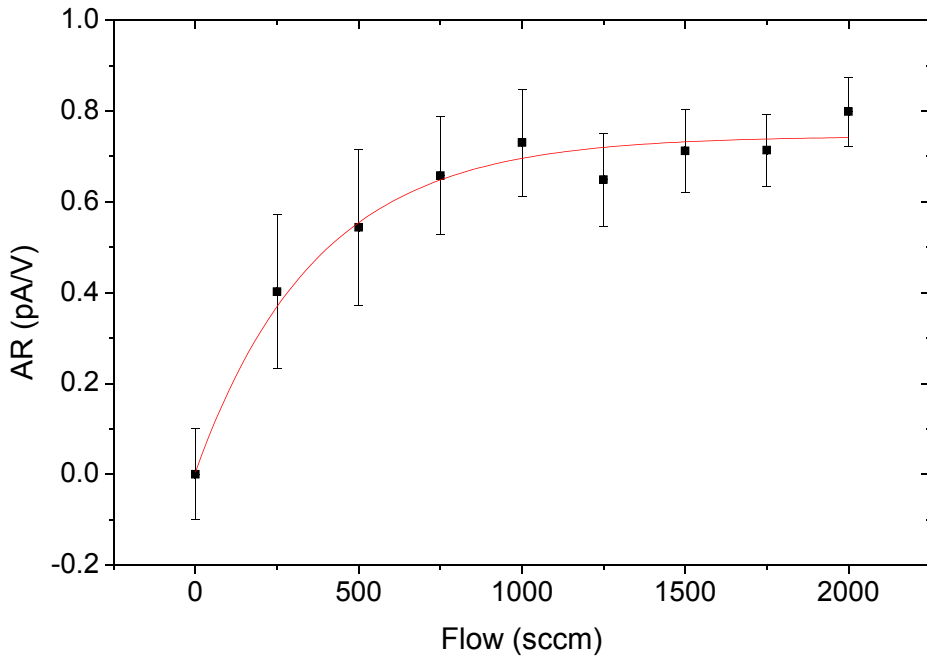


Figure 4-53: Aspect Ratio as a function of the carrier gas flow, for 1 ppm of toluene.

To check the optimum flow, a scan over each carrier gas flow considered, from 250 to 2,000 sccm, is done and results obtained are shown in Figure 4-54 for 1 to 10 ppm when available. For the higher flow rates, concentration values achievable are less than for lower flow rates because of the flow sum of carrier gas (nitrogen has two mass flows at 1,000 sccm) and the toluene (with a mass flow at 50 sccm). The toluene concentration in the gas cylinder is 200 ppm. A simple relation is used to calculate the ppm's of toluene as:

$$C_{Toluene} \text{ ppm} = C_{gas \text{ cylinder}} \text{ ppm} \cdot \frac{Q_{Toluene} \text{ sccm}}{Q_{Total} \text{ sccm}} \quad (4.2)$$

From Figure 4-54 can be seen that, when increasing the flow, also the intensity is increased for the same concentration until reaching intensities saturation for flow values higher than 1,000 sccm. This result supports the chosen optimum flow of 1,000 sccm.

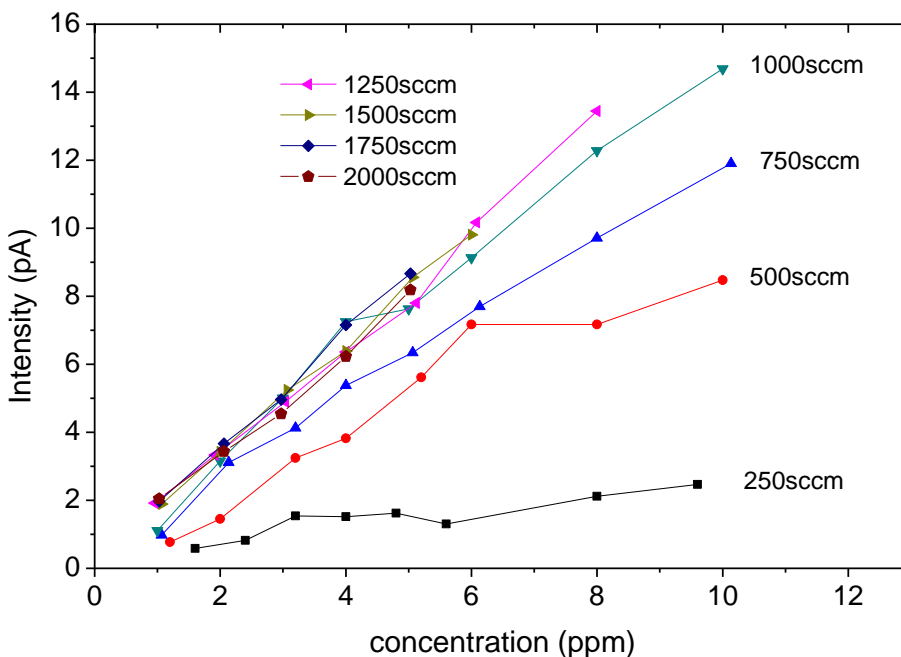


Figure 4-54: Toluene peak intensity dependence on total flow from 250 to 2,000 sccm, for concentrations ranging from 1 to 10 ppm.

4.3.c Detection of Toluene Ions with RF field

Next step was the addition of the High Voltage waveform that is obtained through the combination of a high voltage or dispersion voltage (DV) and a bisinusoidal asymmetric waveform, as explained in the Section 4.2.b *Experimental set-up*. The maximum applied dispersion voltage has been 300 V because the used HV source (Kethley 2410) is an ‘smart’ source and ensures the voltage for a low frequency, and when the DEI PVX-4140 (that takes the HV inputs and the low voltage waveform and returns the HV waveform) demands the HV to the source for voltages up to 300 V it worked properly, but for higher voltages the source ‘cuts’ the voltage giving. A way to solve this problem was to use a ‘non-intelligent’ source without this protection mechanism. The used source was an available Agilent (before Hewlett Packard) 6035A Series Single-Output, DC Power Supplies of 1000 W (0-500V/0-5A 1000W) [27], with which at least we should arrive to 500 V. The source worked well until arriving to 350 V at which value the transformer of the source ‘burned’, so we run out of HV sources up to the desired 1,000 V. Nevertheless, with a DV = 300 V, when measuring 1 ppm of toluene in a total flow of 1,000 sccm the p-FAIMS showed small variations in CV values from the previous case studied without applying DV as shown in Figure 4-55 for a bisinusoidal waveform at 2 MHz, with a duty cycle of 33%. It can be seen that without DV applied, the toluene peak appears at a

CV = 0.0 V, while for having a DV of 300 V applied toluene peak appears at a $CV_{\text{bisin}}(\text{DV}=300\text{V}) = -0.32 \pm 0.05$ V after Gaussian de-convolution. From the simulations, the value expected for a gap of 0.5 mm for a DV = 375 V is -0.25 V, so the increase of the experimental gap to 1 mm also increases the compensation voltage.

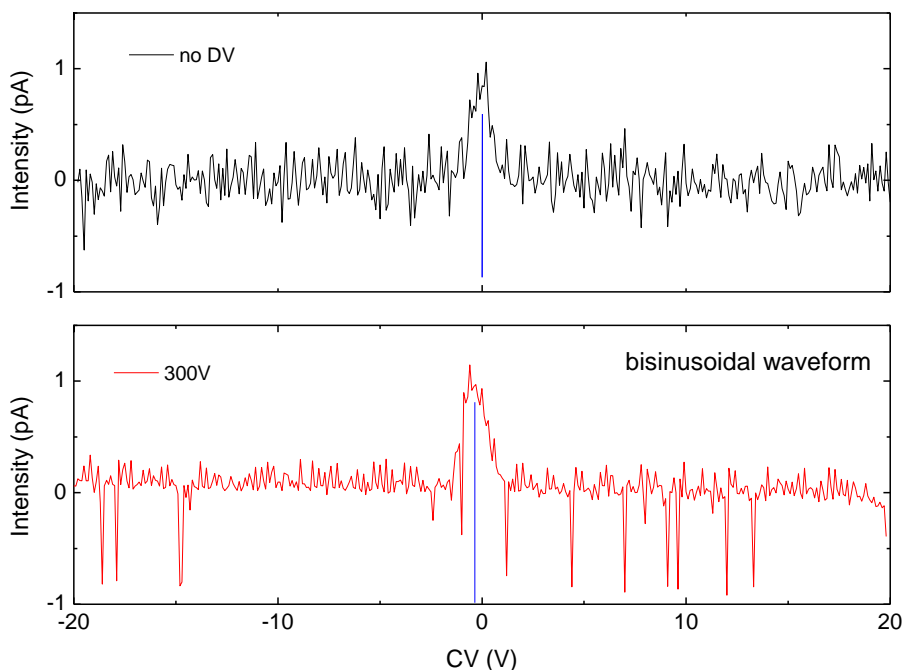


Figure 4-55: Obtained intensities without and with DV applied (300 V) for a bisinusoidal waveform at 2 MHz, for 1 ppm of toluene in a total flow of 1,000 sccm.

In Table 4-4 are summarized the obtained results for two different dispersion voltages using a bisinusoidal waveform. The CV's obtained for 100 and 300 V are almost the same if we consider the associated errors. However the intensity decreases somewhat at 300 V compared to the value obtained at 100 V, and also the full width at half maximum ($w_{1/2}$), so increasing the DV decreases the intensity and narrows the peak, meaning that the resolving power is increased for higher DV, this is in concordance to the experimentally found for Miller *et al.* [28]. The value Rp/L is one order of magnitude lower than the expected, but this is due to the low DV available, it is expected that increasing the DV, the absolute value of CV will increase and therefore the Rp and the Rp/L ratio, obtaining similar values to the reported in the literature (Section 2.3.c *Detection: Resolution and Resolving Power*) from 1.1 to 4.3 cm^{-1} are expected.

DV (V)	CV _{bisin} (V)	I (pA)	w _{1/2} (V)	Rp	Rp/L (cm ⁻¹)
100	-0.28±0.05	1.06±0.05	1.35±0.05	0.21±0.04	0.12±0.02
300	-0.32±0.05	0.96±0.05	1.26±0.05	0.25±0.04	0.14±0.02

Table 4-4: Summary of obtained results for the bisinusoidal waveform.

Once proved the filtering condition with the bisinusoidal asymmetric waveform, it was proved also with a rectangular waveform as the waveform generator from Tabor Electronics WW1071 allows it. A pulse of 1 MHz and a duty cycle of a 30% was used, being the obtained voltage at the exit of the DEI instrument shown in Figure 4-56. Obtained waveform is a good rectangular waveform, even though the experimental complexity of generating a perfect rectangular waveform.

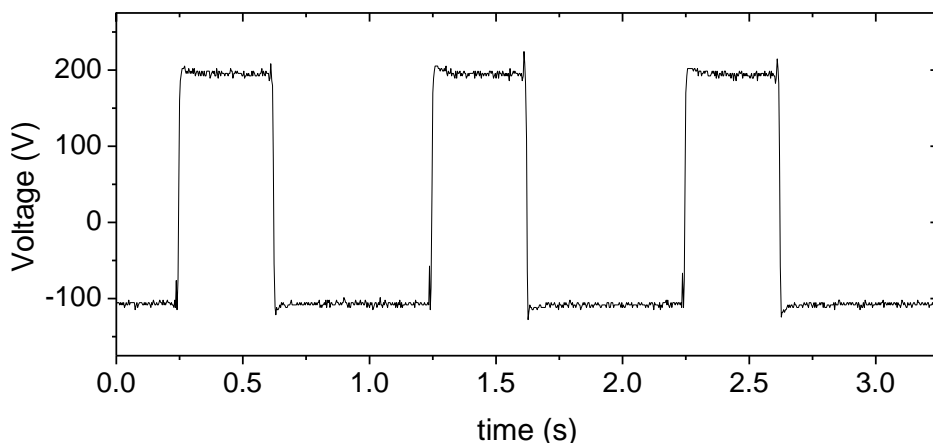


Figure 4-56: Obtained rectangular waveform at the outside of the DEI instrument for DV = 300V and for a rectangular waveform of 1MHz having a duty cycle of 30%.

Figure 4-57 shows the obtained intensities when applying a rectangular waveform. Again, it can be seen that without DV applied, the toluene peak appears at a CV = 0.0 V, while for having a DV of 300 V applied it is CV_{rect}(DV=300V) = -0.87 ± 0.05 V after Gaussian de-convolution. This increase of the compensation value in absolute terms, is concordant with the experimentally found by Prieto *et al.* [29] in Section 2.3.c *Detection: Waveform shape effects*. Prieto found that the CV was higher for a rectangular waveform than for a bisinusoidal waveform one (see Figure 2-46), because each different waveform will have a different portion of high electric

field, and consequently the ions movement inside the filtering electrodes gap also will be different for each waveform, and therefore the detected compensation voltage. A rectangular waveform is the ‘ideal’ waveform to be used as it will have higher portion of maximum dispersion voltage than for the bisinusoidal waveform.

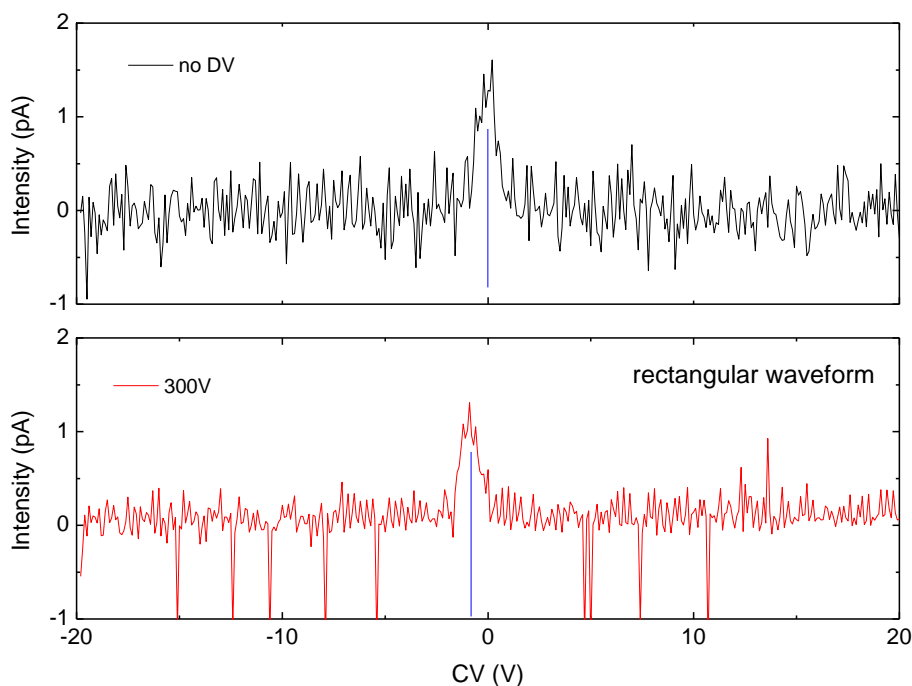


Figure 4-57: Obtained intensities without and with DV applied (300 V) for a rectangular waveform at 1 MHz, for 1 ppm of toluene in a total flow of 1,000 sccm.

In Table 4-5 are summarized the obtained results for two different dispersion voltages using a rectangular waveform. The CV's obtained for 100 and 300 V are clearly different. The intensity can be considered the same for the two values, but the full width at half maximum ($w_{1/2}$) is clearly decreased, so increasing the DV narrows the peak but more evident that for the bisinusoidal obtained peaks. As in the case of the bisinusoidal waveform, the value R_p/L is one order of magnitude lower than the expected, being due to the low DV available and it is expected that increasing the DV, the absolute value of CV will increase and therefore the R_p and the R_p/L ratio obtain similar values to the reported in the literature (Section 2.3.c *Detection: Resolution and Resolving Power*) from 1.1 to 4.3 cm^{-1} are expected.

DV (V)	CV _{rect} (V)	I (pA)	w _{1/2} (V)	Rp	Rp/L (cm ⁻¹)
100	-0.68±0.06	1.04±0.05	1.57±0.05	0.43±0.04	0.24±0.03
300	-0.87±0.05	1.02±0.05	1.12±0.05	0.78±0.06	0.43±0.04

Table 4-5: Summary of results obtained for the rectangular waveform.

Discussion and Summary

Initially the p-FAIMS design was thought to be micro-fabricated using a sandwich-like configuration of Glass-Silicon-Glass being the ‘glass’ used Pyrex® 7740 Borosilicate Glass. This simple design has involved a huge work that finally has not end satisfactorily to an available p-FAIMS device. The first step and one of the major problems we’ve got was to have a hole in the pyrex substrate to let the UV light pass through. Three different ways to do the hole were studied: 1) with HF etching, all the wafer was clearly damaged, and the hole was bigger than expected; 2) with Deep RIE, we were unable to even do a 10 μm depth hole to the pyrex substrate, so a through hole was not contemplated; 3) with Powder blasting, the through hole with the shape and dimensions desired was accomplished, but the anodic bounding failed in this case. The anodic boding of the Glass with the silicon did not worked properly, being partially solved using silver lac but it increased the gap of the p-FAIMS and also in some cases short-circuit of pads occurred. Finally, the Teflon® encapsulation system did not fit properly the p-FAIMS device and do not seal properly so gas leaks were detected. All those problems made impossible the operation of the GL-Si-GL p-FAIMS device.

Next p-FAIMS design was a PCB-PMMA-PCB sandwich-like design using a FORMIGA prototyped polyamide design for the tub connections and the UV-lamp positioning, all jointed by screws. A faraday cage (a metal noise shield) has been done using the sides of the PCB’s that do not define the drift tube. This design has been the used for toluene detection. A big effort in the measurement set-up was carried out as a home-made mass-flow system was designed and implemented. Also the needed instrumentation was huge, and some connections were not as simple as initially thought. The UV lamp was characterized with an easy home-made system of copper tubes to ensure that it worked properly. An extra faraday cage (a metal safety shield) was used to ensure that high voltage would not damage the system or the operator. Some of the instrumentation has been controlled with their own software and some others with different LabView programs depending on the studio realized.

Final p-FAIMS prototype has been characterized with toluene for different experimental conditions. Studios included: (1) check that the UV positioning was correct and its capacity to ionize a sample gas (acetone at high concentration, ~1500 ppm). It was also measured the amount of ions detected at each pair of

electrodes of the p-FAIMS. Then the UV-gate was studied both for positive and negative voltages, obtaining that for negative voltages the signal is reduced more quickly than for positive voltages being due to the non-uniform charge distribution of the toluene molecule. And, the detector polarity was changed to detect positive or negative ions, having a little signal for the negative mode due to other anions formed in the ionization region from some impurities. (2) Detection of toluene without DV. The detection of 1 ppm of toluene was not achieved for low total flows (50 sccm) but it was achieved for higher flows. (3) The repeatability of the measurement of 1 ppm of toluene was studied for consecutive measurements and for different days measurements. (4) Measurements of toluene at different concentrations ranging from 1 to 10 ppm were done, and a linear increase of the intensity with the increase of the concentration was found. Also measurements in a low range of concentrations from 200 ppb (minimum achievable with the available mass-flow system) to 1 ppm were done, the recorded intensities showed that detection was also linear in this range, as it was used a UV-lamp instead of a radioactive source for which the detection is non-linear in the low ppb range. The limit of detection LOD is 200 ppb, as it is the minimum concentration of toluene that our mass-flows system can provide, but decreasing the voltage step of the compensation scan the noise is reduced and based upon signal to noise calculations, LOD is estimated at 100 ppb. (5) The carrier gas flow studio done for 1 ppm of toluene for a flow range from 250 to 2,000 sccm showed that as the flow is increased, the intensity obtained for 1 ppm is increased, being the optimum flow at 1,000 sccm using the aspect ratio variations with the total flow. Different concentrations from 1 to 10 ppm were studied for total flows from 250 to 2,000 sccm, confirming that the optimum flow of 1,000 sccm found was correct, as the signal intensities saturates at this flow value; and finally (6) the addition of the DV was achieved only up to 300 V due to instrumentation issues, but even though at this low DV the toluene compensation voltage changed from 0.0 V (without DV) to -0.32 V (with 300 V of DV) and also the intensity and the full width at half maximum were slightly decreased, when using a bisinusoidal waveform with a duty cycle of 33%. The same studio was done for a rectangular waveform with a duty cycle of 30%, obtaining a higher CV of -0.87 V (with 300V of DV), and also the intensity and the FWHM decreased in a more evident way. Decrease of the intensity with applying a high DV and the fact that with a rectangular waveform a higher CV is achieved, are fully agreed with experimental data found in the literature.

The final p-FAIMS prototype has been characterized for toluene, showing an agreement with the expected ions behaviour even the low DV used. It has been presented the proof-of-concept of the p-FAIMS with a PCB-PMMA-PCB configuration. It is expected that with an appropriate high asymmetric field at higher DV of 1,000 V ($E_D/N \sim 80\text{Td}$) it will be able to differentiate various compounds.

References

1. Perkin Elmer Optoelectronics. *Low Pressure Gas Discharge Lamps for Photoionization Detectors*. [cited 2013 10th May]; Available from: www.perkinelmer.com/opto.
2. ACI Analytical Control Instruments GmbH. *UV Lamps*. [cited 2013 10th May]; Available from: http://www.aci-berlin.com/index.php?option=com_content&view=article&id=62&Itemid=81&lang=en.
3. Keithley Instruments Inc. *Model 2410 1100V SourceMeter®*, *Service Manual*. [cited 2013 12th May]; Second ed.: [Available from: <http://www.keithley.com/products/dcac/voltagesource/highvoltage/?mn=2410>].
4. Keithley Instruments Inc. *Model 2400 Series Sourcemeter®*, *User's Manual*. [cited 2013 12th May]; Eighth ed.: [Available from: <http://www.keithley.com/products/dcac/voltagesource/broadpurpose/?mn=2400>].
5. Keithley Instruments Inc. *Model 6487 Picoammeter/Voltage Source*, *Reference Manual*. [cited 2013 12th May]; First ed.: [Available from: <http://www.keithley.com/products/dcac/voltagesource/application/?mn=6487>].
6. ALCO. *Catálogo de vidrio*. [cited 2013 12th May]; Available from: <http://www.alco.es/principal/>.
7. Aalborg Instruments & Controls Inc. *Rotameters Catalog*. [cited 2013 12th May]; Available from: http://www.aalborg.com/images/file_to_download/en_Aalborg_EM201302_Rotameter_Catalog.pdf.
8. IUPAC. *IUPAC Compendium of Chemical Terminology - the Gold Book*. [cited 2013 21st May]; Available from: <http://goldbook.iupac.org/index.html>.
9. RAE systems. *MiniRAE 3000 User's Guide*. [cited 2013 12th May]; Available from: <http://www.raesystems.com/products/minirae-3000>.
10. Corning Inc. *Properties of PYREX®*, *PYREXPLUS®* and *Low Actinic PYREX Code 7740 Glasses*. Available from: http://catalog2.corning.com/Lifesciences/media/pdf/Description_of_7740_Glasses.pdf.
11. Madou, M.J., 2002, *Fundamentals of Microfabrication: The Science of Miniaturization*. Second ed. Boca Raton: CRC Press. 752.
12. Micronit Microfluidics BV. [cited 2013 14th May]; Available from: <http://www.micronit.com/footer/technologies/foundry-capabilities/microstructuring/powderblasting-2/>.
13. DuPont™. *Teflon®*. [cited 2013 15th May]; Available from: http://www2.dupont.com/Teflon_Industrial/en_US/store/index.html.
14. Epidor S.A. *JuntasTóricas*, *Juntas EQ*. [cited 2013 20th May]; Available from: http://www.epidor.com/documentos/296_B-JuntasTóricas_JuntasEQ.pdf.
15. NIST. *Chemistry WebBook*. [cited 2013 18th March]; Available from: <http://webbook.nist.gov/chemistry>.
16. Brooks Instrument. *Model 5850E Mass Flow Controller*. [cited 2013 20th May]; Available from: <http://www.brooksinstrument.com/downloads/Product%20Documentation/Thermal%20Mass%20Flow%20Meters%20Controllers%20Analog%20Gas/Instruction%20Manuals/x-tmf-5850e-mfc-eng.pdf>.
17. Agilent Technologies. *E3631A 80W Triple Output Power Supply, 6V, 5A & ±25V, 1A*. [cited 2013 20th May]; Available from: <http://www.home.agilent.com/en/pd-836433-pn-E3631A/80w-triple-output-power-supply-6v-5a-25v-1a?&cc=ES&lc=eng>.
18. Tabor Electronics Ltd. *Datasheet: MODELS WW1071/2, 100MS/s Single/Dual Channel Arbitrary Waveform Generators*. [cited 2013 21st May]; Available from: <http://www.taborelec.com/pdf/WW1071.pdf>.
19. IXYS Colorado (IXYSRF and DEI Scientific products). *Directed Energy Inc. (DEI) PVX-4140* [cited 2013 20th May]; Available from: http://www.directedenergy.com/index.php?page=shop.product_details&flypage=flypage.tpl&product_id=26&category_id=3&option=com_virtuemart&Itemid=29.
20. Teledyne LeCroy. *WaveRunner 44Xi-A*. [cited 2013 21st May]; Available from: <http://teledyneleeroy.com/oscilloscope/oscilloscopemodel.aspx?modelid=1943>.

21. Sensirion AG. *Evaluation Kit EK-H4 for Humidity Sensors SHTxx*. [cited 2013 21st May]; Available from: <http://www.sensirion.com/en/products/humidity-temperature/evaluation-kits/evaluation-kit-ek-h4/>.
22. *The Molfield Project, A Molecular Field Approach to the Mechanisms of General Anaesthesia*. [cited 2013 25th May]; Available from: <http://molfield.org/>.
23. Tuttle, T.R. and S.I. Weissman, *Electron Spin Resonance Spectra of the Anions of Benzene, Toluene and the Xylenes I*. *Journal of the American Chemical Society*, 1958. **80**(20): p. 5342-5344.
24. Miller, R.A., et al., *A MEMS radio-frequency ion mobility spectrometer for chemical vapor detection*. *Sensors and Actuators A: Physical*, 2001. **91**: p. 301-312.
25. Cottingham, K., *Ion mobility spectrometry rediscovered*. *Analytical Chemistry*, 2003: p. 435A.
26. Shvartsburg, A.A., K. Tang, and R.D. Smith, *Modeling the resolution and sensitivity of FAIMS analyses*. *Journal of the American Society for Mass Spectrometry*, 2004. **15**(10): p. 1487-1498.
27. Agilent Technologies. *6035A System Autoranging DC Power Supply, 500V, 5A*. [cited 2013 29th May]; Available from: <http://www.home.agilent.com/en/pd-839427-pn-6035A/system-autoranging-dc-power-supply-500v-5a?&cc=ES&lc=eng>.
28. Miller, R.A., et al., *A novel micromachined high-field asymmetric waveform-ion mobility spectrometer*. *Sensors and Actuators B: Chemical*, 2000. **67**(3): p. 300-306.
29. Prieto, M., et al., *Comparison of Rectangular and Bisinusoidal Waveforms in a Miniature Planar High-Field Asymmetric Waveform Ion Mobility Spectrometer*. *Analytical Chemistry*, 2011. **83**(24): p. 9237-9243.

[This page intentionally left blank]

Chapter

5

Medical Applications

Online Monitoring of an
Exhaled analgesic in
Patients under Anesthesia

Chapter 5: Medical Applications: Online Monitoring of an Exhaled analgesic in Patients under Anesthesia	207
5.1 MCC-IMS for Medical Applications	209
5.2 MCC-IMS description	210
5.2.a Room Air variations	212
5.2.b Devices data alignment	214
5.3 Control Group	216
5.4 <i>in vitro</i> Blood test with Remifentanil	218
5.4.a Blood measurements procedure	220
5.4.b Remifentanil calibration	220
5.4.c Blood measurements with remifentanil	222
5.5 Medical Considerations	225
5.5.a Pre-operative evaluation	225
5.5.b Anesthesia administration	227
5.5.c Experimental Set-up while surgical anesthesia	234
5.6 Operational Background - Plastic Emissions	237
5.6.a Intubation methods	237
5.6.b Measurements methods	238
5.6.c Laboratory Measurements — MCC-IMS and GC-MSD	241
5.6.d Plastic emissions in Patients Measurements — MCC-IMS	245
5.7 Exhaled Remifentanil in Patients under Anesthesia	249
Discussion and Summary	253
References	255

Patients under surgery receive several different drugs to maintain the anesthesia. These drugs are metabolized in the body and could be or not exhaled in the breath. The injection method used to supply the drugs also displays a theoretical value of the anesthetics concentration in the blood based on mathematical algorithms models in function of the infusion rate, but nowadays there is no possibility to measure this concentration in the blood in real-time. An approach would be to measure the anesthetic in the breath of the patient and correlate with the blood concentration.

The objective of this work is to study the feasibility of online-monitoring of an analgesic (remifentanil) in exhaled breath of patients during a surgery using a commercial Ion Mobility Spectrometer device. Three commercial ion mobility spectrometers were used. Basic investigations of background emissions and about the alignment of the three different devices were done. Also Gas Chromatograph - Mass Spectrometry (GC-MS) analysis of gases from the plastic materials involved in anesthesia were done.

5.1 MCC-IMS for Medical Applications

There are numerous analytical detection methods available for human breath investigations. The major spectrometric methods used are proton transfer reaction mass spectrometry (PTR-MS) [1-5], solid phase micro extraction-gas chromatography coupled to mass spectrometry (SPME-GC-MS) [6-9], selected ion flow tube mass spectrometry (SIFT-MS) [10-15], and multi-capillary column coupled to ion mobility spectrometry (MCC-IMS) [16-21]. In all cases mentioned, non-invasive and easy methods for early diagnosis or therapy monitoring are developed by identifying disease-specific biomarkers in the breath of patients.

Metabolomics is the “systematic study of the unique chemical fingerprints that specific cellular processes leave behind” [22], where the IMS has been used for headspace measurements of fungus, bacteria or cell cultures to characterize their volatile metabolome [23-25]. Breath studies with IMS have demonstrated the capability for early diagnostics of lung cancer [26], and discrimination between different states of chronic obstructive pulmonary diseases (COPD) [27]. Also it turned out that even carcinoma in situ can be detected [28], and that different kinds of tumors can also be distinguished [29]. In addition, the utilization of IMS for online-monitoring of drug levels in a patient undergoing anesthesia is also possible, for example propofol anesthetic monitoring [30, 31].

In a so called total intravenous anesthesia (TIVA), the patient gets an intravenously infusion of an opioid (used to treat the pain), in addition with propofol. One of the used opioids is the remifentanil (Ultiva®), characterized by a short-acting time. A preliminary study of remifentanil or its metabolites is done using a MCC-IMS device.

Laboratory measurements of the reconstructed drug were carried out. Also *in vitro* blood experiments were done for a concentration of 20 ng/mL of remifentanyl, which is the maximum dose that a patient can assume. Patient and laboratory reference measurements were realized using an Ion Mobility Spectrometer coupled to a multi-capillary column MCC-IMS, and in some cases also a mass spectrometric determination was done coupling the gas chromatograph to a mass spectrometer detector GC-MSD.

5.2 MCC-IMS description

The Ion Mobility Spectrometer used is a commercial MCC-IMS as described in Section 2.2.e *Hyphenated Methods with Ion Mobility Spectrometers*, a BioScout from B&S Analytik GmbH shown in Figure 5-1. Three different MCC-IMS were used during this study. They are named as IMS-1, IMS-2 and IMS-3. The devices IMS-1 and IMS-2 were placed at the laboratory of the Korean Institute of Science and Technology in Europe, Saarbrücken (Germany), being the IMS-2 placed inside the fume cupboard. IMS-3 was placed at the *Chirurgische Universitätsklinik* from Homburg (Germany), in a moving platform that allows moving it easily to the operations rooms.

210

The filtering region is 12 cm length and is surrounded by around 20 drift rings. An electric voltage is applied to each drift ring to generate a homogenous and weak electric field of ~330 V/cm. The drift gas opposite to the analytes flow, avoids in an ideal case the entry of any neutral molecule in the drift region. Its role is also to induce collisions with the ions in order to decelerate and separate them before reaching the detector.

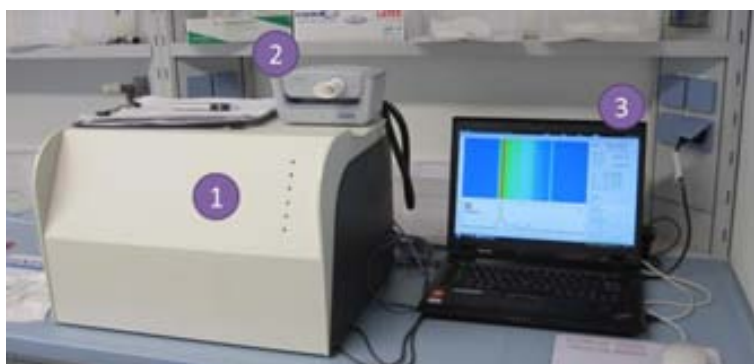


Figure 5-1: BioScout from B&S Analytik GmbH 1; Ganshorn's Spirometer Spiroscout® 2; laptop for data acquisition 3. Available at KIST-Europe.

The B&S Analytik system devices are provided with the operating software named VOCan. The main task of VOCan is to provide a graphical user interface for the control and supervision of the system. Data interpretation has been done using B&S Analytik software VisualNow, being the data plotted as indicated in Figure 5-2. A 3D plot is shown in Figure 5-2top, left as retention time RT (from the multi-capillary column) versus the reduced inverse ion mobility $1/K_0$ (from the IMS), being the inverse ion mobility related with the drift time as seen previously in Section 2.2.c *Drift region*, as

$$t_{drift} = \frac{1}{K_0} \frac{L}{E} \quad (5.1)$$

Also are shown the Intensity versus the retention time RT (from the multi-capillary column) in the Figure 5-2right and Intensity versus the reduced inverse ion mobility $1/K_0$ (from the IMS), Figure 5-2bottom.

Peak Analysis and fitting can be done automatically or manually. A square region is defined in the position of RT and $1/K_0$ for the automatically identified peaks by the software (signal intensity must be higher than 0.05 V). The width of the square is fixed at $0.06 \text{ Vs}\cdot\text{cm}^{-2}$, while the high depends on the time.

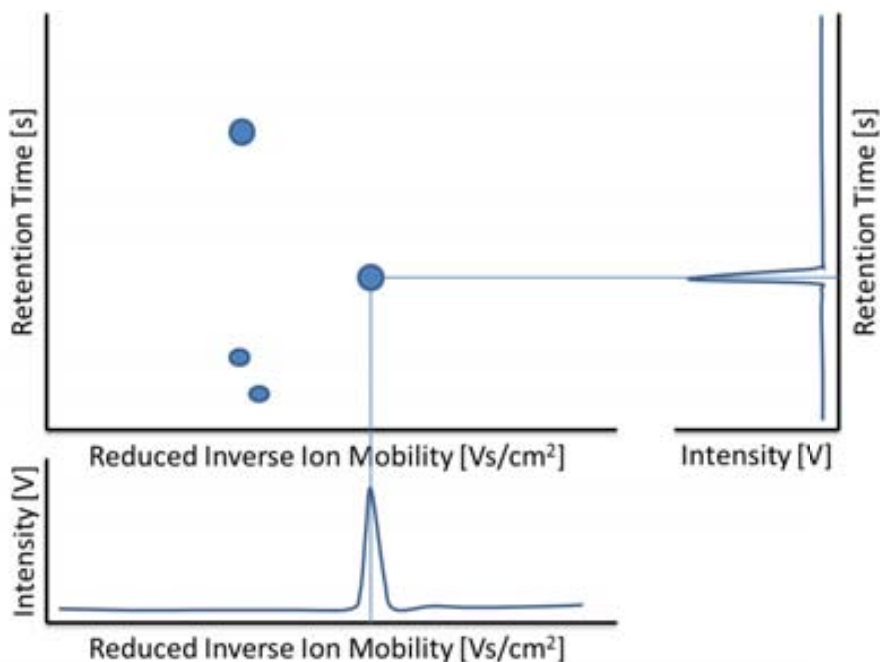


Figure 5-2: Representation of 3D plots obtained with a commercial MCC-IMS (BioScout from B&S Analytik, using VisualNow software).

5.2.a Room Air variations

During the analysis of breath, also room air variations have to be considered since the total signal detected will be the sum of both. For this purpose, the stability of the spectrometric system regarding to two volatile organic compounds (Benzothiazol and Nonanal) found in all room air Chromatograms analyzed in positive mode (detecting only positive ions) with the MCC-IMS was studied, results obtained are shown in Figure 5-3. The room air variation have been studied over 6 months, for the inverse of the ion mobility $1/K_0$ and the retention time RT, without intensity considerations.

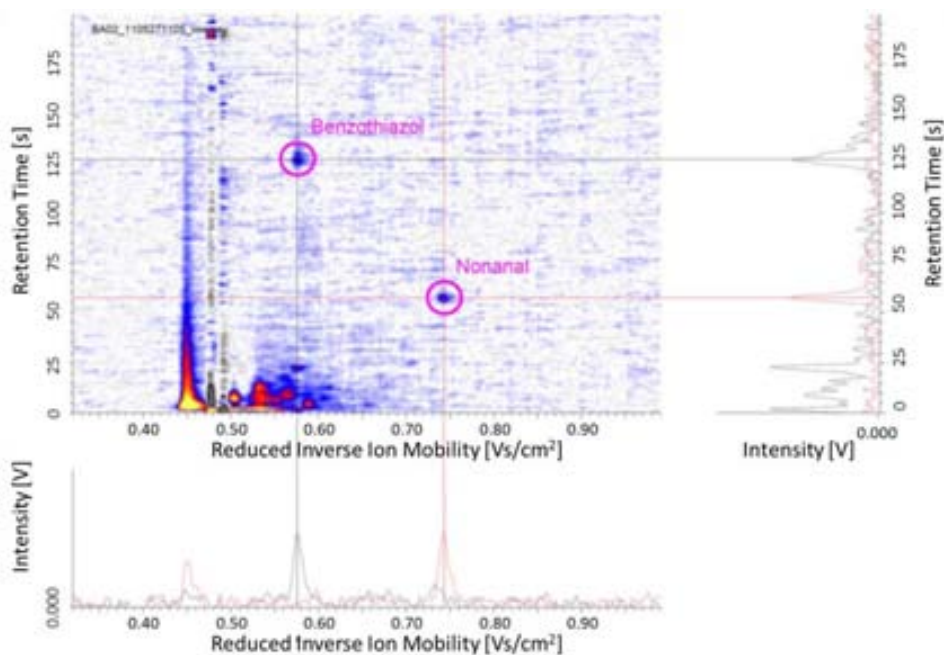


Figure 5-3: MCC-IMS chromatogram obtained for a measure of dry room air (IMS-1 device). The studied compounds are highlighted inside purple circles: Benzothiazol and Nonanal.

Studies of Room Air with MCC-IMS show a wide variety of peaks depending on the location of the device, the day of the week, and the time of day. So, to compare different chromatograms, there is a need to have at least one peak always in the chromatogram to align the different measurement data.

To assure that both compounds are found in all room air chromatograms, measures over 6 months giving up to more than 2000 measurements for IMS-1 device have been analyzed. Figure 5-4 shows the histograms of the inverse of the mobility and the retention time distributions for Benzothiazol and Nonanal. It can be easily seen that

Benzothiazol follows a Gaussian curve for both $1/K_0$ ($R^2 = 0.95$) and RT ($R^2 = 0.93$), while Nonanal does not have this behavior. This is due to the fact that Benzothiazol evaporates from the plastic compounds of the MCC-IMS, while Nonanal comes from the air-conditioning system and its presence in the room air is more unpredictable. The obtained mean values are available in Table 5-1 where is also listed the standard deviation range.

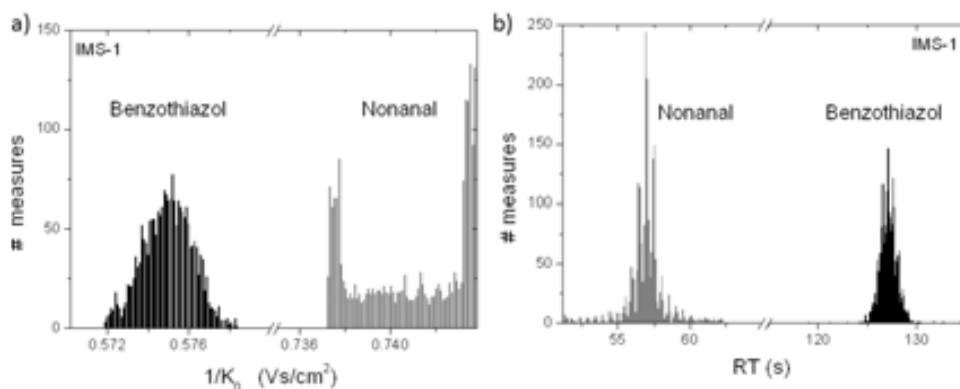


Figure 5-4: Benzothiazol and Nonanal distributions of A) $1/K_0$ and B) RT.

	$1/K_0$ (Vs/cm ²)	RT (s)
Benzothiazol	0.575 ± 0.001	127 ± 1
Nonanal	0.741 ± 0.002	57 ± 2

Table 5-1: Mean values of RT and $1/K_0$ of the IMS-1 device.

The analysis for Benzothiazol and Nonanal (see Figure 5-5) shows that for the $1/K_0$ there is a declining linear tendency of the inverse reduced mobility value, while for the RT there is a constant linear tendency and almost all results are within the range of standard deviation. Variations in the mobility can be explained due to the appearance of $M(H_2O)_nH^+$ like cluster ions formed from small variations of humidity content of the carrier gas. The standard deviation for Nonanal is the double than for Benzothiazol for both $1/K_0$ and RT, as seen in Figure 5-5.

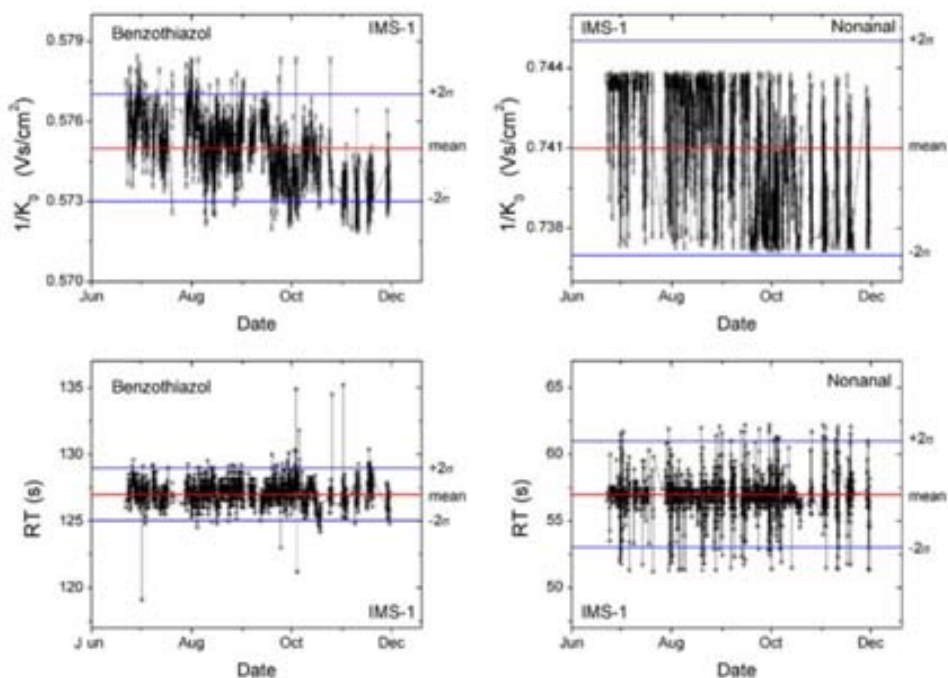


Figure 5-5: $1/K_0$ and RT distributions along the time for Benzothiazol and Nonanal, for IMS-1 device.

5.2.b Devices data alignment

The present section considers the influence of parameters related to the IMS device and that may vary slightly from one instrument to another. General remarks could be found in [32, 33], the influence of temperature in [34-43], pressure in [44], electric field in [45, 46], carrier gas flow in [34, 42], and geometrical parameters in [47, 48]. Therefore, we discuss the inter-comparison of different instruments. Theoretical aspects and explanations were discussed in the literature mentioned above. The present section deals with practical points of inter-comparison using different instruments and show, that a proper alignment is really needed for such purpose.

Three different MCC-IMS devices have been used for the analysis of Benzothiazol and Nonanal, and in this section the comparison of the responses obtained with each one was done. The box-and-whisker plots (see Annex 5-1) have been used to show the variation in the mobility and also in the RT for the studied devices.

The variation observed in the inverse reduced mobility and also in the RT for the studied devices is shown in Figure 5-6, and the results are summarized in Table 5-2. The expected $1/K_0$ values have to be similar for all three devices, as it was obtained. However for the retention time, it was expected that for different devices with different oldness the RT values may vary sustainably. Thus, the way to adjust the

temperature of the MCC will be different. Small changes in the temperature adjustment will affect the retention time scale. So, the results show the importance to align the data of different devices especially for the RT. In addition, a more sensitive regulation of temperature over the MCC should be considered. As shown in Figure 5-6, linear alignment on the Retention time scale is possible.

The older the device, (i.e. multi-capillary column) the sooner the analytes elute out from the MCC, i.e., the lower RT for the analytes. As Benzothiazol comes from the materials of which the MCC-IMS is built, it will appear in all the chromatograms either from Room Air or from Breath Analysis, so all these properties make Benzothiazol a suitable peak for the alignment of different devices in positive mode.

It should be noted, that the software package of B&S Analytik, VisualNow includes functionality for alignment on both the inverse reduced mobility and the retention time scales.

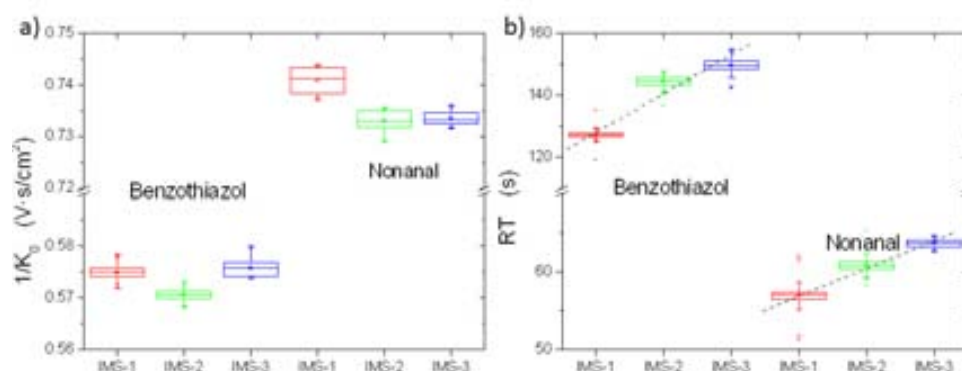


Figure 5-6: Box-and-whisker plots of the inverse of the mobility $1/K_0$ (top) and the retention time RT (bottom) of Benzothiazol and Nonanal for three studied MCC-IMS devices.

	Benzothiazol		Nonanal		
	$1/K_0$ (Vs/cm ²)	RT (s)	$1/K_0$ (Vs/cm ²)	RT (s)	
IMS-1	0.575 ± 0.001	127 ± 1	0.741 ± 0.002	57 ± 2	2066 files
IMS-2	0.571 ± 0.001	144 ± 2	0.734 ± 0.002	61 ± 1	127 files
IMS-3	0.574 ± 0.002	148 ± 3	0.734 ± 0.002	64 ± 1	43 files
mean	0.573	-	0.739	-	

Table 5-2: Mean values of RT and $1/K_0$ of the studied MCC-IMS devices.

5.3 Control Group

In any medical experiment, there is the need to have a control group that is used as a standard of comparison in a control experiment. A control group is a set of items or people that serves as a reference for comparison with an experimental group [49]. A control group must be similar to the experimental group in number and identical in their specified characteristics, such as sex, age, annual income, among other factors, but does not receive the experimental treatment or intervention.

Following information has been extracted from the *Choice of Control Group and Related Issues in Clinical Trials guide* [50] done by the International Conference on Harmonization (ICH) which was adopted in 2001 by the regulatory bodies of the European Union (European Medicine Agency, EMA) [51], USA (Food and Drug Administration, FDA) [52], and Japan (Pharmaceuticals and Medical Devices Agency, PDMA) [53].

Control groups can be classified on the basis of two critical attributes:

- A. type of treatment or experimental test used
- B. method of determining who will be in the control group

The type of control treatment may be any of the following four:

1. placebo
2. no treatment
3. different dose or regimen of the study treatment
4. a different active treatment

Control Group – configuration

A randomized control group has been performed. The control group was configured for 10 people (CG#) of different ages (range from 25-55), having the same number for females (F) and males (M). Some significant questions were asked about their health status: if they have asthma, if they have ever smoked, if they have any allergy and if they have any stomach problem. A total amount of 156 measures were taken (87 F / 69 M) in positive mode and for 1200 spectra. No control group was studied in negative mode, just for time problems.

Breath sample was taken using the Ganshorn's Spirometer Spiroscout® as can be seen in Figure 5-7 for one of the participants in the control group. Breath samples were taken over fifteen working days. The mouthpieces were kept for each control group participant, because no difference is shown in the IMS chromatograms for using a used or a new mouthpiece.

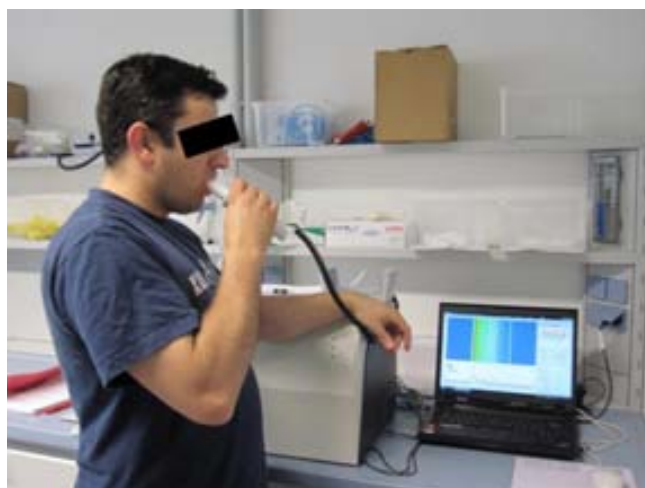


Figure 5-7: Control group participant showing how the breath sample was taken with a MCC-IMS using a Spirometer Spiroscout®.

Before and after each row of measurements, a room air measure was taken (RL#). As 1200 spectra were taken, a measurement will take nearly 10min. So we decide to give a 5 minutes gap between successive measurements, to let the control group members to attend the appointment. Two samples with a gap of 1 hour, of four of the control group members were taken every day, according to their disposability. This means that every day a total of 10 measurements (~2.5 h) were done.

In our case, as we would measure the breath of patients under anesthesia while surgery, they would not have eaten and they would be intubated, so their breath will be taken ‘directly’ from the lungs. Therefore we need to avoid digestion cross-linking in our control group. For this reason, breath samples were taken in the morning. However, not always all the control group members accomplish this. For each measurement was noted down if the measurement was done before or after breakfast and with or without teeth brushing. Sometimes, the control group member came after smoking or after eating a sweet or chewing a bubblegum. The discriminated control group had two conditions 1) have not brushed the teeth, and 2) have not eaten any candy or chewed a bubblegum. The summary of the data discrimination is found in [Annex 5-2](#).

From the total amount of 156 measurements (87 F / 69 M) available from our control group, if both conditions are met only 94 measurements (46 F/48 M) could be taken into account.

5.4 *in vitro* Blood test with Remifentanyl

To check the possibility that remifentanyl is metabolized in its primary metabolic pathway to the carboxylic acid metabolite (GI90291) in a fast way, an *in vitro*¹ blood test of remifentanyl was done. The remifentanyl can undergo an ester cleavage in fresh human blood (*in vitro*) in the same manner as its metabolic pathway *in vivo*² [54, 55].

The blood of a volunteer was taken, being the blood stored in a syringe with a citrate solution inside to avoid blood's coagulation. Once taken the blood, it was stored in a laboratory incubator at a constant temperature of ~37°C. The incubator used was an INCUCCELL 55 –Standard, from MMM Medcenter Einrichtungen GmbH [1], and is characterized by noiseless run and soft air flow. Laboratory measurements of *in vitro* blood test were carried out with the IMS-3 device.

To determine if the syringe with the anticoagulation solution (citrate) was present in the blood measurements, its head space was measured for both positive and negative modes. A list of peaks for the coagulation tube (CT) in the chromatograms have been obtained: 4 peaks in the positive mode (CT_p#), and 3 peaks in the negative mode (CT_n#) being resumed for positive mode in Table 5-3 and Figure 5-8; and for the negative mode in Table 5-4 and Figure 5-9. Measurements were done at the Anesthesia Laboratory of the Homburg Hospital, so room air peaks are different again. For the positive mode, we have found 18 peaks (RL_p#) while for the negative mode there are only 5 peaks (RL_n#) due to the room air.

Mode	Peak	1/K ₀ (Vs/cm ²)	RT (s)
Positive	CT_p1	0.585	4
	CT_p2	0.892	121
	CT_p3	0.618	144
	CT_p4	0.713	205

Table 5-3: Identified Peaks of Coagulation Tube (CT) present in MCC-IMS chromatograms for positive (_p#) and negative (_n#) modes.

Mode	Peak	1/K ₀ (Vs/cm ²)	RT (s)
Negative	CT_n1	0.599	12
	CT_n3	0.589	36
	CT_p4	0.713	205

Table 5-4: Identified Peaks of Coagulation Tube (CT) present in MCC-IMS chromatograms for positive (_p#) and negative (_n#) modes.

¹ *in vitro* refers to studies in experimental biology that are conducted using components of an organism that have been isolated from their usual biological context in order to permit a more detailed or more convenient analysis than can be done with whole organisms.

² *in vivo* refers to work that is conducted with living organisms in their normal, intact state.

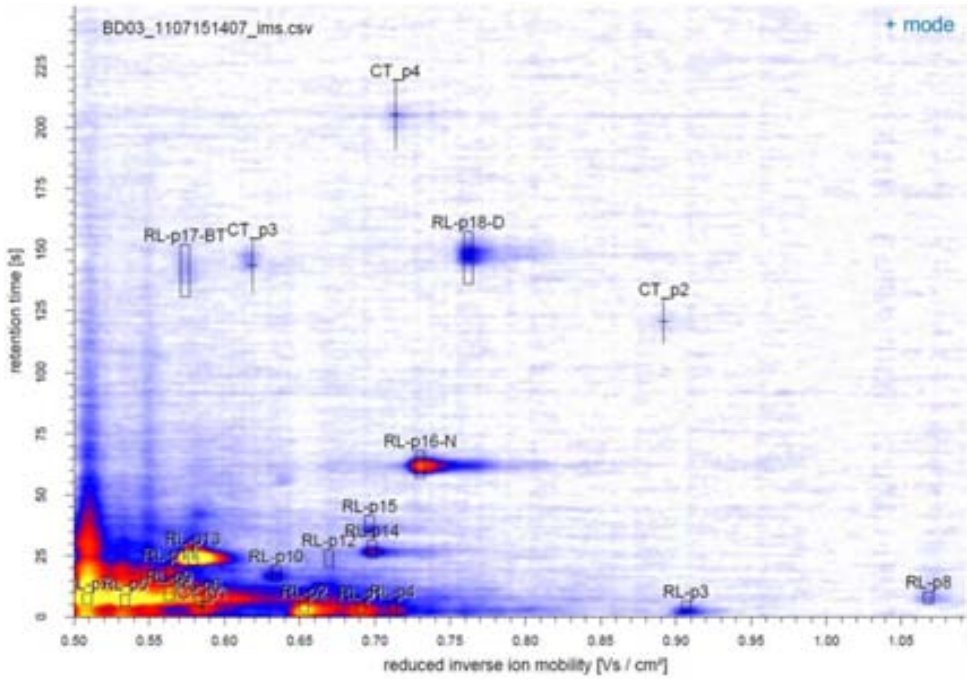


Figure 5-8: MCC-IMS chromatogram of the anticoagulation tube in + mode. Crosses show the identified peaks for the Coagulation Tube (CT_p#) and rectangles are from Room Air (RL_p#).

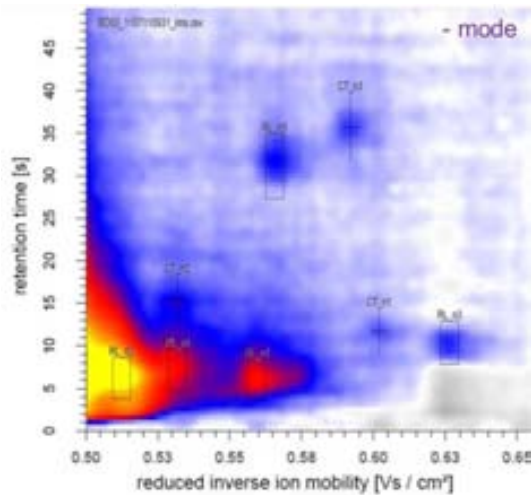


Figure 5-9: MCC-IMS chromatogram of the anticoagulation tube in - mode. Crosses show the identified peaks for the Coagulation Tube (CT_n#) and rectangles are from Room Air (RL_n#).

5.4.a Blood measurements procedure

As the maximum dose of remifentanyl that can be administrated to a patient is 20 ng/mL, the aim was to add the remifentanyl at this concentration to 1 mL of blood.

Measurements of blood with remifentanyl were done for both positive and negative modes. First the head space (HS) of the blood itself was measured, then with the reconstructed remifentanyl after 1 min (time at which remifentanyl achieves its maximum activity, see Figure 5-18 in Section 5.5.b *Anesthesia administration*), and finally the blood with remifentanyl was measured after 13, 26 and 39 min (13min is the time that a full measure needed to be done for a 1500 spectra collection). All measurements of blood with remifentanyl were done in the same vial. Also the HS of the diluted remifentanyl of 20 ng/mL was measured.

5.4.b Remifentanyl calibration

To determine the concentration at which remifentanyl is detected, a calibration was done. The head space of reconstructed remifentanyl was measured for 0.5, 1, 2, 5, 10, and 20 μL with a concentration of 1 ng/ μL . In positive mode, one peak named as Remi_1 was found to be due to remifentanyl, as shown in Table 5-5. In Figure 5-10 is shown the MCC-IMS chromatogram for the measure of the head space for 0.5 μL .

Peak	$1/K_0$ (Vs/cm ²)	RT (s)	Aligned
Remi_1	0.598	63	✓

Table 5-5: Identified Peaks for the Remifentanyl calibration in + mode.

In Figure 5-11 is shown the intensity signal over concentration. The signal intensity is higher as less concentration of remifentanyl is measured, because remifentanyl will suffer hydrolysis and for less concentration, more water will be present and more hydrolysis could be done. This result means that for a patient who has been administered with a low remifentanyl concentration, more hydrolysis is possible in the blood, metabolizing the drug and do not letting it to arrive to the lungs. For a high remifentanyl concentration of 20 ng/mL (the maximum that a patient can receive), the concentration will be enough to not metabolize the entire drug immediately and letting a little amount to arrive to the lungs.

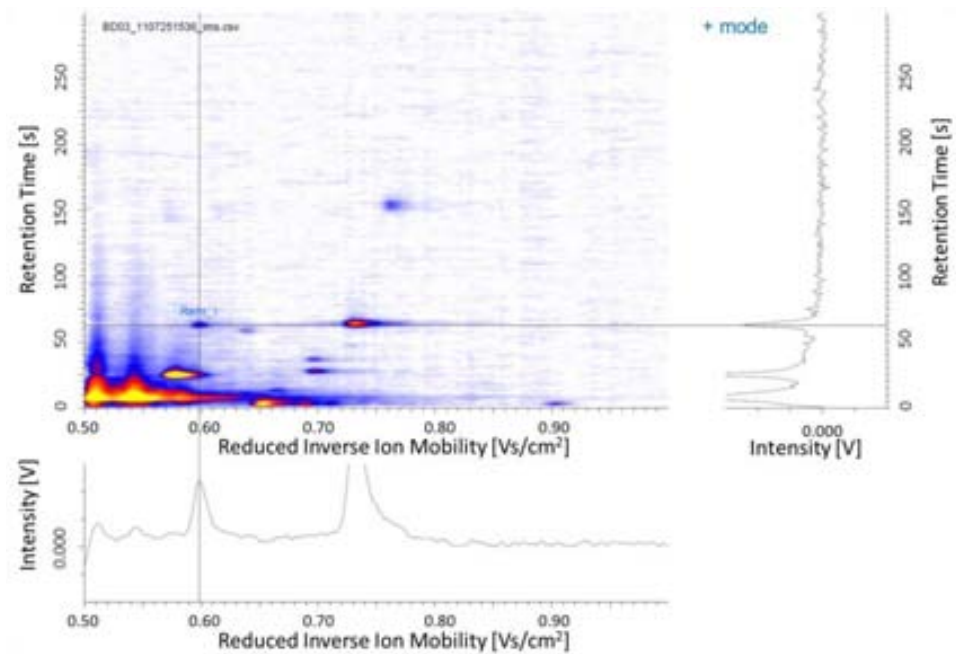


Figure 5-10: MCC-IMS chromatogram of the head space of remifentanyl blood containing 0.5 ng of remifentanyl in + mode. Cross show the identified peak Remi_1.

Remi_1

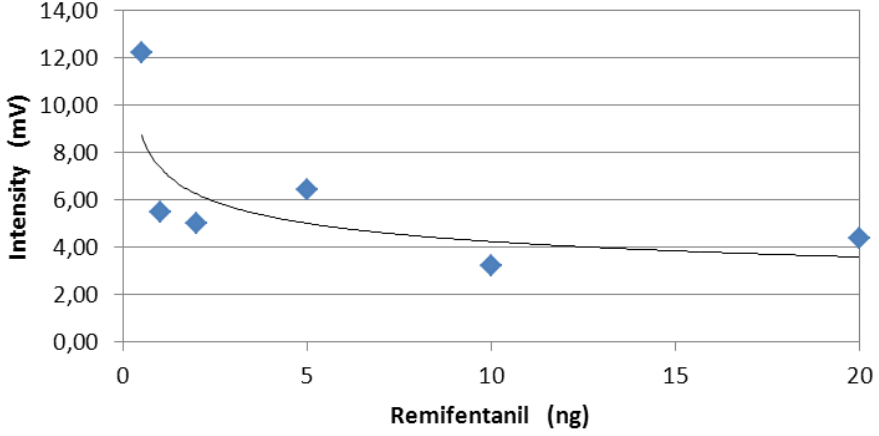


Figure 5-11: Intensity of the identified Remi_1 peak of HS of remifentanyl in + mode.

5.4.c Blood measurements with remifentanil

Experiments for the positive mode of blood within remifentanil, showed 2 more peaks due to the remifentanil, being summarized in Table 5-6. For the negative mode, only one peak has been found to be due to the remifentanil. However, no peaks due to the anticoagulation solution were found either in both polarity modes.

	Peak	1/K ₀ (Vs/cm ²)	RT (s)	Aligned
Positive mode	Remi_1	0.598	63	✓
	Remi_2	0.598	238	✓
	Remi_3	0.594	59	✓
Negative mode	Remi_4	0.711	59	✗

Table 5-6: Identified Peaks of Remifentanil present in the HS of Blood with remifentanil.

A comparison of the peak images for the whole blood test sequence for the identified peaks of remifentanil is shown in Figure 5-12 for both polarity modes. Remi_1 and Remi_3 peaks have an amplification of 50%, while for Remi_2 and _4 is of 100%.

The first two peaks Remi_1 and Remi_2, appear just after the addition of remifentanil to the blood (see Figure 5-13), while Remi_3 (+ mode, Figure 5-14) only appear in the measurements done after 13", and Remi_4 (- mode, Figure 5-15) appear after 13" and 26". 'Identified' peaks (Remi_1, 2 and 3) are due to the remifentanil drug added to the blood because they are not present in the measurements made in the blood itself, or in the room air, or in the measure of the reconstructed remifentanil with a concentration of 20 ng/mL.

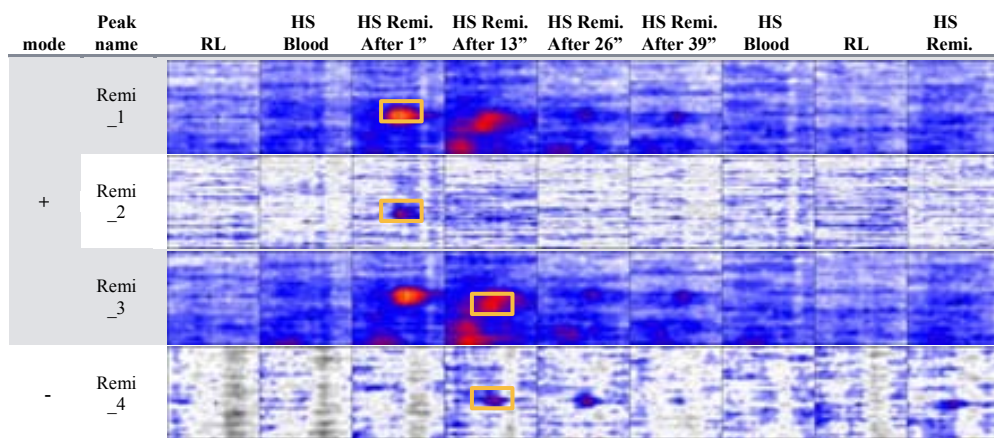


Figure 5-12: Compared peak images for the identified peaks of Remifentanil, for the blood test sequence measurement. Inside yellow squares are shown the first time the peak was detected: after 1" for Remi_1 and Remi_2 peaks; and after 13" for Remi_3 and Remi_4 peaks.

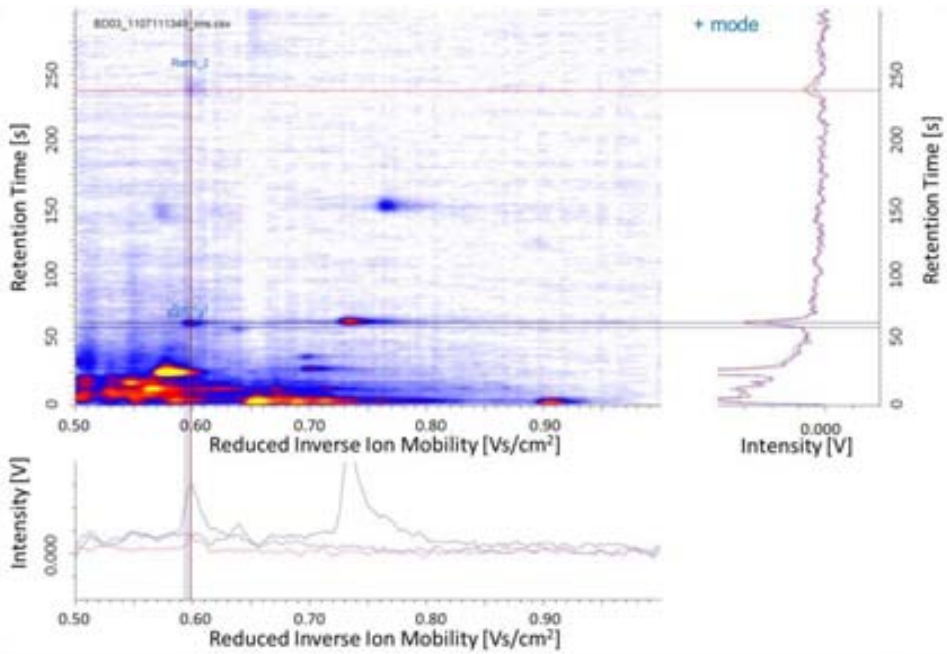


Figure 5-13: MCC-IMS chromatogram of the head space of blood containing 20 ng/mL of remifentanyl in + mode after 1 minute adding the drug. Crosses show the identified peaks, being in black the spectra for the Remi_1, in red for Remi_2 and in blue for Remi_3.

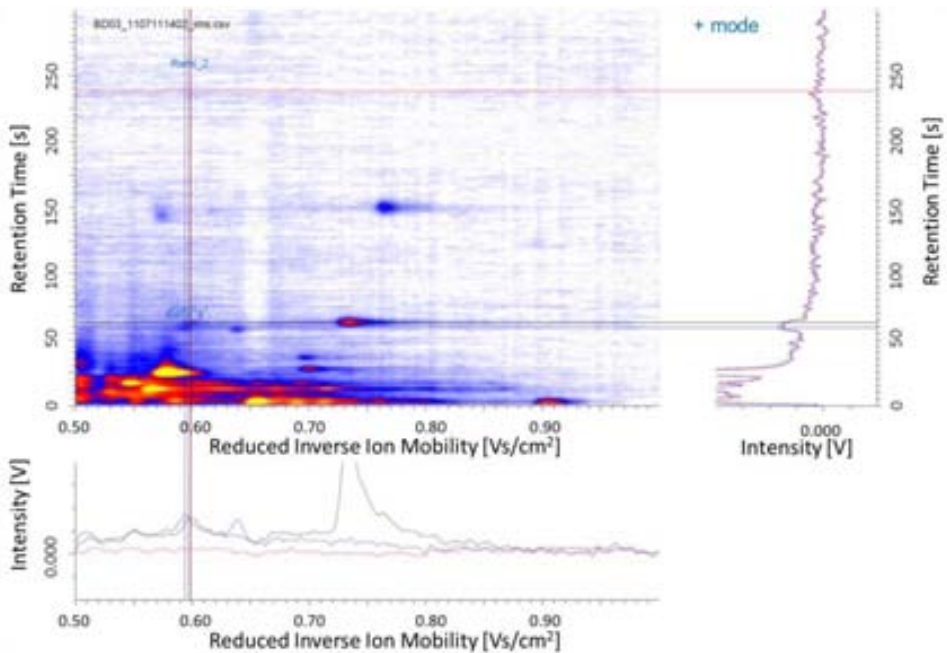


Figure 5-14: MCC-IMS chromatogram of the head space of blood containing 20 ng/mL of remifentanyl in ± mode after 13 minutes adding the drug. Crosses show the identified peaks, being in black the spectra for the Remi_1, in red for Remi_2 and in blue for Remi_3.

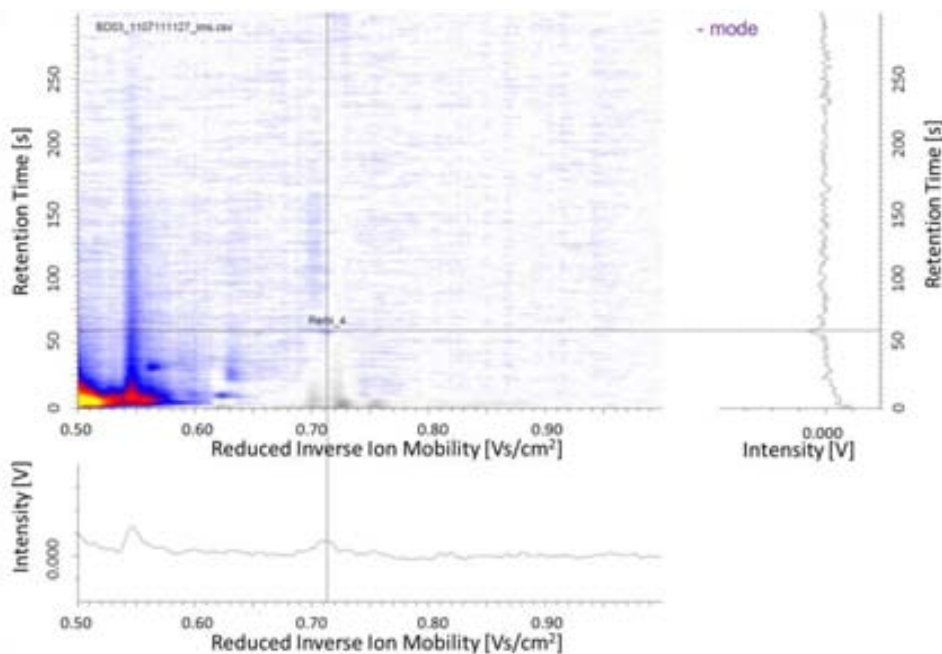


Figure 5-15: MCC-IMS chromatogram of the head space of blood containing 20 ng/mL of remifentanyl in *- mode* after 13 minutes adding the drug. The cross shows the identified peak, in black the spectra for the Remi_4.

Remi_1 peak can be due to the remifentanyl itself because the peak was present in the whole blood samples with the drug and with a decreasing intensity (measurements were done using the same vial, so the head space after one measurement was almost clean leading to a new head space for the next measurement). Remi_2 and Remi_3 could be due to the metabolites of remifentanyl, because they just appear in one of the measurements. Remi_4 peak appeared after 13" and 26" and also in the head space of the remifentanyl, so maybe is due to some compound present in the Ultiva® solution (like glycine) that can interact with the blood when it is added in the first measurement, or from degradation products (not considering contamination). In order to confirm these hypotheses, the headspace of a glycine reference could be measured. It is also possible to obtain the metabolites or to synthesise them. For example, the major metabolite GI90291 can be synthesised by hydrolysis of the remifentanyl hydrochloride as shown by Lehner *et al.* [56].

To determine which peak (Remi_2 or Remi_3) corresponds to which metabolite (major GI90291 or minor GI94219), the intensities of each identified peak are plotted, as can be seen in Figure 5-16. So, as the main pathway of remifentanyl is the metabolite GI90291, it is supposed to have major peak intensity and it can be identified with the Remi_3 peak, leading the Remi_2 peak to be the minor secondary metabolite GI94219. In Table 5-7 are summarized the identification of the peaks.

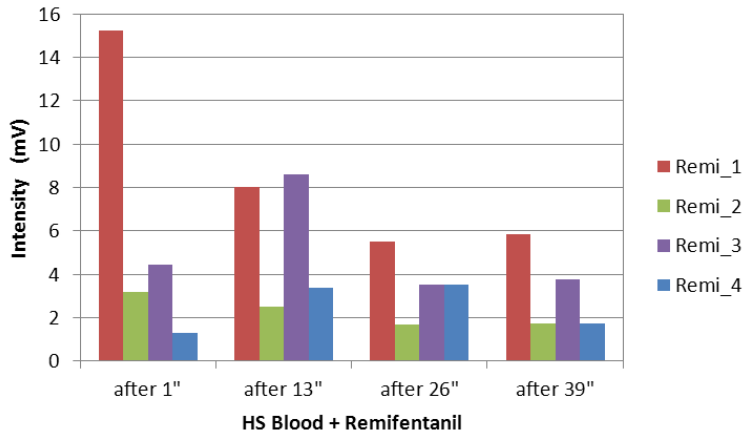


Figure 5-16: Identified peaks intensities for the remifentanyl in blood.

	Peak	1/K ₀ (Vs/cm ²)	RT (s)	Aligned	Identification
Positive mode	Remi_1	0.598	63	✓	Remifentanyl
	Remi_2	0.598	238	✓	minor metabolite GI94219
	Remi_3	0.594	59	✓	major metabolite GI90291
Negative mode	Remi_4	0.711	59	✗	others

Table 5-7: Identified Peaks of Remifentanyl and their correlation.

5.5 Medical Considerations

In this section some anesthetic considerations are shown. First is shown how the pre-operative evaluation is performed. Then, an explanation of how the anesthesia is administrated, being all involved drugs shown and taking an especial attention to the drugs in which this work is focused, the opiod-like analgesic remifentanyl. Finally the medical machines used in anesthesia during this thesis, are shown.

5.5.a Pre-operative evaluation

General anesthesia is a drug-induced, reversible condition that includes specific behavioral and physiological traits — unconsciousness, amnesia, analgesia, and akinesia³ — with concomitant stability of the autonomic, cardiovascular, respiratory, and thermoregulatory systems [57]. General anesthesia produces distinct patterns on the electroencephalogram (EEG), the most common of which is a progressive increase in low-frequency, high-amplitude activity as the level of general anesthesia deepens [58]. How anesthetic drugs induce and maintain the behavioral states of general anesthesia is an important question in medicine and neuroscience, but remains beyond the scope of this work.

³ Akinesia is the absolute loss or cessation of motion.

Status

ASA I	normal healthy patient
ASA II	patient with mild controlled systemic disease that does not affect normal activity, for example, mild diabetes, mild hypertension
ASA III	patient with severe systemic disease which limits activity, for example, angina, chronic bronchitis
ASA IV	patient with incapacitating systemic disease that is a constant threat to life
ASA V	moribund patient not expected to survive 24 hours either with or without an operation
E	emergency procedure

Table 5-8: ASA physical status classes.

Pre-operative evaluation is used to assess the anesthetic risks in relation to the proposed surgery, to decide the anesthetic technique (general, regional, or a combination) and to plan the post-operative care including any analgesic regimens. Explanation of the relevant details of the anesthetic can be given, and the use of pre-medication can be discussed. Patients waiting for surgery are vulnerable; therefore a friendly, professional approach by the anesthetist is essential.

Sometimes is difficult to convey an overall impression of the complexity of a patient medical condition and this can be done by referring to one of the five American Society of Anesthesiologists (ASA) Physical Status Classes (Table 5-8). This only refers to the physical status of the patient and does not consider other relevant factors such as age, and nature and duration of surgery.

All studied patients had a **scheduled operation** and an ASA status of I or II. The data recorded for all patients included:

- Date of the intervention
- Operation room number
- Patient data: code number of the patient
- Protocol number: number of the chirurgic protocol to identify it
- Gender: male or female
- Year of birth
- Height (m)
- Weight (kg)
- ASA code. Studied patients were ASA I or II.
- Risking: Respiratory infection, asthma, COPD⁴, HIV⁵, Hepatitis virus, alcoholic, smoker, drug addict, ...
- Daily medication: affecting lungs or other pre-medication
- Pre-medication
- Intubation method: endotracheal (ET) or laryngeal mask airway (LM)
- Anesthetic used and its bolus dose
- Opioid-like used and its infusion rate
- Relaxant used and its bolus
- Other drugs used using surgery: antibiotics or hypotension treatment

⁴ COPD: chronic obstructive pulmonary disease

⁵ HIV: Human immunodeficiency virus

The use of pre-medication is declining, although most anesthetists demand heavy sedation for a patient undergoing surgery. The main reasons for giving pre-medication are: anxiolysis, analgesia, amnesia, to decrease gastric acidity, as a part of anesthetic technique (assist induction), for the prevention of unwanted vagal responses, or for the prevention of needle pain. A variety of drugs [59-61] including opiates, benzodiazepines, anticholinergics, phenothiazines and H₂ receptor blocking drugs are used. Topical EMLA cream can be used to prevent the pain of insertion of a cannula. This eutectic mixture of prilocaine and lidocaine (1 g of EMLA contains 25 mg of each) is applied to the dorsum of the hands for a minimum of 1 hour to a maximum of 5 hours before induction of anesthesia.

5.5.b Anesthesia administration

Anesthesiologists administer drugs to produce hypnosis, amnesia, analgesia, and muscle relaxation, and to support physiologic homeostasis while minimizing side effects and toxicity. Anesthesiologists select appropriate doses through a combination of scientifically guided administration and empirical estimation. Both approaches are enhanced by a thorough understanding of the basic principles of pharmacology.

The fundamental pharmacokinetic processes are dilution into volumes of distribution and clearance⁶. These processes are governed by the physical properties of the drug and the metabolic capacity of the patient. Anesthetic drugs tend to be highly bound to protein in plasma and highly bound to lipid in peripheral tissues. **Most anesthetic drugs are metabolized in the liver.**

Target-controlled infusion (TCI) allows the anesthetists to achieve a target blood concentration of drug for a given patient. The system delivers the required amount of drug (optimized by factors such as the patient's weight, gender, and age) and maintains this calculated target value until changed by the anesthetists.

In the *Klinik für Anästhesiologie, Intensivmedizin und Schmerztherapie* from the *Universitätsklinikum des Saarlandes* at the *Chirurgische Universitätsklinik* from Homburg Hospital in Germany, there were available only two TCI pumps. All drugs were administered to the patients using these TCI pumps: one for the anesthetic and the other one for the analgesic. The TCI pumps consists of two Orchestra® Module DPS VISIO integrated into an Orchestra® Base Primea WorkStation that allows monitoring of the drugs administered, being both elements from Fresenius Kabi [62] as can be seen in Figure 5-17. The Workstation offers a simultaneous control of both the hypnotic (propofol) and analgesic (sufentanil or remifentanil) effects in TCI.

⁶ Clearance is a pharmacokinetic parameter used to characterize the uptake or elimination of a drug in an organ. It is generally expressed in units of L/min, meaning the volume of blood totally cleaned per minute by the organ.



Figure 5-17: Drug infusion system available at the Chirurgische Universitätsklinik of the Homburg Hospital: two target-controlled infusion (TCI) integrated into a Workstation.

Patients must be sedated and relaxed so the anesthetist could intubate them easily. Intravenous fluids and electrolytes are administered, often empirically, to replace or maintain the body's own requirements. Patients are starved preoperatively to ensure an empty stomach. The main choice is between crystalloid or colloid solutions.

Available Anesthesia Drugs

The aim of this work was to detect the delivered drugs intravenously in the exhaled breath of patients under anesthesia. In agreement with the anesthetists from the Homburg Hospital, there were selected some drugs to be studied, being summarized in Table 5-9 .

In [Annex 5-3](#) can be found the approval letter of the ethics committee from the Homburg Hospital, allowing the measurement of patients breath during anesthesia.

- The essential drugs used in anesthesia are:
1. **anesthetic:** to get asleep
 2. **analgesic:** to relieve pain
 3. **muscle relaxant:** to make intubation easier

Our study was focused in the analgesic opioid-like remifentanil (Ultiva®). During the study, patients were sedated with the anesthetic Propofol, and they also were administrated with a muscle relaxant (Mivacron® or Nimbex® as the anesthetist designed).


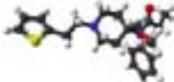
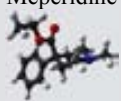
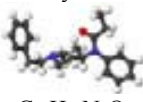
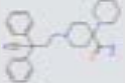
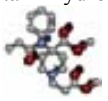

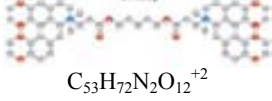
	Brand	Drug, Structure and Formula	Company	CAS #	MW (uma)
Anesthetic	Propofol-Lipuro	Propofol  C ₁₂ H ₁₈ O	B. Braun Melsungen AG	2078- 54-8	178
Analgesics (Opioids-like)	Sufenta® (epidural)	Sufentanildi-hydrogen-Citrate  C ₂₂ H ₃₀ N ₂ O ₂ S	JANSSEN-CILAG GmbH	60561-17-3	386
	Dolantin®	Meperidine  C ₁₅ H ₂₁ NO ₂	Sanofi-Aventis Deutschland GmbH	57-42-1	247
	Fentanyl®-Janssen	Fentanyl-citrate  C ₂₂ H ₂₈ N ₂ O	JANSSEN-CILAG GmbH	437-38-7	336
	Dipidolor (post-surgery)	Piritramide  C ₂₇ H ₃₄ N ₄ O	JANSSEN-CILAG GmbH	302-41-0	430
	Ultiva®	Remifentanil hydrochloride  C ₂₀ H ₂₈ N ₂ O ₅	GlaxoSmithKline GmbH	132875-61-7	376
Relaxants	Mivacron®	Mivacurium chloride  C ₅₈ H ₈₀ N ₂ O ₁₄ ⁺²	GlaxoSmithKline GmbH	106861-44-3	1029
	Nimbex®	Cisatracurium besylate  C ₅₃ H ₇₂ N ₂ O ₁₂ ⁺²	GlaxoSmithKline GmbH	96946-42-8	929

Table 5-9: Selected Intravenous drugs used by anesthetists.

Anesthetic: Propofol

The most commonly used anesthetic is propofol, an alkylphenol presently formulated in a lipid emulsion. Propofol provides rapid onset and offset with context-sensitive decrement times of approximately 10 minutes when infused for less than 3 hours and less than 40 minutes when infused for up to 8 hours [57].

At therapeutic doses, propofol produces a moderate depressant effect on ventilation. It causes a dose-dependent decrease in blood pressure primarily through a decrease in cardiac output and systemic vascular resistance. A unique action of propofol is its antiemetic effect, which remains present at concentrations less than those producing sedation. The induction dose is 1 to 2 mg/kg for loss of consciousness with a maintenance infusion of 100 to 200 $\mu\text{g}/\text{kg}/\text{min}$. For conscious sedation, rates of 25 to 75 $\mu\text{g}/\text{kg}/\text{min}$ are usually adequate. The context-sensitive⁷ half-time for propofol for infusions of up to 8 hours is less than 40 minutes.

After a single bolus injection, whole-blood propofol levels decrease rapidly as a result of redistribution and elimination. The initial distribution half-life of propofol is 2 to 8 minutes [63]. Blood levels required for anesthesia during surgery are 2 to 5 $\mu\text{g}/\text{mL}$, with awakening usually occurring at a blood level less than 1.5 $\mu\text{g}/\text{mL}$ [63].

230

The metabolism of propofol takes place mainly in the liver. The principal metabolite consists of a glucuronide form of propofol (a glucuronic acid is attached on the oxygen) and is mainly eliminated in the urine. Several works showed that the blood concentration of the anesthetic propofol can be correlated to its concentration in the exhaled air [30, 31], being the obtained propofol peaks in the MCC-IMS chromatograms summarized in [Annex 5-4](#). The propofol was confirmed as suitable for an online-monitoring breath analysis using MCC-IMS, as it was observed in both positive and negative mode in all the measurements of the patients' breath. From this point, it was supposed that other drugs and intravenous anesthetics could be exhaled in the breath.

Remifentanyl: an opioids-like analgesic

Opioids suppress pain by their action in the brain, spinal cord, and peripheral nervous system [57]. Opioids affect many organ systems, including the respiratory and cardiovascular systems, and can cause a variety of adverse effects. Proper dosing and monitoring allow the adverse effects to be minimized. New pharmacokinetic principles have allowed more intelligent use of opioids along with more predictable durations of action. The pharmacokinetic and pharmacodynamic properties of opioids

⁷ The context-sensitive half-time is the time for the plasma level of the drug to decrease 50% after cessation of infusion.

are affected by a variety of factors, such as age, body weight, organ failure, and shock. To appropriately use opioids, these factors should be taken into consideration.

During total intravenous anesthesia, the use of opioids is a vital part of providing the analgesic component of anesthesia. Short-acting drugs, such as remifentanyl, allow dissipation of total intravenous anesthesia even more rapidly than with inhaled anesthetics.

We will now focus on the characterization of remifentanyl in exhaled breath of patients under anesthesia. Other drugs as Propofol® [30] and Fentanyl® were already studied for the Clinical Diagnostics group at KIST-Europe.

Although chemically related to the fentanyl congeners, remifentanyl is structurally unique because of its ester linkages. Remifentanyl's ester structure renders it susceptible to hydrolysis by blood- and tissue-nonspecific esterases, which results in rapid metabolism and rapid reduction of blood concentrations after cessation of infusion. Remifentanyl constitutes the first "ultrashort"-acting opioid (Figure 5-18).

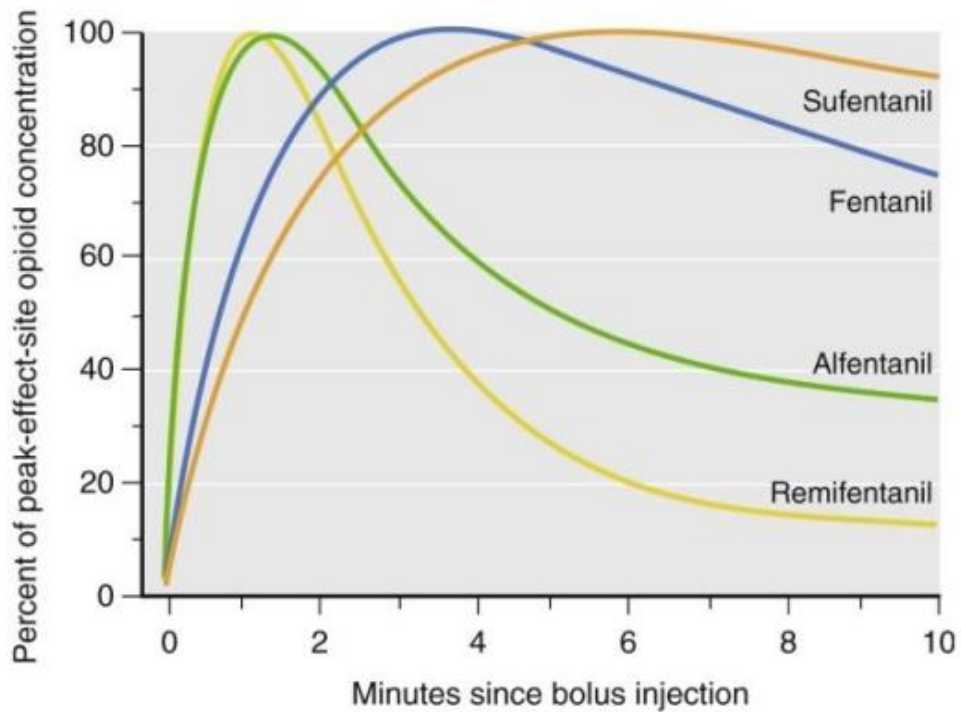


Figure 5-18: Simulated onset and time to peak effect of commonly used opioids based on their pharmacokinetic parameters [63].

The primary metabolic pathway of remifentanyl (GI87084B) is de-esterification to form a carboxylic acid metabolite, GI90291 (Figure 5-19), which is 0.003 to 0.001 times as potent as remifentanyl [54, 64, 65]. A minor secondary metabolic pathway of remifentanyl to GI94219 [63] is also shown in Figure 5-19. The low *in vivo* potency of GI90291 can be explained by low affinity to the μ -receptor in combination with poor brain penetration. Excretion of GI90291 is dependent on renal clearance mechanisms. Evidence from dogs suggests that the remifentanyl metabolites are, for practical purposes, completely inactive, even in patients with renal failure. Its pharmacokinetics is not appreciably influenced by renal or hepatic failure. In blood, remifentanyl is metabolized primarily by enzymes within erythrocytes.

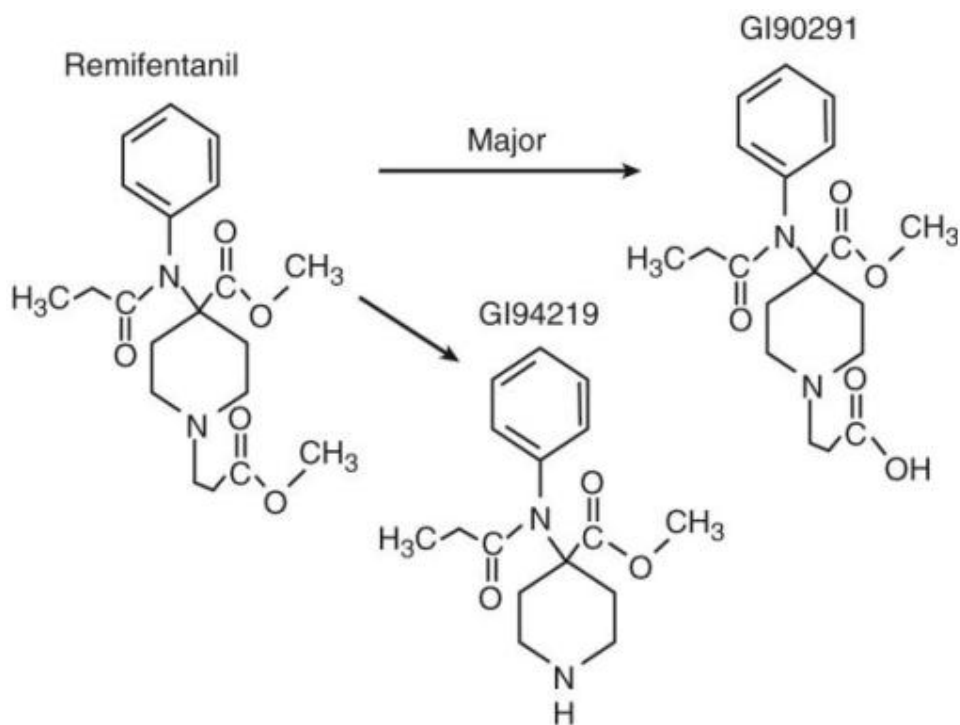


Figure 5-19: Remifentanyl Metabolic pathway [63]. De-esterification by nonspecific plasma and tissue esterases to form a carboxylic acid metabolite (GI90291) that has only 1/300 to 1/1000 the potency of the parent compound is the primary metabolic pathway. N-Dealkylation of remifentanyl to GI94219 is a minor metabolic pathway.

Another factor that has to be considered is the process which takes place in the lung. Lungs are organs that take part in the excretory system as well as the liver or the kidney. Drugs can undergo an uptake in the lungs and be extracted in as alveolar gas, leading them to be found in the exhaled air. Duthie *et al.* [66] determined a remifentanyl clearance (the volume of blood totally cleaned per minute by the organ)

of 2.03 L/min, similar to the value of 2.8 L/min found in volunteers given remifentanyl by infusion for 20 minutes [54]. It is less than the clearance of 4 to 5 L/min [64] calculated after single doses given over one minute. Therefore, **lungs take part in the elimination of remifentanyl** but in a low way. No information concerning the vapor pressure other than the clearance value was found for the remifentanyl metabolites.

Relaxants

The muscle relaxants are used to facilitate the intubation of the patient, being Mivacurium chloride (Mivacron®) and cisatracurium besilate (Nimbex®) the used ones in this study (see Table 5-9). Both are non-depolarizing neuromuscular agents and exert their actions by a competitive binding on specific receptors in the brain.

Other drugs

During a anesthesia, some other drugs must be required, as antibiotics or for the treatment of hypotension. Below are shown the used ones during surgery in this study, being in parenthesis (Drug, CAS#, Formula, Molecular Weight in uma or u):

- Hypotension treatment: Ephedrin (Ephedrin, 299-42-3, C₁₀H₁₅NO, 165u)
- Corticosteroid: (used as an anti-inflammatory and immunosuppressant) Fortecotin® (Dexamethasone, 50-02-2, C₂₂H₂₉FO₅, 392u)
- Analgesic and antipyretic: Novaminsulfon® or Novalgin® (Metamizole, 68-89-3, C₁₃H₁₆N₃NaO₄S, 333u)
- Prevent nausea and vomiting: Zofran® (Ondansetron, 99614-02-5, C₁₈H₁₉N₃O, 293u)
- Antibiotics: Clont® (Metronidazol, 443-48-1 C₆H₉N₃O₃, 171u); Rocephin (Ceftriaxone, 73384-59-5 C₁₈H₁₈N₈O₇S₃, 554u); Cefuroxime (Cefuroxime, 55268-75-2, C₁₆H₁₆N₄O₈S, 424u); Sobelin® (Clindamycin, 18323-44-9, C₁₈H₃₃ClN₂O₅S, 425u); Unasyn® (Ampicillin sodium and sulbactam sodium, no CAS, C₃₂H₃₈N₄O₁₂S₃, 766u)
- Paralytic drug: Lysthenon® 2% (Succinylcholine, 306-40-1, C₁₄H₃₀N₂O₄, 290u)

5.5.c Experimental Set-up while surgical anesthesia

In Figure 5-20 is shown the set-up for breath sampling while a patient is being anesthetized. A patient undergoing anesthesia is intubated (with an endotracheal tube or a laryngeal mask airway), is maintained with Propofol and a common Opioid is used as analgesic (in our case Remifentanyl) by using a Target-controlled infusion or TCI machine. To control how deep it's the anesthesia, a brain monitoring is used; the Bispectral Index™ or BIS™, which directly monitors a patients level of consciousness. For breath sampling a connector is introduced between endotracheal tube and airway filter to connect the sample tube to the MCC-IMS. While the patient breaths normally, 50 mL of exhaled breath is collected for analysis.

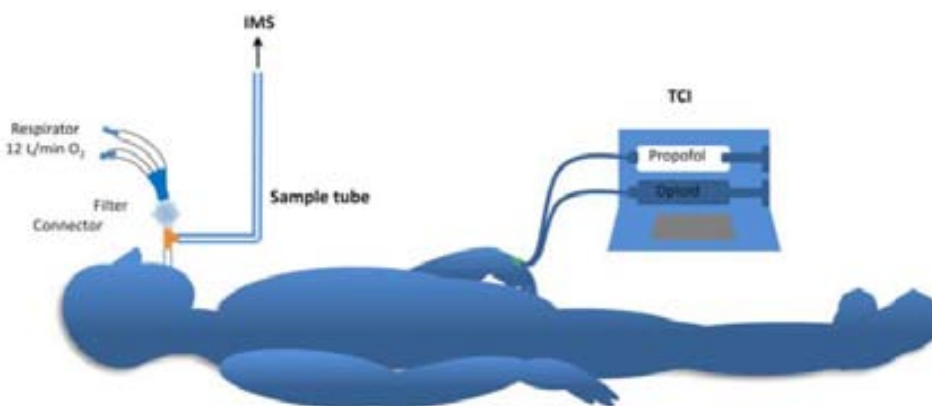


Figure 5-20: Set-up for breath sampling. A patient intubated (endotracheal) undergoing anesthesia, maintained with Propofol and a common Opioid as analgesic. For breath sampling a connector is introduced between endotracheal tube and airway filter to connect the sample tube to the MCC-IMS. Adapted from [30].

Respirator system

The anesthetic machine or respirator system delivers known gas and vapor concentrations which are variable in amount and composition. The machine is of a ‘continuous-flow’ nature and is designed so that gases are delivered at safe pressures.

For surgical purposes, patient will pass through different rooms. In the entering room (ER) the patient is anesthetized, then is introduced to the operation room (OP) where patient will undergo the surgery and finally, it will be moved to the outing room (OR) where the patient can be placed in case of necessity or moved directly to the post-surgery room. In the ER and the OP rooms there are available different respiratory systems or anesthetic machines. The respirator systems of the ER’s and the OP’s are different. Both systems are from Dräger [62], being the ER system the model Fabius Tiro® and the OP system the model Primus®, a detail of them is shown in Annex 5-5. In Figure 5-21 are shown the respirator systems being used in a patient under anesthesia in the ER (top), and while surgery operation in the OP (bottom).



Figure 5-21: Pictures of a patient after being anesthetized in **(top)** the entering room (ER). **(bottom)** the operating room (OP). 1 oxygen ventilation provided by the respirator system Fabius Tiro® from Dräger; 2 Target-controlled infusion (TCI); 3 MCC-IMS with the laptop for acquisition of data and the synthetic air; 4 oxygen ventilation provided by the respirator system Primus® from Dräger.

Target-Controlled Infusion TCI

We have already seen the target-controlled infusion (TCI), but now we will specify it for the drugs of interest for this studio:

- **TCI – propofol:** Target concentrations of 0.5–2.5 $\mu\text{g/ml}$ are required to produce good-quality sedation during surgery performed under local and regional anesthesia.
- **TCI – remifentanyl:** Remifentanyl has a rapid onset of action, a short elimination half-life, and a context-sensitive half-time of approximately 3 min, which does not change as the infusion time increases.

The pharmacokinetics of remifentanyl and propofol are incorporated into the TCI system of Orchestra® Base Primea WorkStation. The advantage of using a TCI pump is that a calculated plasma concentration is provided and can be used for correlation studies.

Co-administration of drugs by the same giving set is not ideal as a change in the rate of one infusion can affect the other, especially if there is a significant dead-space after the common connection or T-piece. The most reliable method is to use a separate, dedicated access site, but in the practice they are introduced by the same cannula as can be seen in Figure 5-22.



Figure 5-22: Cannula where drugs are introduced to anesthetize a patient using a Target-controlled infusion (TCI).

5.6 Operational Background - Plastic Emissions

During Breath Analysis operational background emissions have to be considered. In the study reported here we analyze the background emissions of two different intubation methods, an endotracheal tube and a laryngeal mask used in anesthesia. Also a straight connector used to collect the patients breath is studied. Laboratory measurements have been carried out with MCC-IMS and also with a Gas Chromatograph - Mass Selective Detector (GC-MSD), showing different plastic compositions and MCC-IMS chromatographs. Patients breath measurements were carried out while the patients were anesthetized and intubated. In the breath analysis of patients under anesthesia we will study if there is one or more specific peaks due to the endotracheal tube, the laryngeal mask or the straight connector.

5.6.a Intubation methods

There are four methods of airway control that are used to ensure unobstructed gas exchange: Facemask and Guedel airway; Laryngeal mask; Endotracheal tube; and Tracheostomy. The studied patients in this work were intubated some with an Endotracheal tube ET and others with Laryngeal mask airway LM.

1. **Endotracheal tube**, once inserted into the trachea, maintains airway patency and minimizes gastric aspiration into the lungs. All endotracheal tubes have information written upon the tube (Figure 5-23a). The used one in patients measurements was a Lo-Contour® Tracheal Tube with Murphy tip from Nellcor [67], shown in Figure 5-23b. The tube is inserted by holding the laryngoscope in the left hand and passing the blade into the right side of the mouth. The tongue is then pushed to the left as the blade is passed down the tongue and inserted anterior to the epiglottis in the vallecula.
2. **Laryngeal mask airway** was developed in the 1980's (Figure 5-24) has supplanted tracheal intubation for many general anesthetics. The device is basically the progeny of a facemask mated with an endotracheal tube, allowing positioning of the mask just above the glottic opening. (Figure 5-24a) It is inserted using a blind technique and provides a patent airway for spontaneous breathing; it is used occasionally for ventilation and management of difficult intubation. The used one in patients measurements is a LMA® Supreme Laryngeal Mask from LMA North America, Inc. [68], shown in Figure 5-24b.

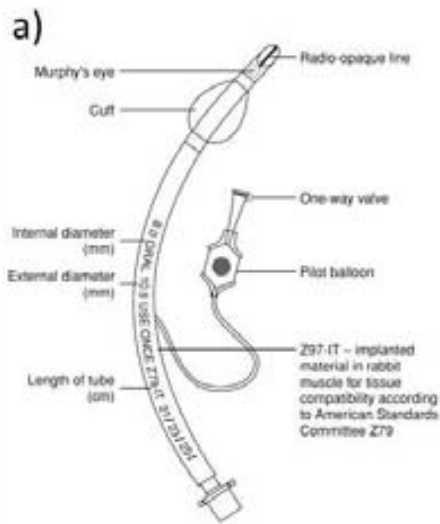


Figure 5-23: (a) Typical cuffed endotracheal tube [69]. (b) Picture of the endotracheal tube used in the patients.

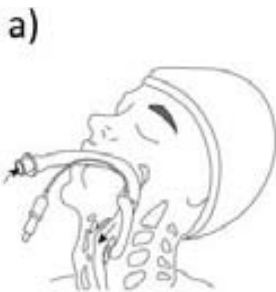


Figure 5-24: (a) Laryngeal mask correctly positioned before inflation, with the tip of the mask in the base of the hypopharynx [69]. (b) Picture of the Laryngeal mask airway used in the patients.

5.6.b Measurements methods

The patient under anesthesia with endotracheal intubation is shown in Figure 5-25, also the straight connector, placed between the endotracheal tube (or the laryngeal mask) and the filter, used to collect the sample for the MCC-IMS measurements is shown. The filter is used to clean the exhaled breath of the patient connected to the respirator system. The Straight connector used is from VBM Medizintechnik GmbH [70].

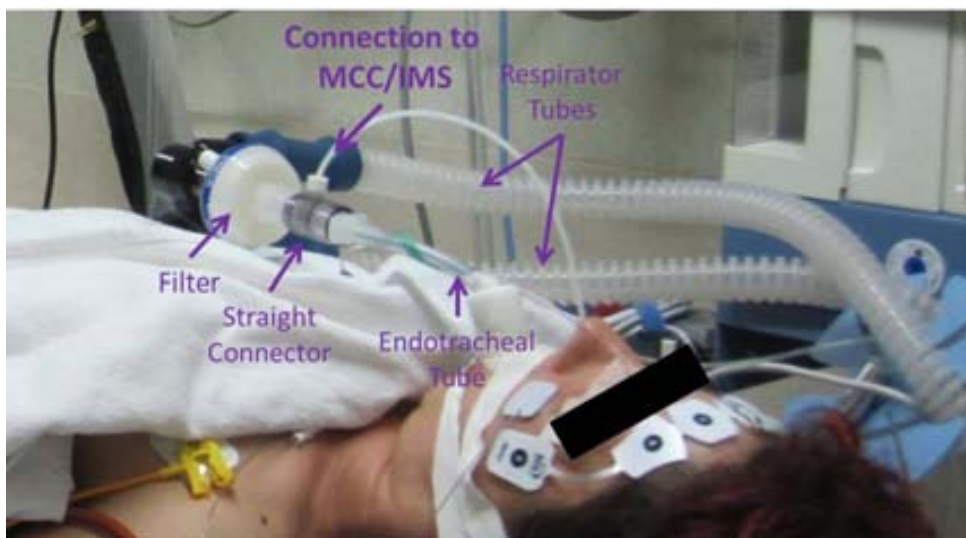


Figure 5-25: Patient under anesthesia being intubated with an Endotracheal Tube. A Straight Connector situated between the endotracheal tube and the filter was used to collect the patients breath for the MCC-IMS measurements.

Laboratory measurements of MCC-IMS were carried out with the IMS-1 device, while the patients measures were performed with the IMS-3 device. Chromatograms of both devices must be aligned. The aligning chromatogram peak used was Benzothiazol, with a Retention Time of $RT = 144$ s and a reduced inverse mobility coefficient of $1/K_0 = 0.571$ Vs/cm², because it comes from the materials of which the MCC-IMS device internally is made and will be present in all kind of MCC-IMS measurements in positive mode (see Section 5.2.b *Devices data alignment*, [71]).

Also, mass spectrometric measurements of the studied plastic material used for anesthesia were carried out for the compounds present in them (ET, LM and SC). The measurements were done using a Gas Chromatograph (Agilent 6890N Network) – Mass Selective Detector (Agilent 5973 Network), GC-MSD that can be seen in Figure 5-26. Gas sample for the packed plastic material were acquired by solid phase extraction technique using TENAX GR as the adsorption material in the thermal desorption tubes. Samples were taken with a flow rate of 250 mL/min, during about 15 min for each measurement. The GC oven temperature program was set as following: initial temperature of 50 °C for 2 minutes, followed with a gradient of 10°C/min until 260° C and finally held for 15 minutes. The total run time was 38 minutes. A MDIS software (Automated Mass Spectral De-convolution and Identification System) is used to analyze the GC-MSD data using the NIST (National Institute of Standards and Technology, from the U.S.) mass spectra library.



Figure 5-26: GC-MSD available at KIST-Europe.

Samples were collected by making two small cuts to the sealed packages of the plastic material, one for the MCC-IMS and TDS (Thermal Desorption System) sampling inlets of the GC-MSD, and the other for the air inlet (see Figure 5-27). For this reason, also room air was also studied.

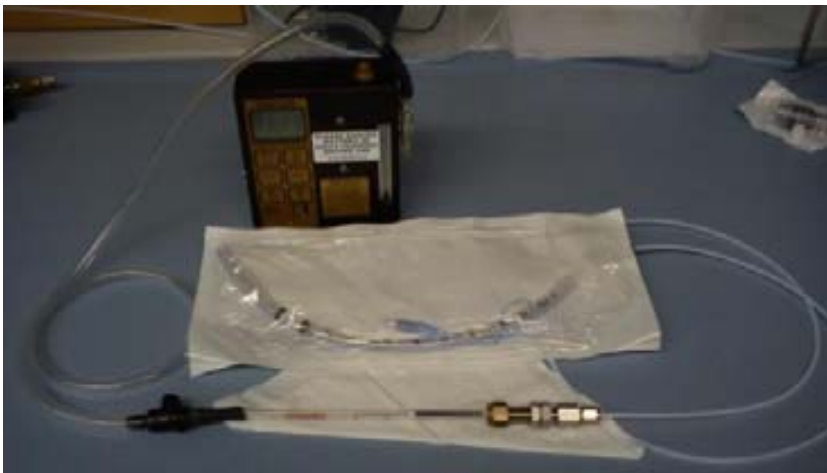


Figure 5-27: Sample taking of the Endotracheal Tube using a TDS sampling inlet.

5.6.c Laboratory Measurements — MCC-IMS and GC-MSD

Laboratory Room Air measurements with MCC-IMS device has been considered as blank measurements. A 10 peaks list has been found and named as RL_#, as can be seen in Figure 5-28. Three of the peaks have been identified as Benzothiazol ($RT = 144$ s, $1/K_0 = 0.571$ Vs/cm²) used for chromatographs alignment, Nonanal ($RT = 61$ s, $1/K_0 = 0.734$ Vs/cm²) and Decanal ($RT = 149$ s, $1/K_0 = 0.760$ Vs/cm²). Once the room air was analyzed, the plastic measurements with the MCC-IMS device were done.

Laboratory MCC-IMS chromatogram of the studied operational background is showed in Figure 5-29 for the Endotracheal Tube (ET), in Figure 5-30 for the Laryngeal Mask (LM), and in Figure 5-31 for the Straight Connector (SC); all of them measured inside their original packages, with the same MCC-IMS device. For each plastic material analyzed, a list of peaks in the chromatograms have been obtained: 19 for the endotracheal tube (ET_#), 13 for the laryngeal mask (LM_#), and 11 for the straight connector (SC_#). From the 19 peaks obtained for the endotracheal tube analysis, 12 peaks have been found also in the laryngeal mask chromatogram showed as crosses in Figure 5-30 (ET_#/LM), and from this 12 peaks present in both ET and LM, 3 peaks have also been found in the straight connector chromatogram showed also as crosses in Figure 5-31 (ET_#/LM/SC). Different peaks were expected due to the fact that plastic materials have different composition.

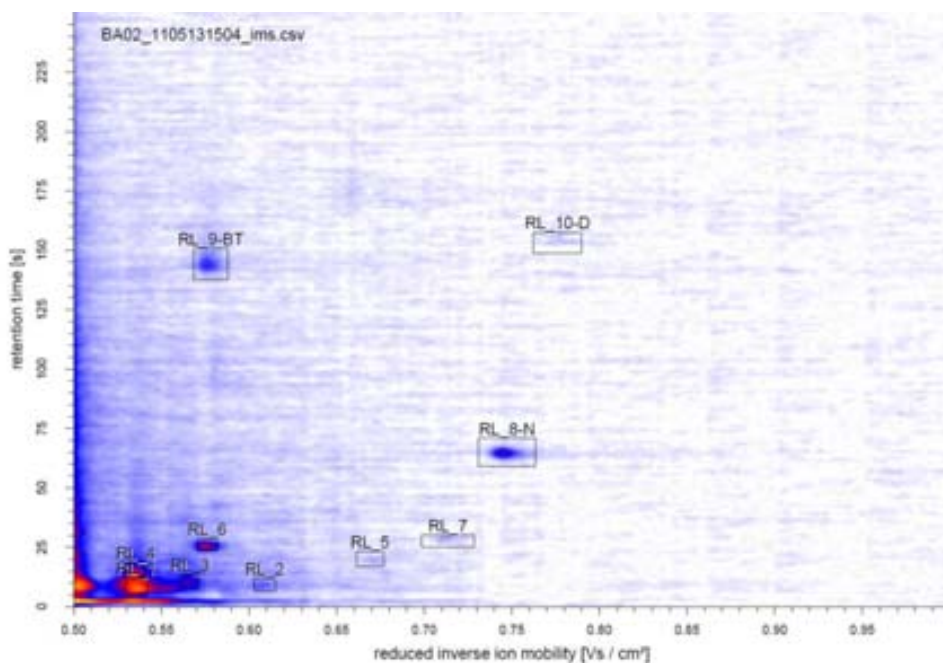


Figure 5-28: MCC-IMS chromatogram of the laboratory room air (RL). Rectangles show the identified peaks for RL.

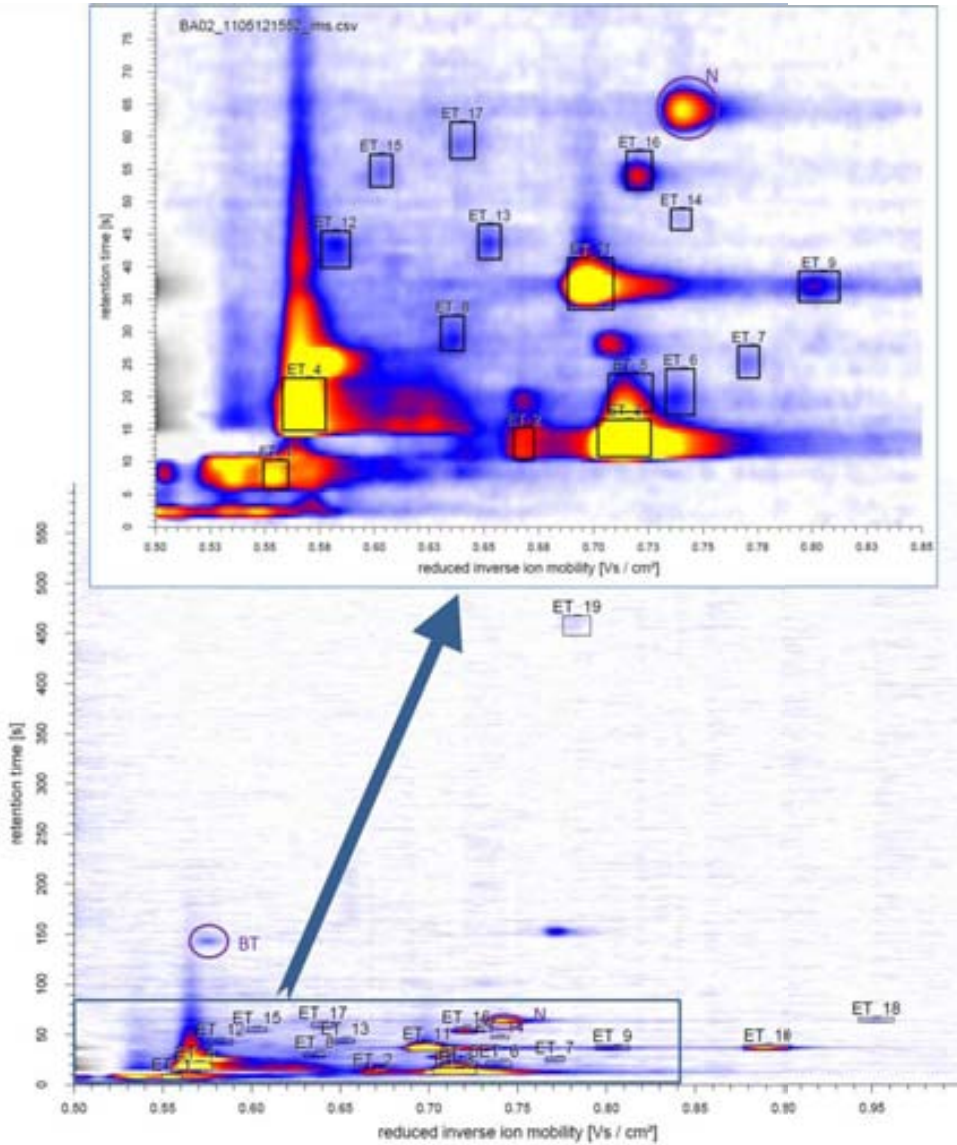


Figure 5-29: MCC-IMS chromatogram of the Endotracheal Tube (ET) inside its original package. Rectangles show the identified peaks for ET, the rest are Room Air peaks. Benzothiazol (BT) and Nonanal (N) are shown inside purple circles.

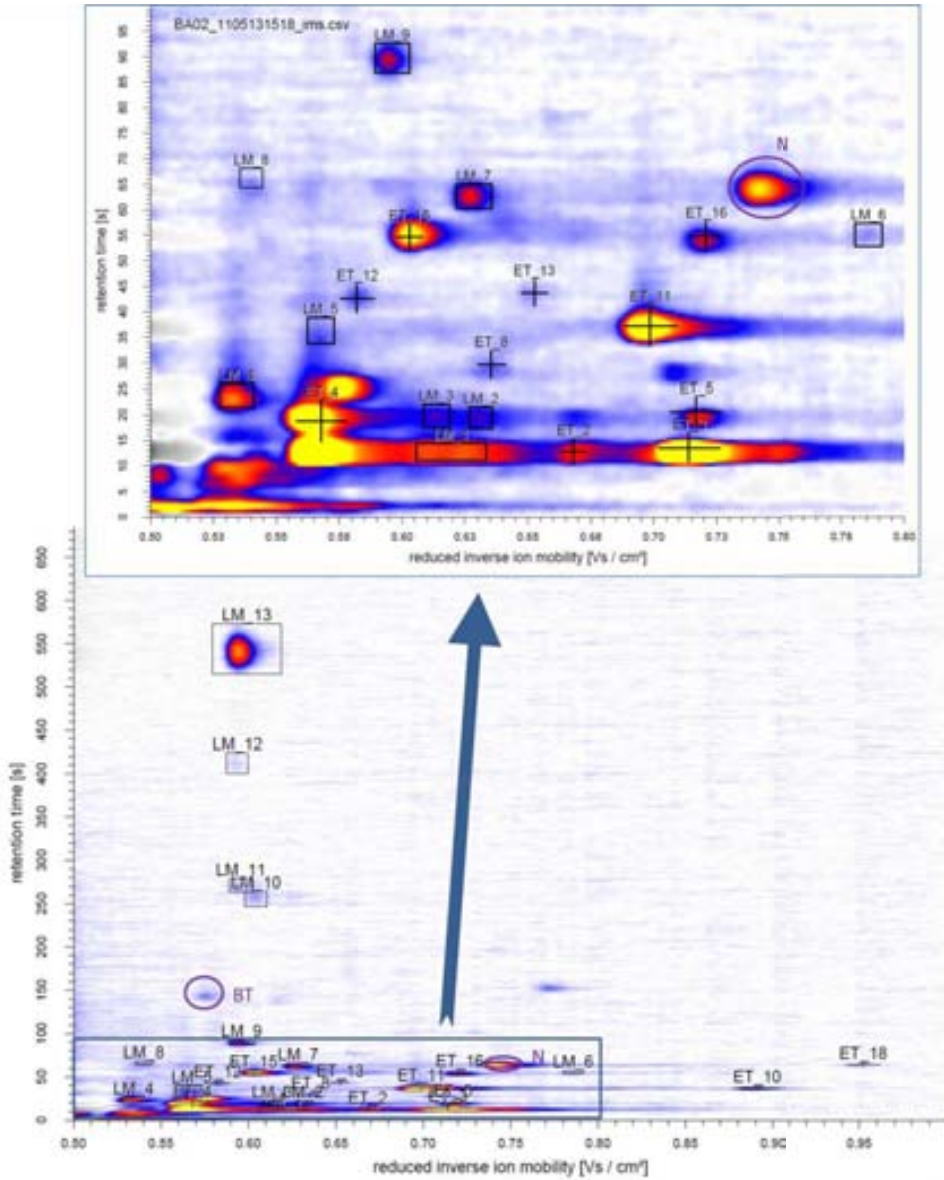


Figure 5-30: MCC-IMS chromatogram of the Laryngeal Mask (LM) inside its original package. Rectangles show the identified peaks for LM and crosses show the identified peaks that are also in the Endotracheal Tube (ET) chromatogram, the rest are Room Air peaks. Benzothiazol (BT) and Nonanal (N) are shown inside purple circles.

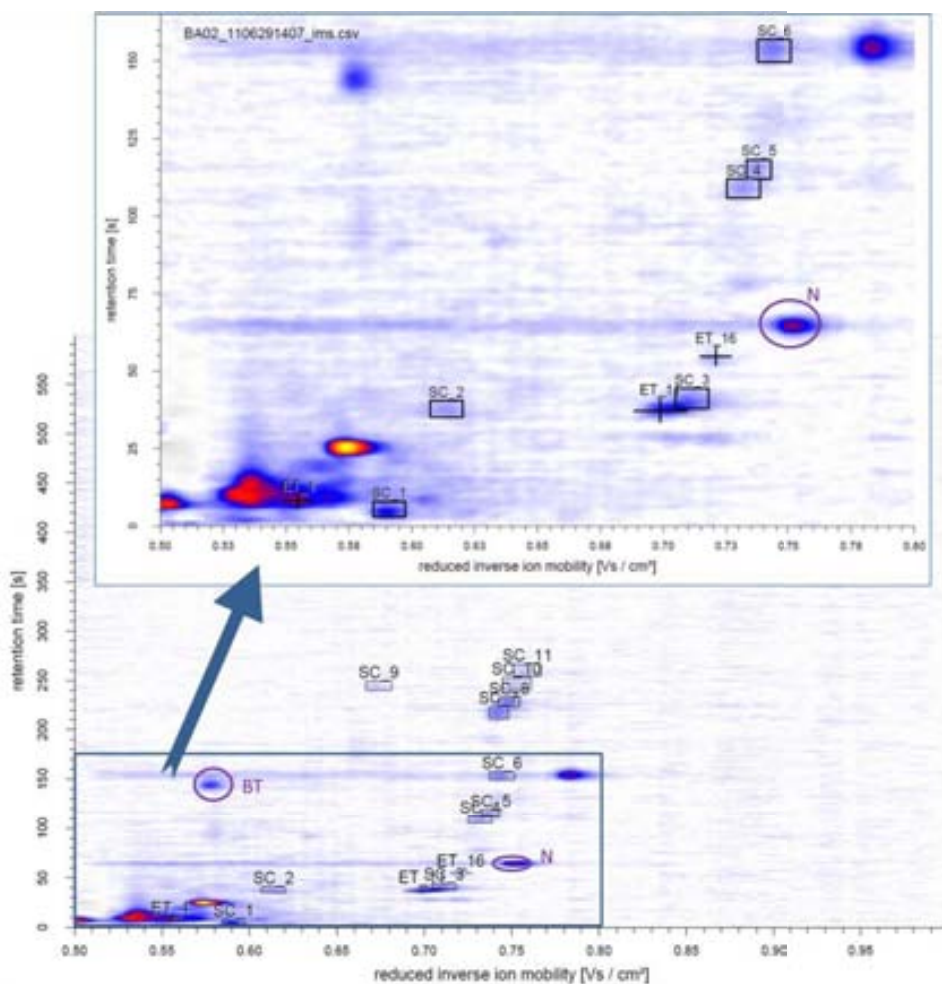


Figure 5-31: MCC-IMS chromatogram of the Straight Connector (SC) inside its original package. Rectangles show the identified peaks for SC and crosses show the identified peaks of ET and LM that are also present in the SC chromatogram, rest are Room Air peaks. Benzothiazol (BT) and Nonanal (N) are shown inside purple circles.

Once analyzed the plastic materials with the MCC-IMS, they have been measured with a GC-MSD also. In Figure 5-32 is shown the obtained GC-MSD chromatogram for the endotracheal tube. Some plastic compounds of the endotracheal tube have been clearly identified. For the endotracheal tube, the main compound found is diethyl phthalate or DEP ($RT_{GC} = 15.77$ min), which is used as plasticizer. For the straight connector (SC) also a GC-MSD measurement was done, and the main compound has been identified as di-butyl phthalate ($RT_{GC} = 19.72$ min). Also some other compounds used as adhesive in the packaging have been found: phthalic acid, diisobutyl ester ($RT_{GC} = 18.77$ min) for the ET and limonene diepoxide ($RT_{GC} = 12.93$ min) for the SC. From the GC-MSD analysis, the compounds found in both cases are: caprolactam ($RT_{GC} = 11.28$ min) that is the precursor to Nylon 6, a

widely used synthetic polymer. So, GC-MSD measurements show that, as it was expected, the composition of the different elements studied is different.

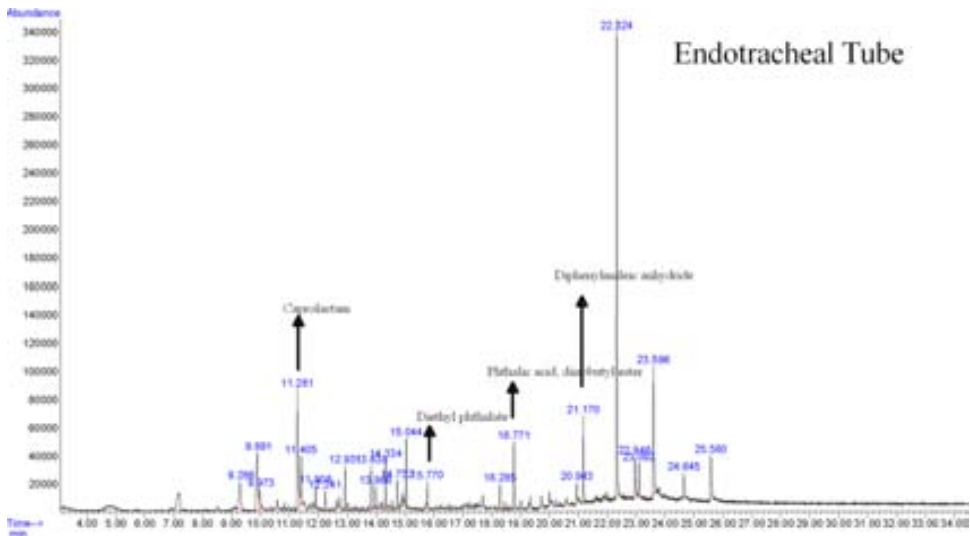


Figure 5-32: GC-MSD chromatogram of the Endotracheal Tube measured inside its package.

5.6.d Plastic emissions in Patients Measurements — MCC-IMS

Once analyzed in the laboratory the operational background used in anesthesia, two different patients breaths under anesthesia were analyzed. Both patients have been anesthetized with propofol. Room air and Respirator Blank measurements have been considered in the entering room from the operation room (OP) where the patient was anesthetized. Twenty three peaks have been obtained, six of them being identified and corresponding to Benzothiazol, Nonanal, Decanal, RL_3 from the laboratory measurements, ET_11 and ET_3/LM from endotracheal and laryngeal mask analysis in the laboratory. These measurements corresponding to ET peaks can be explained because the respirator system has a lot of plastic materials connected in order to carry the oxygen to the patient, as can be seen in Figure 5-25. The rest of the obtained peaks have been named as RL-OP_# for the peaks only present in the Room Air; Resp_# for the peaks only present in the Respirator system; and RL-Resp_# for the peaks present in Room Air and in the Respirator system.

The first patient (PAT-ET) was intubated with an endotracheal tube and the second one (PAT-LM) with a laryngeal mask; both having the straight connector placed just after the chosen intubation method. Patients were induced with 2-6 mg/kg propofol by Target Control Infusion (TCI) or by manual bolus injection, and with analgesics, for PAT-ET 0.1-0.5 µg/kg/min remifentanyl while for PAT-LM 0.1-0.3 mg/fentanyl. For

PAT-ET, a list of 32 peaks (Pet_#) has been obtained, as is shown in Figure 5-33. And for PAT-LM, a list of 35 peaks has been obtained (Plm_#), as is shown in Figure 5-34. Peaks shown as crosses are the identified peaks corresponding to peaks from the laboratory analysis of the endotracheal tube, the straight connector and the anesthetic propofol; and also the operation room blank measurements.

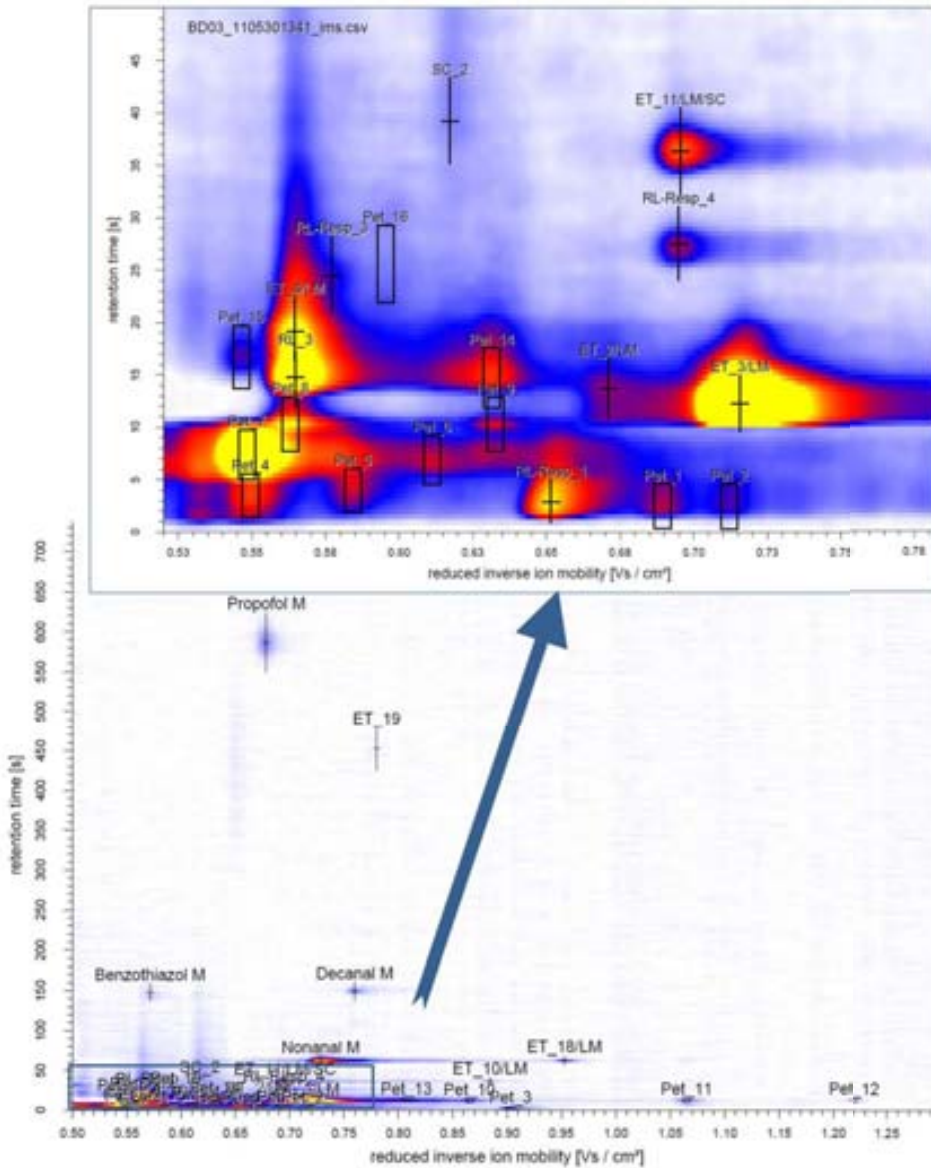


Figure 5-33: MCC-IMS chromatogram of PAT-ET, the patient intubated with an endotracheal tube and with a straight connector used to collect breath. Crosses indicate the identified peaks with the laboratory and the operation room blank measurements, while rectangles represent the rest of the peaks of the patient (Pet_#).

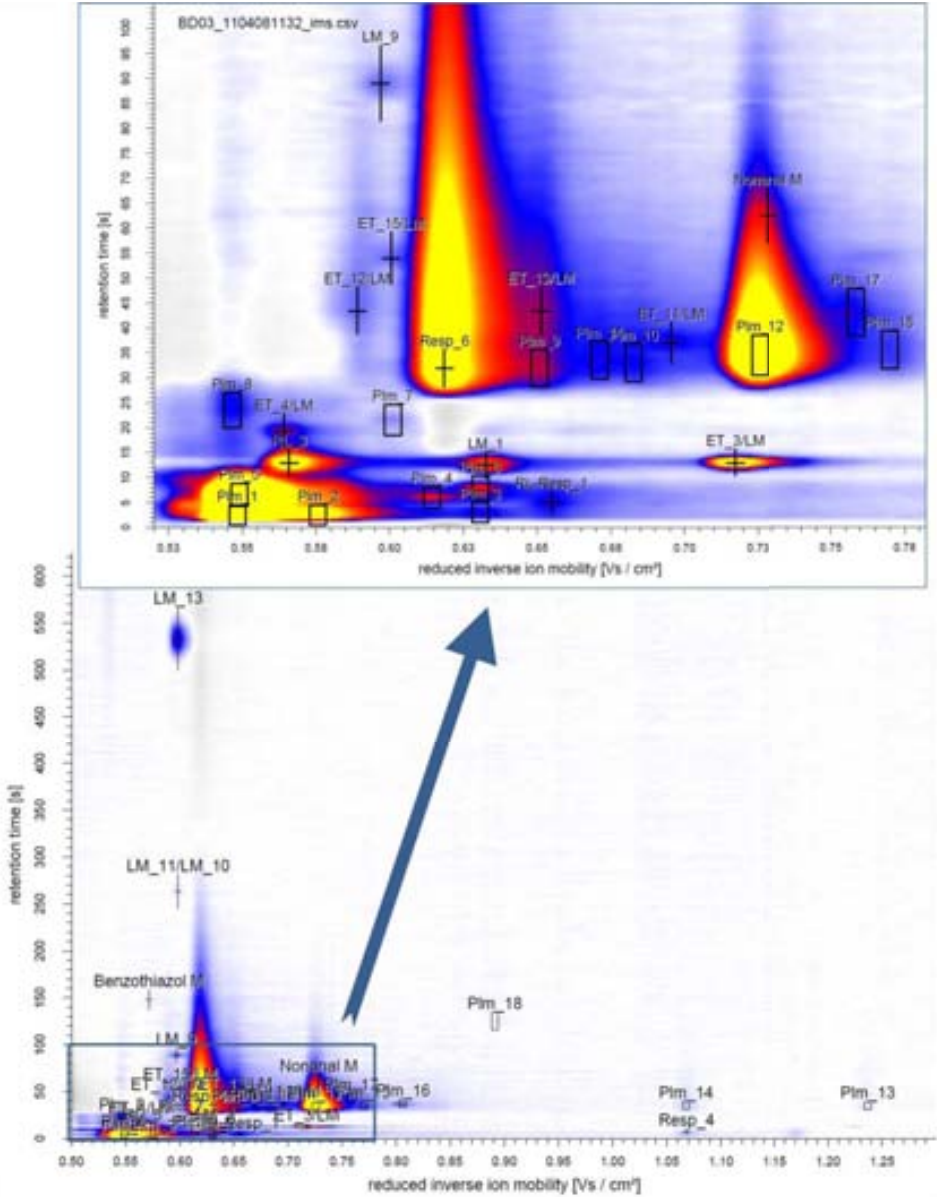


Figure 5-34: MCC-IMS chromatogram of PAT-LM, the patient intubated with a laryngeal mask and with a straight connector used to collect the breath. Crosses indicate the identified peaks with the laboratory and the operation room blank measurements, while rectangles represent the rest of the peaks of the patient (Pim_#).

From the MCC-IMS chromatograms of the patients, some peaks of the endotracheal tube and the laryngeal mask have been identified, and are reported in Table 5-10. Highlighted in bold are the specific peaks found for the endotracheal tube and the laryngeal mask plastics in the patients measures: ET_19, LM_9 and LM_13; that can be easily distinguished from the rest of the peaks. For the straight connector, not specific peak has been found. Notice that for the PAT-LM chromatogram, propofol peak is not seen because the retention time collected (~600 s without alignment) was not enough.

Intubation	Peak	1/K ₀ (Vs/cm ²)	RT (s)
ET	RL-Resp_3	0.577	25
	RL-Resp_4	0.695	28
	Decanal M	0.760	149
	Propofol M	0.678	587
	ET_2/LM	0.671	14
	ET_10/LM	0.884	37
	ET_11/LM/SC	0.696	36
	ET_18/LM	0.953	63
	ET_19	0.780	453
ET and LM	Nonanal M	0.728	63
	BenzothiazolM	0.572	148
	ET_3/LM	0.716	12
	ET_4/LM	0.565	19
	RL_3	0.566	13
	RL-Resp_1	0.655	5
LM	Resp_4	1.068	8
	LM_1	0.633	13
	Resp_6	0.619	32
	ET_11	0.695	37
	ET_12	0.589	44
	ET_15	0.600	54
	LM_9	0.597	89
	LM_11/LM_10	0.599	263
	LM_13	0.599	533
	ET_13	0.651	44

Table 5-10: Identified Peaks of PAT-ET and PAT-LM present in MCC-IMS chromatograms. Highlighted in bold are the specific peaks found for ET and LM in the patients measures.

5.7 Exhaled Remifentanil in Patients under Anesthesia

For the positive mode, there were studied eight patients (3 F / 5 M), being named as P1p-...-P8p. For the negative mode, there were studied ten patients (5 F / 5 M), being named as P1n-...-P10n. In [Annex 5-6](#) is summarized the recorded data of the patients for both positive and negative modes, as well as the anesthesia treatment that each patient has received during the measurements. For the positive mode, the chromatograms have been aligned to the Benzothiazol peak.

Patients were induced with 2-6 mg/kg (93-200/500 mg) propofol by TCI pump or by manual bolus injection, and 0.1-0.5 µg/kg/min remifentanil. Individual dosages were adapted by the attending anesthetist. Maintenance of anesthesia was accomplished with 1.8-19.2 mg/kg/h propofol (1.1-7.0 µg/ml plasma concentration), and partially with additional 0.1-0.5 µg/kg/min remifentanil, either by TCI pump or with a syringe pump. After induction of anesthesia, the patients were intubated with either an endotracheal tube or a laryngeal mask. The fraction of inspiratory oxygen (FiO₂) was 100%, which means that no room air was used and no air from the patient was recycled. This results in an oxygen supply of about 12 L/min.

The Blood test results obtained in *in-vitro* measurements were compared to the patients data and to the control group used as a reference, as can be seen in the box-and-whisker plots of the four ‘identified’ peaks of remifentanil: Remi_1, Remi_2 and the Remi_3 peaks for the positive mode; and Remi_4 peak for the negative mode. Results do not confirm the presence of the ‘identified’ remifentanil peaks in the exhaled breath of patients, because the results for the control group are in the same range than results obtained for the anesthetized patients.

For all anesthetized patients, the ‘identified’ peaks have a lower intensity than for the control group. But for the Remi_1 and Remi_3 peaks, there is at least one measure above the control group values the patient P8p for the Remi_1 peak and for patient P1p for the Remi_3 peak. In [Figure 5-35](#) is shown the detailed box-and-whisker plot of P8p for Remi_1 peak. The measurement number is detailed as P8p-#. It can be seen that for the first measure of the patient P8p the Remi_1 peak is detected. In [Figure 5-36](#) is shown the detailed box-and-whisker plot of P1p for Remi_3 peak. The measurement number is detailed as P1p-#. It can be seen that for the first measure of the patient P1p the Remi_3 peak is also detected.

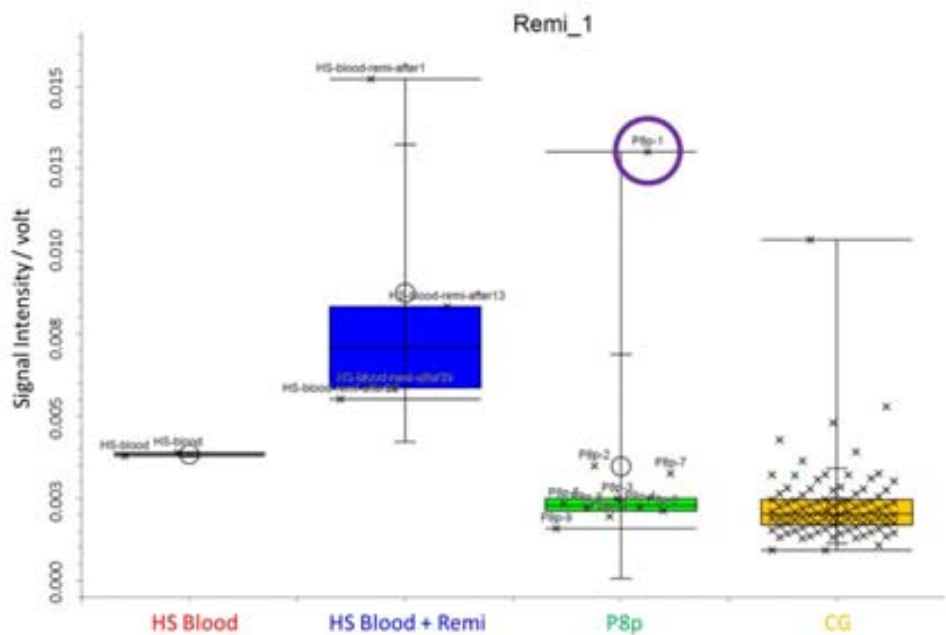


Figure 5-35: Box-and-whisker plot for Remi_1 peak in + mode, for the blood test series (HS Blood and HS Blood + Remi) compared to the patient P8p and to the control group (CG).

250

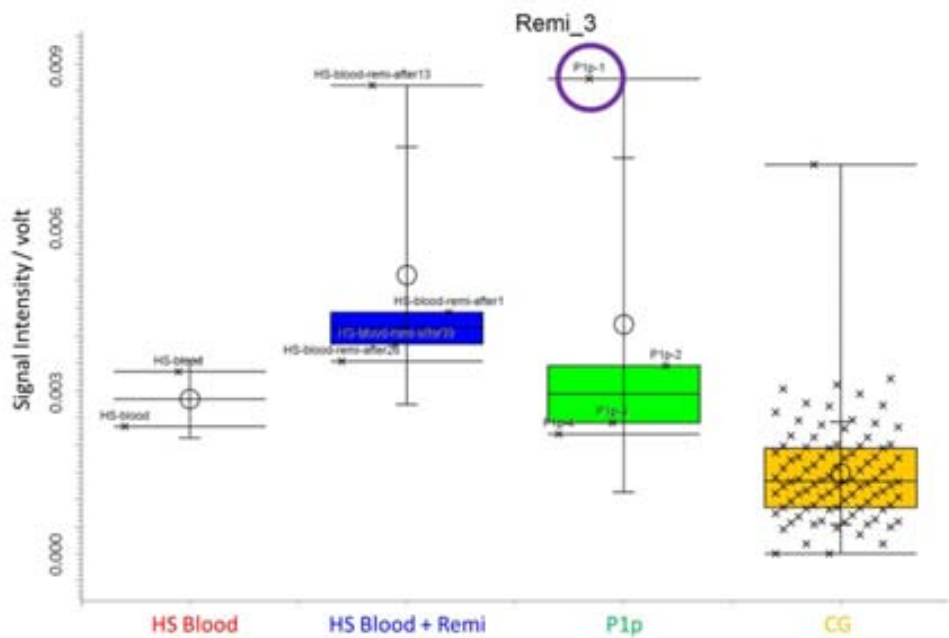


Figure 5-36: Box-and-whisker plot for Remi_3 peak in + mode, for the blood test series (HS Blood and HS Blood + Remi) compared to the patient P8p and to the control group (CG).

So, the question was: **which was the remifentanyl dose that patients received for these measurements?** In Table 5-11 is summarized the remifentanyl flow rate and plasma concentration during measurements of patients in positive mode. It can be seen that for the patient P8p, the first measurement was done at a plasma concentration of 20 ng/mL (the maximum dose that a patient can receive), while for the rest of the measurements it was lower, as for the rest of the patients. The pre-medication data and the medication received by the patient during the measurements are summarized in [Annex 5-6](#).

ID	Remifentanyl flow rate ($\mu\text{g}/\text{kg}/\text{min}$), IN BRACKETS the Plasma concentration (ng/mL)														
	Measurement #														
	1	2	3	4	5	6	7	8	9	10	11	12	13	14	15
P1p	0.5	0.1	0.1	0.1	-	-	-	-	-	-	-	-	-	-	-
P2p	0.2	0.2	0.2	0.2	-	-	-	-	-	-	-	-	-	-	-
P3p	0.5	0.1	0.1	0.1	-	-	-	-	-	-	-	-	-	-	-
P4p	0.5	0.1	0.1	0.1	-	-	-	-	-	-	-	-	-	-	-
P5p	0.5	0.1	0.1	0.1	-	-	-	-	-	-	-	-	-	-	-
P6p	0.3 (10)	0.26 (10)	0.26 (10)	0.25 (10)	0.25 (10)	0.25 (10)	0.25 (10)	0.25 (10)	none (10)	-	-	-	-	-	-
P7p	0.36 (10)	0.36 (10)	0.35 (10)	0.39 (11)	0.39 (11)	0.42 (11)	0.38 (11)	0.38 (11)	0.37 (11)	0.39 (11)	0.38 (11)	0.39 (11)	0.37 (11)	0.21 (7)	none
P8p	0.79 (20)	0.27 (10)	0.35 (10)	0.35 (10)	0.35 (10)	0.54 (15)	0.52 (10)	0.11 (7)	0.26 (8)	none	-	-	-	-	-

Table 5-11: Available Remifentanyl flow rate and plasma concentration according to patients measurements in + mode.

When a patient is anesthetized, it first receives a bolus of the anesthetic (propofol) and a high concentration of the analgesic (in this case remifentanyl), and once anesthetized both concentrations are reduced to maintain the anesthesia. For this studio, patients were anesthetized being present in the entering room (ER) only the anesthetist and the nurses. **Once the patient was anesthetized, we could enter inside the entering room and start the measurements.**

For P8p the concentration of remifentanyl was remained high until we did the first measurement (Figure 5-37) and then reduced to the half. In all other patients, when the first measurement was done the patient already had the concentration of both anesthetic and analgesic reduced at least to the half. For the Remi_3 peak, there is no correlation of the concentration of remifentanyl with the first measurement of patient P1p (Figure 5-38). Note that previously Remi_1 peak was identified as Remifentanyl and Remi_3 peak as its major metabolite GI90291. Further measurements with high concentrations of remifentanyl must be done to confirm the hypothesis that Remi_1 peak was due to the remifentanyl itself.

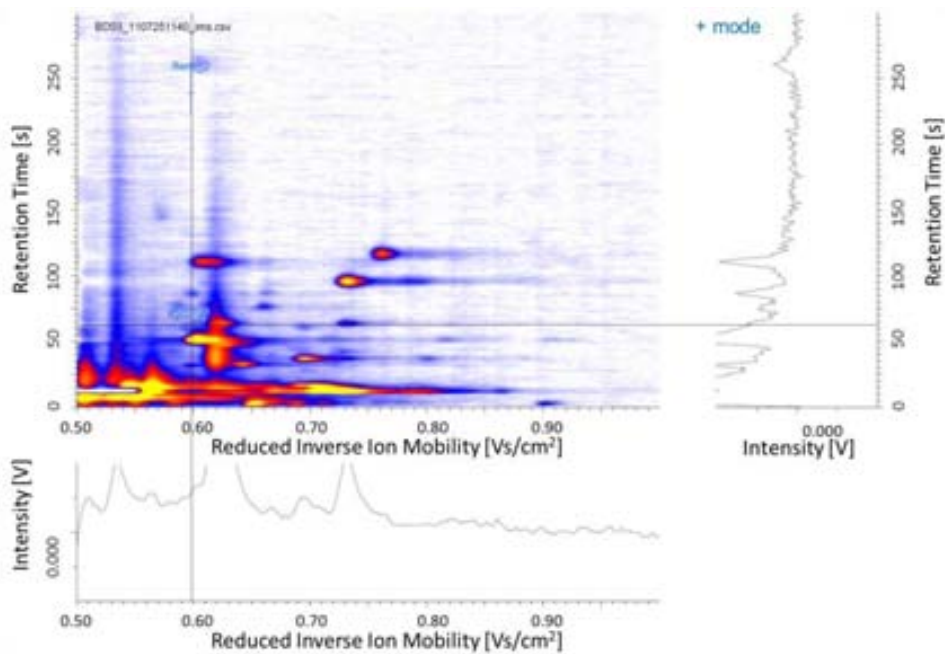


Figure 5-37: MCC-IMS chromatogram of the 1st measurement of P8p containing 20 ng/mL of remifentanyl in + mode. The spectra for the Remi_1 peak, is shown.

252

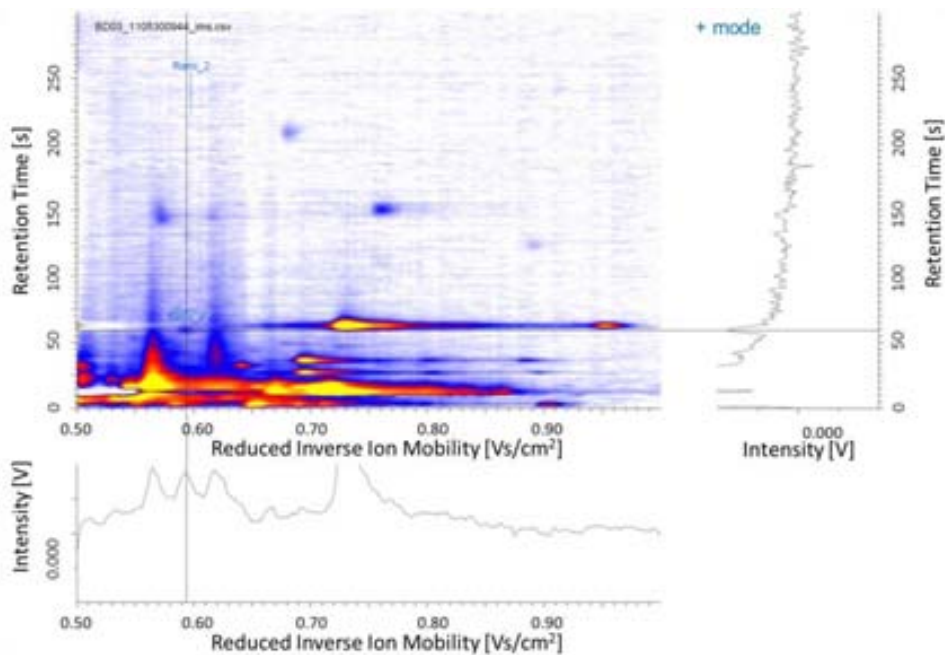


Figure 5-38: MCC-IMS chromatogram of the 1st measurement of P1p containing 10 ng/mL of remifentanyl in + mode. The spectra of the Remi_3 peak, is shown.

Blood *in vitro* experiments were adjusted to the maximal target concentration in the blood of the patients (20 ng/mL), leading to a blood concentration in the order of ppb (ng/ml). In the case of propofol, the blood concentration was in the ppm range (µg/ml). Propofol concentration in the exhaled breath during constant infusion has been determined in the literature between 2.8 and 22.5 ppb_v [72] or between 5 to 15.6 ppb_v with a limit of detection of 700 ppt_v [31]. The remifentanil concentration in the breath should be very low, i.e. in the range of ppt_v. Thus, **detection of the remifentanil in the breath can be difficult.**

The extent of pulmonary uptake is greater with opioids whose pKa⁸ exceeds 8.0 [66]. The opioids with a pKa less than 8.0 have a less first pass pulmonary uptake, being the pKa of remifentanil 7.07 [73]. Opioids with higher pulmonary uptake are likely to be found in the lungs.

As no specific peaks due to remifentanil (or its metabolites) have been found neither in patients nor in blood *in vitro* tests, next step was to detect the pure drug in liquid form by a GC-MSD to be sure that their detection is possible.

Discussion and Summary

Environment and background emissions have to be always considered when measurements series are performed, for this reason room air variation, device alignment and operation background emissions regarding the plastics involved in anesthesia were studied.

Investigations of time series using a single instrument have been done over six months. Results obtained for background emissions showed that different instruments can be used after aligning them to compare and characterize MCC-IMS chromatograms. Benzothiazol peak was found to be suitable for the alignment of different devices in positive mode. Non alignment peak was found for the negative mode.

Analysis of the background emissions of two different intubation methods, an endotracheal tube and a laryngeal mask used in anesthesia were done. Also a straight connector used to collect the patient's breath was studied. Laboratory measurements were carried out with MCC-IMS and also with a GC-MSD, showing different plastic compositions and MCC-IMS chromatographs.

⁸ pKa is a logarithmic measure of the acid dissociation constant: $pKa = -\log_{10}Ka$.

A control group was defined for positive mode. It has been showed what and why has to be taken into account when defining a control group for breath analysis. The initial 156 measurements (87 F / 69 M) obtained from the control group were reduced to 94 measurements (46 F/ 48 M), after eliminating the unwanted ones due to gastric interferences.

In vitro Blood tests with remifentanyl were carrier out to determine possible peaks due to remifentanyl or to any of its metabolites. First it was measured the head space of reconstructed remifentanyl alone for 0.5, 1, 2, 5, 10, and 20 μL with a concentration of 1 $\text{ng}/\mu\text{L}$. Only one peak in positive mode was found to be due to remifentanyl. Then, blood *in vitro* experiments with remifentanyl were done having the adjusted concentration to the maximal target that a patient can tolerate (20 ng/mL). Four peaks due to remifentanyl and their metabolites were found for the *in vitro* blood test, and a possible identification for each peak was proposed. In the positive mode Remi_1 peak was identified as Remifentanyl being this peak also the one found in the head space of reconstructed remifentanyl alone; Remi_2 peak as the minor metabolite GI94219; and Remi_3 peak as the major metabolite GI90291. For the negative mode, Remi_4 peak was identified to be due to other compounds present in the remifentanyl reconstruction.

Breath measurements were carried out while patients were anesthetized and intubated. In the breath analysis of patients under anesthesia one specific peak of the endotracheal tube has been found, and also two specific peaks from the laryngeal mask.

During the analysis of complex sample matrices, e.g. human breath, volatile organic compounds from bacteria, fungi etc., there are many unknown peaks in the IMS chromatogram due to the voluminous amount of substances in the sample matrix. Identifying all the detected substances is one of the major problems. There are a huge number of possible analytes emanating from these matrices which could be the detected peak in the chromatogram. Measuring each and every possible substance as a reference and probing to identify the detected analyte is a very time consuming process. Was in that context where the online monitoring of an analgesic (remifentanyl) in the breath of patients under anesthesia and surgery was studied.

A control group was defined in positive mode. It has been showed what and why has to be taken into account when defining a control group for breath analysis. Initial control group of 156 measurements (87 F / 69 M), after eliminating the unwanted gastric interferences for our exhaled drug breath under anesthesia studio, leads a final control group of 94 measurements (46 F/ 48 M).

Once found the possible peaks, exhaled remifentanyl in patients under anesthesia was studied. Patients were induced with propofol by Target-controlled infusion TCI pump or by manual bolus injection, and remifentanyl. Two of the identified peaks of

remifentanil, the Remi_1 and Remi_3 peaks, were found only one time each in two different measures of patients. Remi_1 peak was obtained for the highest remifentanil dose (20 ng/mL) a person can receive, but not for lower concentrations of remifentanil in patients. For Remi_3 peak no relation with remifentanil dose was observed. From the *in vitro* blood test, the Remi_1 peak was identified as Remifentanil and Remi_3 peak as its major metabolite GI90291, so even the identified peaks are only found in two measurements, it's a promising result. As remifentanil is metabolized in the blood, its metabolites have to be taken into account and investigated in further experiments.

References

1. Lindinger, W., A. Hansel, and A. Jordan, *Proton-transfer-reaction mass spectrometry (PTR-MS): on-line monitoring of volatile organic compounds at pptv levels*. Chemical Society Reviews, 1998. **27**: p. 347-354.
2. Lindinger, W., A. Hansel, and A. Jordan, *On-Line Monitoring of Volatile Organic Compounds at pptv Levels by Means of Proton-Transfer-Reaction Mass Spectrometry (PTR-MS). Medical Applications, Food Control and Environmental Research*. International Journal of Mass Spectrometry and Ion Processes, 1998. **173**: p. 191-241.
3. Schwarz, K., W. Filipiak, and A. Amann, *Determining concentration patterns of volatile compounds in exhaled breath by PTR-MS*. Journal of Breath Research, 2009. **3**: p. 1-15.
4. Thekedar, B., et al., *Investigations on the variability of breath gas sampling using PTR-MS*. Journal of Breath Research, 2009. **3**: p. 1-11.
5. Wisthaler, A., *PTR-MS: a new tool for the rapid detection and quantification of VOCs in air at ultra-trace levels*, 2004, Institut für Ionenphysik, Leopold-Franzens-Universität Innsbruck: Innsbruck.
6. Ligor, M., et al., *Determination of volatile organic compounds in exhaled breath of patients with lung cancer using solid phase microextraction and gas chromatography mass spectrometry*. Clinical Chemistry and Laboratory Medicine, 2009. **47**(5): p. 550-560.
7. Buszewski, B., et al., *Analysis of exhaled breath from smokers, passive smokers and non-smokers by solid-phase microextraction gas chromatography/mass spectrometry*. Biomedical Chromatography, 2009. **23**(5): p. 551-556.
8. Ligor, T., et al., *The analysis of healthy volunteers' exhaled breath by the use of solid-phase microextraction and GC-MS*. Journal of Breath Research, 2008. **2**: p. 1-8.
9. Schubert, J.K., et al., *Determination of antibiotic drug concentrations in circulating human blood by means of solid phase micro-extraction*. Clinica Chimica Acta, 2007. **386**(1-2): p. 57-62.
10. Smith, D., et al., *Isoprene levels in the exhaled breath of 200 healthy pupils within the age range 7-18 years studied using SIFT-MS*. Journal of Breath Research, 2010. **4**: p. 1-7.
11. Enderby, B., et al., *Concentrations of some metabolites in the breath of healthy children aged 7-18 years measured using selected ion flow tube mass spectrometry (SIFT-MS)*. Journal of Breath Research, 2009. **3**: p. 1-11.
12. Spanel, P. and D. Smith, *Quantification of trace levels of the potential cancer biomarkers formaldehyde, acetaldehyde and propanol in breath by SIFT-MS*. Journal of Breath Research, 2008. **2**: p. 1-10.
13. Spanel, P., K. Dryahina, and D. Smith, *The concentration distributions of some metabolites in the exhaled breath of young adults*. Journal of Breath Research, 2007. **1**: p. 1-8.

14. Dryahina, K., M. Polasek, and P. Spanel, *A selected ion flow tube, SIFT, study of the ion chemistry of H₃O⁺, NO⁺ and O₂⁺ ions with several nitroalkanes in the presence of water vapour*. International Journal of Mass Spectrometry, 2004. **239**: p. 57-65.
15. Baumbach, J.I., *Process analysis using ion mobility spectrometry*. Analytical and Bioanalytical Chemistry, 2006. **384**(5): p. 1059-1070.
16. Jünger, M., B. Bödeker, and J.I. Baumbach, *Peak assignment in multi-capillary column - ion mobility spectrometry using comparative studies with gas chromatography - mass spectrometry for exhaled breath analysis*. Analytical and Bioanalytical Chemistry, 2010. **396**(1): p. 471-482.
17. Maddula, S., et al., *Detection of volatile metabolites of Escherichia coli by multi capillary column coupled ion mobility spectrometry*. Analytical and Bioanalytical Chemistry, 2009. **394**(3): p. 791-800.
18. Baumbach, J.I., *Ion Mobility Spectrometry coupled with Multi-Capillary Columns for Metabolic Profiling of Human Breath*. Journal of Breath Research, 2009. **3**: p. 1-16.
19. Bödeker, B., W. Vautz, and J.I. Baumbach, *Peak Comparison in MCC/IMS – Data – Searching for potential biomarkers in human breath data*. International Journal for Ion Mobility Spectrometry, 2008. **11**(1): p. 89-93.
20. Baumbach, J.I. and M. Westhoff, *Ion mobility spectrometry to detect lung cancer and airway infections*. Spectroscopy Europe, 2006. **18**(6): p. 22-27.
21. Moseley, J.T., et al., *Measurement of Transport Properties of Ions in Gases; Results for K⁺ Ions in N₂* Physical Review, 1969. **178**(1): p. 234-239.
22. Daviss, B., *Growing pains for metabolomics*. The Scientist, 2005. **19**(8): p. 25-28.
23. Smedsgaard, J. and J. Nielsen, *Metabolite profiling of fungi and yeast: from phenotype to metabolome by MS and informatics*. Journal of Experimental Botany, 2005. **56**(410): p. 273-286.
24. Maddula, S., *Volatile Metabolite fingerprints of Escherichia coli*, in *Dept. of Biochemical and Chemical Engineering 2005*, University Dortmund: Dortmund. p. 52.
25. Griffin, J.L. and R.A. Kauppinen, *Tumor metabolomics in animal models of human cancer*. Journal of Proteome Research, 2007. **6**(2): p. 498-505.
26. Davies, A.N. and J.I. Baumbach, *Early lung cancer diagnostics by ion mobility spectrometry data handling*. Spectroscopy Europe, 2008. **20**(5): p. 18-21.
27. Westhoff, M., et al., *Differentiation of chronic obstructive pulmonary disease (COPD) including lung cancer from healthy control group by breath analysis using ion mobility spectrometry* International Journal for Ion Mobility Spectrometry, 2010. **13**(3-4): p. 131-139.
28. Bader, S., *Atemluftüberwachung mittels mikrostrukturierter Ionenbeweglichkeitsspektrometrie: Statistische Analyse zum Auffinden von Biomarkern für Lungenkrebs*, in *Fachbereich Statistik 2005*, Universität Dortmund: Dortmund. p. 113.
29. Baumbach, J.I., et al., *Breath Discovery based on Ion Mobility Spectrometry and Classification and Differentiation Models for Lung Diseases*. Biomedizinische Technik, 2010. **55**(Suppl. 1).
30. Kreuder, A.E., et al., *Characterization of propofol in human breath of patients undergoing anesthesia*. International Journal for Ion Mobility Spectrometry, 2011. **14**(4): p. 167-175.
31. Perl, T., et al., *Determination of serum propofol concentrations by breath analysis using ion mobility spectrometry*. British Journal of Anaesthesia, 2009. **103**(6): p. 822-827.
32. Borsdorf, H., et al., *Recent Developments in Ion Mobility Spectrometry*. Applied Spectroscopy Reviews, 2011. **46**(6): p. 472-521.
33. Eiceman, G.A. and Z. Karpas, 2005, *Ion Mobility Spectrometry*. 2nd ed. Boca Raton: CRC Press.
34. Perl, T., et al., *Alignment of retention time obtained from multicapillary column gas chromatography used for VOC analysis with ion mobility spectrometry*. Analytical and Bioanalytical Chemistry, 2010. **397**(6): p. 2385-2394.
35. Viitanen, A.K., et al., *Experimental study of the effect of temperature on ion cluster formation using ion mobility spectrometry*. Atmospheric Research, 2008. **90**(2-4): p. 115-124.
36. Barnett, D.A., et al., *Characterization of a Temperature-Controlled FAIMS System*. Journal of the American Society for Mass Spectrometry, 2007. **18**(9): p. 1653-1663.

37. Jia, J., et al., *Effects of drift tube temperature on ion mobility spectra*. Chinese Journal of Analytical Chemistry, 2006. **34**(12): p. 1783-1786.
38. Tabrizchi, M., *Temperature effects on resolution in ion mobility spectrometry*. Talanta, 2004. **62**(1): p. 65-70.
39. Tabrizchi, M., *Temperature Corrections for Ion Mobility Spectrometry*. International Journal for Ion Mobility Spectrometry, 2002. **5**(1): p. 59-62.
40. Ewing, R.G. and C.J. Miller, *The effects of temperature on the detection of volatile vapors emitted from explosives using ion mobility spectrometry*. International Journal for Ion Mobility Spectrometry, 2001. **3**(1): p. 56.
41. Eiceman, G.A., E.G. Nazarov, and J.E. Rodriguez, *Chemical class information in ion mobility spectra at low and elevated temperatures*. Analytica Chimica Acta, 2001. **433**: p. 53-70.
42. Eiceman, G.A., et al., *Positive Reactant Ion Chemistry for Analytical, High Temperature Ion Mobility Spectrometry (IMS): Effects of Electric Field of the Drift Tube and Moisture, Temperature, and Flow of the Drift Gas*. International Journal for Ion Mobility Spectrometry, 1998. **1**(1): p. 28-37.
43. Chen, Y.H., H.H. Hill, Jr., and D.P. Wittmer, *Thermal effects on electrospray ionization ion mobility spectrometry*. International Journal of Mass Spectrometry and Ion Processes, 1996. **154**: p. 1-13.
44. Eiceman, G., et al., *Analysis of a drift tube at ambient pressure: Models and precise measurements in ion mobility spectrometry*. Review of Scientific Instruments, 2001. **72**(9): p. 3610-3621.
45. Borsdorf, H. and T. Mayer, *Electric field dependence of ion mobilities of aromatic compounds with different ionic mass and different functional groups*. International Journal for Ion Mobility Spectrometry, 2010. **13**(3-4): p. 103-108.
46. Soppart, O. and J.I. Baumbach, *Comparison of electric fields within drift tubes for ion mobility spectrometry*. Measurement Science & Technology, 2000. **11**(10): p. 1473-1479.
47. Guevremont, R. and R. Purves, *Comparison of experimental and calculated peak shapes for three cylindrical geometry FAIMS prototypes of differing electrode diameters*. Journal of the American Society for Mass Spectrometry, 2005. **16**(3): p. 349-362.
48. Young, D., et al., *Automated control and optimisation of ion mobility spectrometry responses using a sheath-flow inlet*. Analytica Chimica Acta, 2002. **463**(2): p. 143-154.
49. 2009, *Mosby's Medical Dictionary*. 8th ed. St Louis, MO: Mosby/Elsevier.
50. ICH Harmonised Tripartite Guideline, *Choice of Control Group and Related Issues in Clinical Trials (ICH-E10)*, in *international conference on harmonisation of technical requirements for registration of pharmaceuticals for human use*.
51. European Medicine Agency (EMA). *Regulatory. Human medicines. Scientific guidelines. ICH guidelines*. [cited 2012 5th December]; Available from: http://www.emea.europa.eu/ema/index.jsp?curl=pages/regulation/general/general_content_0_00035.jsp&mid=WC0b01ac0580027645.
52. Food and Drug Administration (FDA). *Regulatory Information. Import and Export Guidance Documents*. [cited 2012 5th December]; Available from: <http://www.fda.gov/RegulatoryInformation/Guidances/ucm122048.htm>.
53. Pharmaceuticals and Medical Devices Agency (PDMA). *International Conference on harmonisation of Technical Requirements for Registration of Pharmaceuticals for Human Use*. [cited 2012 5th December]; Available from: http://www.pmda.go.jp/ich/ich_index.html.
54. Egan, T.D., et al., *The Pharmacokinetics of the New Short-acting Opioid Remifentanyl (GI87084B) in Healthy Adult Male Volunteers*. Anesthesiology, 1993. **79**(5): p. 881-892.
55. Feldman, P.L., et al., *Design, synthesis, and pharmacological evaluation of ultrashort- to long-acting opioid analgesics*. Journal of Medicinal Chemistry, 1991. **34**(7): p. 2202-2208.
56. Lehner, A.F., et al., *Remifentanyl in the horse: identification and detection of its major urinary metabolite*. Journal of Analytical Toxicology, 2000. **24**(5): p. 309-315.
57. Brown, E.N., R. Lydic, and N.D. Schiff, *General Anesthesia, Sleep, and Coma*. New England Journal of Medicine, 2010. **363**(27): p. 2638-2650.
58. Kennedy, D. and C. Norman, *What Don't We Know?* Science, 2005. **309**(5731): p. 75.
59. *Drugs: Drug Information online*. [cited 2012 23rd February]; Available from: <http://www.drugs.com/>.

60. *DrugBase: your one-click drug source*. [cited 2012 23rd February]; Available from: <http://drugbase.org/>.
61. *Vademecum*. [cited 2012 23rd February]; Available from: <http://www.vademecum.es/>.
62. *Dräger*. [cited 2012 15th March]; Available from: <http://www.draeger.com/ES/es/>.
63. Miller, R.D., 2010, *Miller's Anesthesia*. Seventh ed.: Churchill Livingstone.
64. Westmoreland, C.L., et al., *Pharmacokinetics of Remifentanyl (GI87084B) and Its Major Metabolite (GI90291) in Patients Undergoing Elective Inpatient Surgery*. *Anesthesiology*, 1993. **79**(5): p. 893-903.
65. Glass, P.S.A., et al., *Preliminary Pharmacokinetics and Pharmacodynamics of an Ultra-Short-Acting Opioid*. *Anesthesia & Analgesia*, 1993. **77**(5): p. 1031-1040.
66. Duthie, D.J., et al., *Remifentanyl and pulmonary extraction during and after cardiac anesthesia*. *Anesthesia & Analgesia*, 1997. **84**(4): p. 740-744.
67. *Nellcor*. [cited 2012 16th March]; Available from: <http://www.nellcor.com/>.
68. *LMA North America, Inc.* [cited 2012 16th March]; Available from: <http://www.lmana.com>.
69. Robinson, N. and G. Hall, 2007, *How to Survive in Anaesthesia: A guide for trainees*. Third ed. Oxford, UK: Blackwell Publishing Ltd.
70. *VBM Medizintechnik GmbH*. [cited 2012 16th March]; Available from: <http://www.vbm-medical.de/>.
71. Cumeras, R., et al., *Stability and alignment of MCC/IMS devices*. *International Journal for Ion Mobility Spectrometry*, 2012. **15**(1): p. 41-46.
72. Grossherr, M., et al., *Propofol concentration in exhaled air and arterial plasma in mechanically ventilated patients undergoing cardiac surgery*. *British Journal of Anaesthesia*, 2009. **102**(5): p. 608-613.
73. Egan, T.D., *Remifentanyl Pharmacokinetics and Pharmacodynamics: A Preliminary Appraisal*. *Clinical Pharmacokinetics*, 1995. **29**(2): p. 80-94.

Conclusions and Future Work

In an ideal world, we might be able to rapidly detect and classify any type of chemical and biological that is found in low concentrations, using instruments of small size and easy implementation. The number of applications for which these devices are required is large: from the diagnosis of disease to the detection of airborne toxins. However, the sensors that are currently available have only some but not all of these attributes.

In this thesis has been presented the development of a micro planar high Field Asymmetric Ion Mobility Spectrometer, including simulation, design, fabrication and characterization. But furthermore, a medical application with a conventional IMS (MCC/IMS) has been done for a breath drugs studio while patients were anesthetized.

259

Finally, to summarize the main goals reached are namely:

- **Simulation of the p-FAIMS device.** The physical phenomena involved in a p-FAIMS are complex due to the interaction of electric fields, fluid flows and other magnitudes into the transport of chemical species through the device. This studio has implied the need of a Multiphysics treatment. Simulations were performed using the COMSOL Multiphysics software, a 2D approximation with a fixed gap of 0.5 mm was performed for different compounds chosen representative for security applications. Special attention has been paid to compounds differentiation through a broad range of conditions, being also the model validated. Simulations showed that p-FAIMS simulation could be achieved with COMSOL software, being a good platform for this kind of applications. Simulations done have allowed us to monitor the effects due to changes in the dispersion field (wave amplitudes and frequencies), to find compensation voltages for different gases under different conditions. Also have been seen the effects due to geometry variations of the device (electrode gap and length of the drift tube) as well as changes due to variations in the carrier gas flow.

- Design, Fabrication and Characterization of a micro UV-p-FAIMS for Toluene Detection.** A p-FAIMS prototype was designed, fabricated and characterized for toluene, showing an agreement with the expected ions behavior even the low dispersion voltage used, therefore the proof-of-concept of the p-FAIMS with a PCB-PMMA-PCB configuration was demonstrated. Results were in agreement with the simulated device and of the same order than the ones available in the literature. It is expected that with an appropriate high asymmetric field at higher DV of 1,000 V ($E_D/N \sim 80 \text{Td}$) it will be able to differentiate various compounds. The experimental part was carried out through:

Set-Up organization: Full set-up implementation included new equipment's for the synthesis of the high field asymmetric waveform, UV lamps for the ionization, and laboratory fungle. An effort to control the instrumentation needed was done implementing different LabView Graphical Interfaces, and in the design and implementation of a home-made mass-flow system. Also the needed instrumentation was huge, and some connections were not as simple as initially thought.

Design and fabrication: Two configurations of p-FAIMS were explored. The initial design with a sandwich-like Glass-Silicon-Glass configuration with Pyrex® 7740 Borosilicate Glass was analyzed but due gas leaks found in the packaging and to the large number of problems encountered, some of them unresolved it was decided to completely change the strategies involved in the implementation of the device. The second design consist of a printed circuit board (PCB) and Poly(methyl methacrylate) (PMMA) sandwich-like configuration as: PCB-PMMA-PCB. Packaging was done with a FORMIGA prototyped polyamide design including the tub connections and the UV-lamp positioning, all system jointed by screws. A faraday cage (a metal noise shield) has been done using the sides of the PCB's that do not define the drift tube, and an extra faraday cage (a metal safety shield) was used to ensure that high voltage would not damage the system or the operator. This design has been used for toluene detection.

Characterization of the p-FAIMS fabricated: Final p-FAIMS prototype was characterized for toluene under different experimental conditions. Studies included:

(1) *Electrodes biasing.* UV positioning was checked and also its capacity to ionize a sample gas (acetone at high concentration, ~ 1500 ppm). It was also measured the amount of ions detected at each pair of electrodes of the p-FAIMS which allowed us to observe how the amount of ions detected decrease (due to recombination and collision effects) depending on the distance between the ionization source and the detector. The UV-gate electrodes were studied both for positive and negative voltages, obtaining that for negative voltages the

signal is reduced more quickly than for positive voltages being due to the non-uniform charge distribution of the toluene molecule, as expected a higher signal was obtained when UV-gate electrodes were grounded. And, the detector polarity was changed to detect positive or negative ions, having a little signal for the negative mode due to other anions formed in the ionization region from some impurities.

(2) *Detection without High Field.* The detection of 1 ppm of toluene was not achieved for low total flows (50 sccm) but it was achieved for higher flows. The repeatability of the detection of 1 ppm of toluene was shown for consecutive measurements and for different day's measurements. Different concentrations of toluene were studied, ranging from 1 to 10 ppm and in a low range from 200 ppb (minimum achievable with the mass-flow system) to 1 ppm, showing both a linear tendency, in agreement with results using a UV-lamp from the literature. The limit of detection LOD was 200 ppb (minimum concentration that our mass-flows system can provide), but decreasing the voltage step of the compensation scan the noise was reduced and based upon signal to noise calculations, LOD is estimated at 100 ppb. Also the carrier gas flow ranging from 250 to 2,000 sccm was studied for 1 ppm of toluene, and showed that as the flow is increased the intensity obtained for 1 ppm is increased and also the signal width, being the optimum flow at 1,000 sccm to improve the resolution. Different concentrations from 1 to 10 ppm were studied for total flows from 250 to 2,000 sccm, confirming that the optimum flow of 1,000 sccm found was correct, as the signal intensities saturates at this value.

(3) *Detection of Toluene Ions with RF field.* The addition of the high voltage or dispersion voltage was achieved only up to 300 V due to instrumentation issues, but even though at this low DV the toluene compensation voltage changed from 0.0 V (without DV) to -0.32 V (with 300 V of DV) and also the intensity and the full width at half maximum were slightly decreased, when using a bisinusoidal waveform with a duty cycle of 33%. The same study was done for a rectangular waveform with a duty cycle of 30%, obtaining a higher CV of -0.87 V (with 300 V of DV), and also the intensity and the FWHM decreased in a more evident way. A decrease of the intensity with applying a high DV and the fact that with a rectangular waveform a higher CV is achieved, are fully agreed with experimental data found in the literature.

- **Medical applications: Online Monitoring of an Exhaled analgesic in Patients under Anesthesia.** The work has been carried out during a stage at the Korean Institute of Science and Technology in Europe, Saarbrücken Germany. Work was done with a commercial ion mobility spectrometer: BioScout from B & S Analytik. Investigations were held at the *Chirurgische Universitätsklinik* from Homburg (Germany). Background emissions have showed that different instruments can be used after aligning them to compare and characterize

MCC/IMS chromatograms. The alignment compound found for the positive mode was the monomer Benzothiazol. The main task has been the study of the viability for drugs online monitoring. The analysis of the exhaled breath of patient's before and during surgery was done. Studied drug was a short-acting analgesic (remifentanyl). Initially, as remifentanyl is metabolized in the blood, also an *in vitro* blood test with remifentanyl was done to determine some peaks that would be used to search in the IMS chromatograms of patient's breath. Four candidate peaks were found for the opioid remifentanyl. Eighteen patients were studied, eight in positive mode and ten in negative mode. A control group was defined, for the positive mode. Two of the identified peaks of remifentanyl, the Remi_1 and Remi_3 peaks, were found only one time each in two different measures of patients. Remi_1 peak was obtained for the highest remifentanyl dose (20 ng/mL) a person can receive, but not for lower concentrations of remifentanyl in patients while it was clearly found the *in vitro* blood test. For Remi_3 peak no relation with remifentanyl dose was observed, being identified in the *in vitro* blood test as remifentanyl's major metabolite GI90291.

Further work

All this work and the above-mentioned contributions have opened a very fruitful research field at the Gas Sensors Group at the IMB-CNM and the Clinical Diagnostics group at KIST-Europe. Of course, much work is still to be initiated; some ongoing activities have to carry on. Some of the proposed lines for future development of the p-FAIMS field are:

- Further **simulations** of the micro p-FAIMS device with COMSOL Multiphysics should include a 3D simulation, the study of more geometric parameters affecting the ions detection like variation of the distance between filtering and detection electrodes, also detector electrodes length and ions interactions, among others.
- The **p-FAIMS** should be studied with a gap of 0.5 mm, to ensure the simulation results. Also different filtering electrodes lengths should be analyzed. The acquisition of a high voltage to have a proper asymmetric waveform up to 80 Td, is highly recommended. Different gases should be studied up to 80Td or more to ensure that the p-FAIMS can differentiate them.
- The **remifentanyl** study in patients must be repeated to ensure that the Remi_1 peak 'identified' as the remifentanyl drug is produced in the breath of patients with a high dose of remifentanyl (20 ng/mL), and that the identification of Remi_3 peak as remifentanyl's major metabolite. Also GC-MSD measurements of remifentanyl metabolites and also their interaction with blood should be carried out.

List of Publications

During the work of this thesis, the following works have been published:

1. R. Cumeras, I. Gràcia, E. Figueras, L. Fonseca, J. Santander, M. Salleras, C. Calaza, N. Sabaté, C. Cané
Modeling Vapor Detection in a Micro Ion Mobility Spectrometer for Security Applications
Procedia Engineering 5 (2010) 1236-1239
2. R. Cumeras, I. Gràcia, E. Figueras, L. Fonseca, J. Santander, M. Salleras, C. Calaza, N. Sabaté, C. Cané
Finite-Element Analysis of a Miniaturized Ion Mobility Spectrometer for Security Applications
Sensors and Actuators B – Chemical 170 (2012) 13-20
3. R. Cumeras, I. Gràcia, E. Figueras, L. Fonseca, J. Santander, M. Salleras, C. Calaza, N. Sabaté, C. Cané
Modelling a P-FAIMS with Multiphysics FEM
Journal of Mathematical Chemistry 50 2 (2012) 359-373
4. R. Cumeras, T. Schneider, P. Favrod, E. Figueras, I. Gràcia, S. Maddula, J.I. Baumbach
Stability and Alignment of MCC/IMS devices
International Journal for Ion Mobility Spectrometry 15 1 (2012) 41-46
5. R. Cumeras, P. Favrod, K. Rupp, E. Figueras, I. Gràcia, S. Maddula, J.I. Baumbach
Influence of Operational Background Emissions on Breath Analysis using MCC/IMS devices
International Journal for Ion Mobility Spectrometry 15 2 (2012) 69-78
6. R. Cumeras, E. Figueras, I. Gràcia, S. Maddula, J.I. Baumbach.
What is a good Control Group?
International Journal for Ion Mobility Spectrometry (2013), *published online*

In preparation or Submitted:

1. R. Cumeras, I. Gràcia, E. Figueras, C. Cané
Complementary analysis of design and operational parameters of a p-FAIMS using Multiphysics FEM
Simulation Modelling Practice and Theory, *submitted*
2. R. Cumeras, S. Vallejos, E. Cabruja, E. Figueras, I. Gràcia, C. Cané
Differentiation of Toluene with a novel Low Cost UV p-FAIMS, in preparation
3. R. Cumeras, H. Buchinger, P. Favrod, I. Gràcia, E. Figueras, S. Maddula, Th. Volk, S. Kreuer, J. I. Baumbach
Remifentanyl differentiation by ion mobility spectrometry in patients under anesthesia: First results of a pilot study
Journal of Breath Research, in preparation

Conferences:

Total number of contributions to conferences: 21 (14-international, 7-national)

Invited Contributions

1. C. Cané, I. Gràcia, R. Cumeras, C. Calaza, M. Salleras, J. Santander, E. Figueras, L. Fonseca, N. Sabaté, D. Matatagui, M.J. Fernández, J.L. Fontecha, J. Gutiérrez, M.C. Horrillo
Micro-Nano Technologies for Gas Sensing Devices
In Proceedings of the Baltic Polymer Symposium 2010: International Session on Nanomaterials: fabrication, characterisation and applications, Page 163
2010 September 8-11th, Palanga (Lithuania)
2. I. Gràcia, S. Vallejos, R. Cumeras, M. Salleras, E. Figueras, J. Santander, N. Sabaté, J.P. Esquivel, C. Calaza, L. Fonseca, C. Cané
Sensors and Micro and Nano Technologies for the Food Sector
In Proceedings of 9th Spanish Conference on Electron Devices (CDE13) 103-106
2013 February 12-14th, Valladolid (Spain)
3. R. Cumeras
Gastric Interferences in Breath Analysis: Sweets case
Breath Summit 2013: International Conference of Breath Research
Workshop III: Ion Mobility Spectrometry
2013 June 9th, Saarbrücken/Wallerfangen (Germany)

Selected Conferences:

- i. R. Cumeras, I. Gràcia, E. Figueras, L. Fonseca, J. Santander, C. Calaza, N. Sabaté, C. Cané
Modeling a P-FAIMS with COMSOL
10th International Conference on Mathematical Methods in Science and Engineering. 2010 June 27-30th, Almería (Spain)
- ii. R. Cumeras, I. Gràcia, E. Figueras, P. Ivanov, L. Fonseca, J. Santander, N. Sabaté, C. Cané

- Modelling of a Micro Ion Mobility Spectrometer for vapour detection in Security Applications*
International Meeting on Chemical Sensors. 2010, July 11-14th, Perth (Australia)
- iii. R. Cumeras, I. Gràcia, E. Figueras, L. Fonseca, J. Santander, M. Salleras, C. Calaza, N. Sabaté, C. Cané
Modeling Vapor Detection in a Micro Ion Mobility Spectrometer for Security Applications
EuroSensors XXIV. 2010, September 5-8th, Linz (Austria)
- iv. R. Cumeras, I. Gràcia, E. Figueras, L. Fonseca, J. Santander, M. Salleras, C. Calaza, N. Sabaté, C. Cané
COMSOL Modelling of a Planar Micro Ion Mobility Spectrometer
COMSOL Conference 2010. 2010, November 17-19th, Paris (France)
- v. R. Cumeras, I. Gràcia, E. Figueras, L. Fonseca, J. Santander, M. Salleras, C. Calaza, N. Sabaté, C. Cané
Planar Micro Ion Mobility Spectrometer Modelling for Explosives Detection
8th Spanish Conference on Electron Devices (CDE11). 2011 February 8-11th, Palma de Mallorca (Spain)
- vi. R. Cumeras, K. Rupp, T. Schneider, P. Favrod, S. Maddula, J.I. Baumbach
Influence of room air and operational background emissions on breath analysis using MCC/IMS
20th Annual Conference on Ion Mobility Spectrometry. 2011 July 24-29th, Edinburgh (England)
- vii. R. Cumeras
A Gas Sensor: the Ion Mobility Spectrometer
1st Interdisciplinary PhD Student Meet (*Primera joranda d'Investigadors Predoctorals Interdisciplinària*, JIPI). 2013 February 7th, Barcelona (Spain)
- viii. R. Cumeras, P. Favrod, H. Buchinger, S. Kreuer, Th. Volk, E. Figueras, I. Gràcia, S. Maddula, J.I. Baumbach
Online-monitoring of drugs with ion mobility spectrometry in patients under anesthesia
Breath Summit 2013: International Conference of Breath Research. 2013 June 9-12th, Saarbrücken/Wallerfangen (Germany)

Other Conferences not related to the Thesis work:

- a. P. Ivanov; I. Gràcia; F. Blanco; J.-P. Raskin; R. Cumeras; N. Sabaté; X. Vilanova; X. Correig; L. Fonseca; E. Figueras; J. Santander; C. Cané
Preconcentrator-based μ -system for low-level benzene detection sensor
Material SPIE Smart, Nano+Micro-Smart Systems. 2008 December 9-12th, Melbourne (Australia)
- b. S. Vallejos, R. Cumeras, E. Figueras, C. Cané, C. Blackman, I. Gràcia
Localized heating to tungsten oxide nanostructures deposition on gas microsensor arrays via aerosol assisted CVD
Transducers 2013 & EuroSensors XXVII. The 17th International Conference on Solid-State Sensors, Actuators and Microsystems. 2013 June 16-20th, Barcelona (Spain)

[This page intentionally left blank]

List of Abbreviations, Contractions, Symbols and Acronyms

Here are resume the main Abbreviations, Contractions, Symbols and Acronyms (ACSA) found in this Thesis.

267

1/K₀	Inverse Reduced mobility (Vs/cm ²)
<i>α</i>	Function $\alpha(E/N)$
<i>α</i>₂	First term of function $\alpha(E/N)$ expansion (Td ⁻²)
<i>α</i>₄	Second term of function $\alpha(E/N)$ expansion (Td ⁻⁴)
Ac	2-propanone or acetone
AC	Alternating current (V(t))
AMDIS software	Automated Mass Spectral De-convolution and Identification System
APCI	Atmospheric Pressure Chemical Ionization
APPI	Atmospheric Pressure Photo Ionization
AR	Aspect Ratio (A/Td)
ASA	American Society of Anesthesiologists
BIS	Bispectral Index™
BNG	Bradbury-Nielsen Gate
BT	Benzothiazol
c	Concentration (ppm)
c-FAIMS	Cylindrical FAIMS
CD	Corona Discharge
CD-APCI	Corona Discharge Atmospheric Pressure Chemical Ionization
CG	Control Group
COPD	Chronic Obstructive Pulmonary Diseases

CT	Coagulation Tube
CT_n#	Peaks due to the CT in negative mode
CT_p#	Peaks due to the CT in positive mode
CV	Compensation Voltage (V)
CWA	Chemical Warfare Agent
D	Diffusion (cm^2/s)
DC	Direct Current (V)
DMA	Differential Mobility Analyzer
DMMP	DiMethyl Methyl Phosphonate
DMS	Differential Mobility Spectrometer
DNT	2,4-DiNitroToluene
DRIE	Deep Reactive Ion Etching
DV	Dispersion Voltage (V)
e	Electron
E	Electric Field (V/cm)
E_C	Compensation Field (V/cm)
E_D	Dispersion Field (V/cm)
E/N	Electric field normalized with Number density (Td)
E_C/N	Compensation Field normalized with Number density (Td)
E_D/N	Dispersion Field normalized with Number density (Td)
EEG	ElectroEncephaloGram
ER	Entering Room (in the operating rooms distribution)
ESI	Electrospray Ionization
ET	EndoTracheal
F	Female
FAIMS	high Field Asymmetric Ion Mobility Spectrometer
FEM	Finite Elements Methods
FT-ICR	Fourier-Transform Ion-Cyclotron Resonance
FWHM	Full width at half maximum
g	Gap (mm)
GC	Gas Chromatography
GC-MSD	Gas Chromatography coupled to a Mass Spectrometer Detector
h	Planck constant ($6.626 \cdot 10^{-34} \text{ J} \cdot \text{s}$)
HF	Hydrofluoric acid
HS	Head Space
HV	High Voltage
I	Intensity (A) When conversion with a current amplifier (V)
IMS	Ion Mobility Spectrometry
K	Ion Mobility Coefficient (cm^2/Vs)
K₀	Reduced mobility (cm^2/Vs)
KIST-Europe	Korea Institute of Science and Technology in Europe
KOH	Potassium hydroxide
L	Drift tube length (cm)
LC	Liquid Chromatography
LM	Laryngeal Mask airway

M	Ion-neutral molecule. Monomer Male
MH⁺	positive Monomer
M₂H⁺	positive Dimer
M₃H⁺	positive Trimer
(M-H)⁻	negative Monomer
MALDI	Matrix-Assisted Laser Desorption/Ionization
MCC	Multi-Capillary Column
MCC-IMS	Multi-Capillary Column Coupled To Ion Mobility Spectrometry
MS	Mass Spectrometry
MSD	Mass Spectrometer Detector
MW	Molecular Weight (uma or u)
N	Number density (the number of molecules per unit volume) (cm ³) Nonanal (medical applications)
N₂	Nitrogen molecule
N_A	Avogadro's number (6.022×10 ²³ mol ⁻¹)
NIST	National Institute of Standards and Technology, from the U.S.
OP	Operation Room (in the operating rooms distribution)
OR	Outing Room (in the operating rooms distribution)
O₂	Oxygen molecule
P	Pressure (Pa)
P_{amb}	Ambient Pressure (101,325 kPa)
P1n-...-P10n or P#n	Patients studied in negative mode
P1p-...-P8p or P#p	Patients studied in positive mode
p-FAIMS	Planar FAIMS
PAT-ET	PATient being intubated with an Endotracheal Tube
PAT-LM	PATient being intubated with a Laryngeal Mask airway
PCB	Printed Circuit Board
PDE	Partial Differential Equation
PDMS	PolyDiMethylSiloxane
Pet_#	Peaks in the MCC/IMS chromatogram of the PAT-ET
Plm_#	Peaks in the MCC/IMS chromatogram of the PAT-LM
PMMA	PolyMethyl MethAcrylate
ppb	parts per billion
ppm	parts per million
PTR-MS	Proton Transfer Reaction – Mass Spectrometry
Q	Flow (sccm)
R	Resolution between two neighboring peaks (dimensionless)
R-APCI	Radioactive Atmospheric Pressure Chemical Ionization
Remi_#	Peaks due to Remifentanyl
RH	Relative Humidity (%)
RIE	Reactive Ion Etching
RL	Room Air
RL_n#	Peaks due to the RL in negative mode
RL_p#	Peaks due to the RL in positive mode

RIP	Reactant Ion Peak
R_p	Resolving Power (dimensionless)
R_p/L	Ratio R _p /L (cm ⁻¹)
RT	Retention Time (s), for a MCC
SALDI	Surface-Assisted Laser Desorption/Ionization
SC	Straight Connector
sccm	Standard centimeter cubic per minute
SIFT-MS	Selected Ion Flow Tube Mass Spectrometry
S/N	signal-to-noise ratio
SPME	Solid Phase Micro Extraction
SPME-GC-MS	Solid Phase Micro Extraction-Gas Chromatography Coupled To Mass Spectrometry
T	Temperature (K) Toluene
T_{amb}	Ambient Temperature (298.15 K)
TCI	Target-Controlled Infusion
TDS	Thermal Desorption System
TG	Tyndall Gate
TIVA	Total Intravenous Anesthesia
TOF	Time-Of-Flight
TMIMS	Transversal Modulation IMS
TNB	1,3,5-TriNitroBenzene
TNT	2,4,6-TriNitroToluene
t	Time (s)
t_{res}	Residence Time (s), for an IMS
TWIMS	Traveling-wave IMS
UV	Ultra violet
UV-lamp	Photoionization lamp in the UV range
v	Frequency (MHz)
V	Voltage (V)
VOC	Volatile Organic Compound
w_{1/2}	peak Full width at half maximum (FWHM)
w_b	peak width at the base

Annexes

[This page intentionally left blank]

Annex 4-1: LabView program to control the ACI UV-lamp

A Graphical Interfaces with LabView have been done to control the UV lamps lightning and turning off [CDL 1021-0X](#) from ACI Analytical Control Instruments GmbH [1]. Figure A4-1 shows the Graphical Interface from the *UV_ACI.vi* program. Are indicated the initial and final voltages to light the ACI UV lamp with the power supply; a file name path can be chosen; a switch is used to choose either to turn the light on or to turn it off; a plot of the $V(t)$ from the Keithley 2400 is record and plotted. Measurements do not start until the OK button is pressed.

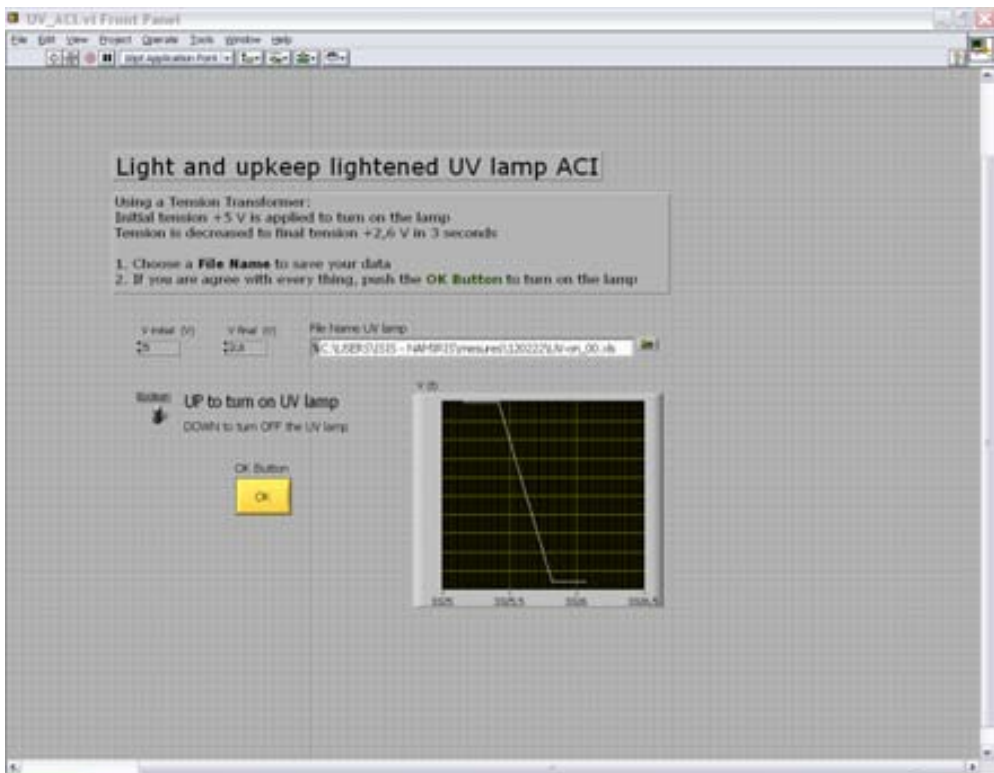


Figure A4-1: Graphical Interface of the *UV_ACI.vi* lamp control program.

Annex 4-2: LabView program to acquire data of picoAmmeter for UV lamp test

A Graphical Interfaces with LabView have been done to control the Keithley 6487 picoAmmeter [2]. Figure A4-2 shows the Graphical Interface from the *pA_UV-lamps-test.vi* program. Are indicated the number of measures desired; the voltage of operation; the file name path can be chosen; a plot of the $V(t)$ from the Keithley 6487 is record and plotted; and also is shown an array with the results. Measurements do not start until the OK button is pressed.

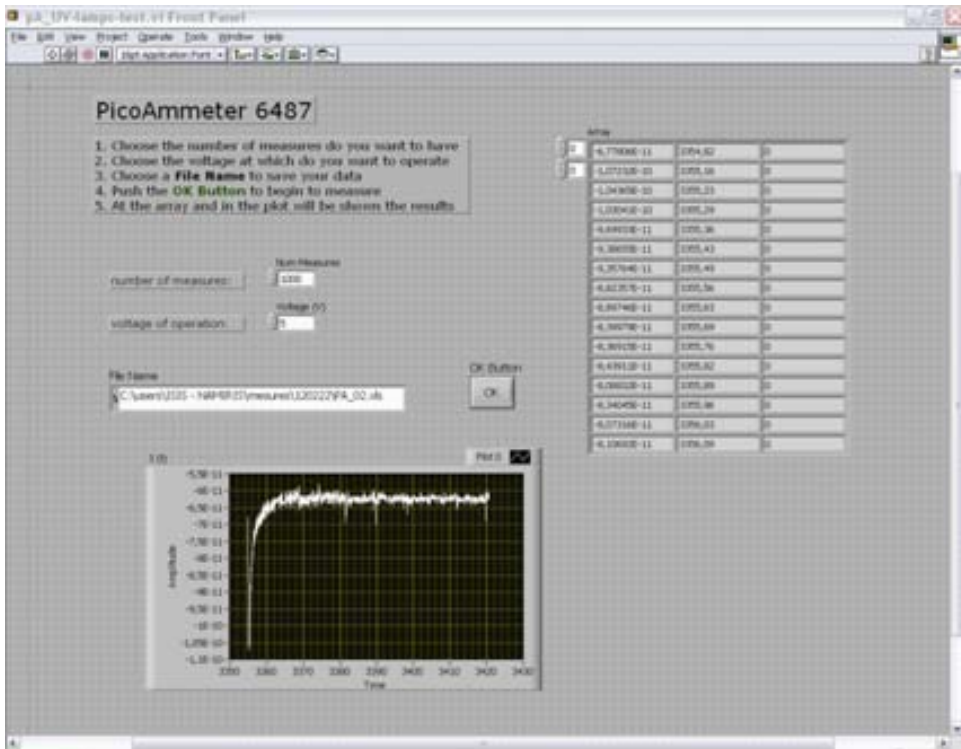


Figure A4-2: Graphical Interface of the *pA_UV-lamps-test.vi* control program.

Annex 4-3: Errors: Propagation of Uncertainty

Suppose you have a set of measurements of some magnitudes $\{A_1, A_2, A_3, \dots\}$, $\{B_1, B_2, B_3, \dots\}$, $\{C_1, C_2, C_3, \dots\}$, Now you want to calculate some other quantity f which depends on a and b and so forth. What is the uncertainty in f ? The answer can get a little complicated, but it should be no surprise that the uncertainties δA , δB , etc. “propagate” to the uncertainty of f . Here are some rules which have been used using this thesis, assuming that the quantities A , B , etc. have errors which are uncorrelated and random. Therefore, given a magnitude $f = f(a, b)$ its error δf can be calculated using the standard variation (σ) as [3]:

$$\delta f = \sigma = \sqrt{\left(\frac{\partial f}{\partial A} \cdot \delta A\right)^2 + \left(\frac{\partial f}{\partial B} \cdot \delta B\right)^2}$$

Table A4-1 shows the variances (σ^2) of simple functions of the real variables A , B and known real-valued constants a , b .

	Function	Error
	$f = aA$	$\delta f = \sqrt{a^2 \delta A^2}$
Addition or subtraction	$f = aA \pm bB$	$\delta f = \sqrt{a^2 \delta A^2 + b^2 \delta B^2}$
Multiplication or division	$f = AB, f = \frac{A}{B}$	$\delta f = f \sqrt{\left(\frac{\delta A}{A}\right)^2 + \left(\frac{\delta B}{B}\right)^2}$

Table A4-1: Examples of errors calculated by propagation of uncertainties used in this thesis.

Annex 4-4: LabView program to acquire data of picoAmmeter continuously

A Graphical Interface with LabView has been done to control the data acquisition of the picoAmmeter 6487. Figure A4-3 shows the Graphical Interface from the *pAcontinuous.vi* program. User can choose the file name and path, the Voltages up and down from the step, the number of repetitions desired and the variable y defined as $t(V_{\text{down}}) = y \cdot t(V_{\text{up}})$ that is the number of measures for each part of the step. Plots of $V(t)$, $I(V)$ and $I(t)$ are plotted. Measurements do not start until the OK button is pressed.

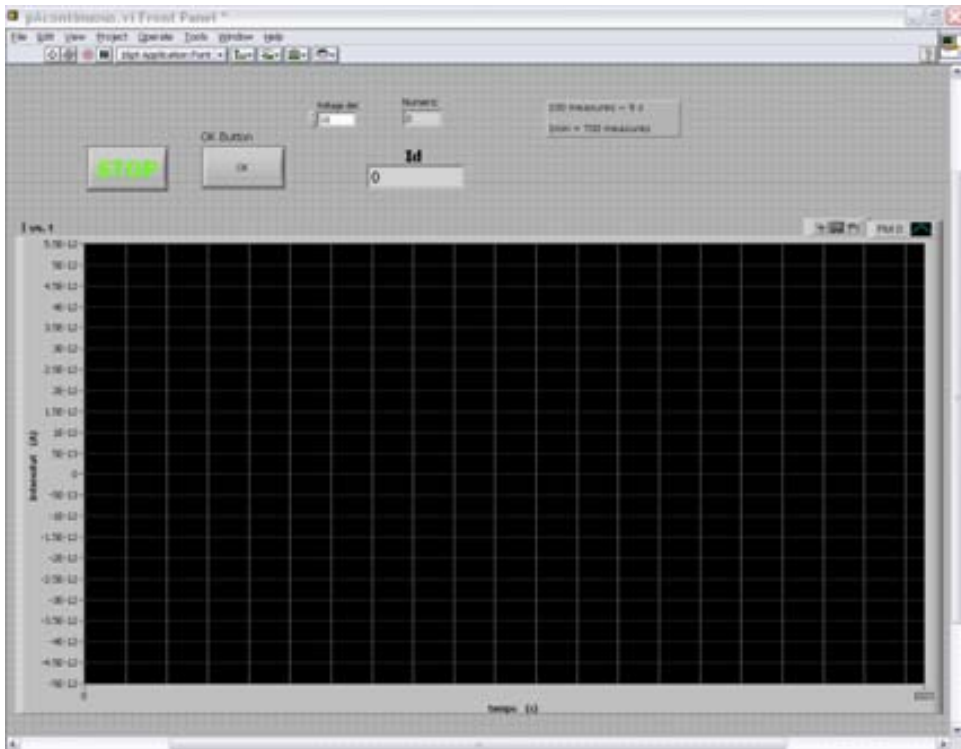


Figure A4-3: Graphical Interface of the *pAcontinuous.vi* control program.

Annex 4-5: LabView program to acquire data of picoAmmeter for a fixed Compensation Voltage Scan

A Graphical Interface with LabView has been done to control the data acquisition of the picoAmmeter 6487 while with a Keithley 2400 a compensation voltage (CV) scan was done. Figure A4-4 shows the Graphical Interface from the *pA_VcScan.vi* program. User can choose the detector voltage, the initial and final compensation voltages and the step of the scan between them. Plots of CV(t) and I(t) are plotted. Measurements do not start until the OK button is pressed. Figure A4-4 shows the results of 1 ppm of Toluene twice and in between a measurement only with nitrogen, all at a flow rate of 1,000 sccm.

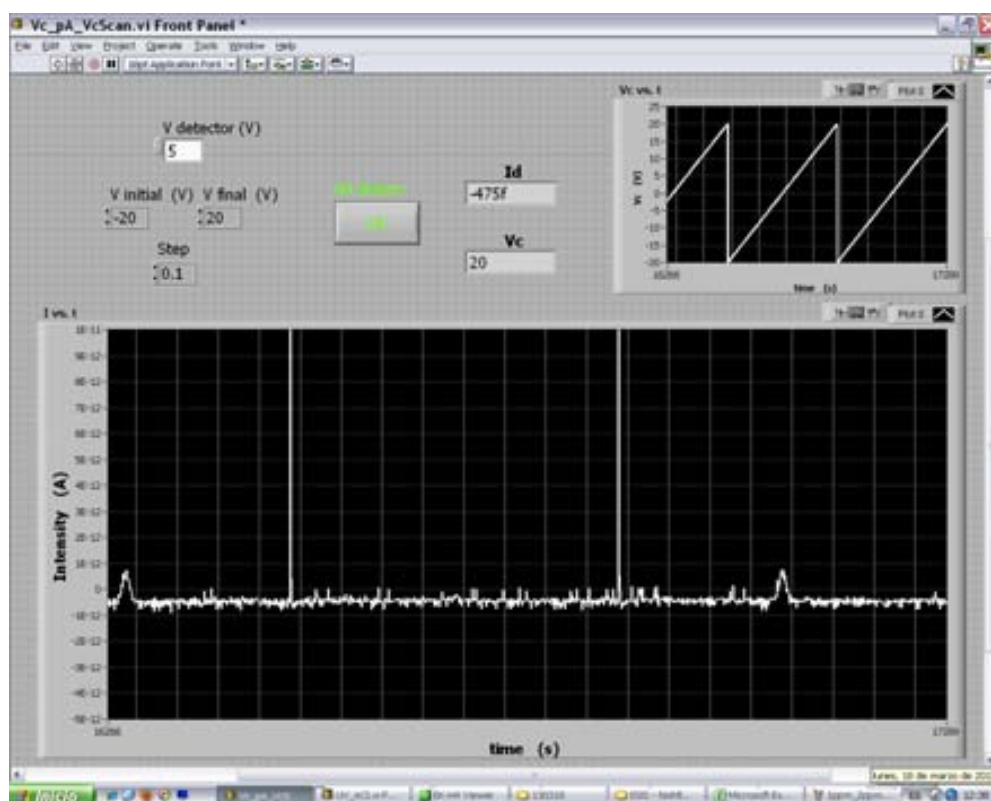


Figure A4-4: Graphical Interface of the *pA_VcScan.vi* control program.

Annex 5-1: Box-and-whisker plot

A box -and-whisker plot (sometimes called simply a box plot) is a histogram-like method of displaying data, invented by J. Tukey. An example of a box plot is presented in the Figure A5-5. The most important parts of the plot are indicated and explained. There are 3 main parts of the box-and-whisker plots:

- 1) **Box** definition. The horizontal line inside the " box" is the 2nd quartile (Q2 or median). The lower border of the " box" is the 1st quartile (Q1) and 25 % of observations have lower value than Q1. The upper border of the " box" is the 3rd quartile (Q3) and 75 % of observations have higher value than Q3. The interquartile range is defined as $IQR = Q3 - Q1$.
- 2) **Edges** definition. The edge of the lower whisker is the smallest, not outlying observation (value of smallest observation which lays between Q1 and $Q1 - 1,5 \times IQR$.); the edge of the higher whisker is the highest, not outlying observation (value of highest observation which lays between Q3 and $Q3 + 1,5 \times IQR$, where $IQR = Q3 - Q1$).
- 3) **Outliers**. The outlying observations are those suspicious observations you should investigate: *mild outlier* - value is between $Q3 + 1,5 \times IQR$ and $Q3 + 3 \times IQR$, or between $Q1 - 1,5 \times IQR$ and $Q1 - 3 \times IQR$); *extreme outlier* - value is higher than $Q3 + 3 \times IQR$, or lower than $Q1 - 3 \times IQR$).

278

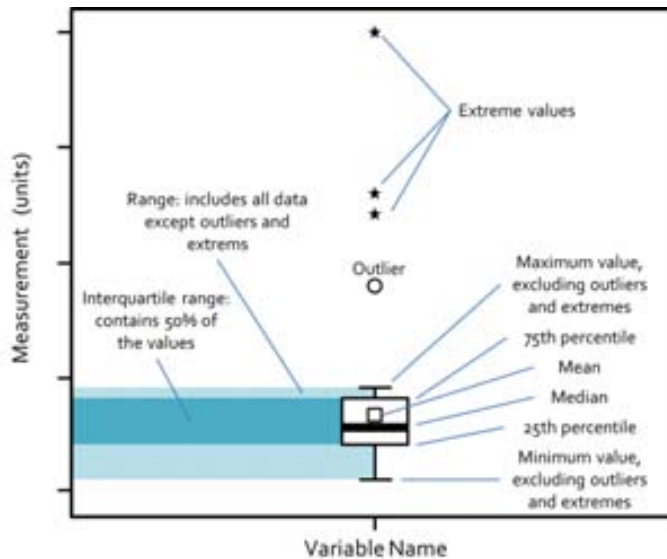


Figure A5-5: The main features of a box plot, including outliers or extreme values excluded from the range.

Annex 5-2: Control Group definition

The defined control group was reduced with two conditions, to be comparable to breath taken ‘directly’ from the lungs: 1) not having done the teeth brushing, and 2) without having eaten a candy or chewed a bubblegum. The peaks used to discriminate the chromatograms of the control group that accomplish the fixed conditions from the ones that not, have been chosen to be clearly identifiable.

A5-2.a Tooth brushing condition

In Figure A5-6 is shown an MCC-IMS chromatogram of one measurement of the control group members CG-5, showing the peaks due to the toothpaste. The toothpaste peak chosen was the peak at $RT = 120$ s and $1/K_0 = 0.889$ Vs/cm².

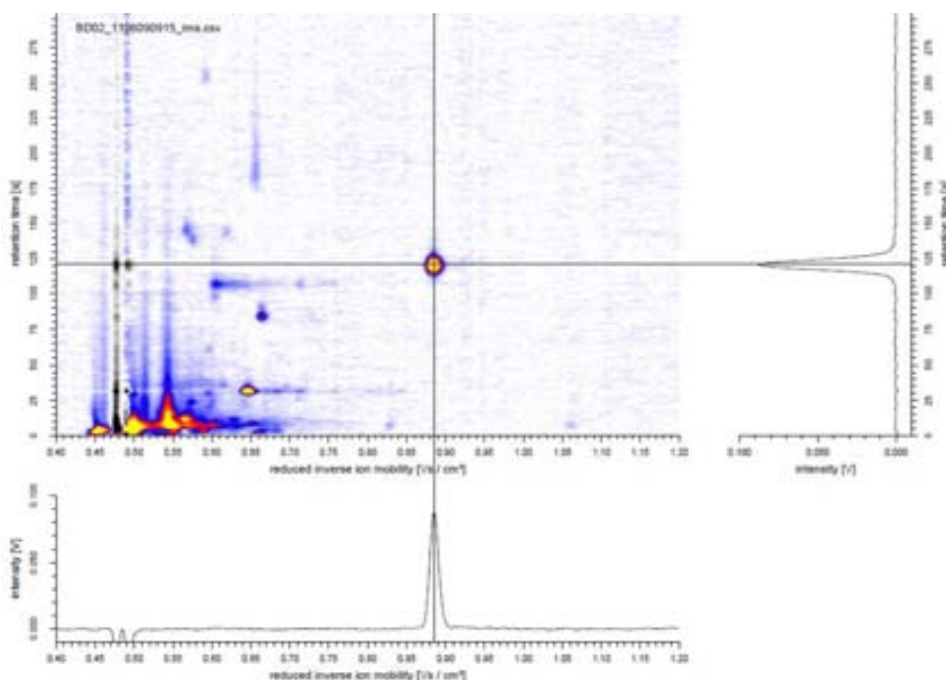


Figure A5-6: MCC-IMS chromatogram of CG-5 with recent teeth brush. The marked peak corresponds to the toothpaste peak.

From the 156 measurements available, only 44 had the peak due to toothpaste. From these, 32 measurements were from females and only 12 males. The $CG_{\text{toothpaste}}$ condition

would be of 112 measurements (55 F / 57 M). In Figure A5-7 is shown the Box and whisker plot discriminating the control group measurements that have no toothpaste from the one that have it. In Figure A5-7 is shown the Box and whisker plot discriminating the control group measurements that have no toothpaste from the one that have it.

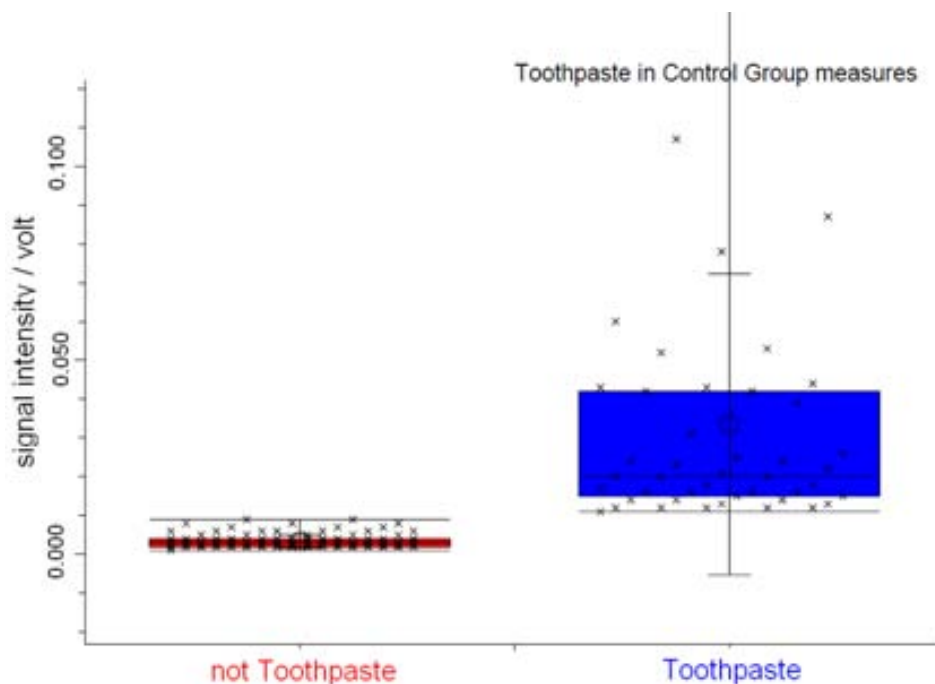


Figure A5-7: Box-and-whisker plots of the samples with toothpaste peak in the control group measures.

A5-2.b Candy's condition

In Figure A5-8 is shown an MCC-IMS chromatogram of one measurement of the control group members CG-9, showing the peaks due to a candy. The chosen peak to carry out the candy's discrimination was the Menthol monomer peak, that appears at a $RT = 115$ s and $1/K_0 = 0.613$ Vs/cm².

In Figure A5-9 is shown the Box and whisker plot discriminating the control group measurements that have no candy from the ones that have it. From the 156 measurements available, only 18 had the menthol peak due to a candy. From these, half were found to be from females and the other half were from males. The $CG_{\text{candy condition}}$ would be of 138 measurements (78 F / 60 M).

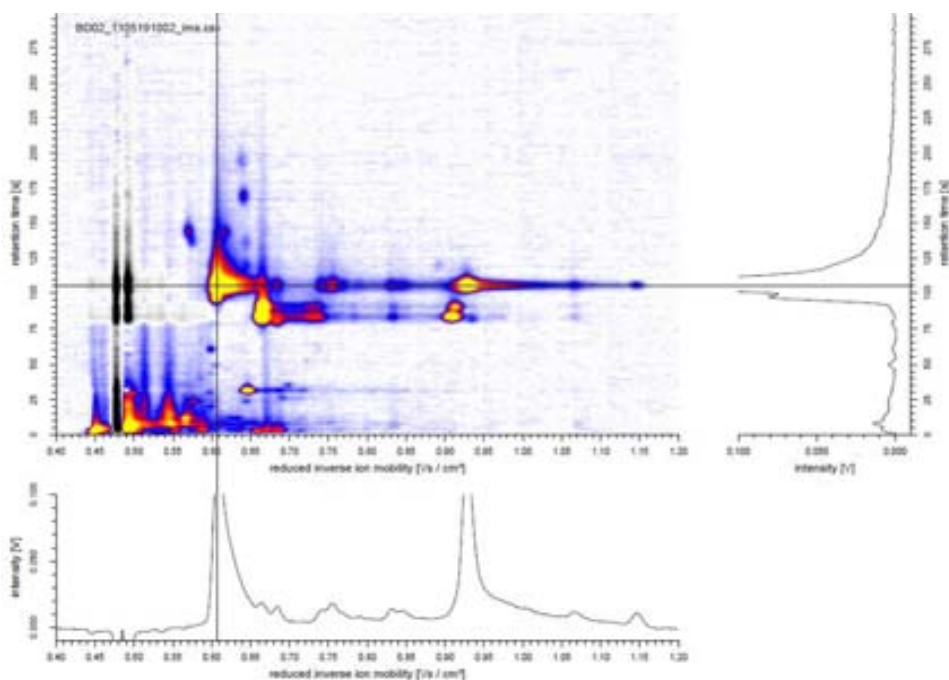


Figure A5-8: MCC-IMS chromatogram of CG-9 with a candy. The marked peak corresponds to Menthol monomer.

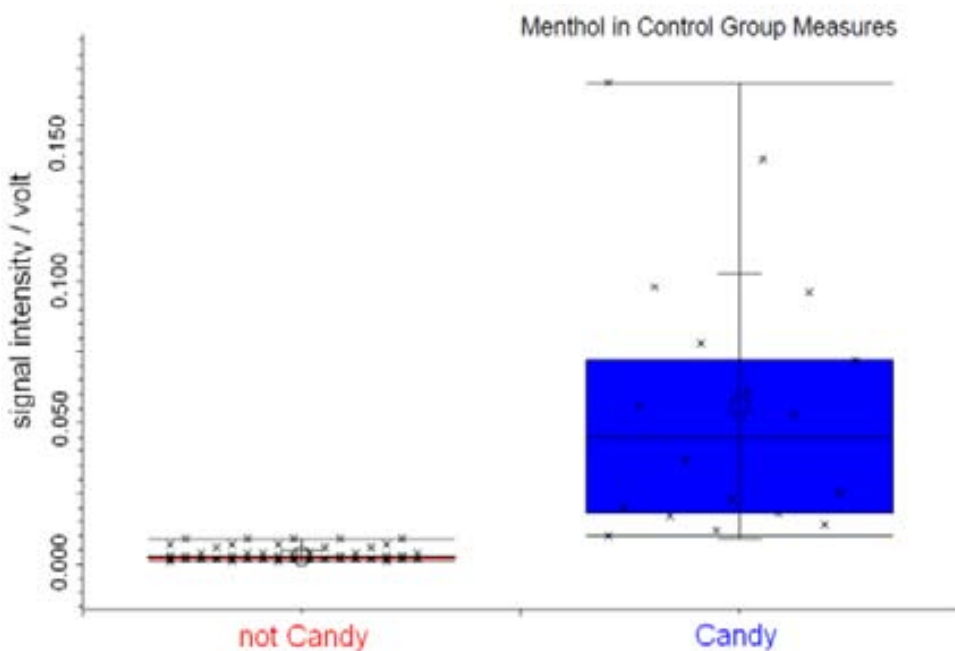


Figure A5-9: Box-and-whisker plots of the samples with Menthol monomer peak in the control group measures.

Annex 5-3: Ethics committee approbation



Figure A5-10: Ethics committee approbation document.

Annex 5-4: Propofol peaks in the MCC-IMS Chromatograms

The obtained propofol peaks in positive mode, once aligned with Benzothiazol at RT = 144 s, is $1/K_0 = 0.676 \text{ Vs/cm}^2$ and a RT = 512 s, shown in Figure 5-11. Without alignment appears a RT = 595 s. Unlike in the positive mode, propofol forms dimers in the negative mode at high concentrations, as can be seen in Figure 5-12. The dimer is formed in the ionization chamber after the separation by the MCC. Obviously, the monomer and the dimer have the same RT (514s), being the $1/K_0$ value higher for the dimer (0.952 Vs/cm^2) than the monomer (0.727 Vs/cm^2). The dimer is effectively larger than the monomer, leading to more collisions with the drift gas and therefore to a higher drift time. The probability of a formation of dimer or polymer is enhanced by a high concentration of analytes in the ionization chamber.

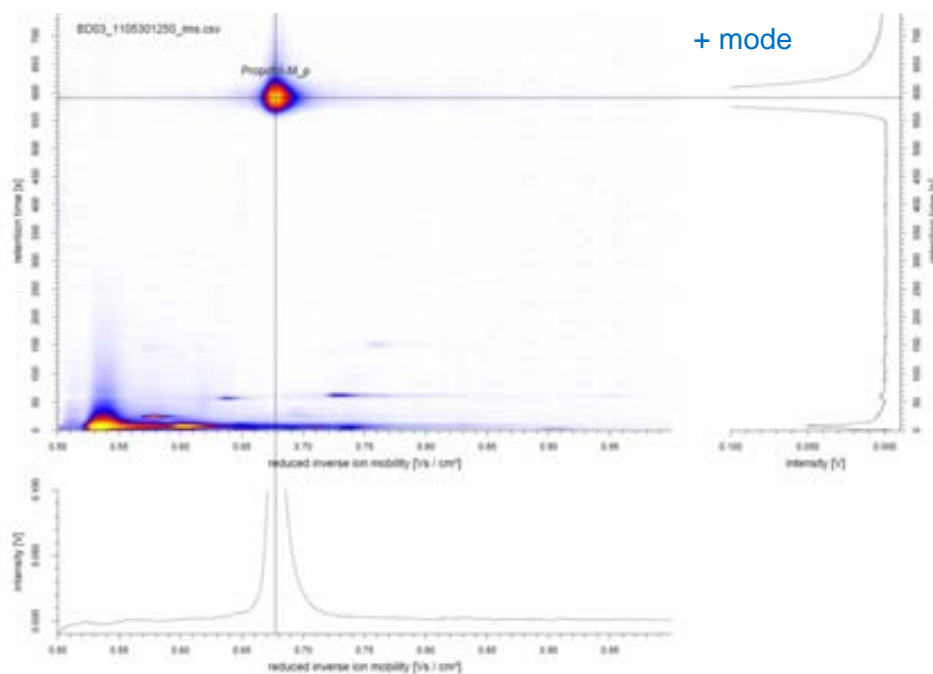


Figure 5-11: MCC-IMS chromatogram the head space of propofol in + mode. Cross show the identified monomer peak Propofol-M_p.

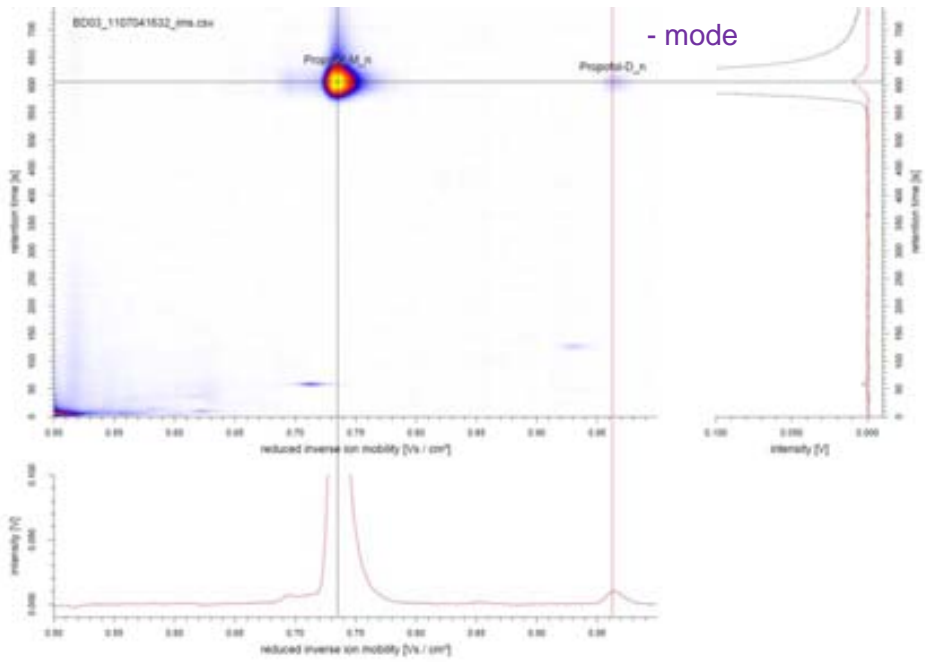


Figure 5-12: MCC-IMS chromatogram the head space of propofol in - mode. Cross show the identified monomer Propofol-M_n and dimmer Propofol-D_n peaks.

Annex 5-5: Respirator systems

Here are shown the respirator systems from an entering room (ER) and an operation room (OP).

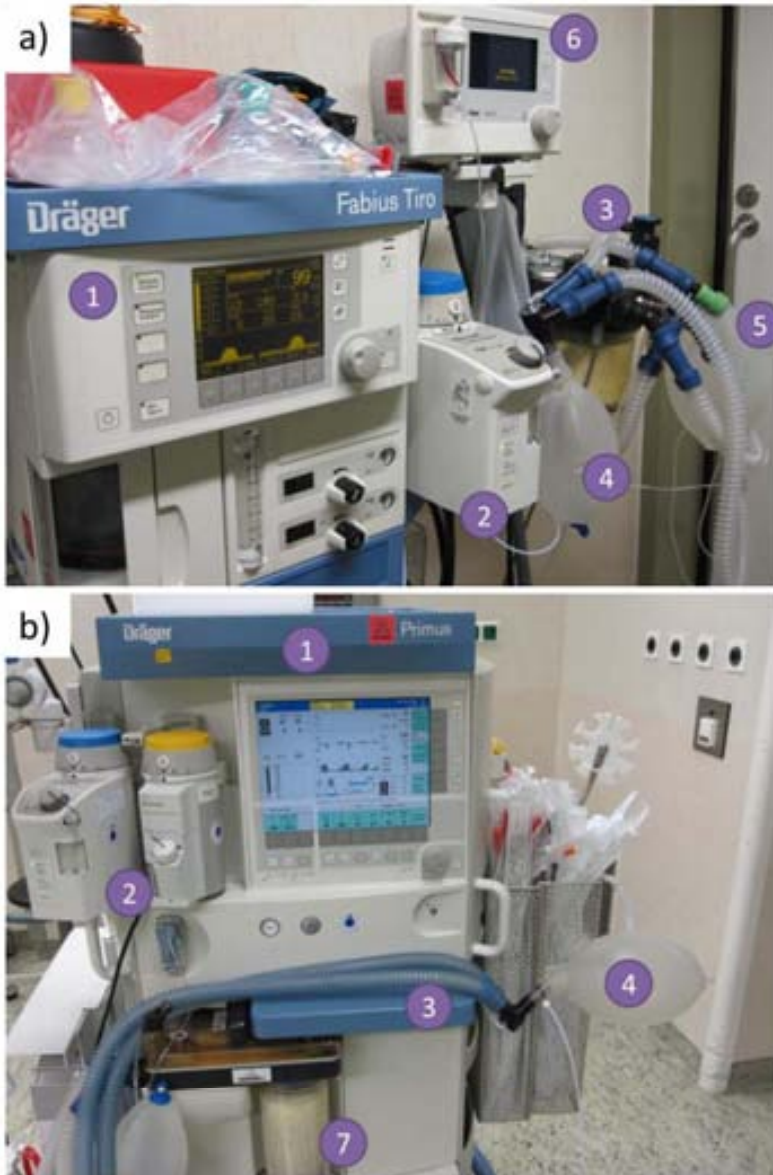


Figure A5-13: (a) Picture of the Fabius Tiro® respirator system available in the ER's. (b) Picture of the Primus® respirator system in the OP's. 1 Respiratory system; 2 Gas-anesthetic's (not used); 3 inspiratory and expiratory tubes; 4 artificial lung; 5 air reservoir; 6 Anesthetic gas Monitor Vamos® from Dräger; 7 Absorber filled with soda lime to eliminate the CO₂ excess.

Annex 5-6: Patient's data

Here are resumed the data patient and the drugs they received while anesthetized under surgery.

A5-6.a Positive mode

ID	OP #	Patient data	Protocol #	Intubation method (ET/LM)	Gender (M/F)	Age (years)	Risking	Daily-medication	Pre-medication
P1p	3	CA3338938	498961	ET	M	62	Smoker	-	7.5mg Dormicum®
P2p	3	CA3339923	498959	ET	M	78	COPD	Delix®, Symbicort®, Spiriva®	7.5mg Dormicum® 40mg Pantazol®
P3p	3	CA3339279	498356	ET	M	63	Smoker	-	10mg Dormicum®
P4p	1	CA3341100	498987	ET	M	42	-	-	7.5mg Dormicum®
P5p	1	CA3337232	498982	ET	F	54	Smoker, Diabetica	Anti-diabetic	7.5mg Dormicum®
P6p	1	CA3365237	519873	ET	M	75	Alcoholic	Carvedilol, Aggrenox®, Ramipril, Zocor®	7.5mg Dormicum® 40mg Pantazol®
P7p	3	CA3376409	519880	ET	F	57	-	-	7.5mg Dormicum®
P8p	2	CA3373544	519806	ET	F	41	-	-	7.5mg Dormicum®

Table A5-2: Data recorded of the studied patients in + mode.

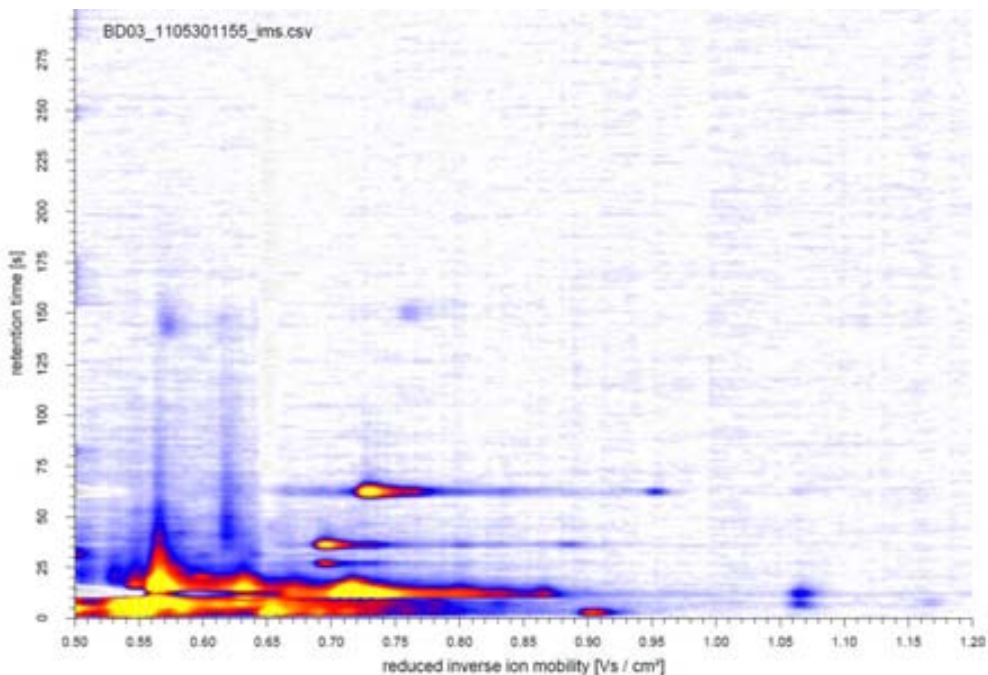


Figure A5-14: MCC-IMS chromatogram of the first measurement of patient P2p.

ID	anesthetic	analgesic	relaxant	others	place	Comments
P1p	Propofol	Remifentanyl Fentanyl	Mivacron	-	ER	
P2p	Propofol	Remifentanyl Fentanyl	Mivacron	-	ER	
P3p	Propofol	Remifentanyl Fentanyl	Mivacron	-	ER	
P4p	Propofol	Remifentanyl Fentanyl	Mivacron	-	ER	
P5p	Propofol	Remifentanyl Fentanyl	Mivacron	-	ER	
P6p	Propofol	Remifentanyl	Nimbex	Clont, Ceftriaxon, Ephedrin, Lysthenon® 2%, Dipidolor and Metamizol	ER/OP	
P7p	Propofol	Remifentanyl	Nimbex	Ephedrin, Zofram, Fortecortin, Clont, Ceftriaxane, propofol (150mg), Metamizol, Dipidolor and Nimbex ¹	ER/OP	Cannula not well injected. Patient was awaking, so there was injected extra propofol
P8p	Propofol	Remifentanyl	Mivacron	Ceftriaxane, Metronidazole, Fortecortin, Zofram, Dipidolor, Metamizol and Mivacron	ER/OP	

Table A5-3: Patient's anesthesia treatment received during the measurements in + mode.

A5-6.b Negative mode

ID	OP #	Patient data	Protocol #	Intubation method (ET/LM)	Gender (M/F)	Age (years)	Risking	Daily-medication	Pre-medication
P1n	4	CA3330882	495930	ET	F	49	-	-	7.5mg Dormicum®
P2n	4	CA3314921	508241	ET	F	37	Smoker (15/day)	Femoston®, Targin®, Novalgin®	7.5mg Dormicum® 40mg Pantazol®
P3n	3	CA3342724	517197	ET	M	51	Asthma	Salbutamol	7.5mg Dormicum®
P4n	3	CA3354540	518525	ET	M	55	-	Ibuprofen	10mg Valium®
P5n	3	CA3344140	518533	ET	F	47	Smoker (30/day)	Neomercazole®	10mg Valium® 40mg Pantazol®
P6n	3	CA3341027	518529	ET	F	43	Smoker (15/day)	Propycil	7.5mg Dormicum® 40mg Pantazol®
P7n	3	CA3340847	495935	ET	M	74	-	Aspirin®, Diovan®, Zocor®	7.5mg Dormicum® 40mg Pantazol®
P8n	3	CA3355732	518480	ET	M	79	-	L-Thyroxine, Rocaltrol®, Ramipril	7.5mg Dormicum® 40mg Pantazol®
P9n	2	CA3342831	515694	LM	F	58	Smoker (8/day)	L-Thyroxine, Atosil®, Lexotanil®	7.5mg Dormicum® 40mg Pantazol®
P10n	2	CA3349626	515689	ET	M	51	-	Clexane®	10mg Valium® 40mg Pantazol®

Table A5-4: Data recorded of the studied patients in - mode.

¹ A relaxant is supplier at the end of the surgery to relax the trachea to let the intubation be taken away easily.

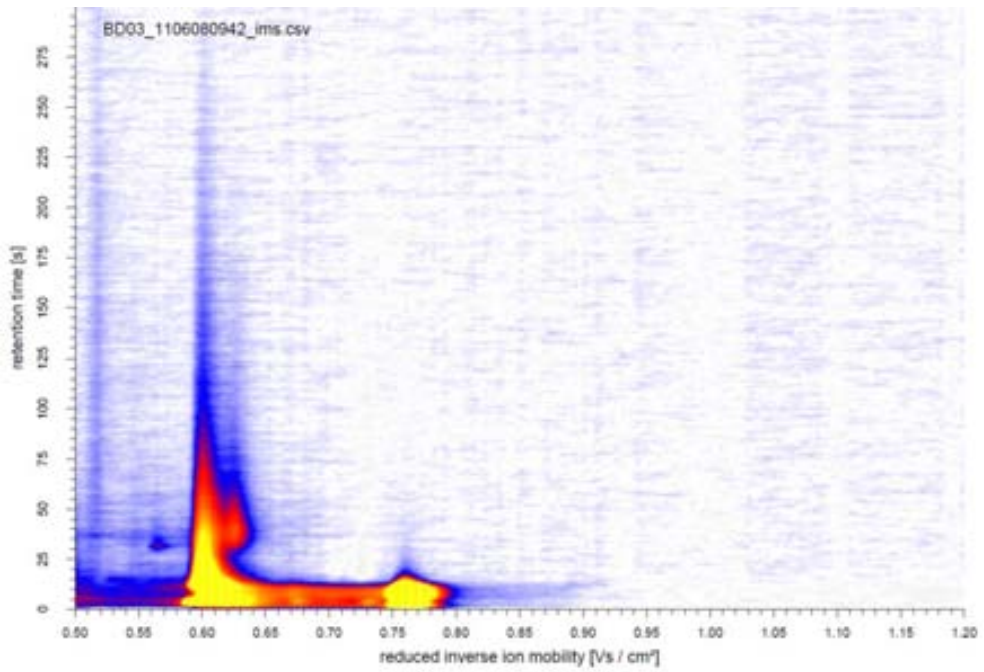


Figure A5-15: MCC-IMS chromatogram of the first measurement of patient P3n.

288

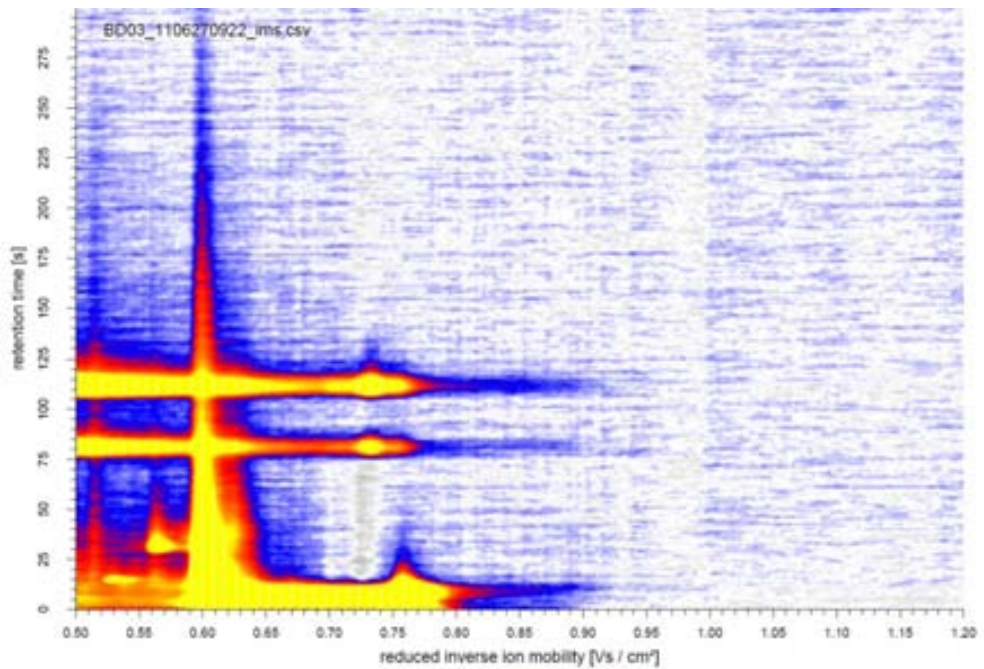


Figure A5-16: MCC-IMS chromatogram of the first measurement of patient P4n, showing a different chemistry due to the cleaning of the endotracheal tube with ethanol.

ID	anesthetic	analgesic	relaxant	others	place	Comments
P1n	Propofol	Remifentanil Fentanyl	Mivacron		ER	
P2n	Propofol	Remifentanil	Mivacron	Ephedrin	ER	
P3n	Propofol	Remifentanil	Nimbex		ER	
P4n	Propofol	Remifentanil	Nimbex	Ephedrin, Metronidazol, Ceftriaxon	ER	
P5n	Propofol	Remifentanil	Nimbex	Ceforoxin	ER	
P6n	Propofol	Remifentanil	Nimbex	-	ER/OP	
P7n	Propofol	Remifentanil	Nimbex	Ephedrin, Clont, Ramipril, Dipidolor	ER/OP	
P8n	Propofol	Remifentanil	Nimbex	Clont, Ephedrin, Ceftriazone Dipidolor, Zofram, Fortacotin, novaminsulfon	ER/OP	
P9n	Propofol	Remifentanil	-	-	ER/OP	No relaxant is supplied for LM intubation
P10n	Propofol	Remifentanil	Nimbex	Deftriazon, metronidazole, novalgin, dipidolor, Ephedrin	ER/OP	

Table A5-5: Patient's anesthesia treatment received during the measurements in - mode.

References

1. ACI Analytical Control Instruments GmbH. *UV Lamps*. [cited 2013 10th May]; Available from: http://www.aci-berlin.com/index.php?option=com_content&view=article&id=62&Itemid=81&lang=en.
2. Keithley Instruments Inc. *Model 6487 Picoammeter/Voltage Source, Reference Manual*. [cited 2013 12th May]; First ed.: [Available from: <http://www.keithley.com/products/dcac/voltagesource/application/?mn=6487>].
3. NIST/SEMATECH. *e-Handbook of Statistical Methods*. [cited 2013 22nd May]; Available from: <http://www.itl.nist.gov/div898/handbook/mpc/section5/mpc55.htm>.

[This page intentionally left blank]

